Balkan Journal of Electrical & Computer Engineering

An International Peer Reviewed, Referred, Indexed and Open Access Journal

Aim & Scope
The journal publishes original papers in the extensive field of Electrical-Electronics and Computer engineering. It accepts contributions which are fundamental for the development of electrical engineering, computer engineering and its applications, including overlaps to physics. Manuscripts on both theoretical and experimental work are welcome. Review articles and letters to the editors are also included.

Application areas include (but are not limited to): Electrical & Electronics Engineering, Computer Engineering, Software Engineering, Biomedical Engineering, Electrical Power Engineering, Control Engineering, Signal and Image Processing, Communications & Networking, Sensors, Actuators, Remote Sensing, Consumer Electronics, Fiber-Optics, Radar and Sonar Systems, Artificial Intelligence and its applications, Expert Systems, Medical Imaging, Biomedical Analysis and its applications, Computer Vision, Pattern Recognition, Robotics, Industrial Automation.

CONTENTS

The Requirement to Increase the Quality of Power Electronics in Warships

M. TURHAN

Abstract—**Today's and future warship electrical systems are very different from traditional warship electrical systems in the past. Power electronics, which are found in systems such as propulsion systems, power distribution systems, auxiliary systems, weapon systems, sonar and radar systems, is the most fundamental difference in warship design. The technical specs also vary in parallel with the development of materials used in power electronic elements. Analysis results, which vary with respect to volume, yield and temperature, change more and more in a positive manner. However, what we cannot see in the positive sense of change in the power electronics technology is the inaccuracies that arise from experience. These faults are usually due to design faults, the interference caused by the switching elements such as IGBT, tristar and triac used in power electronics, current harmonics, voltage harmonics, malfunction of sensitive devices due to AC and DC leakage in the warship's body. To prevent this, it is necessary to develop systems using power electronic elements which will not interfere with the operation of the system but may prevent them from these faults.**

Index Terms — **Capacitor, Electronic, IGBT (Insulated Gate Bipolar Transistor), Fault**

I. INTRODUCTION

VERY DIFFERENT from civilian ships, design of warships can be seen as a work of art due to the requirement of a dense usage of devices, the possession of a large number of complex systems, the survival conditions and their dependence on each other [1].

Similar to the terrestrial power system, naval warships have employed electrical power systems for over 100 years [2]. The design philosophy for naval power systems is expressed as follows: The primary aim of the electric power system design will be for survivability and continuity of the electrical power supply. to insure continuity of service, consideration shall be given to the number, size and location of generators, switchboards, and to the type of electrical distribution systems to be installed and the suitability for segregating or isolating damaged sections of the system [3].

MAHMUT TURHAN, is with Department of R&D of Medel Elektronics Company, Istanbul, Turkey, (e-mail: mahmutturhan@medelelectronik.com).

https://orcid.org/0000-0001-7633-4830

Electrical power systems did play a big role in the design of warships. The first change occurred with the introduction of electrically propelled warships. A further major push originated from the introduction of the concept of the all-electric ship proposed by the U.S. Navy. The key technology that has really changed the design options is power electronics and, in particular, the idea of a power electronic building block. The all-electric ship, at least as design concept, is one of the first real power-electronics-based power system that was ever considered [4-6].

A modern warship designed with today's technology and the technological equipments used in it are presented in Figure 1.
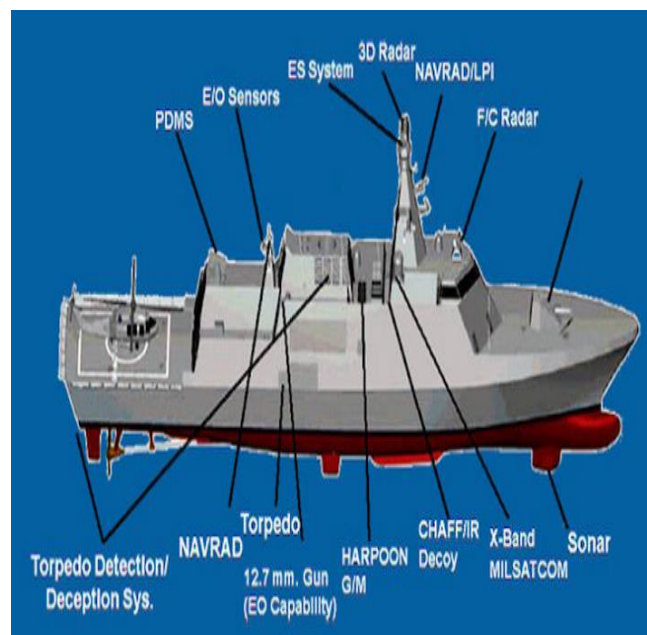
Fig.1. Modern warship and its technological equipments

The warships, which have been designed and launched in recent years and started to be produced in series, now contain quite a lot of electronic systems [7]. More electronic equipments have begun to be used because of the technological requirements such as reducing the number of personnel required, improving the efficiency of the device's survival, and facilitating the execution. Valves for control and control purposes are normally opened and closed by personnel for 10 years or even today [8]. But in newer systems, as seen in Figure 2, valve systems are opened and closed electrically at remote locations and can be seen on the machine control, on

the bridge, on the open bridge, or on the scada screen [9]. Similarly, instead of mechanical governors electronic governors are used in order to get more efficiency from the propulsion machines and generators to reduce the fuel consumption and increase cruise range [10-16].

Fig.2. Examples for traditional and new technological equipments

Main engines and related machine control systems, communication systems, some communication devices, radar etc. used in civil ships are commercial products. They are not only used in civil ships but also in warships after modification for usage in warships. All of the vital components of warships, such as communication, fire control, war systems, navigation systems, machine control systems, require 24 VDC. To be able to use these type of devices globally, even when the power is cut off, the control systems part is generally operated with 24 VDC in order to prevent the energy requirement from being cut down by providing the energy requirement from the battery.

The need for 24 VDC in warships is fulfilled with AC/DC converters and these devices are designed to backup each other. If the current protection does not work, a voltage elevation that may occur at the output of the 24 VDC source may damage all devices that are fed by itself as a result of domino effect. The damage of the vital components may result in sinking of the warship and this may cause the loss of war. [17-19]

II. PROPOSED METHOD

There are two important components that can fail in the power electronics: electronic filtering capacitors and controllable power semiconductors (MOSFET and IGBT) [20]. The increase in the need for power electronics has led us to increase the quality of the power electronics. The capacitors and MOSFETs used in the power electronics have started to lose their technical values temporarily depending on the operating conditions. Related international shipbuilding

enterprises has not yet proposed a system to protect against instantaneous change of devices.

Input voltage used on board having 440VAC 60 Hz output 30A 24VDC single output AC / DC converter is shown in Figure 3 and its open circuit diagram in Figure 4.

Fig.3. AC/DC converter

Fig.4. Open circuit diagram of AC / DC converter with 380

Because of the IGBT structure at the output of the AC / DC inverter shown in Figure 4, the latching of the microprocessors used in these systems may cause the inverter to generate an instantaneous 50-55 VDC voltage due to the wrong control signal sent to the power elements. This situation is based on a real scenario in life. In this case, we will see that 24 VD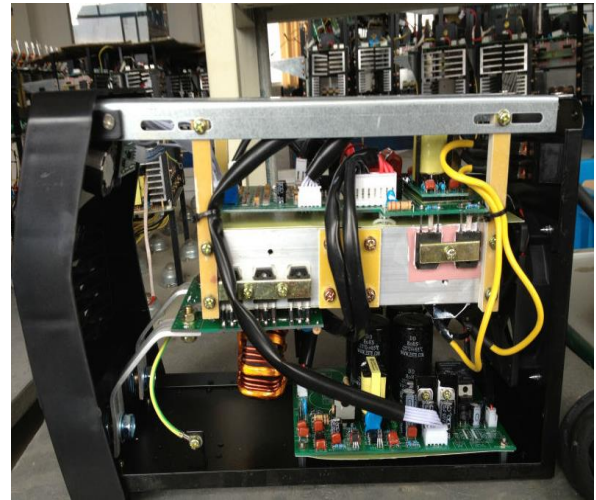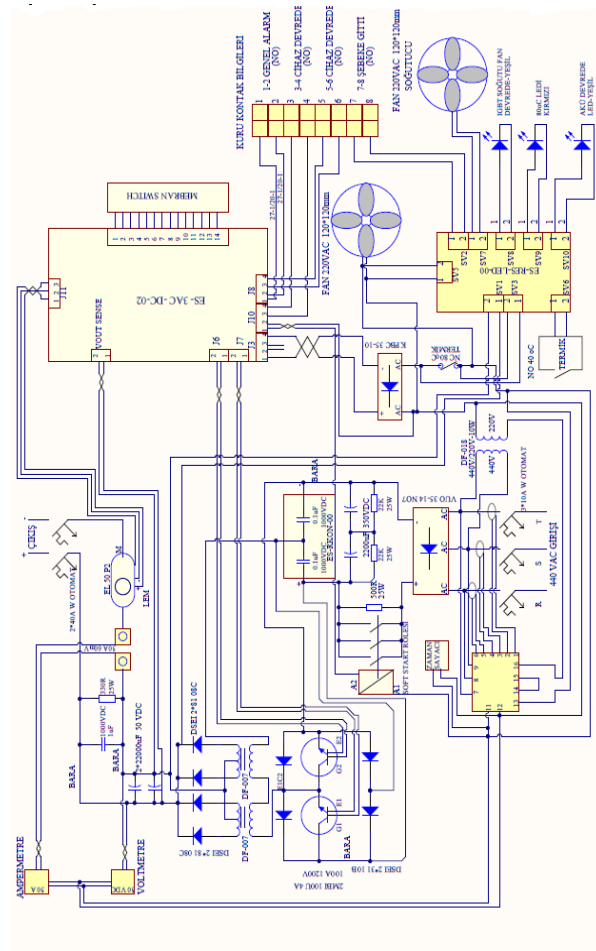C power units of all devices powered by 24 VDC in the warship suffer from damage as there is no protection against instantaneous 50-55 VDC of the devices supplied by the device. After this situation, the warship becomes an easy target. This scenario unfortunately happened in the past.

We designed a voltage protection card that can protect the device from instantaneous voltage surges due to the sudden high DC stress-free protection of the systems that require 24 VDC from the input sources. The aim is to protect this card, which is intended to prevent the malfunction of the devices, and to protect the ability of the ship to move and strike.

The open circuit diagram of the voltage protection card is presented in Figure 5.

III.   DETAILS OF THE OPEN CIRCUIT DIAGRAM

The purpose of this circuit is to stabilize the device supply voltage by trimming the rising voltage of the devices, which are fed to the high-voltage-supply devices, that rise above the critical voltage level of 33 VDC, which is the critical level voltage of the precision electro-static devices, provided that the 24 VDC voltage is fixed instantaneously or permanently due to any reason, the operation is kept at 24 VDC so that the operation of the device or devices is maintained.

All of the electronic systems (navigation systems main control systems, battle systems, etc.), that we experienced in the past years, have experienced the burning of all systems by raising the 24 VDC system voltage, which is a high voltage resulting from the ship. This is because the operating voltage of the electronic systems used in the new type warships is max 33 VDC and in these systems the operating voltage of 24 VDC is not controlled in any way and the voltage level is not protected but the system is not protected. It has become a necessity to prevent such incidents in our new type warships.

Our aim is to minimize the likelihood of failure in such events and to prevent ships from becoming inactive. Because, the damage caused by these events is too high to be underestimated. However, with this system that we designed, we will have a chance to overcome these events at a very low cost. The cost of repairs of new types of warships, as well as the cost of operation and cost of tackling, as long as the operating costs are defective, will also be seen if the time taken for the ship to be active is calculated. For this reason, we proposed that this design must be used in all warships very soon. In addition, the cost of a module will not even be a problem in the face of enormous damage.

The circuit is powered from the system battery supply or from the DC source. On the output side, the systems to be protected are connected.

The fuses F1 and F2 at the input of the circuit prevent any excessive current draw from the system during a short circuit that occurs in any of the circuit elements. Fault conditions that

VAC 50 Hz / 24 VDC at 15 kVA
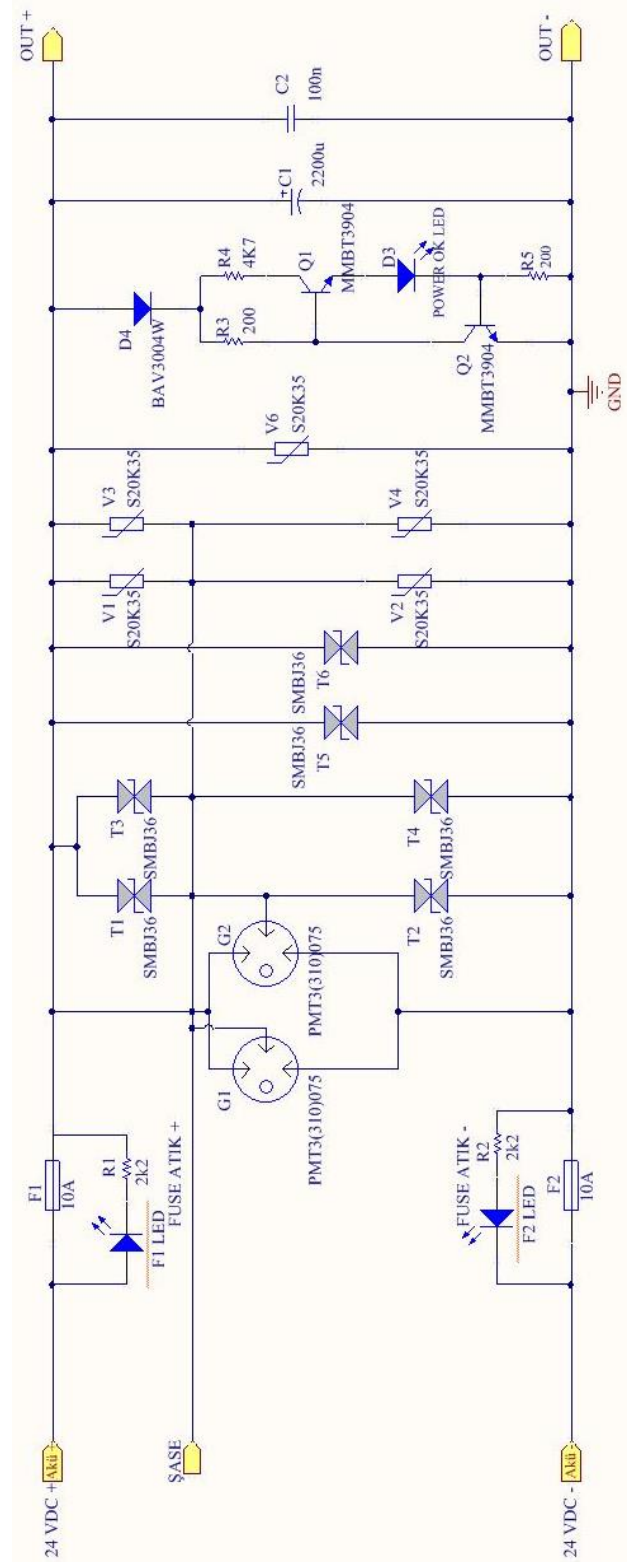will occur in the F1 or F2 fuse will alert the user with the F1 led and F2 led indicators.

Fig.5. Open circuit diagram of the proposed voltage protection card

The G1-coded PMT3 (310) 075, which is to be used in the circuit, provides a flow of current through the electrodes in the

case of a voltage higher than 75 VDC between ground and DC plus or minus and prevents the voltage level from exceeding 75 volts.

The varistors V1 and V2 try to reduce the voltage level by decreasing the internal resistances at 45 volts and over which will occur between the chassis and the plus and minus. It prevents the voltage level from exceeding 45 volts.

The V3 varistor directly prevents the 45 volt potential between the plus and minus from rising.

The T1 transient protection diode is activated at voltages up to 36 volts and tries to limit the voltages that occur on this voltage to its voltage.

In addition, these protection elements are active in a very short period of time to prevent this rise, even if there is any increase in AC or DC. They try to protect the system at high speed.

If the system protection elements remain on their protection voltage for a certain period of time, they short-circuit themselves to ensure that the F1 and F2 protection fuses at the system entrance are protected.

System protection elements temporarily or permanently stop the voltage which does not exceed the maximum operating voltage of 33 VDC. Thus, a system that is connected to proposed device can be protected by operating in any voltage condition.

In the proposed circuit we have three types component to protect our instrument in the output from voltage transient at the input. We have Transient Voltage Suppression Diodes (TVS diode) in bidirectional type (SMBJ36A) (See Figure 6).

The SMBJ is designed specifically to protect sensitive electronic equipment from voltage transients induced by lightning and other transient voltage events.

Fig.6. Uni-directional and bi-directional TVS diodes

It is used between "+24v line and -2v line", "+24v line and ground" and "ground and -24v line". This component limit the output at maximum 36 volts, the SMBJ diode is an ultra-fast protection diode, so it is working in the fast voltage transient but in maximum 600W Power, but incase our input has a big and powerful voltage transient, we have another component, that is Gas Discharge Tube (GDT) Products, as part number PMT3(310) Series (See Figure 7).

Three electrode PMT3(310) series GDTs are designed primarily to protect telecommunications equipment requiring simultaneous crowbar action of two signal lines. GDTs function as switches; dissipating a minimum amount of energy

and can handle much higher currents than other types of transient voltage protection. It is used between "+24v line and -2v line" with base voltage of ground. If any voltage transient happens that is more than SMBJ-diode's power, we have PMT3(310)075 for maximum 25k amperes to protect the system.
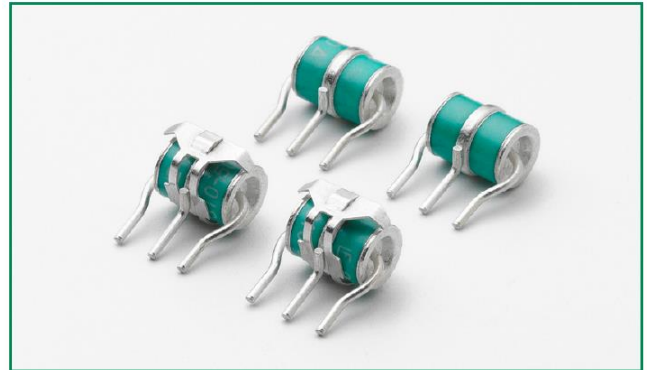
Fig 7. Three electrode PMT3(310) series GDTs

For more protection, we have SIOV metal oxide varistors (S20K35). Varistors are nonlinear two-element semiconductors that drop in resistance as voltage increases. Voltage-dependent resistors are often used as surge suppressors for sensitive circuits. It is used between "+24v line and ground" and "ground and -24v line" (See Figure 8).

Fig 8. SIOV metal oxide varistors (S20K35)

We also used 2 types of capacitors: Electrolyte capacitor (2200uF) and Ceramic capacitor (100nF). Our aim is to stabilize output voltage for filtering the high-frequency noise.
Various voltage tested on the board.
The input and outpu voltage of the voltage protection card was optained. (See Figure 9)
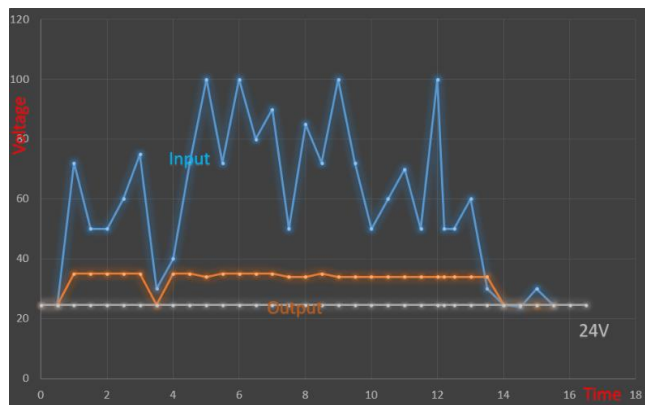
Fig.9. The input and output voltage of the voltage protection card

IV. CONCLUSION

In electronic systems, care must be taken to prevent malfunctions. In this case, we must change capacitors and IGBTs even if they do not fail at certain intervals, but we must take precautions before the malfunctions that may occur on the power generation components.

Due to the power electronics of the currently used inverter in battery charging systems used as a 24 VDC generator, it is necessary to put devices that will dampen the instantaneous voltage rise to the input of 24 VDC voltage demanding systems, because all the devices fed by the system will be damaged if the device generates momentary high voltage.

Furthermore, we believe that the design of the oscillator as an individual analog in such systems would be a more suitable design in the output control units by controlling the analog plus microcontroller with microcontrollers on the output side.

This system can be improved by further technological possibilities. Progressive protection systems can be created to provide continuous protection against future shocks.

REFERENCES

[1] B.J. Baliga, "Fundamentals of Power Semiconductor Devices", Springer, New York, 2008.
[2] E. Ziwi, "Design of robust shipboard power automation systems", Annual Reviews in Control, 29(2), 261-272, 2005.
[3] N. Doerry, "Naval Power Systems: Integrated power systems for the continuity of the electrical power supply.," in *IEEE Electrification Magazine*, vol. 3, no. 2, pp. 12-21, June 2015.
[4] N. Doerry and K. Moniri, "Specifications and Standards for the Electric Warship", US Navy, 2013.
[5] M. Cupelli *et al*., "Power Flow Control and Network Stability in an All-Electric Ship," in *Proceedings of the IEEE*, vol. 103, no. 12, pp. 2355-2380, Dec. 2015.
[6] A. Riccobono and E. Santi, "Comprehensive Review of Stability Criteria for DC Power Distribution Systems," in *IEEE Transactions on Industry Applications*, vol. 50, no. 5, pp. 3525-3535, Sept.-Oct. 2014.
[7] S. Castellan, R. Menis, A. Tessarolo, F. Luise and T. Mazzuca, "A Review of Power Electronics for All-Electric Ship MVDC Power Ssytems", International Journal of Electrical Power&Energy Systems, vol. 96, 306-323, March 2018.
[8] N. D. Banavides, T. J. McCoy and M. A. Chrin, "Reliability improvements in integrated power systems with pressure-contact semiconductors", ASNE Day, 2009.
[9] N. Mohan, T. Undeland and W. Robbins, "Power Electronics: Converters, Applications and Design", John Wiley & Sons, 2003.
[10] M. Gasperi, N. Gollhardt and R. Sladky, "A model for equivalent series resistance in aluminum electrolytic capacitors", Capacitor and Resistor Technology Symposium (CARTS), Jupiter, Florida, 71–75, 1997.
[11] M. L. Gasperi, "Life prediction modeling of bus capacitors in ac variable-frequency drives", IEEE Transactions on Industrial Applications, 41(6), 1430–1435, 2005.
[12] M. Gasperi, N. Gollhardt and R. Sladky, "A model for equivalent series resistance in aluminum electrolytic capacitors", Capacitor and Resistor Technology Symposium (CARTS), Jupiter, Florida, 71–75, 1997.
[13] J. Holtz, "Pulsewidth modulation for electronic power conversion", Proceedings of the IEEE, 82(8), 1194–1214, 1994.
[14] D. Kastha and B. K. Bose, "Investigation of fault modes of voltagefed inverter system for induction motor drive", IEEE Transactions on Industrial Applications, 30, 1028-1038, 1994.
[15] J. Morroni, A. Dolgov, R. Zane and D. Maksimovi, "Online health monitoring in digitally controlled power converters", IEEE Power Electronic Specialists Conference, Orlando, FL, 2007.
[16] R. Orsag.h, D. Brown, M. Roemer, T. Dabnev and A. Hess, "Prognostic health management for avionics system power supplies", 2005 IEEE Aerospace Conference, Montana, 3585 – 3591, 2005.
[17] N. H. Doerry, "Institutionalizing the electric warship", Naval Engineers Journal, 118(4), 57–64, 2006.
[18] C. Lotspeich and A. Lovins, "Energy efficiency survey aboard USS Princeton CG-59", Rocky Mountain Institute, Technical Report, 2001
[19] Military Handbook 217 F, "Reliability prediction of electronic equipment", revision F, Notice 1, 10 July 1992, Notice 2, Feb. 28, 1995, ed., Dec. 1991.
[20] J. Celaya, N. Patil, S. Saha, P. Wysocki and K. Goebel, "Towards accelerated aging methodologies and health management of power MOSFETs" (technical brief), Annual Conference of the Prognostics and Health Management Society, San Diego, 2009.

BIOGRAPHIES

MAHMUT TURHAN Gaziantep-TURKEY, in 1977. He received the B.S. in Electrical and Electronics Engineering from Gaziantep University in 1999, M.S. degree in Energy Systems Engineering from Gebze Technical University in 2005 and the Ph.D. degree in Electrical Engineering from Kocaeli University in 2011.

From 2000 to 2016, he was an engineer and team leader in Naval Military Shipyards at Golcuk and Izmir. Since 2011, he gave lectures in Katip Celebi University and Turkish Naval Academy. Now, he is the executive of research and development department of Medel Electronics Company. His research interests include power electronics, fuel cell technologies, li-ion batteries and solar energy.

Unknown Input Observer Based Robust Actuator Fault Detection and Isolation in Interconnected Power Systems

V. M. I. GENC and F. CALISKAN

Abstract— **In this paper, the performance degradation of a generating unit in a multi-area power system regulated by an area-wise decentralized load frequency control is detected and isolated via a scheme of unknown input observers. This scheme is robust to the changes in the load demand, which are considered as the unknown inputs. The actuator faults studied in this work are meant to be the performance degradations in generating units under load frequency control. Both stuck and non-stuck actuator faults are analyzed and the performances of the proposed method in both cases are tested through computer simulations on a two-area power system composed of five generating units. The results show that a performance degradation in any generating unit can be detected and isolated successfully provided that the faults in the sensors measuring generator outputs are absent.**

Index Terms— **actuator fault, fault diagnosis, fault detection and isolation, interconnected power systems, load frequency control, power generation control**

I. INTRODUCTION

LOAD Frequency Control (LFC) is a widely used method for maintaining the nominal frequency in an interconnected power system while keeping the net active power interchanges as scheduled between its control areas. As in any feedback control system, faults related to the actuators, sensors or controllers used in the LFC loops can result in unexpected and undesired operations. These types of faults occurring in the LFC system can cause abnormal steady-state deviations in the system's frequency as well as in the power interchanges and the loadings of the generating units. Therefore, it is crucial to detect and isolate (identify) these

V. M. ISTEMIHAN GENC, is with the Department of Electrical Engineering, Istanbul Technical University, Istanbul, 34469, Turkey (e-mail: gencis@itu.edu.tr).

https://orcid.org/0000-0001-7077-8895

FIKRET CALISKAN, is with the Department of Control and Automation Engineering, Istanbul Technical University, Istanbul, 34469, Turkey (e-mail: caliskanf@itu.edu.tr).

https://orcid.org/0000-0002-9108-6553

faults in a short time to prevent a sustained undesired LFC operation caused by them.

In a model based Fault Detection and Isolation (FDI) technique, faults are detected and isolated based on a comparison between the system's available measurements and its mathematical model. Specifically, Unknown Input Observers (UIOs), which are insensitive to disturbances or unknown inputs, are extensively used for a robust FDI [1]-[6]. In recent years, the studies about the application of FDI in power system dynamics and control have greatly increased. For instance, a software approach to fault detection and identification in the LFC loops of interconnected power systems is introduced in [7], where the faults occurring in the load frequency control loops and the communication channels are detected using a failure detection filter. The transmission network faults are detected and their exact locations are found in [8] using UIOs, where the faults are modeled as unknown inputs decoupled from the state and output measurements.

A new approach for fault detection in a power system based on independent component analysis is proposed in [9], and tested on a typical power system's simulated data and compared with the approaches available in literature. In [10], the fault diagnosis problem for power systems is solved using two nonlinear observers for generating the fault signals for comparison: an extended Kalman estimator and a new extended Kalman filter with moving horizon.

A fault-tolerant controller for linear time-invariant (LTI) systems with multiple actuators, including a fault tolerant speed governor, is designed in [11] so that the closed-loop system satisfies the following two properties: stability under all permissible sets of faults, and better performance after clearing every subset of the existing faults in the system. A robust load frequency control is proposed in [12] for multi-area power systems with stochastic disturbances induced by the integration of large number of renewable energy resources.

In [13], an FDI method in electrical energy systems based on techniques developed in the context of invertibility of switched systems is proposed. The existence of unknown input observers for networks of interconnected second-order linear time invariant systems is studied in [14] and a bank of unknown input observers is used for detecting and isolating faults in the network.

In [15], a robust FDI procedure to detect and isolate sensor and controller faults occurring in the LFC loops is proposed. In [16], the FDI scheme developed in [15] is also applied to power systems including electric vehicles and renewable

energy sources to detect and isolate sensor faults within the control system. A sensor fault tolerant control system is proposed in [17] for distributed energy resource units in a microgrid.

Although improper actions of controllers fed by the Area Control Error (ACE) signals are treated in [15] as faults, the performance degradation caused by the actuator faults in the generating units are more likely to occur in an LFC system. Therefore, unlike the study in [15], in this paper, governors are characterized as actuators, and the detection and isolation of a performance degradation in a generating unit is studied by means of a robust actuator FDI scheme. This approach necessitates a distinct modeling approach from the LFC system studied in [15].

Both stuck and non-stuck faults are studied in this paper. Since stuck faults in the governors can lead more severe misoperations, UIOs are designed to detect and isolate the stuck governor faults besides non-stuck governor faults, whereas, in [15], only the non-stuck faults in the integral controllers of the LFC system have been considered. A stuck fault in a governor of a generating unit under LFC may easily lead to an unscheduled generation dispatch as well as a drastic degradation in the transient response of the LFC system. A non-stuck fault, on the other hand, can be less severe and could only affect the transient response. Both types of faults can be detected and isolated with the proposed scheme in this paper. The implications caused by them can be avoided by replacing the faulty components that are identified (isolated) by the method.

Simulations are performed for a benchmark model of a power system composed of two areas. The effectiveness of the FDI scheme for detection and isolation of a performance degradation in a generating unit has been demonstrated. The applicability of the proposed scheme in the presence of sensor faults is also studied, simulated and the results are analyzed. A preliminary work considering only the non-stuck governor faults neglecting the possibility of sensor faults is given in [18].

II. DESIGN OF ACTUATOR FDI ALGORITHM ROBUST TO UNKNOWN INPUTS

A state space representation of a dynamical system with actuator faults can be expressed as follows:

$$\dot{x} = Ax + B^i u^i + B^i f_a^i + b_i(u_i + f_{ai}) + Ed$$

$$\dot{x} = Ax + B^i u^i + B^i f_a^i + \begin{bmatrix} E & b_i \end{bmatrix} \begin{bmatrix} d \\ u_i + f_{ai} \end{bmatrix}, \quad i = 1,2,....r$$

$$\dot{x} = Ax + B^i u^i + B^i f_a^i + E^i d^i$$

$$y = Cx \quad , \tag{1}$$

where $b_i \in R^{nx1}$ is the i-th column of the matrix B, $B^i \in R^{nx(r-1)}$ is obtained from B by discarding the i-th column b_i, $u_i \in R^{1x1}$ is the i-th element of u, $u^i \in R^{(r-1)x1}$ is obtained

from u by discarding the i-th element, u_i, $f_{ai} \in R^{1x1}$ is the i-th element of f_a, $f_a^i \in R^{(r-1)x1}$ is obtained from f_a by deleting the i-th element f_{ai}, $y \in R^m$ is the output (measurement) vector. E^i and d^i respectively are

$$E^i = \begin{bmatrix} E & b_i \end{bmatrix}, d^i = \begin{bmatrix} d \\ u_i + f_{ai} \end{bmatrix}, \quad i = 1,2,....r . \tag{2}$$

Moreover, the dynamic equations of the unknown input observer UIO$_i$ to be used for detection and isolation of an actuator fault i are given as

$$\dot{z}^i = F^i z^i + T^i B^i u^i + K^i y \tag{3}$$

$$\hat{x} = z^i + H^i y \qquad i = 1,2,....r \quad , \tag{4}$$

where $\hat{x} \in R^n$ is the estimated state vector and $z^i \in R^n$ is the state of the full-order observer [3]. F^i, T^i, K^i, and H^i are the design parameter matrices to be determined such that the FDI design based on UIOs is robust to unknown inputs (disturbances).

The error dynamics, where state estimation error $e = x - \hat{x}$ can be obtained as

$$\dot{e} = \begin{bmatrix} (I - H^i C)A - K_1^i C \end{bmatrix} e + \\ \begin{bmatrix} F^i - (I - H^i C)A - K_1^i C \end{bmatrix} z^i - \\ \begin{bmatrix} K_2^i - ((I - H^i C)A - K_1^i C)H^i \end{bmatrix} y - \\ \begin{bmatrix} T^i - (I - H^i C) \end{bmatrix} B^i u^i - (H^i C - I)E^i d^i \tag{5}$$

where

$$K^i = K_1^i + K_2^i. \tag{6}$$

Followed by the equalities,

$$\begin{aligned} H^i C E^i &= E^i \\ T^i &= I - H^i C \\ F^i &= T^i A - K_1^i C \; must \; be \; Hurwitz \\ K_2^i &= F^i H^i, \end{aligned} \tag{7}$$

the error dynamics becomes

$$\dot{e} = F^i e . \tag{8}$$

If all eigenvalues of F^i have negative real parts, the error asymptotically approaches zero.

The necessary and sufficient existence conditions [4] for the UIO$_i$ are :

(i) $rank(CE^i) = rank(E^i)$

$$\tag{9}$$

(ii) (C, A_1) is a detectable pair, where

$$A_1 = A - E^i \left[(CE^i)^T CE^i \right]^{-1} (CE^i)^T CA \cdot \qquad (10)$$

Since the residual $r = Ce$, it can be rewritten as

$$r = y - C\hat{x} = (I - CH^i)y - Cz^i, i = 1,2,...r \cdot \qquad (11)$$

UIO$_i$ is driven by all outputs and all inputs but input i (see, Fig.1). If the actuator i fails, then the norms of the residual vectors meet the following inequalities:

$$\left\| r^i \right\| < T_{AFI}^i \; and \; \left\| r^k \right\| \geq T_{AFI}^k \; for \; k = 1,..i-1, i+1,...r \;, \qquad (12)$$

where T_{AFI}^i s are predefined isolation threshold values, which are determined based on the comparison between fault-free and faulty operations for the specific system under study. Since the residuals differ greatly for the two opposing cases, the proper threshold values can easily be selected in such a way that any false alarm is not produced nor does the scheme miss any fault.

A robust and UIO-based actuator fault detection and isolation scheme, which consists of a bank of UIO's is depicted in Fig. 1.

III.   FDI APPLICATION TO A TWO-AREA POWER SYSTEM UNDER LFC

A two-area power system with an area-wise decentralized LFC is given in the block diagram in Fig.2. The areas are modeled with a number of coherent generating units, each of which is represented by a turbine-speed governor system. Area 1 is represented by a group of three generating units while Area 2 is assumed to be composed of two generating units. In Fig. 2, inertia and load damping constants of area j are denoted by H_j and D_j, respectively, where f_o is the nominal frequency. In each area j, the turbine and governor time constants of any generating unit k are represented by T_{tjk} and T_{gvjk}, respectively, whereas R_{jk} is the regulator droop constant. The area control error ACE$_j$ is obtained using the bias setting β_j and the synchronizing torque coefficient T_{12} and fed back to each area control center through an integral controller with the constant K_{Ij} . Distribution coefficient for the loading of unit k in area j is denoted by α_{jk} . In order to analyze and develop a FDI scheme for the actuator faults, the actuator and plant dynamics have to be separated. Assuming that the system is subject to actuator faults, the dynamics of the plant involving the turbines and generators can be expressed as

$$\dot{x} = Ax + Bu_R + Ed \quad y = Cx. \qquad (13)$$

The state vector,

$$x = \left[\int \Delta P_{tie} \quad \int \Delta f_1 \quad \Delta f_1 \quad \Delta P_{g11} \quad \Delta P_{g12} \right. \qquad (14)$$
$$\left. \Delta P_{g13} \quad \int \Delta f_2 \quad \Delta f_2 \quad \Delta P_{g21} \quad \Delta P_{g22} \right]$$

where Δf_j is the frequency deviation in area j and ΔP_{gjk} is the deviation in the generation at the k-th unit of area j and ΔP_{tie} is the tie-line power flow deviation. The disturbance vector,

$$d = \begin{bmatrix} \Delta d_1 & \Delta d_2 \end{bmatrix}, \qquad (15)$$

where the change in the load demand of area is represented by Δd_j .

$$A = \begin{bmatrix}
0 & T_{12} & 0 & 0 & 0 & 0 & -T_{12} & 0 & 0 & 0 \\
0 & 0 & 1 & 0 & 0 & 0 & 0 & 0 & 0 & 0 \\
0 & -\frac{fT_{12}}{2H_1} & -\frac{fD_1}{2H_1} & \frac{f}{2H_1} & \frac{f}{2H_1} & \frac{f}{2H_1} & \frac{fT_{12}}{2H_1} & 0 & 0 & 0 \\
0 & 0 & 0 & -\frac{1}{T_{t11}} & 0 & 0 & 0 & 0 & 0 & 0 \\
0 & 0 & 0 & 0 & -\frac{1}{T_{t12}} & 0 & 0 & 0 & 0 & 0 \\
0 & 0 & 0 & 0 & 0 & -\frac{1}{T_{t13}} & 0 & 0 & 0 & 0 \\
0 & 0 & 0 & 0 & 0 & 0 & 0 & 1 & 0 & 0 \\
0 & \frac{fT_{12}}{2H_2} & 0 & 0 & 0 & 0 & -\frac{fT_{12}}{2H_2} & -\frac{fD_2}{2H_2} & \frac{f}{2H_2} & \frac{f}{2H_2} \\
0 & 0 & 0 & 0 & 0 & 0 & 0 & 0 & -\frac{1}{T_{t21}} & 0 \\
0 & 0 & 0 & 0 & 0 & 0 & 0 & 0 & 0 & -\frac{1}{T_{t22}}
\end{bmatrix}$$

$$B = \begin{bmatrix}
0 & 0 & 0 & \frac{1}{T_{t11}} & 0 & 0 & 0 & 0 & 0 & 0 \\
0 & 0 & 0 & 0 & \frac{1}{T_{t12}} & 0 & 0 & 0 & 0 & 0 \\
0 & 0 & 0 & 0 & 0 & \frac{1}{T_{t13}} & 0 & 0 & 0 & 0 \\
0 & 0 & 0 & 0 & 0 & 0 & 0 & 0 & \frac{1}{T_{t21}} & 0 \\
0 & 0 & 0 & 0 & 0 & 0 & 0 & 0 & 0 & \frac{1}{T_{t22}}
\end{bmatrix}^T$$

$$E = \begin{bmatrix}
0 & 0 & -\frac{f}{2H_1} & 0 & 0 & 0 & 0 & 0 & 0 & 0 \\
0 & 0 & 0 & 0 & 0 & 0 & 0 & -\frac{f}{2H_2} & 0 & 0
\end{bmatrix}^T$$

The control input vector, which is composed of actuator outputs,

$$u_R = \begin{bmatrix} \Delta X_{gv11} & \Delta X_{gv12} & \Delta X_{gv13} & \Delta X_{gv21} & \Delta X_{gv22} \end{bmatrix}, \qquad (16)$$

where ΔX_{gvjk} is the deviation in the governor valve or gate position of the k-th unit in area j.

The dynamics of the actuators involving governors with the LFC system can be represented as

$$\dot{x} = A_R x_R + B_R u_c + F_R x$$
$$u_R = C_R x_R = x_R, \qquad (17)$$

where

$$u_c = -Kx = \begin{bmatrix} \Delta P_{c11} & \Delta P_{c12} & \Delta P_{c13} & \Delta P_{c21} & \Delta P_{c22} \end{bmatrix} \quad (18)$$

comprises the deviations in the speed governor changer positions ΔP_{cjk} of the k-th unit in area j.

$$A_R = B_R = diag\left[-\frac{1}{T_{g11}} \quad -\frac{1}{T_{g12}} \quad -\frac{1}{T_{g13}} \quad -\frac{1}{T_{g21}} \quad -\frac{1}{T_{g22}} \right]$$

$$F_R = \begin{bmatrix} 0 & 0 & -\dfrac{1}{T_{g11}R_{11}} & 0 & 0 & 0 & 0 & 0 & 0 & 0 \\ 0 & 0 & -\dfrac{1}{T_{g12}R_{12}} & 0 & 0 & 0 & 0 & 0 & 0 & 0 \\ 0 & 0 & -\dfrac{1}{T_{g13}R_{13}} & 0 & 0 & 0 & 0 & 0 & 0 & 0 \\ 0 & 0 & 0 & 0 & 0 & 0 & 0 & -\dfrac{1}{T_{g21}R_{21}} & 0 & 0 \\ 0 & 0 & 0 & 0 & 0 & 0 & 0 & -\dfrac{1}{T_{g22}R_{22}} & 0 & 0 \end{bmatrix}$$
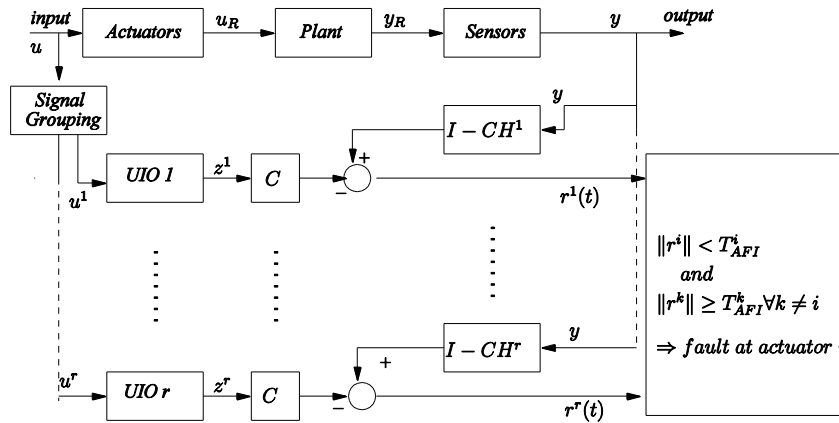

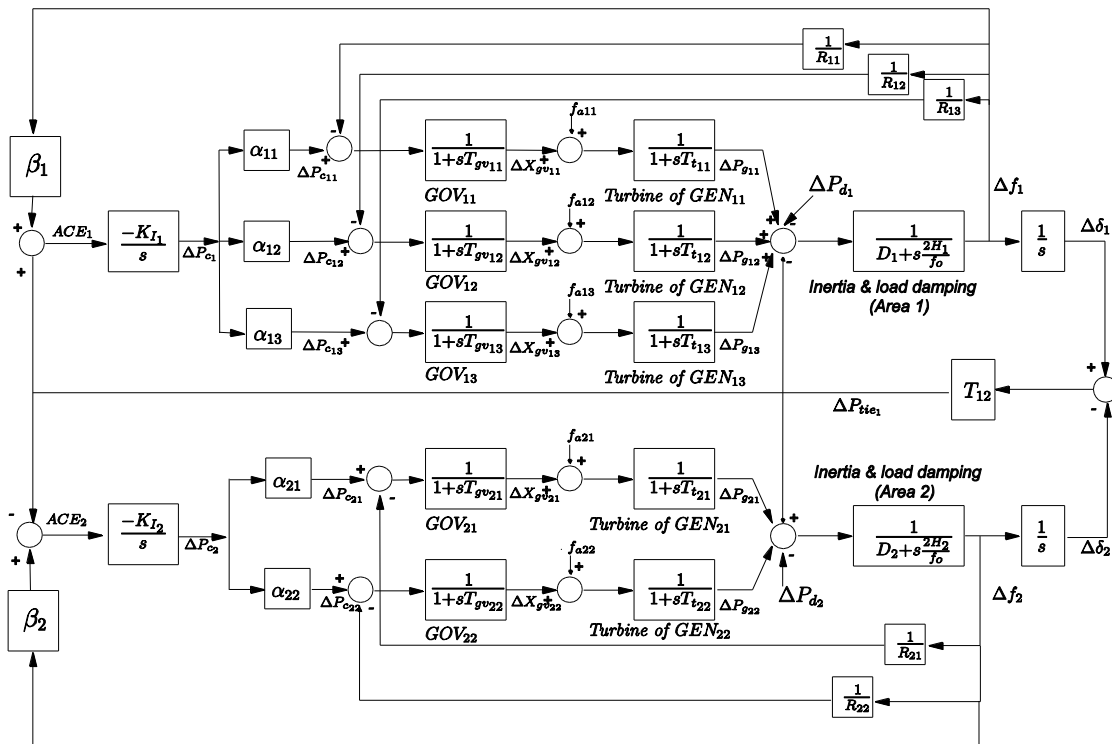Fig. 1 A robust actuator fault isolation scheme.

Fig. 2. Block diagram of LFC applied to a two-area system.

IV. SIMULATION RESULTS

In this section, we provide the simulation results to demonstrate the performance of the proposed FDI algorithm which successfully detects and isolates the governor faults in a two-area load frequency controlled power system described in the previous section with the parameters given in Table I. Two types of actuator faults are considered: stuck faults and non-stuck faults.

TABLE I
PARAMETERS OF THE LFC SYSTEM

Symbol	Quantity
H_j	5 s
D_j	0.0083pu MW/Hz
Tt_{jk}	0.3 s
Tgv_{jk}	0.08 s
R_{jk}	2.4 Hz/pu MW
T_{12}	0.545puMW
β_j	0.425puMW/Hz
f	60 Hz
$\alpha_{11} = \alpha_{12}$	0.3
α_{13}	0.4
α_{21}	0.2
α_{22}	0.8
K_{Ij}	1

A. Case I (Stuck faults)

If any governor does not respond to the changes in the load demand due to a fault where the valve or gate positions are stuck, an undesired generation dispatch as well as a degraded transient response of the LFC system can be observed.
The bank of UIOs generates the residuals such that the detection and isolation of the faults in the actuators can be performed. The successful design for the UIOs is robust to the unknown disturbances, which are the changes in the load demand in power system control areas.

In the simulations, we assume only a single governor fault at a time in one of the generating units belonging to an area. The existence of the UIOs and the success in the operation of the proposed FDI method are strongly dependent on the selected set of observed variables. Due to the necessary and sufficient condition in (9), $rank(CE^i) = rank(E^i)$. Since the matrix B is as given in Section III, $rank(CE^i) = rank(E^i) = n_A + 1 = 3$, where $n_A = 2$ is the number of areas. This condition implies that in order to design the full set of UIOs, the vector of measured variables, y, must include all the frequency measurements Δf_j and the actuator outputs ΔP_{gjk} as follows:

$$y = \begin{bmatrix} \Delta f_1 & \Delta P_{g11} & \Delta P_{g12} & \Delta P_{g13} & \Delta f_2 & \Delta P_{g21} & \Delta P_{g22} \end{bmatrix}$$

The following simulation results show that this selection of the measured variables based on the necessary and sufficient condition above leads to successful detection and isolation of the actuator faults in the power system model under study.

As an example, in the two area test system, we assume that the governor GOV_{11} is stuck while the generating units controlled by the other governors are attempting to maintain the generation-load balance. Fig. 3 illustrates the output of the generating unit GEN_{11} as the governor GOV_{11} is stuck with a deviation in its output by 0.01 pu after an increase in the load demand of 0.1 pu in Area 1 at t=0.2 s. The stuck fault in (1) can be characterized as

$$f_{a1} = \begin{cases} 0 & 0 < t < t_f \\ 0.01 & t \geq t_f \end{cases} \quad and \ u_1(t) = 0 \ for \ t \geq t_f,$$

where the output of the generating unit reaches 0.01 pu at the instant of fault occurrence $t = t_f$, i.e. $\Delta P_{g11}(t_f) = 0.01 pu$.

The effect of this fault on the transient response in the frequency of Area 1 is given in Fig. 4.

The undesired dispatch of generation due to the stuck fault can be seen, as the Fig. 5 and Fig. 6, which depict the change in generator outputs for fault free and stuck fault cases, are compared.

The FDI method described in Section II is applied for detecting and isolating the stuck actuator fault through the computation of the residuals. The comparison of the squared norms residuals given in Fig. 7 reveals the occurrence of the fault in GOV_{11} as all the residuals except for r_{11} change significantly.
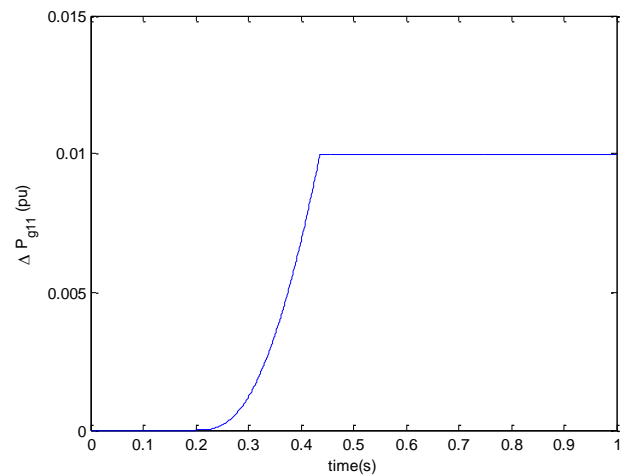
Fig. 3 The output of generating unit GEN_{11} in case of a stuck actuator fault.
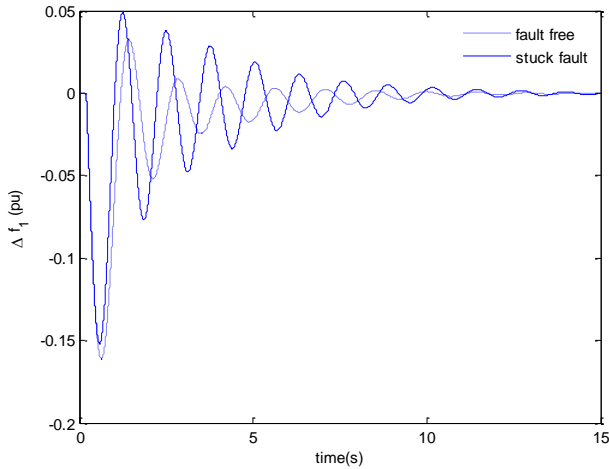
Fig. 4 The change in frequency in Area 1 in case of no fault and in case of stuck fault.

B. Case II (Non-Stuck faults)

In this case, a non-stuck actuator fault in GOV_{11} causing a degradation in the transient response of the system is assumed. In this case study, the fault occurs at GOV_{11} at $t=1.5$ s after a change in the load demand 0.1 pu at $t=0.2$ s. The non-stuck fault in (1) can be characterized as

$$f_{a1} = \begin{cases} 0 & 0 < t < 1.5s \\ 0.01 & t \geq 1.5s \end{cases}$$

Although the non-stuck fault does not result in any undesired dispatch of generation and the LFC corrects all the steady-state deviations, the fault, depending on its magnitude, may cause a deviation in the transient response of the system from its nominal behavior.

The deviation in the output of the generating unit GEN_{11} and the deviation in the frequency of area 1 are given in Fig. 8 and Fig. 9, respectively.

Fig. 5 Deviations in generating unit outputs in Area 1 in case of no fault.

Fig. 6 Deviations in generating unit outputs in Area 1 when there is a stuck fault at GOV_{11}.

Fig. 7 Squared norms of residuals indicating the stuck actuator fault at GOV_{11}.

Fig. 8 Deviation in generating unit output GEN_{11} in case of no fault and in case of non-stuck fault.
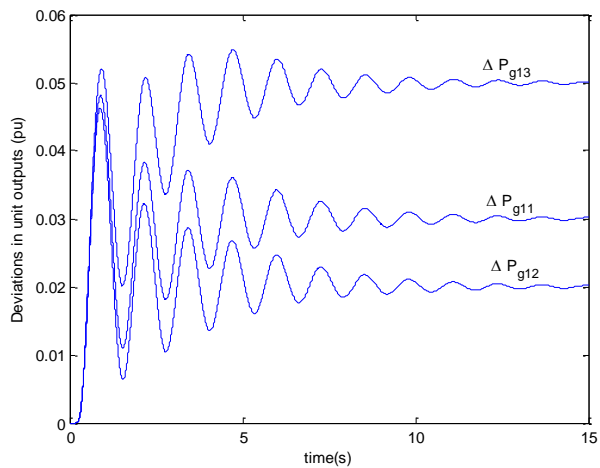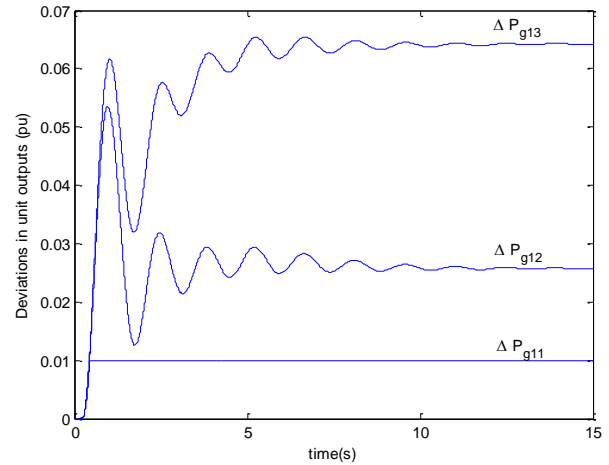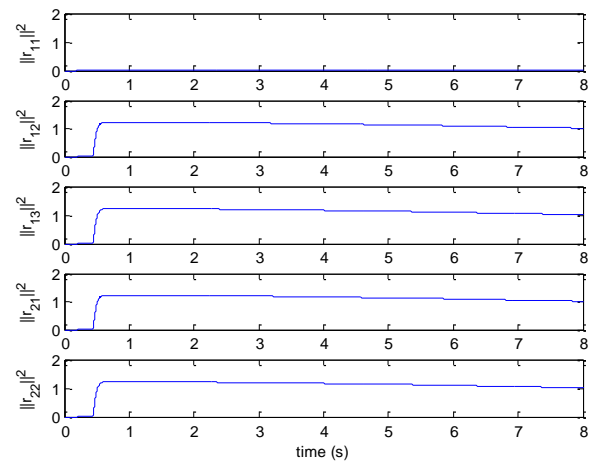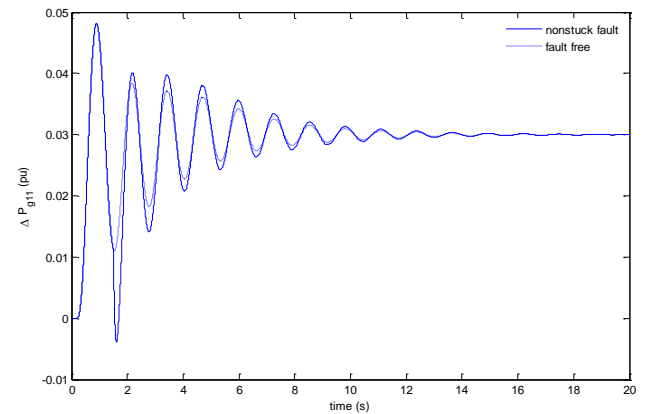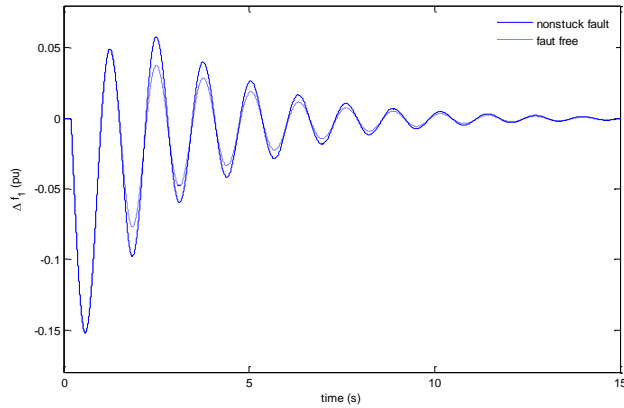
Fig. 9 Change in frequency in area 1 in case of no fault and in case of non-stuck fault.

Fig. 10 illustrates the squared norms of the residuals. Through the observation of the residuals, the fault in GOV_{11} can be detected and isolated clearly since only the residual r_{11} is insensitive to the fault whereas the rest of the residuals are sensitive.
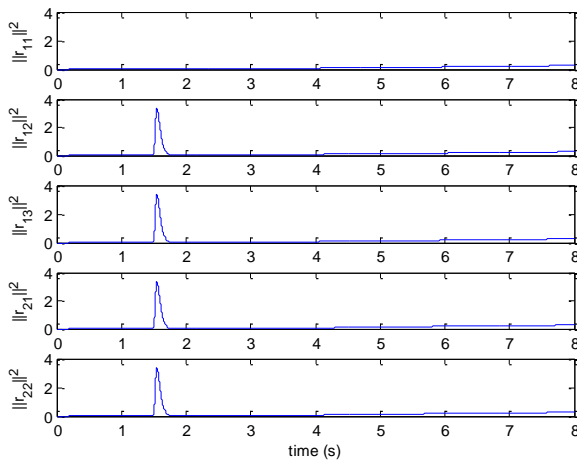
Fig. 10 Squared norms of residuals indicating the non-stuck actuator fault at GOV_{11}.

Stuck faults cause nonzero residuals whereas the residuals fall to zero rapidly when non-stuck faults occur, see Fig. 7 and Fig. 10. Thus, the two cases can be differentiated by simply observing this characteristic of the residuals.

If inclusion of sensor faults is assumed, UIOs for isolating the sensor faults can be designed as in [15], (in which isolation of sensor faults including only the ones measuring the frequencies and the tie-line power flow is studied and successfully implemented.) This requires an extension of the output vector (inclusion of $\Delta f_1 + \Delta f_2$) since the existence of UIOs is not maintained with the output vector chosen previously. This results in selecting the vector of measured variables as

$$y = \begin{bmatrix} \Delta f_1 & \Delta P_{g11} & \Delta P_{g12} & \Delta P_{g13} & \Delta f_2 & \Delta P_{g21} & \Delta P_{g22} & \Delta P_{tie} & \Delta f_1 + \Delta f_2 \end{bmatrix}$$

However, even if the condition for the existence of UIOs is satisfied, the algorithm fails to differentiate the sensor and actuator faults from each other. Fig. 11 illustrates the residual norms that falsely indicate a sensor fault at GOV_{11} despite of a non-stuck actuator fault occurrence that can be isolated by means of the residuals given in Fig. 10. Similarly, in case of a fault at a sensor measuring an actuator output, it is not possible to distinguish it from a fault occurring at the same actuator. This is illustrated in Fig. 12 and Fig. 13, in which a fault that takes place only at the sensor measuring P_{g11} is assumed.

Fig. 11 Squared norms of residuals indicating a false sensor fault at GOV_{11}.
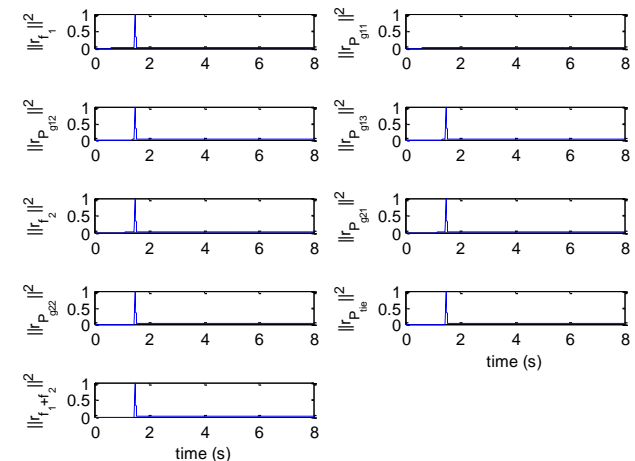
Fig. 12 Squared norms of residuals indicating a sensor fault at GOV_{11}.

If no fault occurs in the sensors measuring the actuator outputs, the actuator faults can be easily distinguished from the faults in the sensors measuring the frequencies and tie-line power flow. For example, in case of a sensor fault in measuring Δf_1, the squared norms of residuals given in Fig. 14, show that no actuator faults is detected or isolated whereas Fig. 15 shows an existence of a sensor fault. With the chosen measurement vector, the faults in the sensors measuring Δf_1 and Δf_2 cannot be isolated although they can be detected. The successful isolation of the sensor fault can be achieved by the

inclusion of the governor output measurements as shown in [15].
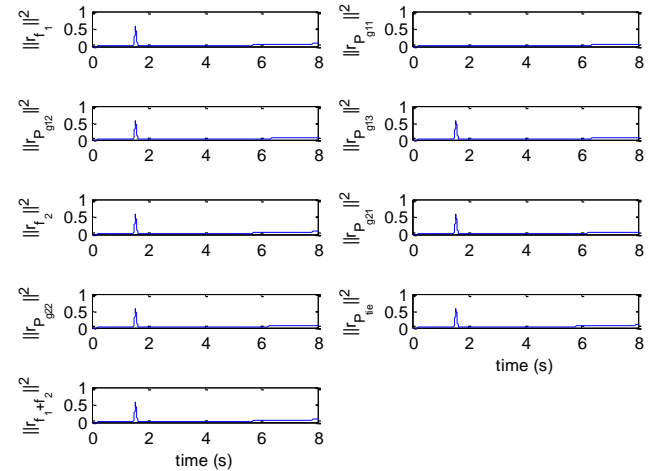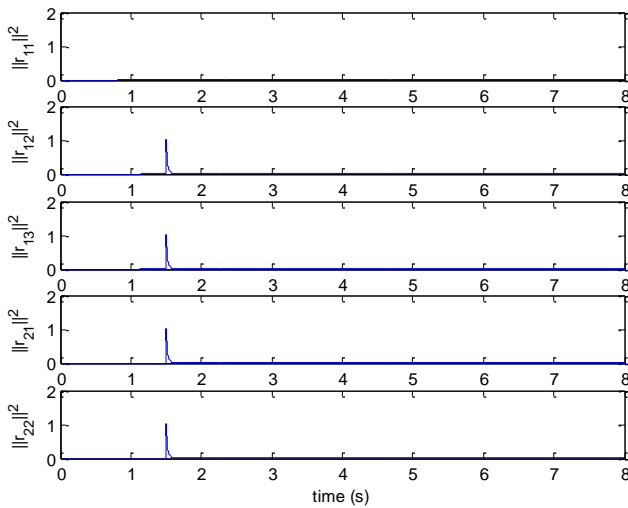

Fig. 13 Squared norms of residuals indicating a false actuator fault at GOV_{11}.
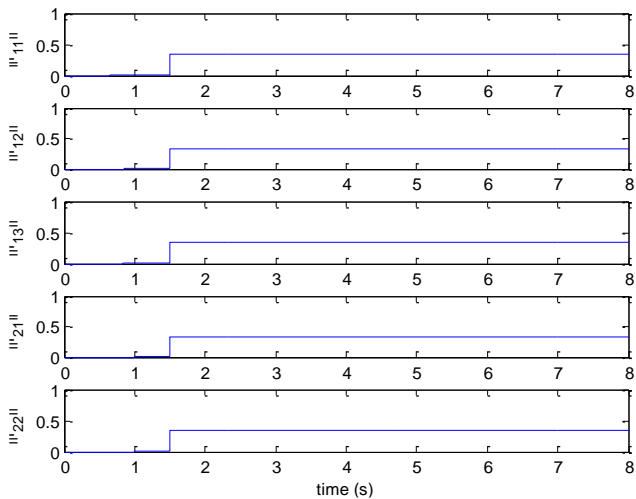
Fig. 14 Squared norms of residuals indicating no actuator fault.
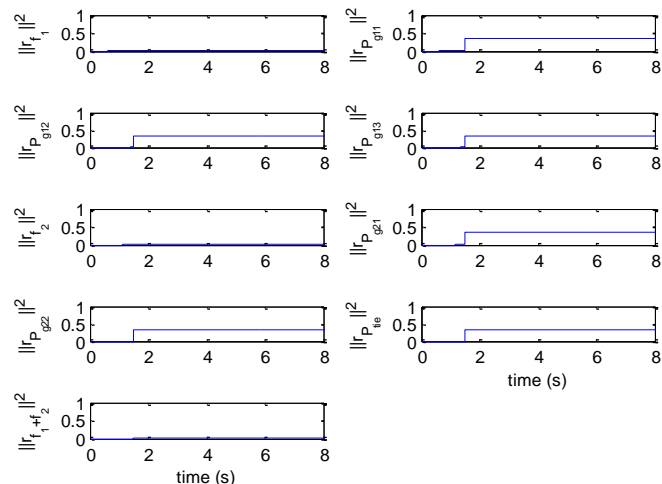
Fig. 15 Squared norms of residuals indicating an existence of a sensor fault.

V. CONCLUSION

In this paper, it has been shown that governor faults can be detected and isolated successfully in an interconnected power system with LFC by means of an elaborately designed bank of unknown input observers and treating these faults as actuator faults in the proposed method. This is achieved by a proper and feasible selection of observed variables that satisfies the condition for existence of the unknown input observers.

Both stuck and non-stuck faults have been explored. As a stuck fault in a governor is detected and isolated, an undesired generation dispatch as well as degradation in the transient behavior of the system can be avoided by replacing the faulty component. Non-stuck faults, which are less severe and affecting only the transient response, can also be detected and isolated through the same design.

The proposed method assumes no fault occurrence in sensors measuring the governor outputs and fails to distinguish the actuator faults from these sensor faults. The method is demonstrated on an example of a two-area power system model and can be easily applied to a more extensive power system having larger number of areas and generating unit models of higher order. The simulation results have shown the actuator fault detection and isolation can be carried out in real-time.

REFERENCES

[1] Y. Guan and M. A. Saif, "A new approach to robust fault detection and identification", *IEEE Trans. on Aerospace and Electronic Systems*, vol. 29, no. 3, pp. 685-695, 1993.

[2] F. Yang, and R. W. Wilde, "Observers for linear systems with unknown inputs", *IEEE Trans. on Automatic Control*, vol. 33, no. 7, pp. 677-681, 1998.

[3] J. Chen and R. J. Patton, *Robust model-based fault diagnosis for dynamic systems*, Kluwer Academic Publisher, pp. 68-84, 1999.

[4] C. C. Tsui, "A new design approach to unknown input observers", *IEEE Trans. on Automatic Control*, vol. 41, no. 3, pp. 464-468, 1996.

[5] Y. Guan and M. Saif, "A novel approach to the design of unknown input observers", *IEEE Trans. on Automatic Control*, vol. 36, no. 5, pp. 632-635, 1991.

[6] M. Hou and P. C. Müller, "Design of observers for linear systems with unknown inputs", *IEEE Trans. on Automatic Control*, vol. 37, no. 6, pp. 871-875, 1992.

[7] M. Aldeen and R. Sharma, "Robust detection fault in frequency control loops", *IEEE Trans. on Power Systems*, vol. 22, no. 1, pp. 413-422, 2007.

[8] M. Aldeen and F. Crusca, "Observer-based fault detection and identification scheme for power systems", *IEE Proc. of Gener. Transm.Distrib.*, vol. 153, no. 1, pp. 71-79, 2006.

[9] S. Das, S.R. Mohanty, S. Pattnaik, "Abrupt Change Detection of Fault in Power System Using Independent Component Analysis", *International Journal of Computer Science and Information Security*, vol. 9, No. 6, June, 2011.

[10] A. Thabet, M. Boutayeb, G. Didier, S. Chniba, and M.N. Abdelkerim, "Fault diagnosis for dynamic power system", *Proc. 8th International Multi-Conference on Systems, Signals & Devices*, 2011.

[11] S. Sojoudi, J. Lavaei, R. M. Murray, "Fault-Tolerant Controller Design with Applications in Power Systems and Synthetic Biology", *Proc. American Control Conference*, California, USA, 2011.

[12] Y. Sun, N. Li, X. Zhao, Z. Wei, G. Sun, C. Huang, "Robust H∞ load frequency control of delayed multi-area power system with stochastic disturbances", *Neurocomputing*, 193, 58-67, 2016

[13] A. Tanwani, A. D. Domínguez-García, D. Liberzon, "An Inversion-Based Approach to Fault Detection and Isolation in Switching Electrical Networks", *IEEE Trans. on Control Systems Technology*, vol. 19, no. 5, pp. 1059-1074, 2011.

[14] I. Shames, A. M. T Teixeria, H. Sandberg, K. H. Johannson, "Distributed fault detection for interconnected second-order systems", *Automatica*, vol. 47, no. 12, pp. 2757-2764, 2011.

[15] F. Caliskan, I. Genc, "A Robust Fault Detection and Isolation Method in Load Frequency Control Loops", *IEEE Trans. on Power Systems*, vol. 23, no. 4, pp. 1756-1767, 2008.

[16] H. H. Alhelou, M. H. Golshan, J. Askari-Marnani, "Robust sensor fault detection and isolation scheme for interconnected smart power systems in presence of RER and EVs using unknown input observer", *International Journal of Electrical Power & Energy Systems*, doi:10.1016/j.ijepes.2018.02.013, vol. 99, 682-694, 2018.

[17] S. Gholami, S. Saha, M. Aldeen, "Fault tolerant control of electronically coupled distributed energy resources in microgrid systems", *International Journal of Electrical Power & Energy Systems*, 95, 327-340, 2018.

[18] I. Genc, F. Caliskan, "Robust Actuator Fault Detection and Isolation in a Multi-Area Interconnected Power System", *Proc. the World Congress on Engineering 2011 Vol II*, pp. 1394-1398, London, 2011.

BIOGRAPHIES

V. M. ISTEMIHAN GENC received the B.Sc. degree in electrical engineering from Istanbul Technical University, the M.Sc. degrees in electrical engineering, systems and control engineering, and systems science and mathematics from Istanbul Technical University, Bogazici University, and Washington University, respectively. He received the D.Sc. degree in 2001 from Washington University in St. Louis. He is currently an associate professor in the Department of Electrical Engineering at Istanbul Technical University. His research interests are focused on stability and control of electric power systems.

FIKRET CALISKAN received the B.Sc. degree in electronics and communication engineering, and M.Sc. degree control and computer engineering from Istanbul Technical University in 1984 and 1987, respectively. He received the Ph.D. degree in control systems engineering from the University of London in 1993. He is currently working as a professor in the Department of Control Engineering at Istanbul Technical University. He was involved with various research and teaching activities at Oakland University, MI, and Washington University in St. Louis, MO, between 1999 and 2001, and at SUNY in Binghamton, NY, in 2008-2009. His research interest includes fault diagnosis in dynamic systems, fault tolerant control systems, estimation, robust control, neural networks, and fuzzy logic

A Generic Circuit Model for Memristor-Based One Diode-One Resistor Devices

F. GÜL

Abstract—**Memristor-based resistive random access memory (RRAM) devices are very good competitors for next generation non-volatile crossbar memory applications. The sneak paths problem is one of the main constraints in fabricating crossbar memory devices. The one diode-one resistor (1D1R) structure design is effective for suppressing the sneak paths problem. Suitable circuit models are needed to simulate semiconductor structures.**

A general circuit model for memristor-based one diode-one resistor structures is proposed in this work. The Simulation Program with Integrated Circuit Emphasis (SPICE) environment was used to simulate the designed circuit. Well-known mathematical models such as those of Strukov, Biolek, Joglekar, Prodromakis and Zha were used to simulate the memristor component of the circuit. The current-voltage characteristics were obtained for different mathematical models. All results were compatible with the expected characteristics. The best fit characteristics were acquired using the Zha and Strukov models.

Index Terms— **Circuit model, memristor, One diode-one resistor, resistive random access memory.**

I. INTRODUCTION

PRESENT MEMORY Technologies such as Dynamic Random Access Memory (DRAM), Static Random Access Memory (SRAM), NAND flash and NOR flash will soon encounter challenges due to the continued scaling down of their designs [1]. Several types of memory technologies have been suggested for next generation memory devices including Spin-Transfer Torque RAM (STT-RAM), Phase Change Memory (PCM) and Resistive RAM (ReRAM) [2]. Researchers have focused on the Resistive Random Access Memory (RRAM) because of its ultra-high density production potential, faster switching speed and lower energy consumption for non-volatile memory applications. Memristors, while used as resistive switching memory devices, are very good candidates for forthcoming RRAM devices as they have properties similar to those mentioned above [1]. One of the main problems in the production of crossbar RRAM devices is the sneak paths problem. The sneak paths problem can be defined as the crosstalk

FATİH GÜL, is with Department of Software Engineering Gumushane University, Gumushane, Turkey, (e-mail: fatihgul@atauni.edu.tr).

https://orcid.org/0000-0001-5072-2122

interference from current through nearby cells which can lead to misreading. The one diode-one resistor (1D1R) structure design is effective for suppressing the sneak paths problem [3]. Memristor-based 1D1R devices demonstrate pinched hysteresis memristive loops at the 1st quadrant (Positive – Positive) of the current-voltage (I-V) plane, whereas they show diode curves at the 3rd quadrant (Negative - Negative) [1,4]. A typical I-V curve for the 1D1R memristor device is depicted in Fig.1.
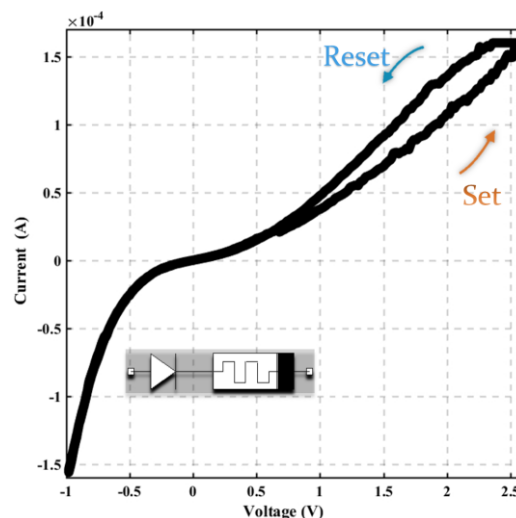
Fig.1. Schematic representation showing typical I-V curve of the memristor-based 1D1R structure [4]

In 2008, Williams et al. of the Hewlett-Packard (HP) Laboratories presented the fabrication and mathematical model of the semiconductor memristor [5], which was first introduced in 1971 by Chua [6]. The memristor provides the missing relationship between charge and flux for the completeness and symmetry of the circuit parameters [6]. A memristor is a two-terminal fundamental passive circuit element having a nonlinear pinched hysteresis I-V characteristic which could not be realized by any arrangement of the other three fundamental passive circuit elements (resistor, inductor and capacitor) [7].

Several mathematical models have been suggested for modeling the memristor, including those of Strukov [5], Biolek [8], Joglekar [9], Prodromakis [10] and Zha [11].

It is necessary to model the semiconductor structures when designing memristor-based circuits and systems because this enables the researchers to simulate some properties of the circuits like memristance and operation frequency without

needing a physical device [12-13]. It seems that the realization of an actual memristor with the desired characteristics will not be possible in the near future. Since it is of great benefit to circuit designers to be able to model the memristor, researchers have focused on the SPICE-based models and emulators in order to use the memristor-based circuits [14]. Several suitable memristor emulators [15-27] and materials [28-29] have been proposed for memristor-based systems.

In this paper, a generic circuit model consisting of two diodes, two resistors and a memristor has been proposed to simulate the 1D1R structures. The current-voltage (I-V) characteristics of the circuit were obtained using different memristor models in a SPICE environment. The results obtained for the presented circuit showed that the models of Strukov [5] and Zha [11] were more compatible with the experimental results compared to the other models.

II. Linear Drift Model and Window Functions of the Memristor

Analysis and simulation of memristor-based systems require a proper model. The distinguishing feature of the memristor is that the I-V characteristics display the pinched hysteresis loop [6]. Several models have been suggested for achieving the pinched hysteresis loop [5,8-11]. The Strukov or HP memristor model based on the drift of oxygen vacancies, also known as the linear drift model, is widely used [5]. It was also the first model to be proposed.
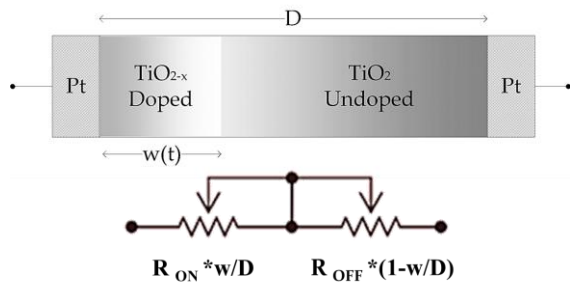
Fig.2. The structure of the TiO_2/TiO_{2-x} based memristor and simplified circuit model.

The amount of total resistance for a memristor can be calculated from the summation of the doped region resistance (R_{ON}*w/D) and un-doped region resistance (R_{OFF}*(1-w/D)). The active-layer thickness of the device is stated as D, with w(t) representing the thickness of the doped region (**Fig. 2.**) [5].

The voltage and current relationship of the memristor is defined by Eq. (1) in the linear drift model.

$$v(t) = \left[R_{ON} x(t) + R_{OFF} (1 - x(t)) \right] i(t) \qquad (1)$$

$$x(t) = \frac{w(t)}{D} \qquad \in (0,1) \qquad (2)$$

where R_{ON} and R_{OFF} are the values of the resistance for w(t) = D and w(t) = 0, respectively.

From Equations (1) and (2), the memristance (M) can be expressed by Eq. (3).

$$M(q(t)) = \frac{v(t)}{i(t)} = R_{ON} x(t) + R_{OFF} (1 - x(t)) \qquad (3)$$

The change of the memristor resistance is represented by the x(t) variable in Eq. (2). The speed of change of the boundary between the un-doped and doped layers is stated by dx / dt in Eq. (4), where μ_v is the ion mobility of the TiO_2.

$$\frac{dx(t)}{dt} = \mu_v \frac{R_{on}}{D^2} i(t) \qquad (4)$$

The following Eq. (5) is derived when Eq. (4) is taken as a time integral.

$$x(t) = \mu_v \frac{R_{on}}{D^2} q(t) \qquad (5)$$

When Eq. (5) is put in its place in Eq. (3), the memristance expression is derived as Eq. (6)

$$M(q(t)) = R_{on} \mu_v \frac{R_{on}}{D^2} q(t) + R_{off} \left(1 - \mu_v \frac{R_{on}}{D^2} q(t) \right) \qquad (6)$$

The simplified form of the linear drift model expression is shown in Eq. (7) on condition that $R_{ON} \ll R_{OFF}$, where M, μ, q, D, R_{ON} and R_{OFF} values are represented by memristance, mobility, charge, active-layer thickness, low-resistance state and high-resistance state, respectively [5].

$$M(q(t)) = R_{off} \left(1 - \mu_v \frac{R_{on}}{D^2} q(t) \right) \qquad (7)$$

In nano scale devices, small voltage fluctuations can produce a large electric field, causing a non-linear drift of the ions near the boundary interfaces. A window function is needed to provide nonlinearity for the boundary problems pointed out above [5,8-11]. This function is realized by rearranging the expression of Eq. (4). In Eq. (8), the $f(x(t))$ indicates the window function.

$$\frac{dx(t)}{dt} = \mu_v \frac{R_{on}}{D^2} i(t) f(x(t)) \qquad (8)$$

Numerous window functions have been proposed for memristor modeling. Some of the suggested window functions include those of Strukov [5], Joglekar [9], Proromakis [10], Biolek [8] and Zha [11], as shown in Table I.

TABLE I
EXPRESSIONS OF WINDOW FUNCTIONS

Name	Expressions
Strukov	$f(x) = x - x^2$
Joglekar	$f(x) = 1 - (2x - 1)^{2p}$
Prodromakis	$f(x) = j \left(1 - \left[(x - 0.5)^2 + 0.75 \right]^p \right)$
Biolek	$f(x) = 1 - (x - stp(-i))^{2p}$
Zha	$f(x) = j \left(1 - \left[0.25(x - stp(-i))^2 + 0.75 \right]^p \right)$

III. SPICE MODEL OF THE CIRCUIT

Modeling of the semiconductor memristor is necessary in the designing of memristor-based circuits and systems. The Simulation Program with Integrated Circuit Emphasis (SPICE) simulators are of great benefit to circuit designers in modeling memristor-based systems [8,13-14,30].

The 1D1R memristor-based circuit model was designed by using two generic diodes, two resistors and one memristor (Fig. 3). The D1 and D2 diodes simulate the forward-bias region and reverse-bias region, respectively. The R3 resistor is used to prevent the reverse bias over-current which flows through the D2 diode. The R2 resistor models the contact resistance of the semiconductor devices. A sinusoidal voltage was applied to the circuit to acquire current-voltage characteristics. Finally, the R1 resistor was used to represent the internal resistance of the active layer.
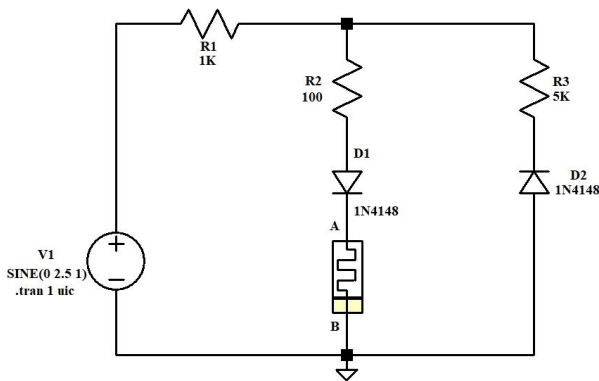
Fig.3. The proposed SPICE circuit model for 1D1R devices

The circuit was simulated using the LTSpice simulation program. The parameters required to achieve the mathematical model of the memristor are given in Table II, where μ is the dopant mobility, D is the active-layer thickness, p is the constant number for the window function, R_{ON} is the ON state resistance, R_{OFF} is the OFF state resistance and R_{INIT} is the initial state resistance. A 2.5 V 1 Hz sinus voltage source was used to run the circuit.

TABLE II
SPICE MODEL PARAMETERS OF THE MEMRISTOR

D	p	μ	R_{ON}	R_{OFF}	R_{INIT}
10 nm	1	$10*10^{-14}$	100 Ω	160 KΩ	35 KΩ

The comparative I-V characteristics of the circuit for all of the models are depicted in Figure 4. All models showed nearly equal characteristics in the 3rd quadrant of the I-V scale. The current-voltage relationship for the Joglekar [9] model exhibited a hard switching mechanism in the 1st memristive quadrant as compared to the other models, which showed smooth switching mechanisms (Fig. 4).

Current-voltage curves were obtained from the proposed circuit based on the memristor modeled with the mentioned window functions. Each I-V curve was then compared to the experimental result. The Joglekar, Biolek and Prodromakis models were not fully fitted to the experimental results (Fig. 5. a-c).
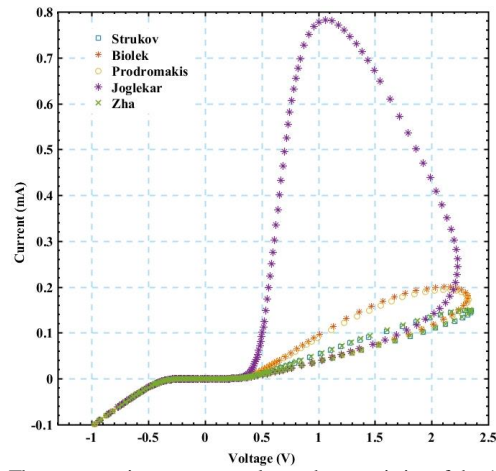
Fig.4. The comparative current - voltage characteristics of the 1D1R circuit model with different window functions

The Joglekar model in particular exhibited greatly different characteristics from the experimental results. Both the Biolek and Prodromakis models showed I-V curves similar to the experimental results, but these results were not fully fitted. The Zha and Strukov models were well fitted with the experimental curve (Fig. 5. d-e)

(a)

(b)
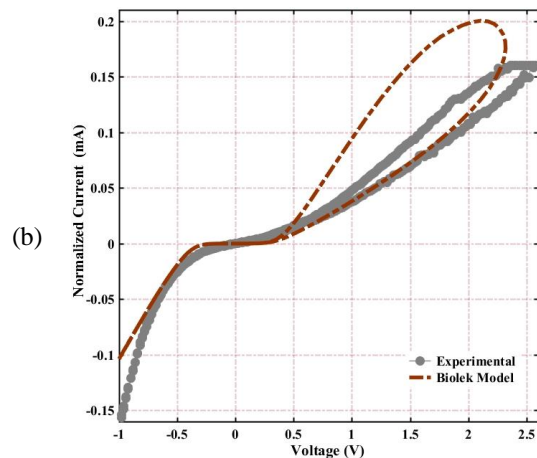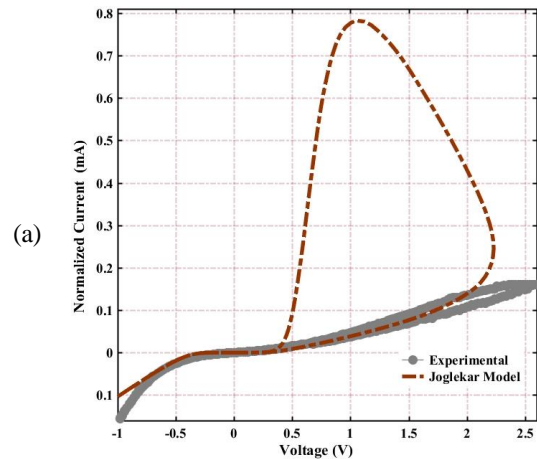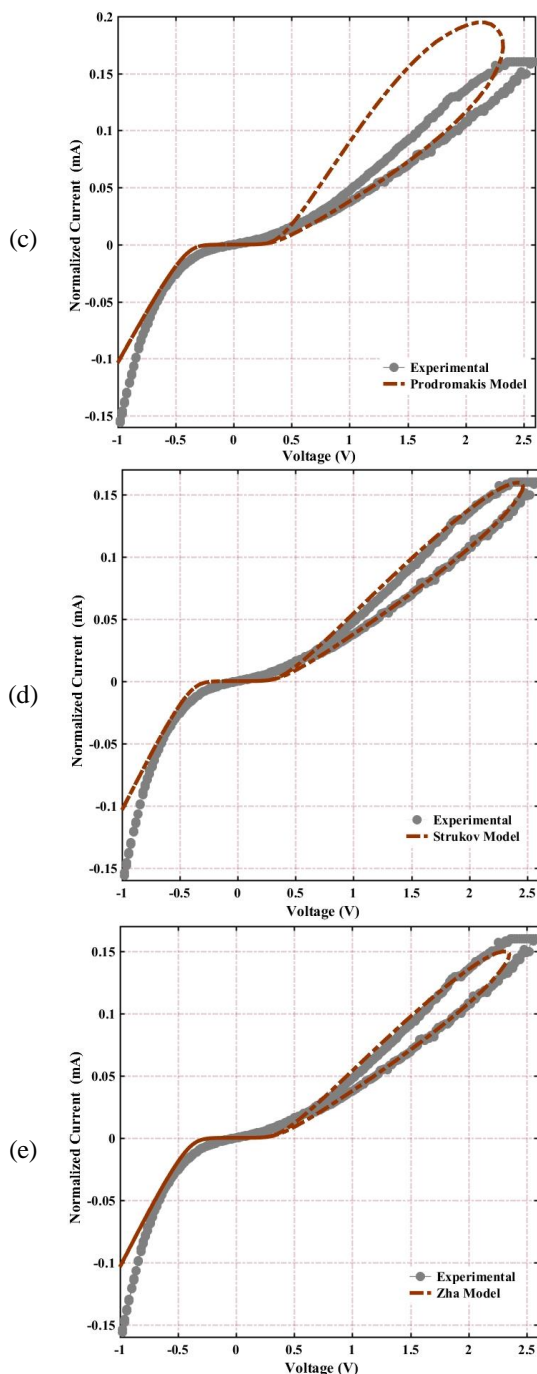
Fig.5. Current - voltage characteristics of 1D1R circuit model with different window functions: (a) Strukov, (b) Biolek, (c) Prodromakis, (d) Joglekar and (e) Zha

As a result, all models exhibited the expected memristor* based one diode-one resistor current-voltage characteristics. In other words, all models demonstrated pinched hysteresis memristive loops at the 1st quadrant (Positive - Positive) and diode curves at the 3rd quadrant (Negative - Negative) of the I-V planes [1,4]. The simulation results of the Zha [11] and Strukov [5] models exhibited the characteristics most similar to the experimental curve when compared to the others.

IV.   CONCLUSIONS

A circuit was designed for the simulation of memristor-

based 1D1R semiconductor structures using LTSpice. One memristor, two generic diodes and three resistors were used to design the circuit. The memristor element was modeled using different window functions. The circuit was simulated for each of the memristor models. All simulation results were compatible to the typical characteristics of 1D1R devices. The best fit results were obtained with the Zha and Strukov models.

REFERENCES

[1]   M. A. Zidan, H. A. H. Fahmy, M. M. Hussain, and K. N. Salama, "Memristor-based memory: The sneak paths problem and solutions," *Microelectronics J.*, vol. 44, no. 2, pp. 176–183, Feb. 2013.
[2]   A. Chen, "Memory Select Devices," in *Emerging Nanoelectronic Devices*, Chichester, United Kingdom: John Wiley & Sons Ltd, 2014, pp. 227–245.
[3]   C. Xu, D. Niu, N. Muralimanohar, R. Balasubramonian, T. Zhang, S. Yu, and Y. Xie, "Overcoming the challenges of crossbar resistive memory architectures," in *2015 IEEE 21st International Symposium on High Performance Computer Architecture, HPCA 2015*, 2015, pp. 476–488.
[4]   F.Gül and Y.Babacan, "A Circuit Model for Single Cell 1 Diode-1 Memristor (1D1M) Semiconductor Device," in *II. International Academic Research Congress*, 2017, p. 548.C.
[5]   D. B., Strukov, G. S., Snider, D. R. Stewart, and R. S., Williams, "The missing memristor found", *Nature*, vol.453, pp.80-83, 2008.
[6]   L.O., Chua, "Memristor - the missing circuit element," *IEEE Trans. Circuit Theory*, vol.18, pp. 507-519, 1971.
[7]   F. Gul and H. Efeoglu, "Bipolar resistive switching and conduction mechanism of an Al/ZnO/Al-based memristor," *Superlattices Microstruct.*, vol. 101, pp. 172–179, Jan. 2017.
[8]   Z. Biolek, D. Biolek, and V. Biolková, "SPICE model of memristor with nonlinear dopant drift," *Radioengineering*, vol. 18, no. 2, pp. 210–214, 2009.
[9]   Y. N. Joglekar and S. J. Wolf, "The elusive memristor: Properties of basic electrical circuits," *Eur. J. Phys.*, vol. 30, no. 4, pp. 661–675, 2009.
[10]   T. Prodromakis, B. P. Peh, C. Papavassiliou, and C. Toumazou, "A versatile memristor model with nonlinear dopant kinetics," *IEEE Trans. Electron Devices*, vol. 58, no. 9, pp. 3099–3105, 2011.
[11]   J. Zha, H. Huang, and Y. Liu, "A Novel Window Function for Memristor Model with Application in Programming Analog Circuits," *IEEE Trans. Circuits Syst. II Express Briefs*, vol. 63, no. 5, pp. 423–427, 2016.
[12]   Y. Babacan and F. Kacar, "FCS Based Memristor Emulator with Associative Learning Circuit Application," *Istanbul Univ. - J. Electr. Electron. Eng.*, vol. 17, no. 2, pp. 3433–3437, 2017.
[13]   A. F. Adzmi, A. Nasrudin, W. F. H. Abdullah, and S. H. Herman, "Memristor Spice model for designing analog circuit," *2012 IEEE Student Conf. Res. Dev.*, pp. 78–83, 2012.
[14]   D. Batas and H. Fiedler, "A memristor SPICE implementation and a new approach for magnetic flux-controlled memristor modeling," *IEEE Trans. Nanotechnol.*, vol. 10, no. 2, pp. 250–255, 2011.
[15]   S. Ç. Yener, R. Mutlu, and H. H. Kuntman, "Analysis of filter characteristics based on PWL Memristor," Istanbul Univ. - J. Electr. Electron. Eng., vol. 14, no. 1, pp. 1709–1719, 2014.
[16]   U. E. Ayten, S. Minaei, and M. Sağbaş, "Memristor emulator circuits using single CBTA," AEU - Int. J. Electron. Commun., vol. 82, pp. 109–118, 2017.
[17]   R. Mutlu and E. Karakulak, "Emulator circuit of TiO2 memristor with linear dopant drift made using analog multiplier," in National Conference on Electrical, Electronics and Computer Engineering (ELECO), 2012, pp. 380–384.
[18]   H. Sözen and U. Çam, "Electronically tunable memristor emulator circuit," Analog Integr. Circuits Signal Process., vol. 89, no. 3, pp. 655–663, 2016.
[19]   H. Sozen and U. Cam, "First-Order Memristor–Capacitor Filter Circuits Employing Hp Memristor," J. Circuits, Syst. Comput., vol. 23, no. 8, p. 1450116, 2014.

[20] C. P. Uzunoglu, Y. Babacan, F. Kacar, and M. Ugur, "Modeling and Suppression of Chaotic Ferroresonance in a Power System by Using Memristor-based System," Electr. Power Components Syst., vol. 44, no. 6, pp. 638–645, 2016.

[21] Y. Babacan, A. Yesil, and F. Kacar, "Memristor emulator with tunable characteristic and its experimental results," AEU - Int. J. Electron. Commun., vol. 81, pp. 99–104, 2017.

[22] Y. Babacan and F. Kaçar, "Floating memristor emulator with subthreshold region," Analog Integr. Circuits Signal Process., vol. 90, no. 2, pp. 471–475, 2017.

[23] Y. Babacan and F. Kaçar, "Memristor emulator with spike-timing-dependent-plasticity," AEU - Int. J. Electron. Commun., vol. 73, pp. 16–22, 2017.

[24] A. Yeşil, Y. Babacan, and F. Kaçar, "A new DDCC based memristor emulator circuit and its applications," Microelectronics J., vol. 45, no. 3, pp. 282–287, 2014.

[25] C. Sanchez-Lopeza, M.A. Carrasco-Aguilar, and C. Muniz-Montero, "A 16 Hz–160 kHz memristor emulator circuit," AEU-International Journal of Electronics and Communications, 1208-1219, 2015.

[26] F. Gul and Y. Babacan, "A novel OTA-based circuit model corroborated by an experimental semiconductor memristor," Microelectron. Eng., vol. 194, pp. 56–60, Jul. 2018.

[27] Y. Babacan, A. Yesil, and F. Gul, "The Fabrication and MOSFET-Only Circuit Implementation of Semiconductor Memristor," IEEE Trans. Electron Devices, 2018.

[28] F. Gul and H. Efeoglu, "ZnO and ZnO1−xbased thin film memristors: The effects of oxygen deficiency and thickness in resistive switching behavior," Ceram. Int., vol. 43, no. 14, pp. 10770–10775, 2017.

[29] F. Gul, "Carrier transport mechanism and bipolar resistive switching behavior of a nano-scale thin film TiO 2 memristor," Ceram. Int., Mar. 2018.

[30] Z. Kolka, D. Biolek, and V. Biolkova, "Hybrid modelling and emulation of mem-systems," Int. J. Numer Model Electronic Netw. Dev. Fields, pp. 216-225, 2012.

BIOGRAPHIES

FATİH GÜL received his B.Sc. degree from Inonu University and his M.Sc. and Ph.D. degrees from Ataturk University, all in Electrical and Electronics Engineering, in 2004, 2008 and 2017, respectively. His main research interests are semiconductors, resistive switching memory devices, memristor and neuromorphic systems.

Benchmarking of Regression and Time Series Analysis Techniques for Sales Forecasting

C. CATAL, K. ECE, B. ARSLAN and A. AKBULUT

Abstract— **Predicting the sales amount as close as to the actual sales amount can provide many benefits to companies. Since the fashion industry is not easily predictable, it is not straightforward to make an accurate prediction of sales. In this study, we applied not only regression methods in machine learning but also time series analysis techniques to forecast the sales amount based on several features. We applied our models on Walmart sales data in Microsoft Azure Machine Learning Studio platform. The following regression techniques were applied: Linear Regression, Bayesian Regression, Neural Network Regression, Decision Forest Regression and Boosted Decision Tree Regression. In addition to these regression techniques, the following time series analysis methods were implemented: Seasonal ARIMA, Non-Seasonal ARIMA, Seasonal ETS, Non -Seasonal ETS, Naive Method, Average Method, and Drift Method. It was shown that Boosted Decision Tree Regression provides the best performance on this sales data. This project is a part of the development of a new decision support system for the retail industry.**

Index Terms—**Machine learning, regression, sales forecasting, time series analysis.**

I. INTRODUCTION

THE IDENTIFICATION of the number of stocks and the replenishment strategy are significant activities for many companies in the retail industry.

If the number of the products is insufficient at a given time, the customer demand cannot be satisfied at that time which causes the company to lose the customer. If there are a sufficient number of products, but there is no potential customer to buy them, then the product stays in stocks. In addition, the fashion industry is volatile. Trends change quickly. Fashion must be closely followed to increase the sales amount.

A company which is out of the trends is not preferred by the customers. Therefore, features which affect the fashion can be examined to increase the sales. In this study, our goal is to predict the actual sales amount accurately by using different machine learning algorithms. Machine learning is a very active research field that helps to learn from the data and uses the data to make a prediction for the future. There are many application areas of machine learning algorithms. For example, Facebook's News Feed feature, which applies the EdgeRank algorithm, can be used for the personalization of the feeds. The algorithm identifies the user interests by using statistical and predictive analysis.

Walmart, one of the best retailers in the world, dramatically increased its online sales and revenue by using advanced data mining techniques. The data prior to the sales and after the sales have been extensively analyzed by the data scientists to change the e-commerce strategy of this retail company. Also, Walmart has changed its shipping policy for the products based on the data analysis performed on big data. According to Walmart's new shipping policy, the minimum amount for free shipping was raised from $45 to $50.

In this study, Walmart's public data was analyzed with different regression algorithms in Azure Machine Learning (ML) Studio. In addition to these algorithms, several time series analysis methods were implemented by using R packages which are available from Azure ML Studio. Since there is no way to add time series analysis methods into the experiment screen graphically, these methods were implemented in the R programming language manually. Later, the best model was transformed into a web service and this web service was deployed on the Azure cloud platform. A client application was implemented to consume this web service. Azure sends the results in JSON format.

The following regression algorithms were applied: Linear Regression, Bayesian Regression, Neural Network Regression, Random Forest Regression, and Boosted Decision Tree Regression. Also, the following time series analysis techniques were applied: Seasonal ARIMA, Non-Seasonal ARIMA, Seasonal ETS, Non-Seasonal ETS, Naive Method, Average Method, and Drift Method. According to the experimental results, the best method was identified. It was

CAGATAY CATAL, is with Information Technology Group Wageningen University, Wageningen, The Netherlands,(e-mail: cagatay.catal@wur.nl).
https://orcid.org/ 0000-0003-0959-2930

KAAN ECE, is with Department of Computer Engineering Istanbul Kültür University, Istanbul, Turkey, (e-mail: 1101020039@stu.iku.edu.tr).
https://orcid.org/0000-0001-7225-047X

BEGUM ARSLAN, is with Department of Computer Engineering Istanbul Kültür University, Istanbul, Turkey, (e-mail: 1201020009@stu.iku.edu.tr).
https://orcid.org/0000-0002-4794-0791

AKHAN AKBULUT, is with Department of Computer Engineering Istanbul Kültür University, Istanbul, Turkey, (e-mail: a.akbulut@iku.edu.tr).
https://orcid.org/ 0000-0001-9789-5012

observed that the regression techniques provide better performance compared to the time series analysis approaches. In this study, it was demonstrated that building an end-to-end sales prediction system on Azure ML Studio is an easy and very efficient task and there are many algorithms to apply.

The remainder of this paper is organized as follows: Section II presents the related work. Section III shows the methodology and the Section IV explains the initial results of this system. Section V shows the conclusion and future work.

II. RELATED WORK

There are many studies on the development of sales forecasting models, but they did not evaluate many models in one study and use Azure Machine Learning Studio platform to build an end-to-end sales prediction system so far.

Kuo [1] applied the fuzzy-neural network for sales forecasting and demonstrated that this model's performance is superior to traditional neural networks. Chen and Ou [2] used a new approach called Gray extreme machine learning with Taguchi method [2]. The system performance was better than the performance of artificial neural networks. Zhao et al. [3] utilized from clustering, regression, and time series analysis techniques for the electricity sales forecasting. Tian et al. [4] applied seasonal time series analysis for auto sales in China. The seasonal effects were calculated by using the exponential weighted moving average. Later, calculated effects and the counted frequency are combined for the linear regression technique. Zhang [5] combined ARIMA and neural network for forecasting. Pandey and Somani [6] implemented a cloud computing based sales forecasting system and applied time series analysis with the moving average method. They deployed the system on Azure cloud and used MySQL database and PHP programming language. Moving average methods are being applied to forecast the sales for a long time in the literature [7]. Vijayalakshmi et al. [8] implemented a sales forecasting engine based on genetic algorithms. Yeo et al. [9] developed a new customer model which uses customer-browsing behavior and tested the model on an e-commerce website. Choi et al. [10] combined the SARIMA and wavelet transform method for sales forecasting. They demonstrated that the new hybrid model provides better performance than the single methods. Chang et al. [11] designed a hybrid model, which combines k-means clustering and fuzzy neural network for sales prediction of circuit boards. Wong et al. [12] implemented a new model, which uses extreme learning machine and harmony search algorithm for sales prediction of retail supply chains and showed that the new model provides better performance than the ARIMA models. Katkar et al. [13] used fuzzy logic and Naive Bayes classifier for sales forecasting. Müller-Navarra et al. [14] applied Recurrent Neural Networks to forecast the sales. Gao et al. [15] used extreme learning machine algorithm.

Omar et al. [16] examined the Back Propagation Neural Network for sales forecasting. Lu et al. [17] proposed a hybrid method based on MARS and SVR techniques for sales prediction of information technology products. They

demonstrated that the new model provides better performance than the single SVR. Stojanović et al. [18] used several features such as fuel price, holiday, unemployment, temperature, store, and date to forecast the weekly sales in Walmart and showed that Support Vector Machine provides the best performance.

As we see in these studies, each study suggests a single model, but we need a comparative assessment of machine learning models to evaluate their performance on the same public dataset. In this study, we performed our experiments to satisfy this goal.

III. METHODOLOGY

In this study, several regression algorithms in machine learning and time series analysis methods were applied for sales forecasting. In this section, these methods are introduced. First, regression algorithms will be explained and then, the time series analysis methods will be introduced.

A. Regression

Linear Regression

Linear Regression is used to create a mathematical equation to produce the relation between independent variables (x) and a dependent variable (y).

B: Coefficients
E: Residue

Linear regression method uses the Formula 1:

$$Y = B_0 + B_1 + B_2 X_2 + \ldots + B_k X_k + Ei \tag{1}$$

The slope of the line is B, and E represents the intercept. Therefore, Y is the response variable which is also called the dependent variable, B's are the weights that are the model parameters, the values of the predictor variables are represented with X's, and finally E is the error term signifying the random sampling noise.

Bayesian Linear Regression

Unlike linear regression, Bayesian Inference is used in the Bayesian approach. The normal distribution in Bayesian approach is calculated based on the Equations 2-3-4-5. Since w is a continuous-valued random variable in R^d, Bayes rule says that the posterior distribution of w is given by y.

$$P(w|y) \propto P(y|w) \, P(w) \tag{2}$$

$$P(w|y) \sim N \, (\mu, S) \tag{3}$$

$$S^{-1} = S_0^{-1} + \frac{1}{\sigma^2} x^t) \tag{4}$$

$$\mu = S \, (\, S_0^{-1} \mu_0 + \frac{1}{\sigma^2} x^t \, y \,) \,) \tag{5}$$

In Bayesian linear regression, the predictive distribution is calculated based on Equation 6:

$$P(y_{new}|y, \; X \; x_{new}, \sigma^2) \; = \; Z \; P(y_{new}|w, \; X, \; x_{new}, \sigma^2)P(w|X) \, dw \tag{6}$$

Predictive distribution evaluates the likelihood of a value y_0 given x_0 for a particular w, by means of likelihood by current belief about w given data (y, X). Finally, sum up all possible values of w.

Neural Network Regression

The neural network regression uses Equation 7:

$$\sum_{i=0}^{M} w_i \, x_i = \text{w.x} \tag{7}$$

In Neural Networks, a perceptron is used to take a vector of real-valued inputs to calculate the linear combinations of inputs. If the output is greater than some threshold, then it outputs 1, in the other case it produces -1. The weights have to be calculated according to the perceptron training rules shown in Equation 8 and 9:

$$w_i \leftarrow w_i + \Delta w_i \tag{8}$$

$$\Delta w_i = \eta (t - o) \, x_i \tag{9}$$

The symbol η refers to the neural network learning rate.

Decision Forest Regression

In the Random Forest algorithm, the primary aim is to make a classification by using several trees. In Random Forest, to obtain the last class of the tree, Gini value is used. Gini value is calculated based on Formula 10:

$$\text{Gini}(T) = 1 - \sum_{i=1}^{n}(p_j) \tag{10}$$

The T dataset is split into T_1, T_2 subsets with N_1, N_2 dimensions, then Gini split value is calculated based on Formula 11:

$$Gini_{split(T)} = \frac{N_1}{N} Gini \, (T_1) + \frac{N_2}{N} Gini \, (T_2) \tag{11}$$

Boosted Decision Tree Regression

Boosted decision trees use gradient boosting algorithm. This algorithm applies the optimization of differentiable loss function by using the weighted sum of functions. The F(x) is calculated based on Equation 12:

$$F_0(x) = \text{arg min} \sum_{i=1}^{n} L(y_{i,\gamma}) \text{ and} \tag{12}$$

The predictions are calculated based on Equation 13:

$$\gamma_m = \text{argmin} \sum_{i=1}^{n} L\left(y_{i,F_{m-1}}(x_i) - \gamma \frac{\partial L(y_{i,F_{m-1}}(x_i))}{\partial F_{m-1}(x_i)}\right) \tag{13}$$

B. Time Series Analysis

ARIMA

ARIMA (autoregressive integrated moving average) model uses the following Equations 14-15 and describes the autocorrelations in the data.

$$Y_t = (1 - L)^d X_t \tag{14}$$

$$Y_t\left(1 - \sum_{i=1}^{p} \Phi_i L^i\right) = \left(1 + \sum_{i=1}^{q} \theta_i L^i\right)\varepsilon_t \tag{15}$$

The parameter L is the lag operator, p is the order which represents the number of time lags of the autoregressive model, and q is the order of the moving-average model. θ are the parameters of the moving average part and Φ are the parameters of the autoregressive part of the model.

Seasonal ARIMA

Seasonal ARIMA (SARIMA) is similar to ARIMA, but it has different elements. SARIMA uses Formula 16-17-18.

$$\Phi(B)\Delta^d X_t = \theta(B)\alpha_t \tag{16}$$

$$\Phi_s(B^s)\Delta_s^D \, \alpha_t = {}_s\Theta(B^s) \, \alpha_t \tag{17}$$

$$\Phi(B)_s\Phi(B^s)\Delta_s^D\Delta^d X_t = \theta(B_s) \, \Theta(B^s) \, \alpha_t \tag{18}$$

SARIMA model has the same structure as the non-seasonal (ARIMA) model: it may have an AR factor, an MA factor (corresponds to α), and/or an order of differencing.

Seasonal ETS

The Seasonal Exponential Smoothing (Seasonal ETS) applies three sub-pass filters recursively with special exponential window functions. The simplest moving averages are the weighting of past observations, but the exponential window functions are multiplied over time to reduce the weight. The simplest formula of seasonal ETS is shown in Formula 19 where α is the smoothing factor and s is the seasonal period.

$$s_t = \alpha. \, X_t + (1 - \alpha) \, s_{t-1} \tag{19}$$

Non-Seasonal ETS

Non-seasonal time series includes a trend component. To estimate the trend component, the simple moving average function is used as shown in Equation 20.

$$SMA = \frac{1}{n} \sum_{i=0}^{n-1} p_{m-i} \tag{20}$$

Naive Method

This method works quite well for economic and financial time series. This approach sets each prediction to be equal to the last observed value of the same season. Equation 21 is used for the calculation.

$$\acute{Y}_{t+h/t} = Y_t \qquad (21)$$

Naive forecast is the model that calculates in the simplest way using the actual demand for the past period as the expected demand for the future period with an assumption of the past will repeat.

Average Method
Estimates of all the future values are equal to the average of the historical data. This approach can be used with any kind of data where historical data is available. Formula 22 shows this simple approach.

$$\acute{Y}_{t+h/t} = (y_1 + \cdots + y_t)/T \qquad (22)$$

To make a forecast using averaging, this formula (22) simply takes the average of selected periods of the past data by summing each period and dividing the result by the number of periods. Therefore, forecast of all future values ($\acute{Y}_{t+h|t}$) is equal to mean of historical data. It is worth pointing out that this technique is very effective and useful for short term forecasts.

Drift Method: This method is the variation of the Naive method, but it provides an increasing or decreasing over time which is called drift for the historical data. Equation 23 shows how the method works.

$$\acute{Y}_{t+h/t} = y_t + h\left(\frac{y_t - y_1}{T-1}\right) \qquad (23)$$

Forecasts are equal to last value plus average change which is an equivalent expression to the extrapolation of a line drawn between the first and last observations.

IV. EXPERIMENTAL RESULTS

Datasets were obtained from Walmart Recruiting Store Sales Competition page of Kaggle website [19]. There are three different files called features.csv, stores.csv and train.csv. In features.csv, there are several features such as temperature, fuel price, and unemployment. In stores.csv, there are features such as store id, store type, and store size. Finally, train.csv has some historical data and real sales amount. The first step is to create a new experiment. Then, the features.csv, stores.csv and train.csv documents are joined to create a single dataset. The next step is to perform feature selection and feature extraction.

Feature.csv file includes store, date, temperature, fuel_price, MarkDown1, MarkDown2, MarkDown3, MarkDown4, MarkDown5, CPI, Unemployment, IsHoliday features. Store.csv includes the store, type, size features, and train.csv includes the store, department, date, weekly_sales, IsHoliday. These three files were imported into MS SQL Server Management Studio and were combined with an inner join operation. The features used in the system are the store, department, date, isHoliday, size, fuel_price, isHoliday. The class label is weekly_sales. As a result of the feature selection, the following features were identified: week of the month, monthOfYear, prevWeekSales, season, store size,

tempCategory. Also, economical features were investigated and used for the prediction such as PPI, TreInf, TNF. These economical features were added to the previous feature set. Therefore, the following features were created in the dataset: Store, department, week of the month, MonthOfYear, PrevWeekSales, isHoliday, period, season, size, PPI, TNF, TreInf, fuel_price.

PPI is the acronym of Producer Price Index and sets the inflation rate incurred by the purchase of goods and services. TreInf indicates the amount of income per household. TNF is the acronym of Total Nonfarm Payrolls which is a monthly report showing how many employers provide employment in private or government sectors for the previous month, or how much reduction occurs in the employment in the United States. Season and period were extracted from the date feature. 1 is used to represent the autumn season, 2 for the winter season, 3 for the spring season and 4 for the summer season.

The Period feature is selected based on the company's yearly plan. Most of the companies start their yearly plan in January. Therefore, 1 represents the first three months, 2 is used for the next 3 months. The week of the month and the month of the year were also extracted from the date feature. The store size feature was extracted from the size feature and the temperature category was extracted from temperature. 1 represents below 15 C°, 2 is between 15 C° - 25 C° and 3 means over 25 C°. Also, previous week sales feature was extracted from the weekly_sales feature by using previous week sales. IsHoliday includes the following days: Super Bowl, Christmas, Labor Day, Thanksgiving. WeekNo feature was extracted from the date feature. Dates on the training dataset were numbered to weeks. Temperature, MarkDown1, MarkDown2, MarkDown3, MarkDown4, MarkDown5, CPI, Unemployment, store size, TempCategory were observed to have negative effects on the models. Therefore, these features were removed. The data which is up to 2012-01-01 were used for training and the remaining four months were used for testing.

During the experiments, parameters of the regression algorithms were optimized by using "tune hyper model parameters" feature of Azure ML Studio platform. After the best model was selected, "Set Up Web Service" button with "Predictive Web Service" option was used to produce the web service. Web service was deployed by selecting "Deploy Web Service" button. Web Services are displayed on the "Web Services" tab on the Azure ML Studio. Web service C# code for a client application is displayed on the REQUEST/RESPONSE page and its API key is displayed on the dashboard screen of the selected web service. The API key is needed to authenticate the user. In this study, MAE and RMSE error parameters were used.

Root Mean Squared Error: It is the square root of the average error. The mean squared error is shown based on Equation 24.

$$\text{RMSE} = \sqrt{\frac{\sum_{i=1}^{n}(Xobs,i - Xmodel,i)}{n}} \qquad (24)$$

X_{obs}: observed value
X_{model}: predicted values at time/place i.

Mean Absolute Error (MAE): It takes the average of absolute errors. Equation 25 is used to calculate this parameter. MAE calculates the average absolute difference between y_i and x_i which are the coordinates of point i.

$$MAE = \frac{1}{n}\sum_{i=1}^{n}|e_t| \qquad (25)$$

Initial experiments were performed for only one store and one department of the Walmart Company because of the time series analysis techniques. Test results were evaluated by several evaluation parameters such as Mean Absolute Error and Root Mean Squared Error. Decision Forest Regression was the best approach based on RMSE and MAE value as shown in Figure 1.
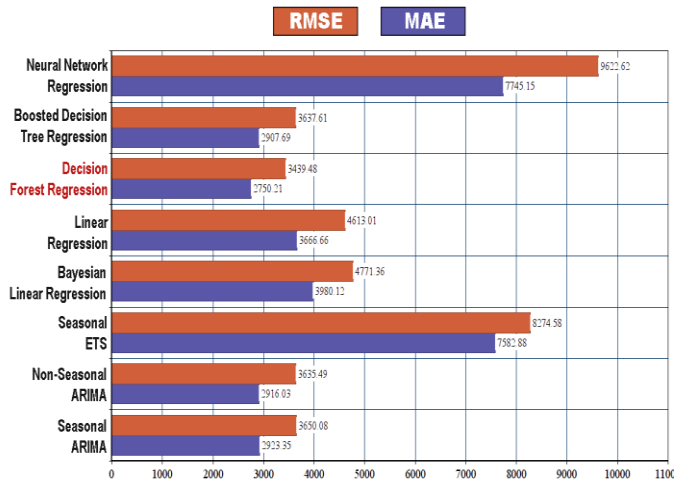

Fig. 1. Evaluation of experiments

Table 1 shows that four methods provide better performance. The difference between Decision Forest Regression, Non-Seasonal ARIMA, Boosted Decision Tree Regression, and Seasonal ARIMA's accuracy is not too much. Decision Forest Regression provides the highest performance.

TABLE 1.
RMSE AND MAE RESULTS

Method	RMSE	MAE
Seasonal ARIMA	3650.08	2923.35
Non-Seasonal ARIMA	3635.49	2916.03
Seasonal ETS	8274.58	7582.88
Bayesian Linear Regression	4771.36	3980.12
Linear Regression	4613.01	3666.66
Decision Forest Regression	**3439.48**	**2750.21**
Boosted Decision Tree Regression	3637.61	2907.69
Neural Network Regression	9622.62	7745.15

To extend the experiment with the entire dataset, all the departments were tested with these regression methods because the use of time series analysis techniques is not appropriate for the entire dataset. Parameters were optimized with Tune Model Hyper Parameters module in Azure ML

Studio. This time, the best approach is Boosted Decision Tree Regression. In Table 2, results are shown.

TABLE 2
ALL THE DEPARTMENTAL RESULTS

Method	MAE	RMSE	Coefficient of Determination
Bayesian Linear Regression	2469.54	4361.40	0.96
Linear Regression	2480.12	4365.04	0.96
Neural Network Regression	14951.09	22499.33	0.00
Boosted Decision Tree Regression	**1669.10**	**3696.59**	**0.97**

The coefficient of determination, which is also known as R^2 (equation 26) represents the predictive power of the model as a value between 0 and 1.

$$R^2 = \frac{\sum(y-\overline{y})^2 - \sum(y-\hat{y})^2}{\sum(y-\overline{y})^2} \qquad (26)$$

The coefficient of determination, R2, signifies the proportion of the total sample variation in y which is measured by the sum of squares of deviations of the sample y values about their mean $\overline{y}$, is attributed to the linear relationship between x and y. It is a standard way of evaluating how well the model fits the data. It can be interpreted as the proportion of variation explained by the model. A higher proportion is better, where 1 indicates a perfect fit. We used the coefficient of determination factor to express our accuracy. Moreover, the highest prediction success in estimates where all stores are used is 0.97 with Boosted Decision Tree Regression method as shown in Table 2.

As explained in the Related Work section, several studies applied the times series analysis approaches [4, 6] and artificial neural network algorithms [14, 16, 20] for predicting the sales amount. In this study, we demonstrated that regression algorithms (i.e., Boosted Decision Tree Regression) work much better than these algorithms used in the literature and it does not require much optimization to provide high performance. We developed our NN model using a standard topology, and therefore this might affect the performance of the model. This can be considered as one of the threats to the validity of this study. Also, our experiments were performed on a specific dataset and hence, the performance might be different on other kinds of datasets. We suggest practitioners apply the Boosted Decision Tree Regression algorithm for sales forecasting.
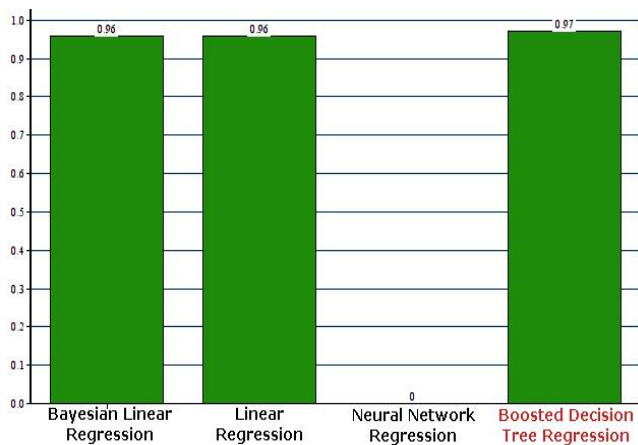
Fig. 2. The coefficient of determination results

V. CONCLUSION

It is crucial to predicting the sales amounts as close as to the actual sales amounts for enterprises to increase their profits [20]. Unless an accurate forecasting model is built, cash flow problems are inevitable. Therefore, building this kind of prediction models for sales forecasting has a high priority for the organizations. In this study, we investigated the effect of Regression and Time Series Analysis methods on the sales forecasting problem. Our experiments show that the regression techniques provide higher performance and accuracy compared to the time series analysis techniques. Boosted Decision Tree Regression algorithm was the best predictor for sales forecasting with the 0.97 coefficient of determination. Prediction results were obtained for weekly sales quantities.

In the future, a hybrid model using ARIMA and Boosted Decision Tree Regression techniques will be investigated to solve this problem. In addition, the implementation of another hybrid model with an SVM model is planned. New experiments will be performed if the new public data is obtained. Also, deep learning algorithms [22, 23] can be investigated for sales prediction problem.

ACKNOWLEDGMENT

REFERENCES

[1]   Kuo, R. J. (2001). A sales forecasting system based on fuzzy neural network with initial weights generated by genetic algorithm. European Journal of Operational Research, 129(3), 496-517.

[2]   Chen, F. L., & Ou, T. Y. (2011). Sales forecasting system based on Gray extreme learning machine with Taguchi method in retail industry. Expert Systems with Applications, 38(3), 1336-1345

[3]   Zhao, J., Tang, W., Fang, X., Wang, J., Liu, J., Ouyang, H., ... & Qiang, J. (2015, September). A Novel Electricity Sales Forecasting Method Based on Clustering, Regression and Time Series Analysis. In Proceedings of the 2015 International Conference on Artificial Intelligence and Software Engineering.,

[4]   Tian, Y., Liu, Y., Xu, D., Yao, T., Zhang, M., & Ma, S. (2012, April). Incorporating Seasonal Time Series Analysis with Search Behavior Information in Sales Forecasting. In Proceedings of the 21st International Conference on World Wide Web (pp. 615-616).

[5]   Zhang, G. P. (2003). Time series forecasting using a hybrid ARIMA and neural network model. Neurocomputing, 50, 159-175.

[6]   Pandey, A., & Somani, R. K. (2013). A Cloud Computing Based Sales Forecasting System for Small and Medium Scale Textile Industries. computing, 3(4).

[7]   Winters, P. R. (1960). Forecasting sales by exponentially weighted moving averages. Management Science, 6(3), 324-342.

[8]   Vijayalakshmi, M., Menezes, B., Menon, R., Divecha, A., Ravindran, R., & Mehta, K. (2010, October). Intelligent sales forecasting engine using genetic algorithms. In Proceedings of the 19th ACM international conference on Information and knowledge management (pp. 1669-1672). ACM.

[9]   Yeo, J., Kim, S., Koh, E., Hwang, S. W., & Lipka, N. (2016, April). Browsing2purchase: Online Customer Model for Sales Forecasting in an E-Commerce Site. In Proceedings of the 25th International Conference Companion on World Wide Web (pp. 133-134). International World Wide Web Conferences Steering Committee.

[10] Choi, T. M., Yu, Y., & Au, K. F. (2011). A hybrid SARIMA wavelet transform method for sales forecasting. Decision Support Systems, 51(1), 130-140.

[11] Chang, P. C., Liu, C. H., & Fan, C. Y. (2009). Data clustering and fuzzy neural network for sales forecasting: A case study in printed circuit board industry. Knowledge-Based Systems, 22(5), 344-355.

[12] Wong, W. K., & Guo, Z. X. (2010). A hybrid intelligent model for medium-term sales forecasting in fashion retail supply chains using extreme learning machine and harmony search algorithm. International Journal of Production Economics, 128(2), 614-624.

[13] Katkar, V., Gangopadhyay, S. P., Rathod, S., & Shetty, A. (2015, January). Sales forecasting using data warehouse and Naïve Bayesian classifier. In Pervasive Computing (ICPC), 2015 International Conference on (pp. 1-6). IEEE

[14] Müller-Navarra, M., Lessmann, S., & Voß, S. (2015, January). Sales Forecasting with Partial Recurrent Neural Networks: Empirical Insights and Benchmarking Results. In System Sciences (HICSS), 2015 48th Hawaii International Conference on (pp. 1108-1116). IEEE.

[15] Gao, M., Xu, W., Fu, H., Wang, M., & Liang, X. (2014, July). A novel forecasting method for large-scale sales prediction using extreme learning machine. In Computational Sciences and Optimization (CSO), 2014 Seventh International Joint Conference on (pp. 602-606). IEEE.

[16] Omar, H. A., & Liu, D. R. (2012, January). Enhancing sales forecasting by using neuro networks and the popularity of magazine article titles. In 2012 Sixth International Conference on Genetic and Evolutionary Computing (ICGEC) (pp. 577-580).

[17] Lu, C. J., Lee, T. S., & Lian, C. M. (2010, December). Sales forecasting of IT products using a hybrid MARS and SVR model. In 2010 IEEE International Conference on Data Mining Workshops (pp. 593-599)..

[18] Stojanović, N., Soldatović, M., & Milićević, M. (2014, June). Walmart Recruiting–Store Sales Forecasting. In Proceedings of the XIV International Symposium Symorg 2014: New Business Models and Sustainable Competitiveness (p. 135). Fon.

[19] Kaggle.com | Kaggle Datasets | Open Datasets for Any Project, "https://www.kaggle.com/" Access date: 25.02.2019.

[20] Bohanec, M., Borštnar, M. K., & Robnik-Šikonja, M. (2017). Explaining machine learning models in sales predictions. Expert Systems with Applications, 71, 416-428.

[21] Hyndman, R. J., & Athanasopoulos, G. (2018). Forecasting: principles and practice. OTexts.

[22] Tsoumakas, G. (2018). A survey of machine learning techniques for food sales prediction. Artificial Intelligence Review, 1-7.

[23] Luce, L. (2019). Deep Learning and Demand Forecasting. In Artificial Intelligence for Fashion (pp. 155-166). Apress, Berkeley, CA.

BIOGRAPHIES

CAGATAY CATAL received the B.S. and M.S. degrees in computer engineering from Istanbul Technical University, Istanbul, and the Ph.D. degree in computer engineering from Yildiz Technical University, Istanbul, in 2008. He worked 8 years at the Scientific and Technological Research Council of Turkey as Senior Researcher. Later, he worked 6 years in Istanbul Kültür University, Department of Computer Engineering as Associate Professor and was the Head of the Department for the last 3 years. On January 2018, he joined the Information Technology Group of Wageningen University in the Netherlands. His research interests are data science, machine learning, software engineering, and experimental software engineering.

KAAN ECE received the B.S. degree in computer engineering from Istanbul Kültür University and has been working in Eteration software company for 2 years. His research interests are machine learning and software engineering.

BEGÜM ARSLAN received the B.S. degree in computer engineering from Istanbul Kültür University. Her research interests are machine learning, data science, and software engineering.

AKHAN AKBULUT received the B.S. and M.S. degrees in computer engineering from Istanbul Kültür University and the Ph.D. degree in computer engineering from Istanbul University, Istanbul. Later, he worked 2 years in the software industry. In 2004, he joined the department of computer engineering in Istanbul Kültür University. He has been working at the department of computer science in North Carolina State University since 2017 as Postdoctoral researcher. His research interests are machine learning, cloud computing, software engineering, and internet architectures.

A Measurement Based Study to Assess Power Line Communication Network Throughput Performance

S. M. ÇÜRÜK and V. ÖZKANER

Abstract— **Power line communications (PLC) is a known low cost technology which is easily installed and extended to the various connections especially to areas with poor wireless coverage. Unfortunately, designers and users experience technical problems that arise from the difficulty of operating on a complex time varying medium and that limits the expected high throughput. Therefore, testing and understanding network dynamics of PLC systems before usage is a necessity. This paper presents the findings obtained from the experiments carried out in order to verify the throughput performance of PLC systems. Experimental measurements are realized in different testbeds, under different times and conditions, in order to achieve an idea of the practical PLC performance. Data obtained from the measurements have been stored and the throughput is analyzed by the help of software. Following, using distribution fitting methods, it is shown that the PLC throughput may be modeled by the extreme value distribution. Furthermore, adding a basic noise to the network, simply by lamps, results with a degraded performance. The noise changes the parameters of the derived distributions; a decrease in expected value and an increase in standard deviation are observed.**

Index Terms— **Experimental measurements, extreme value distribution, distribution fitting, power line communications, throughput performance.**

I. INTRODUCTION

THE NEED of network for broadband applications in local areas is growing rapidly. Although performance of the wireless systems within a room is satisfactory, in room to room connectivity, data throughput decreases dramatically due to high signal attenuation caused by walls or ceilings. On the other hand, wired networks like Ethernet need additional installation effort for cabling. In a home or office network, broadband throughput for room to room without any extra installation is desirable. Power Line Communication (PLC) fulfills these requirements and is an alternative solution. PLC uses the preexisting electrical grid as a communication channel and owing to modern modulation techniques the power network is able to ensure high data rate services [1-5].

The main advantage of PLC technology is that it uses the installed electric power networks. Nevertheless, it is difficult to operate on such a medium, since it is not designed for communication but for power transmission, and is characterized by complex time varying channel. Besides, the cable infrastructure is a potential source of interference for radio communication services since it works as a radiating system. These points give rise to practical problems for designers and testers when network quality of service (QoS) performance parameters such as throughput, latency, jitter, and reliability are under investigation [6, 7].

Theoretical QoS performance of PLC is quite satisfactory. But a critical degradation may be faced because of ambiguity caused by variable corruptive factors. i.e. grid size and topology, channel attenuation and impedance, number and positions of sockets, distance and path between the transmitter and the receiver, number and type of disturbing loads connected, positions of interfering sources in relation to the transmitter and the receiver. Therefore, paying attention to these factors and testing before the installation and usage of a PLC system is a critical task. The available researches are mainly focus on the methods and measurement procedures for channel characterization of PLC systems. The studies related to QoS performance measurement are not sufficient yet, so that no reference tests, set-ups and measurement methodologies [7, 8]. Indeed, standardization is a difficult task because the scenarios in which PLC modems can work and the set of parameters related to the performance are wide.

There are some research papers in the literature interested in the performance of PLC systems: [8] works on standardization of the measurements and proposes reference test setups and measurement methodologies for reliable assessment of PLC network performance. A power line testbed is developed in [9], which provides a platform to simulate the power line environment in a controlled and reproducible manner. The combination of different technologies has motivated authors of [10] and [11]. In [10], authors look for the coverage and

SELVA MURATOĞLU ÇÜRÜK, is with Department of Electrical and Electronics Engineering, Iskenderun Technical University, Hatay, Turkey, (e-mail: selva.curuk@iste.edu.tr).

https://orcid.org/0000-0002-2195-7827

VEDAT ÖZKANER, is with Department of Electrical and Electronics Engineering, Iskenderun Technical University, Hatay, Turkey, (e-mail: vedat.ozkaner@iste.edu.tr).

https://orcid.org/0000-0001-8293-0022

capacity of a hybrid network compared to standalone Wi-Fi and PLC networks and in [11] a comparative study of the performance of PLC, wireless and their combination is given. Authors of [12] give a set of measurements conducted on a laboratory testbed for analyzing the PLC usage in the last mile broadband access. Reference [13] develops a PLC network testbed for understanding the network dynamics of PLC systems. A comparison regarding performance is seen in [14], between different architectures and between testbed and commercial installation. In [15], a set of measurements is carried out over the low voltage networks, in order to characterize the performance of the TCP/UDP/IP (Transmission Control Protocol / User Datagram Protocol / Internet Protocol) protocol stack. Reference [16] proposes a new analytic model to evaluate throughput and delay of HomePlug 1.0 under saturation and under normal traffic conditions. The goal of [17] is to investigate flow-level performance problem of TCP over PLC, and to propose methods for coping with these problems. The authors of [18] explore how simple household devices significantly impact the performance of the PLC networks and show that the performance in the home environment is good, but it is far worse than the best-case promised by the manufacturers. Reference [19] brings into focus the need for a systematic approach to qualify in-house power line equipment and networks for audio and video streaming applications.

We are limited to studying the PLC behavior using end-to-end measurements. Characterized by a large number of variables, it is difficult to forecast the actual network performance that can be achieved under real operating conditions. Thus, it is not easy to realize well-controlled measurement setups for reliable and reproducible results if we use a real PLC system in analyzing where the throughput is time varying because of uncontrollable different noise supplies. Therefore in this study, a measurement based evaluation of throughput for a PLC system has been carried out in a laboratory instead of a real house or office. An efficient measurement procedure was developed to reliably assess the performance of PLC modems. It is based on both creating a reconfigurable grid to which real disturbing loads may be connected. Methods have also been provided to analyze the measurement results and the distribution of throughput. We also aimed to explore the effect of a basic disturbance factor, the lamp, on the performance of PLC, by observing the degradation in throughput performance. Our main findings are that PLC provides a quite satisfactory throughput when there is no load in the network but there is a critical degradation in performance when lamps are added.

II. MEASUREMENT SETUP

We performed experiments with NetMaster PWE-500C power line adapters (Ethernet bridge and power line extender), which are compliant to HomePlugAV 1.0 standard. They are advertised to support PHY data rates of 500 Mbps and information rates up to 150 Mbps. The devices operate in the 2-68 MHz frequency band and are able to communicate over

maximum 300 m ac cabling. We evaluated a power line network in a laboratory setup consists of nine nodes. The network design is limited by the designers' imagination and the research's general goals and frame, since the possibilities of network architecture are virtually endless. The realized PLC throughput measurement setup is shown in Fig. 1. It emulates a standard grid with a star topology. Usually with more connections, the star topology is considered as the optimum architecture with regard to bandwidth usage and throughput [14]. It allows expansions in all directions, thus the given topology can be extended for a typical house size. Another topology would be a straight line of nodes. But it is not a realistic model for houses especially and it is shown that in such a topology although the ping time is increasing as the node get further, the PLC throughput performance is not changing significantly [14].
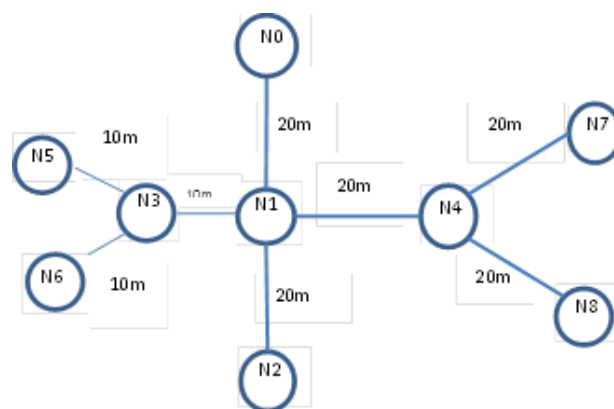

Fig. 1. The power line network topology used in measurement.

The PLC network under test has been separated from the main ac grid with a cabling in order to decrease the effect of noise that may come from the main. In the setup, the wire size of primary lines (segments of 20 m length) is 2.5 mm2 and the size of secondary lines (segments of 10 m length) is 1.5 mm2, and grid designs are compliant with the general rules for the electric installation design. The adapters under test have been controlled by means of two laptop PCs powered by an ac line different from the testbed. The PCs have Ethernet card 100 Mbps and are connected to the network where one acted as a server and the other as a client. As for the measurement setup, all the possible combinations that can be achieved result with huge possible measurement configurations. For the sake of brevity, in order to reduce the number of experiments, a few well rounded scenarios have been selected. In all scenarios PLC transmitter was connected in node 0 (N0) and PLC receiver was moved such as it was connected in each node during the measurements. Measurements have been repeated with a basic load, the lamp, with different placement in the network to understand the relation between the performance and the load, and the locality of transmitter and receiver.

We treated the power line adapters as black boxes and use end-to-end network measurements to reason about the performance of the devices. As suggested by ETSI [7], figures of merit for the assessment of the QoS performance of a PLC network can be selected by considering the throughput, the

latency, the jitter and the reliability. In this study, the throughput has been selected to be the parameter for observing the performance, which is defined as the quantity of data that can be transmitted in a time interval and is typically expressed in Mbps. The PLC network throughput measurements have been performed using a combination of typical software tools, jperf 2.0.2 and ping. Jperf has been used in establishing a link between the transmitter and the receiver, generating the desired traffic conditions and estimating the throughput. The measurements were done during a period of half an hour and were repeated in different time of the day and on various days. The motivation behind this was eliminating the dependence on all possible disturbances. The time delay was estimated using the "ping" application. This application allows to measure the delay time of every packet and, moreover, the average time delay of all packets transmitted since the beginning of the application. Finally, we have obtained the statistics of the throughput.

III. PERFORMANCE EVALUATIONS

The amount of data collected from the measurements was too large to be all presented in details; therefore a well-chosen summary of the findings is presented in this paper. In the first scenario the PLC transmitter was connected to node N0 and the PLC receiver was connected to all nodes, each in turn, during the measurements. Available throughput was monitored using jperf software that generated and measured data traffic transmitted through TCP protocol. For each configuration, the transmission time interval has been fixed to 30 min and the throughput is recorded with a report time interval fixed at 1 s (1800 reported data per interval). The throughput may vary considerably during the tests and therefore its estimation depends on the time interval in which the measurement is performed as well as its length. It is clear that smaller measurement windows reduce the time needed for testing but considerably increase the measurement uncertainty. A total measurement time of about 8 hour per day (between 8:30-16:30) has been considered, with the aim of analyzing the performance of PLC network throughout the day. In addition, the measurements have also been repeated on different days to take into account the uncertainty component due to the arrangement of test setup and the characteristics of test site. For all the results presented, it is guaranteed that every measurement has been repeated in different periods of the day and on different days at least ten times, until we concluded that the real performance was obtained and we have eliminated the nonstandard measurements that may be caused by uncontrollable effects. Finally, the measurement results have been suitably stored.

Fig. 2 shows a sample of the time evolution of throughput when client is connected to node N0 and the server is at node N2 in the absence of external disturbing loads, thus no load is connected to the network. (Note that throughput performance is independent of transmission direction. Measurements were done when client was connected to N2 and server was connected to N0, and it has been proved that the performance

is independent of direction.) In the figure, the combination of 4 time intervals, each 30 min, which makes a total time period of 2 hours (7200 s) is presented. As seen, although it varies slightly, finally the throughput fits to 94.91 Mbps line. Rarely critical drops in the throughput performance are observed with the minimum is 66.6 Mbps.
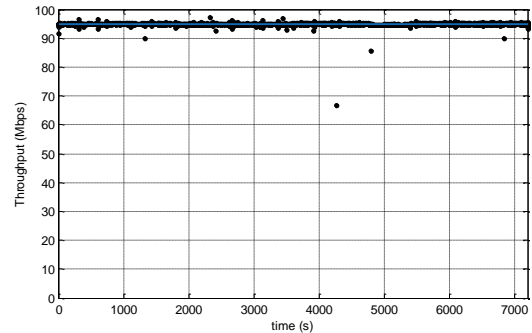

Fig. 2. Throughput versus time, N0 – N2 connection, no load connected.

Fig. 3 and Fig. 4 give the throughput between nodes N0 – N6 and N0 - N8, respectively. The throughput fits to 94.87 Mbps line with minimum 47.8 Mbps in Fig. 3 and to 94.81 Mbps line with minimum 40.0 Mbps in Fig. 4. As seen from the figures, although very close results are obtained, as we get further from the transmitter, slightly lower performance with increased drops is observed. The worse is N0 – N8 throughput performance.
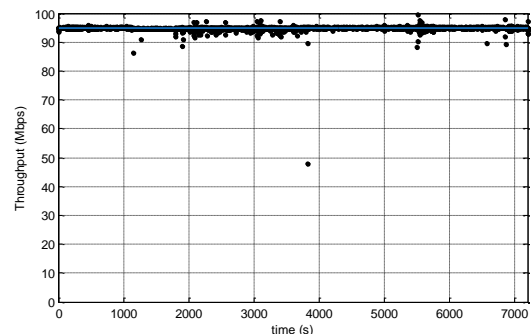

Fig. 3. Throughput versus time, N0 – N6 connection, no load connected.
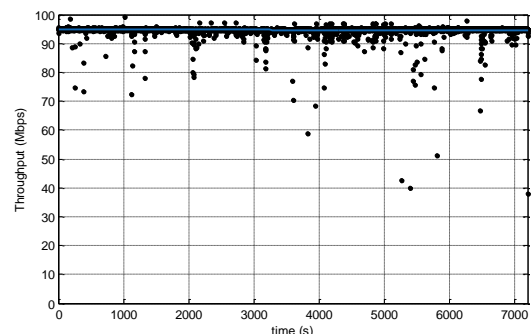

Fig. 4. Throughput versus time, N0 – N8 connection, no load connected.

As disturbing load, compact fluorescent lamps with integrated control gear (energy saver, 24 W) have been selected to be added to the network. The motivation about this

selection is that lamps are the basic elements of power networks in our homes and offices, every time and everywhere present. Some tests have been performed to investigate the performance degradation of the given PLC network under different load configurations and the results are presented in tables and graphs. In the first configuration, lamps have been added to all nodes except node N0. This is expected to be the worst scenario, since the disturbing loads are placed all over the network. Fig. 5, Fig. 6 and Fig. 7 give the throughput of N0 – N2, N0 – N6 and N0 - N8 connections, respectively. The degradation and the activity in the throughput caused by lamps can easily be seen when we compare the figures with the previous ones.
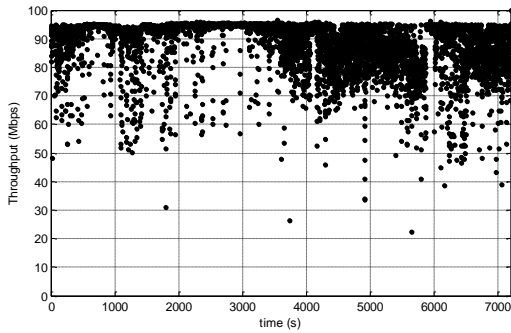

Fig. 5. Noisy throughput versus time, N0 – N2 connection.
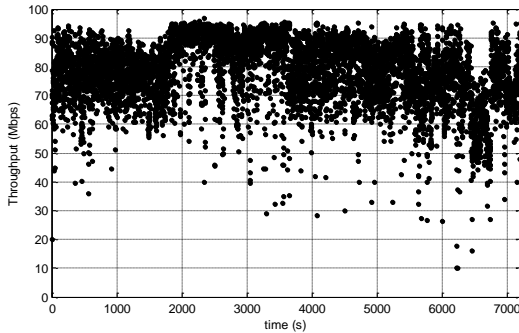

Fig. 6. Noisy throughput versus time, N0 – N6 connection.
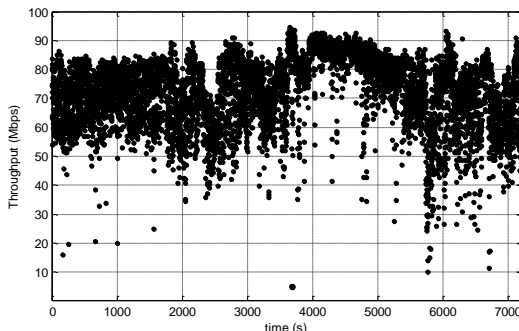

Fig. 7. Noisy throughput versus time, N0 – N8 connection

Table 1 presents the mean value and standard deviation of throughput between node N0 and the other nodes when no load connected to the network and when all nodes have connected lamps. For the configuration with no load, it is clearly seen that the performance of the PLC network is very close in all nodes in terms of mean (only a slight decrease in the furthest nodes performance is observed) but an increase in the standard deviation is realized as we get further from the transmitter. When we connected the lamps to the network, we can easily see the drop in the throughput performance, which we have already noticed in Figure 5, Figure 6 and Figure 7. There is degradation in all connections' performances but the most noticeable one is in the performance of the connection between N0 and N8 (or N7), the furthest nodes. Beside the drop in the throughput mean, the increase in standard deviations is significant. It is also interesting to observe that the performance of N0 – N1 connection is better than that of N0 – N0 connection. This result proves the existence of compensation and amplification effects among the interference generated by the multipath structure of the channel that can significantly affect the throughput. This evidence stresses the significance of testing modems before usage by developing a real grid and by using real disturbing loads.

TABLE I
MEANS AND STANDARD DEVIATIONS OF THROUGHPUTS
BETWEEN N0 AND OTHER NODES.

Connection	No load connected to the network		All nodes have connected lamps	
	mean	Std. dev.	mean	Std. dev
N0 - N0	94.9352	0.4111	94.8512	1.2157
N0 - N1	94.9328	0.2506	94.9286	0.3571
N0 - N2	94.8800	0.4668	88.7530	8.5857
N0 - N3	94.9331	0.2980	89.3220	9.3323
N0 - N4	94.9379	0.4572	86.3286	10.3999
N0 - N5	94.9299	0.6012	78.7611	11.4268
N0 - N6	94.8556	0.6870	78.2866	11.3561
N0 - N7	94.8397	1.5931	71.0347	11.5691
N0 - N8	94.7086	1.6950	72.0789	12.1890

A common method to test the delay characteristics of networks is to send ping packets and measure the round trip return time (RTT) for each transmission. We have measured the RTT by sending ping command with 128 byte for 10 times before and after the throughput measurements and it has been seen that the results are so far close to min 3 ms, max 10 ms and the average 3 ms for all measurements. We have concluded that RTT does not give us informative data; therefore we have analyzed the throughput performance only in the rest of the study.

Table 2 gives the results related to the measurements between N0 and the others (transmitter is at node N0) when lamps are connected to nodes N1, N3 and N4 (lamps are on the center) or N3, N5 and N6 (lamps are placed on one side of the network). As expected, adding lamps to the network decreases the throughput performance. When the lamps are on N1, N3 and N4, the degradation is observed everywhere and it gets more significant as the node gets further from the transmitter. When lamps are locally placed, the significant

http://dergipark.gov.tr/bajece

degradation is observed in the performance of nodes with lamps, but a slight degradation is also observed in nodes N7 and N8 because of the multipath effects.

TABLE II
MEANS AND STANDARD DEVIATIONS OF THROUGHPUTS
BETWEEN N0 AND OTHER NODES.

Connection	N1, N3 and N4 have connected lamps		N3, N5 and N6 have connected lamps	
	mean	Std. dev.	mean	Std. dev
N0 - N0	94.8497	1.6807	94.9272	0.2614
N0 - N1	94.8577	0.3277	94.9266	0.4504
N0 - N2	94.4149	3.5877	94.8235	1.5409
N0 - N3	93.0962	5.3390	94.5119	2.7328
N0 - N4	92.4736	5.0989	93.8660	3.6022
N0 - N5	90.4185	6.5017	85.9407	9.5047
N0 - N6	91.0793	6.3420	84.8404	9.2614
N0 - N7	81.3266	8.8003	92.0392	4.7405
N0 - N8	82.7344	8.8166	92.1321	4.6845

As a result, regardless the distance of the PLC transmitter and receiver the ping time is not changing (since the topology is star it is the expected) whereas the physical speeds (throughputs) slightly decrease when no load is connected to the network. But this degradation becomes significant when loads (noise factors) are connected to the network. The effect of the noise depends on the number and placement of disturbing factors. The performance degradation is more significant close to noise.

IV. THROUGHPUT STATISTICS

Probability distributions can be viewed as tools for dealing with uncertainty. Calling the uncertainty as a random process, distribution fitting allows you to develop valid models of random processes you deal with, and enables you to make better decisions. Distribution fitting forecast the frequency of occurrence of the magnitude of the data in a certain interval and select a statistical distribution that fits to the data set.

There are many potential probability distributions that can be fitted, but depending on the characteristics of the data, some may be fitted more closely than others. For selecting the best fitted one, the histograms of the data were plotted first. Fig. 8, Fig. 9 and Fig. 10 give the throughput histograms while no load is connected to the network, between nodes N0 – N2, N0 – N6 and N0 – N8, respectively. As seen from the figures, all distributions have a shape with skew to the left. The distribution fittings of various left skewed distributions were compared related to the goodness of fit. We have decided whether the probability distribution is a good fit by looking at the plots and by comparing the log likelihood value, Akaike Information Criterion (AIC) and Bayesian Information Criterion (BIC) [20]. Attempts have shown that the extreme value distribution [21] is best fitting to the data. The

distribution fitting results are also given on the same figures with the histograms.
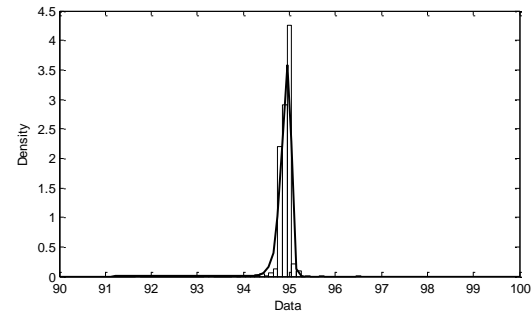

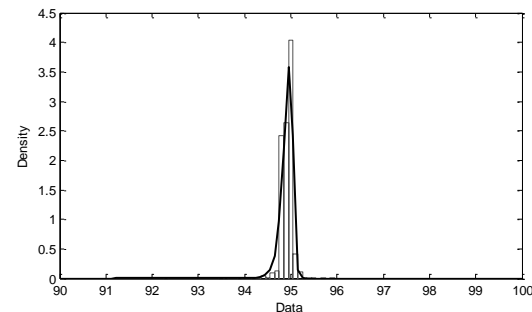Fig. 8. Throughput distribution between N0 – N2, no lamp is connected.

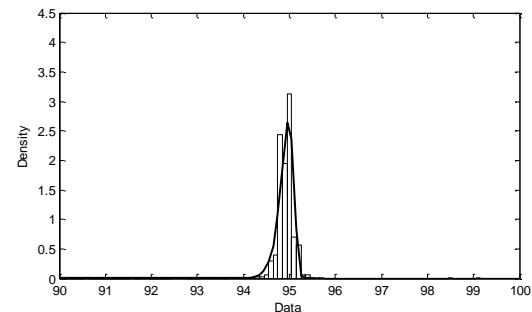Fig. 9. Throughput distribution between N0 – N6, no lamp is connected.

Fig. 10. Throughput distribution between N0 – N8, no lamp is connected.

Extreme value distributions [21] are popular to model the smallest or the largest value among a large set of independent, identically distributed random values representing measurements or observations, as in our case. The probability density function of the standard extreme value distribution is given by [19]

$$g(v) = \exp\left(-\left(e^{-v} + v\right)\right) \quad v \in \Re . \tag{1}$$

The expected value (mean) is equal to Eular constant, i.e. $E\{V\} = \gamma \approx 0.5772$ and the variance is $\text{var}\{V\} = \pi^2/6 \approx 1.6449 \approx 1.2825^2$.

The standard extreme value distribution is generalized by applying a linear transformation. i.e., $X = \mu + \sigma.V$ has the extreme value distribution for maximums with location

parameter $\mu \in \Re$ and scale parameter $\sigma \in (0, \infty)$ and the probability density function

$$f(x) = \frac{1}{\sigma}.\exp\left(-\frac{x-\mu}{\sigma}\right).\exp\left(-e^{-\frac{x-\mu}{\sigma}}\right), \quad x \in \Re . \qquad (2)$$

The extreme value distribution is a flexible model that covers Gumbel, Fréchet, and Weibull distributions by adjusting the parameter values. The reversed Weibull distribution is a quite rarely used model and also well fitted to our data. But since it is a subset of the extreme value distribution, it is not given here. We have found that the distribution parameters are $\mu = 94.96$, $\sigma = 0.10$, and $\mu = 94.97$, $\sigma = 0.10$, and $\mu = 94.98$, $\sigma = 0.13$ in Fig. 8, Fig. 9 and Fig. 10, respectively. The parameter values are close as expected from the results seen in Table 1.

The histograms of throughput while a lamp is connected to each node of the network under test are also investigated. Analyzing these histograms, we have noticed that the histograms of various measurements differ. Fig. 11, Fig. 12 and Fig. 13 give a set of throughput histograms and their distribution fittings of the connections N0 – N2, N0 – N6 and N0 – N8, respectively. Again all distributions are left skewed and extreme value distribution is best fitting to the data, with $\mu = 87.64$, $\sigma = 5.14$, and $\mu = 79.78$, $\sigma = 6.27$, and $\mu = 73.84$, $\sigma = 8.95$ in Fig. 11, Fig. 12 and Fig. 13, respectively. As expected, the location parameter is decreasing whereas the scale parameter is increasing as we get further from the transmitter. Again these results are well matched with Table 1.
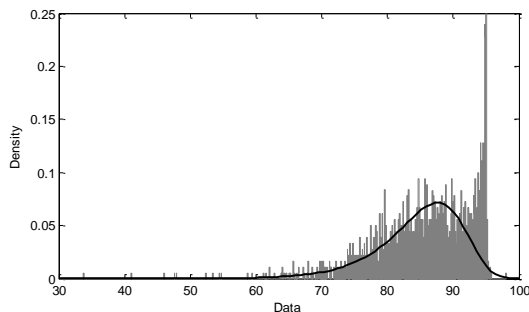

Fig. 11. Throughput distribution between N0 – N2, all nodes have lamps.
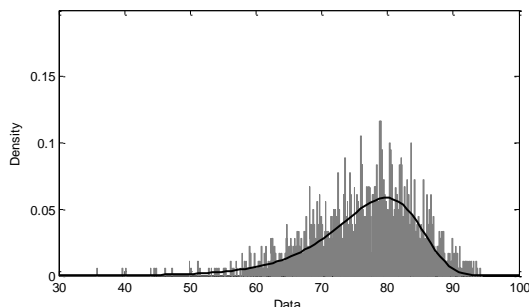

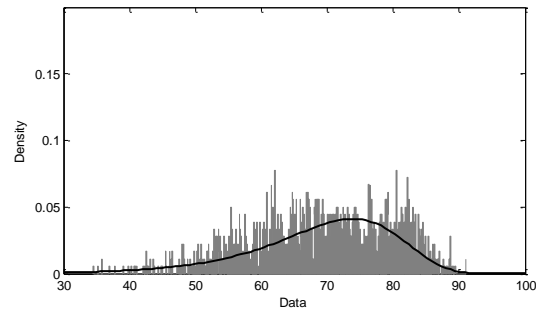Fig. 12. Throughput distribution between N0 – N6, all nodes have lamps.

Fig. 13. Throughput distribution between N0 – N8, all nodes have lamps.

V. CONCLUSIONS

The PLC technology has technical challenges that arise from the difficulty of operating on a complex time varying medium. Frequently degradation is observed in practical PLC performance compared to the manufacturers' expectations. This paper presents the findings obtained from the experiments carried out in order to understand network dynamics of PLC systems and verify the throughput performance. The measurements are realized under different times and conditions and an idea of the practical PLC performance is achieved. Using jperf software the throughput is analyzed and by the help of distribution fitting, it is shown that the PLC throughput may be modeled by the extreme value distributions. Furthermore, the basic noise sources, the lamps, are added to the network and throughput performance is analyzed again. It is seen that this attempt is resulted with a degraded performance even in a small network, as expected. Although the histograms still best fitted to extreme value distributions, the parameters of the derived distributions have been changed: a decrease in expected value and an increase in standard deviation are observed.

REFERENCES

[1] S. Mudriievskyi, "Power Line Communications: State of the art in research, development and application", AEU International Journal of Electronics and Communications, vol. 68, no. 7, pp. 575-577, 2014.
[2] G. López, J. I. Moreno, E. Sánchez, C. Martínez, F. Martín, "Noise Sources, Effects and Countermeasures in Narrowband Power-Line Communications Networks: A Practical Approach", Energies, vol. 10, no. 8, pp. 1238, 2017.
[3] P. Mlynek, Z. Hasirci, J. Misurec, et al., "Analysis of Channel Transfer Functions in Power Line Communication System for Smart Metering and Home Area Network", Advances in Electrical and Computer Engineering, vol. 16, no. 4, pp. 51-56, 2016.
[4] Z. Chen, X. Geng, F. Yin, "A Fractional Lower Order Statistics-Based MIMO Detection Method in Impulse Noise for Power Line Channel", Advances in Electrical and Computer Engineering, vol. 14, no. 4, pp. 81-86, 2014.
[5] A. Ikpehai, B. Adebisi, K. M. Rabie, R. Haggar, M. Baker, "Experimental Study of 6LoPLC for Home Energy Management Systems", Energies, vol. 9, no. 12, pp. 1046, 2016.
[6] I. Tsokalo, "Influence of the channel instability on the PLC QoS", AEU International Journal of Electronics and Communications, vol. 68, no. 7, pp. 581-583, 2014.
[7] ETSI TR 102 049 V1.1.1, "PowerLine Telecommunications (PLT); quality of service (QoS) requirements for in-house systems", 2005, Available: www.etsi.org.
[8] G. Betta, D. Capriglione, L. Ferrigno, M. Laracca, "A measurement-driven approach to assess power line telecommunication (PLT) network

quality of Service (QoS) performance parameters", Measurement Science and Technology, vol. 20, no. 10, pp. 1-11, 2009.

[9] P. L. So, Y. H. Ma, "Development of a test bed for power line communications", IEEE Transactions on Consumer Electronics, vol. 50, no. 4, pp. 1174-1182, 2004.

[10] P. Tinnakornsrisuphap, P. Purkayastha, B. Mohanty, "Coverage and Capacity Analysis of Hybrid Home Networks", International Conference on Computing, Networking and Communications, Communication QoS and System Modeling Symposium, pp. 117-123, 2014.

[11] Y. J. Lin, H. A. Latchman, R.E. Newman, S. Katar, "A Comparative Performance Study of Wireless and Power Line Networks", IEEE Communication Magazine, vol. 41, no. 4: 54-63, 2003.

[12] G. Horvat, Z. Balkic, D. Zagar, "Power Line Communication throughput analysis for use in last mile rural broadband", 20th Telecommunications Forum, pp. 245-248, 2012.

[13] B. Zarikoff, D. Malone, "Construction of a PLC Test Bed for Network and Transport Layer Experiments", IEEE International Symposium on Power Line Communications and Its Applications, pp. 135-140, 2011.

[14] E. S. Kapareliotis, K. E. Drakakis, H. K. Dimitriades, C. Capsalis, "Throughput Analysis on BPL Networks", Microwave Review, pp. 35-40, 2008.

[15] V. Gutierrez, J. A. Galache, R. Aguero, L. Munoz, "Performance Evaluation of a PLC Field Trial: The Behavior of the TCP/IP Stack", IEEE International Symposium on Power Line Communications and Its Applications, pp. 278-284, 2007.

[16] M. Y. Chung, M. H. Jung, T. Lee, Y. Lee, "Performance Analysis of HomePlug 1.0 MAC with CSMA/CA", IEEE International Journal on Selected Areas on Communications, vol. 24, no. 7, pp. 1411-1420, 2006.

[17] M. Mizutani, Y. Miyoshi, K. Tsukamoto, et al., "Network-supported TCP rate control for high-speed power line communications environments", Simulation Modelling Practice and Theory, vol. 19, no. 1, pp. 69-83, 2011.

[18] R. Murty, J. Padhye, R. Chandra, A. R. Chowdhury, M. Welsh "Characterizing the end-to-end performance of indoor powerline networks", Technical report, 2008.

[19] B. Jensen, H. Slavensky, S. Kjaersgaard, "Benchmarking and QoS of In-House Powerline Equipment for AV Streaming Applications", IEEE International Symposium on Power Line Communications and Its Applications, pp. 160-165, 2006.

[20] K. P. Burnham, D. R. Anderson, "Multimodel inference: understanding AIC and BIC in Model Selection", Sociological Methods & Research, vol. 33, no. 2, pp. 261–304, 2004.

[21] S. Kotz, S. Nadarajah, "Extreme Value Distributions: Theory and Applications", London: Imperial College Press, 2000..

BIOGRAPHIES

SELVA MURATOĞLU ÇÜRÜK received the B.S. degree from the Electrical and Electronics Engineering Department, Middle East Technical University (METU), Ankara, Turkey, in 1996, and the M.S. and Ph.D. degrees from the same university, in 1999 and 2008, respectively. She is currently at the Iskenderun Technical University. Her research interests are wireless communication systems, digital communication theory, digital signal processing, multicarrier modulation and channel modeling.

VEDAT ÖZKANER received the B.S. degree from the Electrical and Electronics Engineering Department, Erciyes University, Kayseri, Turkey, in 1992, the M.S. degree from the Electrical and Electronics Engineering Department, Çukurova University, Adana, Turkey, in 1996 and the Ph.D. from Karadeniz Technical University, in 2005. He is currently at the Iskenderun Technical University. His research interests are analog design, biomedical and neuroscience.

ANN Circuit Application of Complementary Resistive Switches

E. UÇAR, E. KARAKULAK and R. MUTLU

Abstract: **Artificial neural networks are successfully used for classification, prediction, estimation, modeling and system control. However, artificial neural networks integrated circuits are expensive and not matured enough. Memristors or memristive systems which show a nonvolatile memory behavior has a high potential for use in artificial neural network circuit applications. Some memristive synapse or memristive neural network applications already exist in literature. The complementary memristor or resistive switch memories have been suggested as an alternative to one-cell memristor memories. Their sensing is more difficult and complex than the others. The complementary memristor memory topologies with a sensing node are also inspected in literature. To the best of our knowledge, a neural network circuit which is based on the complementary resistive switches with a sensing/writing node does not exist in literature yet. In this paper, several neural network circuits which are based on the complementary resistive switches with a sensing/writing node have been designed and examined for the first time in literature. Their analysis are given and simulations are performed to verify their operation. We expect that such a complementary resistive switch implementation may find use in artificial neural networks chips in the future.**

Index Terms— **Memristor, Memristive systems, Complementary resistive switches, Artificial neural networks, ANN circuits.**

I. INTRODUCTION

ARTIFICIAL NEURAL Networks (ANN) are biologically inspired systems which are able to do classification, prediction, estimation, modeling and system control [1]. The neural networks integrated circuits are expensive and not commonly used [2,3]. If new neural networks integrated circuit topologies are found, this may help to cheapen their price and make them more common and rugged. One way to find such ANN topologies is to make use of new-found circuit elements. Memristor is such a new-found circuit element and it has a memory [4,5].

 ERDEM UÇAR, is with Department of Management Information Systems University of Trakya, Edirne, Turkey, (e-mail: erdemucar@trakya.edu.tr).
 https://orcid.org/0000-0002-8465-3396

ERTUĞRUL KARAKULAK, is with Department of Vocational School of Technical Sciences Namık Kemal University, Tekirdağ, Turkey, (e-mail: ekarakulak@nku.edu.tr).
 https://orcid.org/0000-0001-5937-2114

REŞAT MUTLU, is with Department of Electronics and Communication Engineering Namık Kemal University, Çorlu, Tekirdağ, Turkey, (e-mail: rmutlu@nku.edu.tr).
 https://orcid.org/0000-0003-0030-7136

It was predicted as the fourth missing circuit element by Leon Chua in 1971 [5] and has been declared found by a research team in 2008 [4]. Memristors or memristive systems which are systems behaving as memristors are under consideration for memory applications as well as analog applications. Two reviews on memristor and its memory applications can be found in [6,7]. Resistive switches are also declared as memristors by Chua [7]. The complementary resistive switches (CRS), which are anti-series connected memristors, are suggested as a way to decrease leakage current in resistive switches [8,9]. A new CRS topology with a sensing/reading line is suggested in [10].

Since memristor is a nonvolatile memory, it can also be used for making neural network circuits. Memristors or memristive circuit elements are able to provide artificial neural network circuits with adjustable gains required for training and a good performance since they have variable resistance values. Some studies on memristor-based artificial neural network circuits can be found in [11-13]. Recently, memristors have been used to create a chip that borrows design points from the brain and the prototype chip were able to recognize extremely simple black-and-white patterns [14]. A larger, more complex versions of the chip might make computers better at more difficult tasks such as understanding speech, images, and the world around them. That's why the new circuit element memristor is a promising candidate for artificial neural network circuits as well as the non-volatile memory domain with its high density and low power consumption. However, to the best of our knowledge, the complementary resistive switches or complimentary connected memristors have not been used to make a perceptron or an artificial neural network circuit in literature yet. In this paper, the CRS topology with the sensing line is used to make perceptron and ANN circuits. These CRS based perceptron topologies also make use of operational amplifiers for normalization and amplification purposes. The perceptron circuits given in literature do not have automatically adjustable negative or positive gains. Also for the first time in literature, the CRS based opamp amplifiers are able to give not only negative but also positive gains for the perceptron circuit. Then, it is shown how to use the CRS-based perceptrons to make a multi-layer artificial neural network circuit. The CRS model given in [15] is modified to model the CRS with a sensing line and it is used in simulations. A microcontroller-based programmer which can be made using off-shelves components and a cheap microcontroller are suggested for programming such a perceptron or ANN circuit.

The paper is arranged as follows. In the second section, a complementary connected resistive switches without and with a sensing line are briefly explained and the CRS model with nonlinear dopant drift given in [15] is modified for a sensing line. In the third section, first a Hopfield perceptron is reviewed, then various perceptron circuits are made using the CRS cells with sensing line, and as last it is shown how to make an ANN circuit based on the perceptron circuits. In the fourth section, a microprocessor-based programmer for the CRS-based perceptron is introduced and the programmer is simulated using Matlab^{TM}. In the fifth section, the simulation results obtained using Matlab^{TM} for the CRS-based perceptron circuit is given. The paper is concluded with the sixth section.

II. MODELING OF THE COMPLEMENTARY RESISTIVE SWITCHES

A. Complementary Resistive Switch Topology without and with a Sensing Line

In this section, a CRS topology is to be explained briefly. CRS can be made of different materials [16,17]. A CRS made of Pt-GeSe-Cu-GeSe-Pt as in [10], materials is shown in Fig. 1. The CRS consists of a Platinum (Pt) top electrode, an upper solid electrolyte (for instance, made of GeSe), and an oxidizable middle electrode made of a material such as Copper (Cu), a lower solid electrolyte, and a Platinum (Pt) bottom electrode. The equivalent circuit of the CRS can be modelled as a memristive element U and a memristive element L connected in series with opposite polarities as also shown in Fig. 1. The merging copper electrode between the lower and the upper memristive elements. which is connected to outside is usable for writing, reading and sensing purposes of the CRS cells,
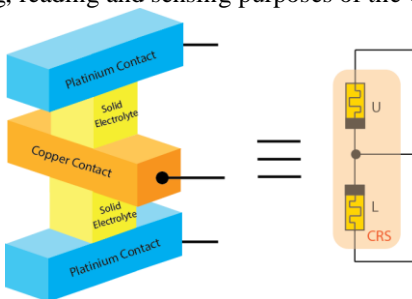

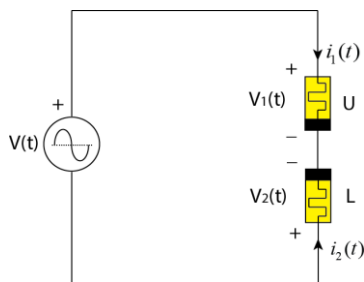Fig.1. The CRS topology with a sensing line given in [10].

Fig. 2. The equivalent circuit of the CRS cell without a sensing line.

B. Analytic Model of the Complementary Resistive Switches without a Sensing Line

In this section, the CRS model given in [15] is briefly explained. The CRS model given in [15] is a nonlinear model and the resistance of a resistive switch in the CRS is dependent on the rate of change of the normalized dopant drift length, two threshold voltages and a two-variable window function. The equivalent circuit of the CRS cell without a sensing line is shown in Fig. 2. Considering the experimental data in [8], the rate of change of the state-variables are presented using two threshold voltages as the following,

$$i_1(t) = -i_2(t) \tag{1}$$

$$V(t) = V_1(t) + V_2(t) = [R_U(x_1) + R_L(x_2)] - i_2(t) \tag{2}$$

$$\frac{dx_1}{dt} = \begin{cases} \dfrac{\mu_v . i_1(t).R_{off}}{D^2} f(x_1, i_1) & , & V_{TH2} \leq V \\ 0 & , & V_{TH1} \leq V < V_{TH2} \\ 0 & , & -V_{TH1} < V < V_{TH1} \\ \dfrac{\mu_v . i_1(t).R_{off}}{D^2} f(x_1, i_1) & , & V_{TH2} < V \leq -V_{TH1} \\ 0 & , & V \leq -V_{TH2} \end{cases} \tag{3}$$

$$\frac{dx_1}{dt} = \begin{cases} \dfrac{\mu_v . i_1(t).R_{off}}{D^2} f(x_1, i_1) & , & V_{TH2} \leq V \\ 0 & , & V_{TH1} \leq V < V_{TH2} \\ 0 & , & -V_{TH1} < V < V_{TH1} \\ \dfrac{\mu_v . i_1(t).R_{off}}{D^2} f(x_1, i_1) & , & V_{TH2} < V \leq -V_{TH1} \\ 0 & , & V \leq -V_{TH2} \end{cases} \tag{4}$$

$x_1 = w_1/D$ and $x_2 = w_2/D$. Where w_1 and w_2 are oxidized length of resistive switches upper and lower respectively, D is physical length of resistive switches. V_{TH1} and V_{TH2} are threshold voltages of upper and lower resistive switches. μ_v is mobility coefficient of oxygen ions, $i_1(t)$ and $i_2(t)$ are currents of resistive switches upper and lower respectively. R_{off} is maximum resistance value, R_{ON} minimum value of resistive element.

Simulink^{TM} toolbox of MATLAB^{TM} is used for all the simulations in this paper. A voltage source of $V(t) = V_m.cos(\omega t) = 1,4.cos(20000\pi t)$ is used to excite the CRS. The CRS current, voltage and resistance (memristance) are given in Fig. 3 and its zero-crossing pinched hysteresis loop is shown in Fig. 4.
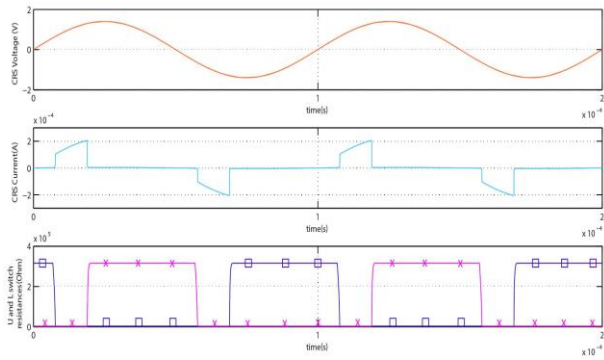
Fig. 3. The CRS current, voltage and memristances when excited with
$$V(t) = 1,4. cos(20000\pi t) \text{ [15]}.$$
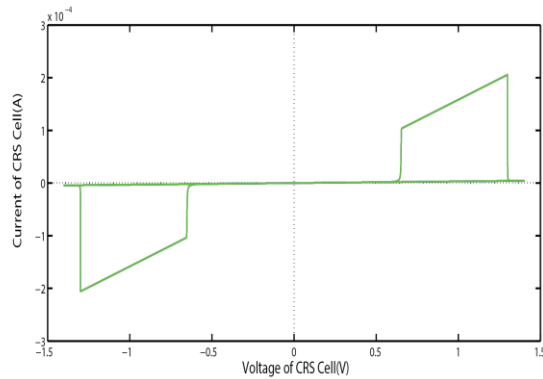

Fig. 6. Current-Voltage and sense voltage of CRS with sensing line.

In this section, the analytical model of the CRS topology with a sensing line is made. V_U and V_L are the node voltages shown in Fig. 5.

$$V_1(t) = V_U - V_{sense} \qquad (5)$$

$$V_2(t) = V_L - V_{sense} \qquad (6)$$

Fig. 4. The zero-crossing hysteresis loop of the CRS model when excited with $V(t) = V_m.cos(\omega t) = 1,4.cos(20000\pi t)$ [15].

In this case, the CRS cell currents are

$$i_1(t) = \frac{V_1}{R_1} = \frac{V_U - V_{sense}}{R_1} \qquad (7)$$

C. Analytic Model of Complementary Resistive Switches with a Sensing Line

In this section, the model of the CRS topology without a sensing line is modified for the CRS topology with a sensing line. The model of the CRS topology without a sensing line suggested in [8] is modified for the CRS topology with a sensing line. Its equivalent circuit can be obtained as shown in Fig. 5. It is same as the CRS circuit except the sensing line in Fig. 2 that makes the current of the resistive switches different than each other during writing and sensing processes.
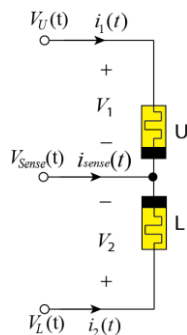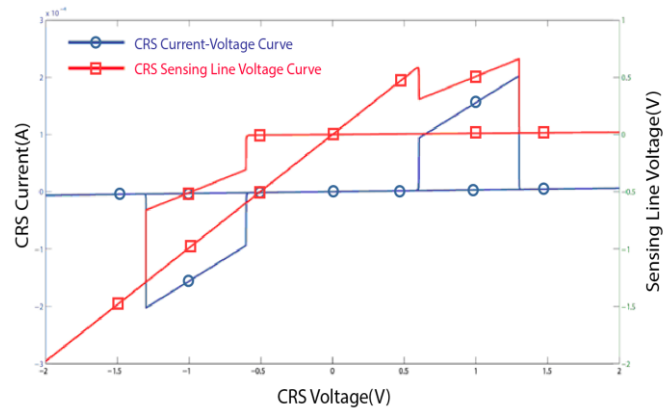
$$i_2(t) = \frac{V_2}{R_2} = \frac{V_L - V_{sense}}{R_2} \qquad (8)$$

In this paper, it is chosen to keep the upper CRS switch at the minimum resistance value and only to tune the lower CRS switch resistance for the perceptron gains desired. If only the lower CRS switch is selected throughout the sense line and the lower terminal,

$$V_U = V_{sense} \text{ and } V_1(t) = 0 \qquad (9)$$

In this case, the current of the upper CRS element is

$$i_1(t) = 0 \qquad (10)$$

Fig. 5. The equivalent circuit of the CRS topology with a sensing line.

In this paper, the upper CRS switch is hold at LRS state during circuit operation. Its purpose is to provide threshold and keep the lower CRS switch voltage is less than the threshold voltage

to prevent its resistance drift. Therefore, the desired resistance or the memristance of the lower resistive switch is given as,

$$R_1 = R_{on} \qquad (11)$$

This means the CRS upper switch resistance must be reset to R_{on} at the beginning of the programming operation. A good CRS switch is needed to keep the memristance drift acceptable and perhaps this can be done using new materials in the future. During programming,

$$i_2(t) = \frac{V_{sense}(t)}{R_2} \qquad (12)$$

During normal operation of the CRS based perceptron, the model given in the previous section can be used for the simulations, i.e.

$$i(t) = i_1(t) = -i_2(t) \text{ and } \quad i_{sense}(t) = 0 \qquad (13)$$

III.   THE CRS-BASED PERCEPTRON MODEL

A.   Hopfield Perceptron Circuit Model and Perceptron Circuit with Memristors

A perceptron is a biologically inspired artificial neural network. Its block diagram is shown in Fig. 7.a. and the Hopfield perceptron circuit, which is the first perceptron circuit given in literature, is shown in Fig. 7.b [18,19]. It is made of a current source for the offset input, resistors, a capacitor and a nonlinear circuit element for the activation function. The following differential equation describes the Hopfield perceptron circuit:

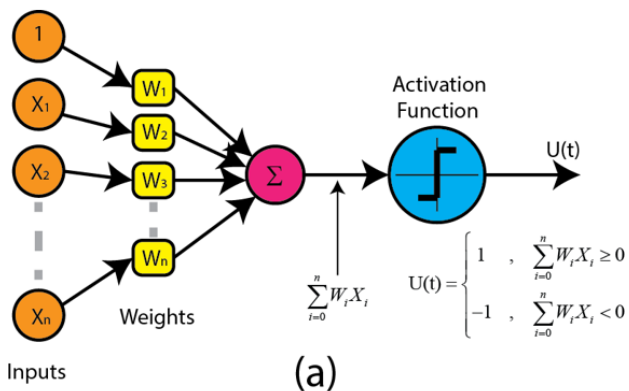$$\frac{du_i}{dt} = -\frac{u_i}{\tau_i} + \sum_{j=1}^{n} T_{ij} v_j + I_i \qquad (14)$$
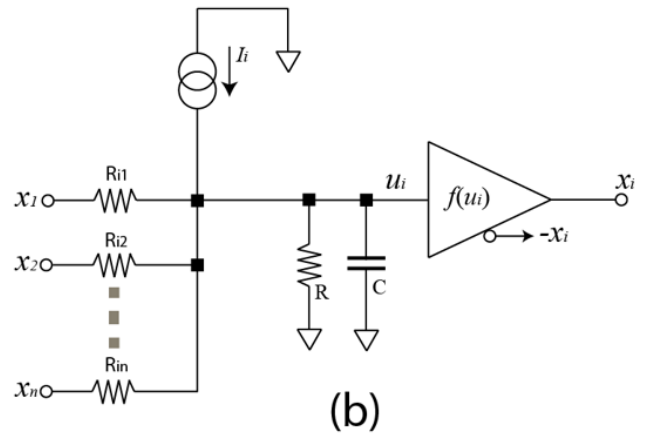

Fig. 7. b) The Hopfield Perceptron Circuit.

B.   The CRS-based Perceptron Topology and Its Model

The circuit in Fig. 7.b has constant resistors and therefore for each perceptron application, different resistors must be mounted to tune the perceptron circuit. If the perceptron is trained again and the gains are changed, the resistors must be replaced. Using variable resistors or potentiometers instead resistors may solve the need to replace the gain resistors. Artificial Neural Network and CRS based perceptron block can be seen in Fig. 8. The CRS-based perceptron circuit is given in Fig. 9. It replaces the resistors with CRS switches. The CRS switches resistances or memristances can be adjustable easily using pulses [20,21]. The upper switches are kept at R_{on} resistance value and the lower switches are tuned to have the necessary resistance value to provide the needed gains. The opposite method of keeping the lower switches at R_{on} and tuning the upper switch resistances can also give the same performance. The input opamps are used for scaling the input voltages and to provide a voltage less than the threshold voltage.
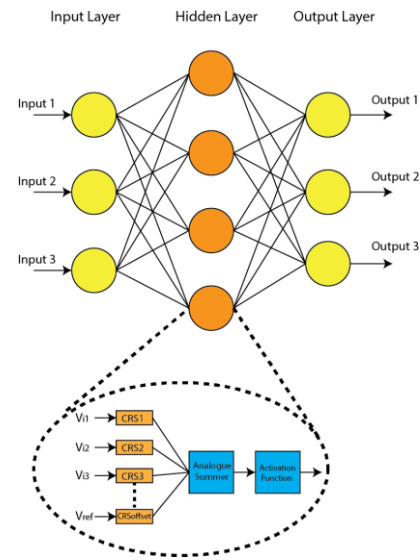

Fig. 7. a) Perceptron block diagram

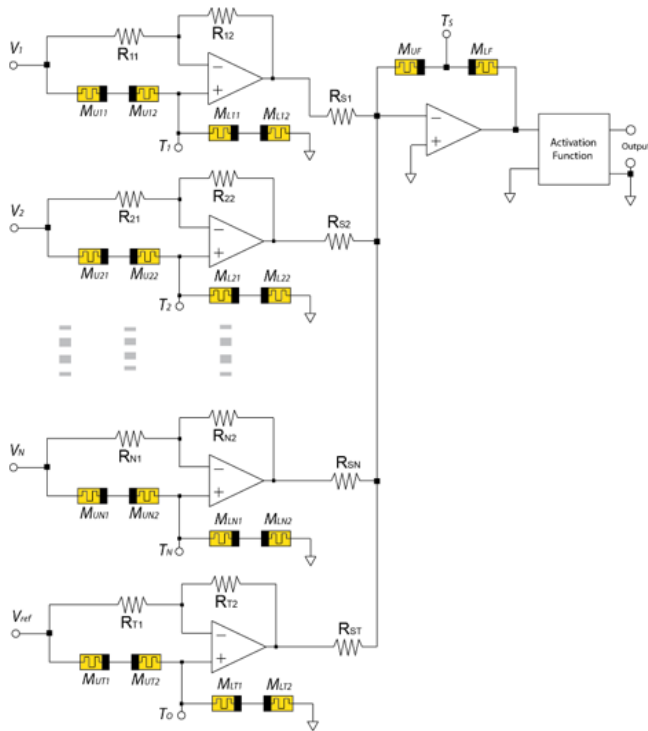Fig. 8. Artificial Neural Network with CRS Block Diagram.

Fig. 9. The Proposed CRS-based Perceptron Circuits.

Fig. 10. a) Differential amplifier b) Differential amplifier for the negative gain or the negative weighting factors.

Perceptron gains may have positive or negative values. The same perceptron may require positive and negative gains at the same time for a given problem. Resistor or memristor based perceptron circuits given in literature have already had either positive or negative gains for weighting factors but not both for the same perceptron application and used dc offset. In this paper, also for the first time in literature, it is also shown how to obtain a weighting factor ranging from -1 to +1. Using differential amplifiers and memristors to obtain not only

negative but also positive weighting factors. An inverting amplifier has negative gain and a non-inverting amplifier has positive gain. A differential amplifier can be made to have either positive or a negative gain by adjusting its gains its resistors. Differential amplifiers are shown in fig. 10. Output voltage of the differential amplifier in Fig. 10 is,

$$V_{out} = \left(1 + \frac{R_2}{R_1}\right)\left(\frac{R_4}{R_3 + R_4}\right).V_2 - \left(\frac{R_2}{R_1}\right).V_1 \qquad (15)$$

For $V_1=V_2$ (The inputs are connected together) and $R_1=R_2$, the gain of the amplifier in Fig. 10.b becomes,

$$G = \left(\frac{R_4 - R_3}{R_4 + R_3}\right) \qquad (16)$$

Considering $R_4>R_3$, the gain becomes positive and vice versa. The amplifier is to be called negative-positive gain amplifier (NPGA) from now on. For the parametric analysis of the gain of negative-positive gain amplifier, a parameter which is the ratio of the resistance R_4 to the resistance R_3 is defined as $\gamma = R_4/R_3$. Therefore, the gain can now be given as,

$$G = \frac{\gamma - 1}{\gamma + 1} \qquad (17)$$

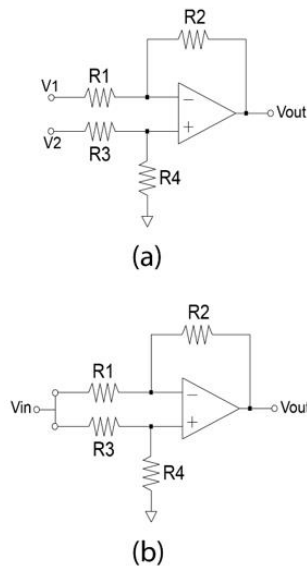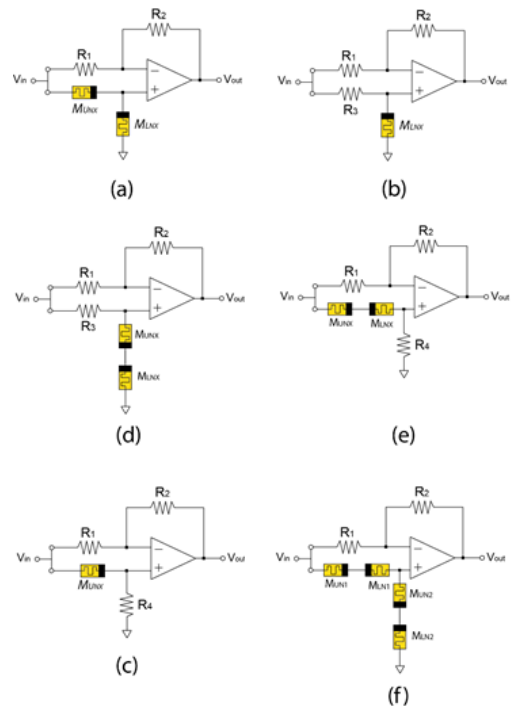Fig. 11. The various negative-positive gain circuits a) The CRS based NPGA circuit b) The NPGA with a lower resistive switch c)The NPGA with an upper resistive switch d) The NPGA with a lower CRS e) The NPGA with an upper CRS f) The NPGA with both upper and lower CRSs.

TABLE I GAIN EQUATIONS OF NEGATIVE POSITIVE GAIN
AMPLIFIERS

Types of Negative Positive Gain amplifiers	Gain Equations	Minimum CRS Threshold Voltage
CRS Based Negative Positive Gain Amplifier	$G = \dfrac{M_{LNX} - M_{UNX}}{M_{LNX} + M_{UNX}}$	V_{TH1}
Lower Resistive Switch Negative Positive Gain Amplifier	$G = \dfrac{M_{LNX} - R_3}{M_{LNX} + R_3}$	V_{TH1}
Upper Resistive Switch Negative Positive Gain Amplifier	$G = \dfrac{R_4 - M_{UNX}}{R_4 + M_{UNX}}$	V_{TH1}
Lower CRS Negative Positive Gain Amplifier	$G = \dfrac{(M_{LNX}+M_{UNX}) - R_3}{(M_{LNX}+M_{UNX}) + R_3}$	V_{TH1}
Upper CRS Negative Positive Gain Amplifier	$G = \dfrac{R_4 - (M_{LNX}+M_{UNX})}{R_4 + (M_{LNX}+M_{UNX})}$	V_{TH1}
Upper And Lower CRS Negative Positive Gain Amplifier	G $= \dfrac{(M_{LNX2}+M_{UNX2}) - (M_{LNX1}+M_{UNX1})}{(M_{LNX2}+M_{UNX2}) + (M_{LNX1}+M_{UNX1})}$	V_{TH2} $=2V_{TH1}$

The resistance of the resistor or the minimum resistance value of the memristor which is connected between the positive input and the input voltage must be chosen. In this paper, we have chosen to calculate the resistance value as the geometric average of maximum and minimum values of memristive element. The resistance equations used for the calculations and the gain equations are given in Table I. All the proposed negative-positive gain amplifiers can be seen in Fig. 11. For the CRS model in [15], $R_{ON}=3,16.10^3$ Ω and $R_{OFF}=316.10^3$ Ω. Using Eq. 15, 16 and the Eq.17 given in Table 1, the gain curves of all negative-positive gain amplifiers are drawn and shown in Fig. 12.

$$R_{reg} = \sqrt{M_{max}.M_{min}} \qquad (18)$$
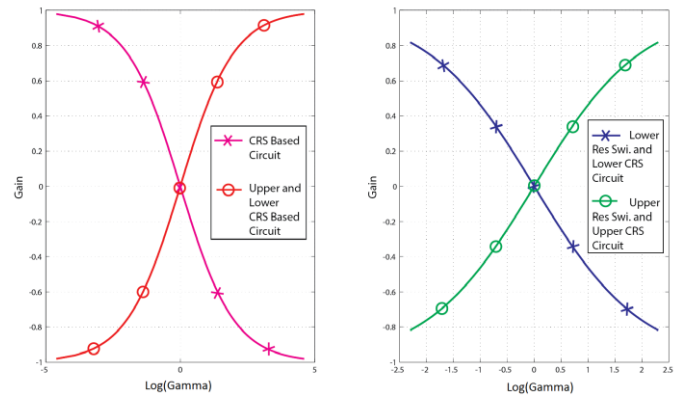
Fig. 12. Gains of the negative-positive gain amplifiers for β=100.

With both upper and lower CRS's converges to +1 and -1 quicker than the other NPGAs do. All the NPGA's given in Fig. 11 can be used to make perceptrons. In this paper, only the CRS based negative-positive gain amplifier is used in the perceptron and ANN circuit simulations. The CRS based perceptron circuit with the CRS based negative-positive gain amplifier can be seen in Fig. 9. β is also an important parameter for CRS based memories [8] and is defined as the ratio of the maximum resistance to the minimum resistance and calculated as

$$\beta = \frac{R_{OFF}}{R_{ON}} \qquad (19)$$

Eq. (16) can be rewritten using β parameter for all of the proposed negative-positive gain amplifiers shown in Fig. 11. The CRS based negative positive gain amplifier gains are derived and put in Table II. The maximum and minimum gain values of the CRS based negative-positive gain amplifier are calculated as

$$G_{max} = \frac{R_{OFF} - R_{ON}}{R_{OFF} + R_{ON}} = \frac{\beta - 1}{\beta + 1} \qquad (20)$$

$$G_{min} = \frac{R_{ON} - R_{OFF}}{R_{ON} + R_{OFF}} = \frac{1 - \beta}{1 + \beta} \qquad (21)$$

TABLE II MAXIMUM AND MINIMUM GAIN RATES DEPEND ON β.

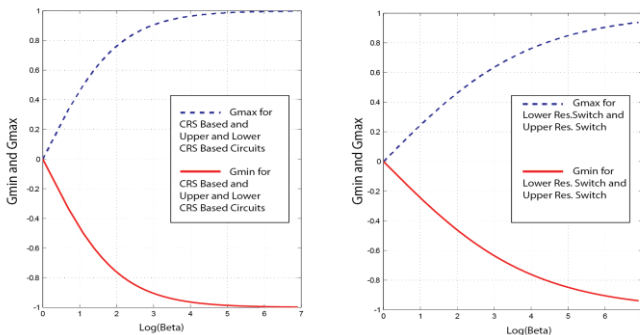| Types of Negative Positive Gain amplifiers	Maximum Gain Equations	Minimum Gain Equations
CRS Based Negative Positive Gain Amplifier	$G_{max} = \dfrac{\beta - 1}{\beta + 1}$	$G_{min} = \dfrac{1 - \beta}{1 + \beta}$
Lower Resistive Switch Negative Positive Gain Amplifier	$G_{max} = \dfrac{\beta - \sqrt{\beta}}{\beta + \sqrt{\beta}}$	$G_{min} = \dfrac{1 - \sqrt{\beta}}{1 + \sqrt{\beta}}$
Upper Resistive Switch Negative Positive Gain Amplifier	$G_{max} = \dfrac{\sqrt{\beta} - 1}{\sqrt{\beta} + 1}$	$G_{min} = \dfrac{\sqrt{\beta} - \beta}{\sqrt{\beta} + \beta}$
Lower CRS Negative Positive Gain Amplifier	$G_{max} = \dfrac{\beta - \sqrt{\beta}}{\beta + \sqrt{\beta}}$	$G_{min} = \dfrac{1 - \sqrt{\beta}}{1 + \sqrt{\beta}}$
Upper CRS Negative Positive Gain Amplifier	$G_{max} = \dfrac{\sqrt{\beta} - 1}{\sqrt{\beta} + 1}$	$G_{min} = \dfrac{\sqrt{\beta} - \beta}{\sqrt{\beta} + \beta}$
Upper And Lower CRS Negative Positive Gain Amplifier	$G_{max} = \dfrac{\beta - 1}{\beta + 1}$	$G_{min} = \dfrac{1 - \beta}{1 + \beta}$

Fig. 13. The maximum and minimum gains of the negative-positive gain amplifiers.

As shown in Fig. 13, two of the six negative positive gain amplifiers have a better convergence than the others according to β parameter. The CRS based, upper and lower CRS based negative positive gain amplifiers shows relatively better reaction to β. Because of this parameter dependency of the gain region, in this paper, it is proposed that the CRS based negative-positive gain amplifier topology must be used. In this study, use of the NPGA with both upper and lower CRSs shown in Fig. 11(f) is also suggested. The threshold voltage of this circuit is equal to almost equal to *2VTH1* which is twice as high in the other topologies in Fig. 11. Therefore, the programmed ANN input voltage range is higher than the other topologies given in Fig. 11. As mentioned before, the CRS memristance varies if input voltages above the threshold voltage get applied to the perceptron inputs and gains of the NPGA circuits undesirably get destructed. Fig. 11(a),(d) and (e) have also CRSs. However, as it can be seen in hysteresis curves as shown in Fig. 4, one of

the resistive switches of the CRSs changes their memristance values when the input voltage exceeds *VTH1* in either direction. The absolute value of the input voltage value required to change the CRS resistance for must be between the threshold voltage values between V_{TH1} and V_{TH2} for the topologies given in Fig. 11(a),(d) and (e) . The circuit in Fig. 11(f) has two CRSs connected in series and, therefore, also doubles the applicable input voltage. The absolute value of the input voltage value required to change the CRS resistance for the topology given in Fig. 11(f) must be between the threshold voltage values between $2V_{TH1}$ and $2V_{TH2}$. It should not be forgotten that only the value of one of the resistive switches in the CRS changes its value not the other considering the input voltage and resistive switch polarity.

C. Activation function

The activation function of an Adaline perceptron circuit can be obtained using an opamp as a saturator as shown in Fig. 14. The activation function of a perceptron can be given as,

$$f(u) = \begin{cases} 1 & , \quad u > 0 \\ -1 & , \quad u \leq 0 \end{cases} \tag{22}$$

The output voltage of the activation function circuit is dependent on the saturation voltage of the opamp:

$$v_{out} = \begin{cases} V_{+SAT} & , \quad u > 0 \\ V_{-SAT} & , \quad u \leq 0 \end{cases} \tag{23}$$

Where V_{+SAT} is the positive saturation voltage and V_{-SAT} is the negative saturation voltage. If $V_{+SAT} = -V_{-SAT}$, the output voltage of the activation function circuit is

$$v_{out} = V_{+SAT} \begin{cases} 1 & , \quad u > 0 \\ -1 & , \quad u \leq 0 \end{cases} \tag{24}$$

The output of the activation function circuit can be limited by using the anti-series connected zener diodes shown in Fig. 14;

$$v_{out} = (V_Z + V_{TH}) \begin{cases} 1 & , \quad u > 0 \\ -1 & , \quad u \leq 0 \end{cases} \tag{25}$$

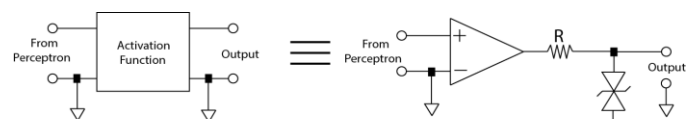Where V_Z and V_{TH} are diode threshold and zener diode voltages.

Fig. 14: The activation function circuit with zener voltage limited output.

IV.   A MICROPROCESSOR-BASED PROGRAMMER FOR THE CRS-BASED PERCEPTRON AND/OR ANN CIRCUIT

In this section, a microcontroller-based programmer circuit is given in Fig. 15. It can be used to program the upper and lower CRS-based perceptron circuits. The programmer circuit is made of also two selector switches. The selective switches can also be made using mosfets or other semiconductor circuit elements. The ADC is used for measuring the voltage across the lower CRS switch. The voltage across the resistor R_s is used to limit and measure the lower CRS switch current. The microcontroller uses the selector switches to select the CRS cell desired to be programmed and then gives a negative pulse to bring (to reset) the lower CRS value to R_{on} and then uses either negative or positive pulses to obtain the memristance value necessary for the desired gains. Using the lower CRS switch current and voltage, microcontroller stops the pulses when the desired memristance value is obtained with an acceptable error in the range of $[R_{on}, R_{off}]$. The voltage of the kth CRS shown in Fig. 15 is

$$V_k = \frac{CRS_k(q_k)}{R_s + CRS_k(q_k)} \cdot V_{pulse} \qquad (26)$$

The current of the selected CRS is

$$i_{mem(k)} = \frac{V_{pulse}}{R_s + CRS_k(q_k)} \qquad (27)$$

Where CRS_k is memristance of kth CRS element and q_k is charge of kth CRS element. R_s is a resistor which is connected to CRS element serially, V_{pulse} is impulse voltage level. V_k is voltage on k.th CRS element, $i_{mem(k)}$ current of CRS element when element exited with V_{pulse} voltage.
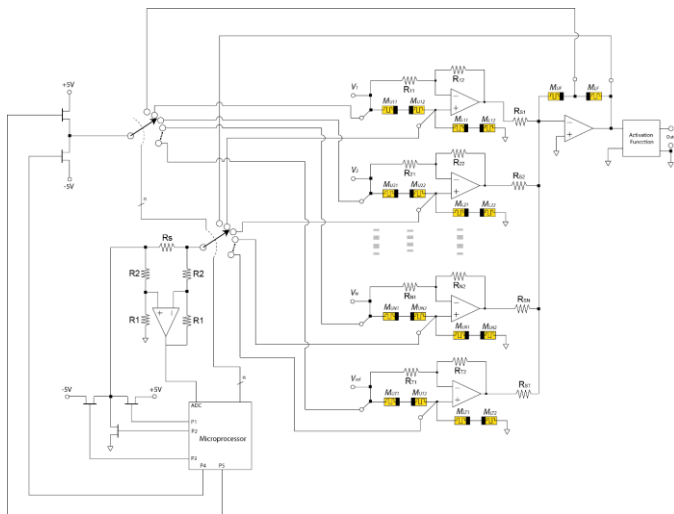
Fig. 15. The Microprocessor based programmer circuit.

A.   Programming Waveforms

By applying consequent pulses, the lower cell resistance of the CRS can be adjusted to the value desired. The resistance modulation waveforms of the lower CRS cell with a pulse train is shown in Fig. 16 and 17.
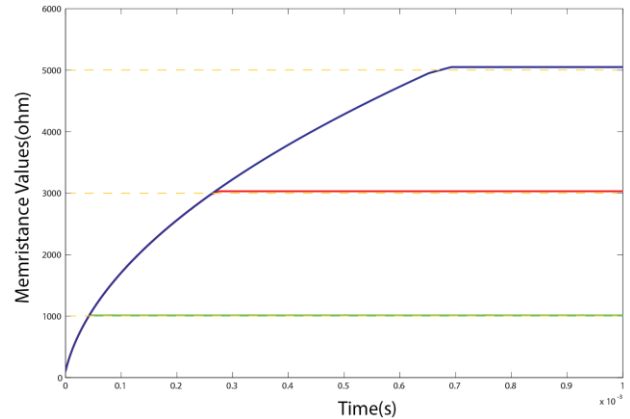
Fig. 15. The lower memristance vs time for the aimed memristance value being 1000Ω with a %1 permitted memristance error gap.
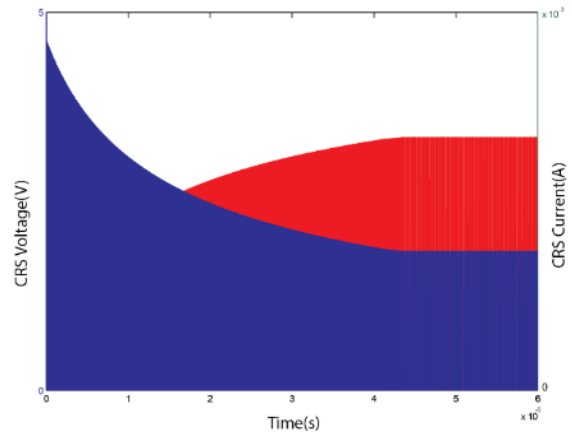
Fig. 16. Memristor voltage and current vs time for the aimed memristance value being 1000Ω with a %1 permitted memristance error tolerance.
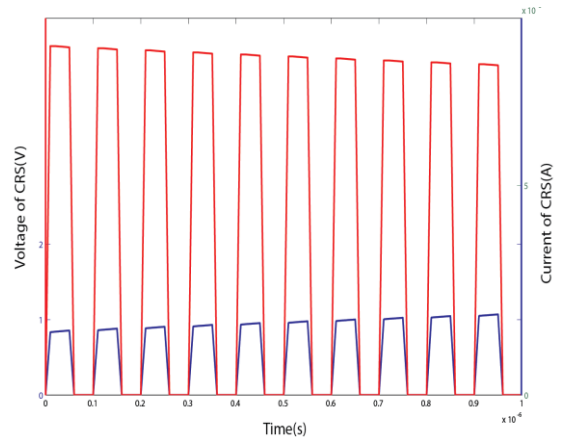
Fig. 17. A zoomed view of a section from Fig. 16.

                                       http://dergipark.gov.tr/bajece

V.   SIMULATION RESULTS OF PROPOSED PERCEPTRON MODEL

Perceptron is a linear separator. In this study, two linear separable set inputs are applied to the perceptron and the simulation results are examined to verify its performance. Due to data in the third column, the set is linearly separable. The set {X, Y} is

$$X = \begin{bmatrix} X_1 \\ X_2 \\ X_3 \\ X_O \end{bmatrix} = \begin{bmatrix} 0.9340 & 0.4694 & 0.0119 & 0.3112 \\ 0.1656 & 0.6541 & 0.6892 & 0.2290 \\ 0.5 & 0.5 & -0.5 & -0.5 \\ 1 & 1 & 1 & 1 \end{bmatrix}, \quad (28)$$

$$Y = [+1 \quad +1 \quad -1 \quad -1]$$

Considering also DC offset input, the CRS-based perceptron circuit requires four inputs. The weighting factors obtained from MATLAB simulations which are needed to linearly separate the set is given in eq. (28).

$$V_O = Y = [+1 \quad +1 \quad -1 \quad -1] \qquad (29)$$

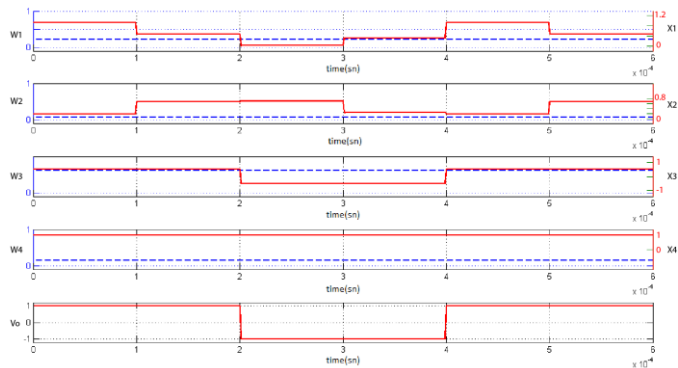The output voltage given in Eq. (29) is the same as the output set given in Eq. (28).

Fig. 18. Inputs and outputs of CRS based perceptron model.

Perceptron simulation results for input voltages higher than the equivalent CRS threshold voltage is given in Fig. 19. The plots drawn with dashed lines shown in the first four rows in Fig. 19 are the gains of the perceptron or the NPGAs for the related inputs. As shown in Fig.19, the perceptron gains belonging to the inputs X_1, X_3 and X_4 gets destroyed in a short time when higher input voltages than the CRS threshold voltages applied. The gain of X_2, the second input of the NPGA is destroyed at 0.1msec since the input voltage exceeds the threshold voltage. As a result, the output voltage plot shows linear separation operation by the perceptron circuit cannot be made by the perceptron due to the fact that its gains have been destroyed with the higher input voltages applied.
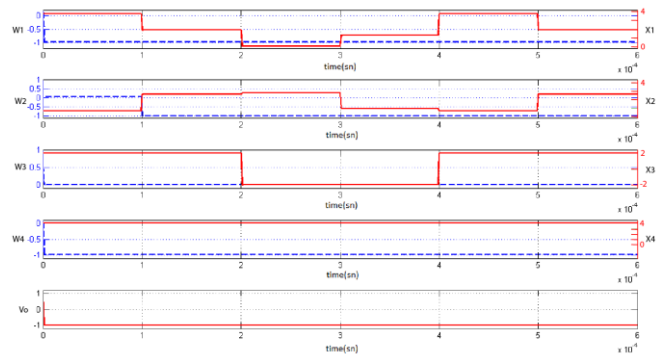

Fig. 19. The CRS-based perceptron simulation results while input voltages exceed the CRS threshold voltage.

VI.   DISCUSSIONS

A CRS-based perceptron and ANN circuits are developed for the first time in the literature. Their operation principles are given. The input voltages applied to the perceptron must be less than the equivalent threshold voltage of the CRS cells and, therefore, is able to keep the memristance values constant. Perhaps, also a scaling circuit may be added to the CRS-based perceptron circuit for future work.

A microcontroller-based programmer circuit is also suggested for the CRS-based perceptron and ANN circuits. A method to program them circuit is given. The CRS cells are programmed using the programmer circuit which is able to apply higher negative or positive voltage pulses than the equivalent threshold voltage to the chosen lower cells to bring their memristances to the value which gives the needed feedback gains or the needed weights by the perceptron circuit.

Also, for the first time in the literature, it is shown how to obtain negative and positive gains with a CRS-based opamp circuit which can be used for all analog perceptron and ANN circuits. In the Future, the CRS based perceptron circuit topology may find usage in the market as a cheap and reliable solution for the needed ANN circuits.

REFERENCES

[1] Dan W. Patterson, *Artificial neural networks: theory and applications*. Prentice Hall PTR, 1998.

[2] M. Janardan, I. Saha, "Artificial neural networks in hardware: A survey of two decades of progress", Neurocomputing Vol:74, No:1, 2010, pp.239-255.

[3] D. F. Morgado, A. Antunes, A. M. Mota, "Artificial neural networks: a review of commercial hardware", Engineering Applications of Artificial Intelligence, Vol:17, No:8, 2004, pp.945-952.

[4] D.B. Strukov, G.S. Snider, , D.R. Stewart, R.S. Williams, "The missing memristor found", Nature, Vol: 453, 2008, pp. 80-83.

[5] L.O. Chua, "Memristor - the missing circuit element", IEEE Trans Circuit Theory, Vol.18, 1971, pp. 507-519.

[6] T. Prodromakis, C. Toumazou "A Review on Memristive Devices and Applications" Electronics, Circuits, and Systems (ICECS), 17th IEEE International Conference on, 2010, pp. 934 – 937.

[7] L. Chua, "Resistance switching memories are memristors." Applied Physics A, Vol.102, No.4, 2011, pp. 765-783.

[8] E. Linn, R. Rosezin, C. Kügeler, R. Waser, "Complementary resistive switches for passive nanocrossbar memories" Nature Mater., vol.9, 2010, pp. 403-406.

[9] M. A. Zidan, H. H. Fahmy, M. M. Hussain, K.N. Salama, "Memristor-based memory: The sneak paths problem and solutions" Microelectronics Journal, Vol.44, No.2, 2012, pp. 176-183.

[10] R. Rosezin, E. Linn, L. Nielen, C. Kügeler, R. Bruchhaus, R. Waser, "Integrated Complementary Resistive Switches for Passive High-Density Nanocrossbar Arrays", Electron Device Letters, vol. 32, No.2, 2011, pp. 191-193.

[11] A. Fabien, E. Zamanidoost, D. B. Strukov. "Pattern classification by memristive crossbar circuits using ex situ and in situ training", Nature communications, Vol. 4, 2013, p.2072.

[12] L. Wang, D. Meitao, D. Shukai, "Memristive perceptron for combinational logic classification", Mathematical Problems in Engineering, 2013.

[13] B. Li, Y. Wang, Y. Wang, Y. Chen, H. Yang, "Training itself: Mixed-signal training acceleration for memristor-based neural network", In Design Automation Conference (ASP-DAC), 2014 19th Asia and South Pacific, 2014, pp. 361-366.

[14] http://www.technologyreview.com/news/537211/a-better-way-to-build-brain-inspired-chips/

[15] E. Karakulak, R. Mutlu, E. Uçar, "Reconstructive sensing circuit for complementary resistive switches based crossbar memories", Turk J Elec Eng & Comp Sci, Vol. 24, 2016,pp. 1371-1383.

[16] Y. Yuchao, P. Sheridan, W. Lu, "Complementary resistive switching in tantalum oxide-based resistive memory devices." Applied Physics Letters, Vol.100 No.20, 2012, p.203112.

[17] C. Yang, "Nanoscale bipolar and complementary resistive switching memory based on amorphous carbon", Electron Devices, IEEE Transactions on Vl.58 No.11, 2011, pp. 3933–3939.

[18] J.J. Hopfield, D. W. Tank, "Neural" computation of decisions in optimization problems." Biological cybernetics, Vol.52 No.3, 1985, pp. 141–152.

[19] J.J. Hopfield, "Neurons with graded response have collective computational properties like those of two-state neurons." Proceedings of the national academy of sciences, Vol.81, No.10, 1984, pp. 3088-3092.

[20] R. Berdan, T. Prodromakis, C. Toumazou, "High precision analogue memristor state tuning." Electronics letters, Vol. 48, No.18, 2012, pp. 1105-1107.

[21] W. Yi, F. Perner, M.S. Qureshi, H. Abdalla, M.D. Pickett, J.J. Yang, R.S. Williams, "Feedback write scheme for memristive switching devices", Applied Physics A, Vol. 102, No. 4, pp. 973-982.

BIOGRAPHIES

Erdem Uçar was born in Edirne, Turkey in 1966. He received B.Sc. degree from Trakya University in Physiscs in 1990, M.Sc and Ph.D. degrees from Trakya University in Computer Engineering in 1993 and 1996 respectively. He is currently professor at Management Information Systems Department, Trakya University, Edirne, Turkey. His research interests include management information systems and operating systems.

Ertuğrul Karakulak was born in Tekirdağ, Turkey in 1979. He received B.Sc. degree from Sakarya University in Electronics Education in 2001, M.Sc degree in 2005 and Ph.D. degree from Trakya University in 2016. He is currently a assistant professor at Electronics Department, Namik Kemal University, Vocational School of Technical Sciences. His research interests include memristor and resistive RAMs.

Reşat Mutlu was born in Tekirdağ, Turkey in 1973. He received B.Sc. degree from YILDIZ Teknik University in Electrical Engineering in 1995 and M.Sc. and Ph.D. degree from Rensselaer Polytechnic Institute in Electric Power Engineering in 1998 and 2004, respectively. He is currently associated professor at Electronics and Telecommunication Engineering Department, Namik Kemal University, Tekirdag, Turkey. His main research interests are modeling of memristor and memristive systems,analog and computer memory applications of memristive systems, and modeling of memcapacitive and meminductive systems.

Evolutionary Computation Based Control for Ball and Plate Stabilization System

H. GÖZDE

Abstract— The platform stabilization systems used in marine, airborne or land vehicle applications are controlled with very different control methods basically including linear, nonlinear and artificial intelligence-based design techniques. Nowadays, evolutionary computation based optimization algorithms also provide new opportunities to engineers in order to design a gain scheduling controller. In this study, an evolutionary computation based gain scheduling controller is proposed for a ball and plate system so as to examine its control performances on a stabilization system. For this purpose, the swarm intelligence based algorithms are chosen due to their better performance than the other evolutionary computation algorithms. The results are comparatively investigated by using time domain and frequency domain analysis methods. Additionally, the robustness analysis is also applied to examine the tuning performances of these controllers in case of changing system parameters in the range of ±50%.

Index Terms— Platform stabilization, Ball and plate system, Gain scheduling control, Evolutionary computation, Particle swarm optimization algorithm, Differential evolution algorithm.

I. INTRODUCTION

NOWADAYS, the platform stabilization systems are commonly used in marine, airborne and land vehicle applications so as to direct satellite or radar antennas, cameras, missiles, guns etc. in the civil or military areas. These systems have been utilized since about 100 years in order to isolate motion of the vehicle from that of the platform by measuring the change of platform's motion and position continuously [1]. Specifically, despite the change of precision and accuracy depending on the application, the platform stabilization systems generally comprise three fundamental components: inertial and/or position sensor system, mechanical platform with two or more degrees of freedom and control system. The inertial or position sensor systems are required to determine the real position of the platform. In the case of employing inertial sensor system; the roll, pitch, and azimuth data of the platform measured by three accelerometers and gyroscopes in their own local reference frames are converted to the absolute

HALUK GÖZDE, is with Department of Electronics and Communication Engineering, National Defence University, Turkish Military Academy, Ankara, Turkey, (e-mail: hgozde@kho.edu.tr).

https://orcid.org/0000-0003-3661-0794

three-dimensional position data in the global reference frame by combining with the direction data obtained by the magnetometer. However, in the applications where the geographical position data is not important, the well-known motor shaft position sensors such as potentiometers or rotary encoders can be used in order to measure only relative position of the platform in its local reference frame. The mechanical platform providing three dimensional movements is specially designed according to the intended use. The issues such as physical dimensions, weight bearing capacity, degree of freedom (DOF), controllability, place of use, vibrations, torsion strengths, ease of maintenance etc. are taken into account in the design procedure. The control system is especially designed as a closed loop position controller. Relative movement data of the platform is taken from the sensors and then is used in order to keep its stabilization according to global reference frame. In this process, since the control system should cope with the sensor noise, measurement errors, system uncertainties, dead-bands and environmental disturbances etc., the advanced noise filtering techniques and/or relatively complex control methods such as adaptive, optimal or robust controllers are commonly exploited in this type of control systems [2-7]. However, when the response speed of the actuators are essential as depending on the nature of application, complexity and memory requirement of the chosen controller turn into big challenges for implementing the system. In this case, fast microprocessors with large memory should be utilized for implementation or less complex but robust artificial intelligence-based control methods such as fuzzy control, genetic algorithm, swarm optimizations or their hybrids can be preferred with less complex microprocessors [8].

In this way, this system can be considered a basic platform which has similar mechanical and control characteristics with the advanced platform stabilizer systems discussed above. It can be generally defined as a typical multi-variable system and basically consists of plate, actuators, mechanical transmissions, ball and ball position sensors as depicted in Fig.1 [9]. Actually, there are some control challenges similar to ones belonging to the advanced platform stabilization systems discussed above. For instance, the sensor noise is fully effective on the ball position accuracy. This problem has been largely solved by using noise-free overhead camera in the ball and plate system, instead of using noise filters and advanced microprocessors. On the other hand, the control technique is still very important issue for transient and steady-state control performances of the system on account of stabilization and trajectory tracking control as well as mechanical impressions such as frictions and backlash.
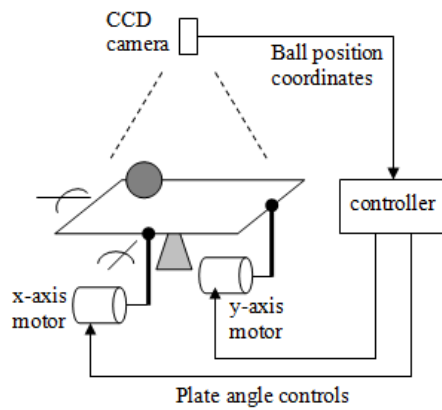
Fig.1. Basic scheme of ball and plate system [9].

If the literature related to control of ball and plate system is investigated, it is seen that various linear, nonlinear or artificial intelligence based control methods have been applied to the system since the beginning of 2000s. In 2004, Fan et al studied on the trajectory planning and tracking control of the ball moving on plate designed as a maze [10]. After that, Bai et al performed a fuzzy controller to control moving of the ball [11]. In 2008, while Hongrui et al designed a non-linear controller [12], Bai et al used an Adaptive Neuro Fuzzy Inference System (ANFIS) controller for the same purpose [13]. Dong et al realized a fuzzy neural network controller optimized by genetic algorithm, then applied the genetic algorithm-based neuro-PID controller to the same system in 2009 [14, 15]. In the same year, Casagrande et al designed a stable nonlinear controller based on Lyapunov function [16]. Moreno-Armend´ariz et al implemented a fuzzy controller on FPGA based hardware to control ball and plate system in 2010 [17]. In 2011, Dong et al used PSO based neuro-fuzzy controller [18], and one year later Han et al also applied PSO to tune the PID controller parameters for ball and plate system [19]. Mochizuki et al proposed a design method of PID controller based on the generalized Kalman-Yakubovich-Popov lemma in 2013 [20]. PSO was applied to the ball and plate system again by Roy et al for tuning the parameters of PD trajectory controller in 2014 [21]. Zhao et al designed a fuzzy multi-variable control combined neural networks in the same year [22]. In 2015, Han et al proposed a fuzzy based indirect adaptive controller [23], Oravec et al suggested model predictive controller [24], and Negash et al designed fuzzy based sliding mode controller [25] in order to control ball and plate system. Xiao et al implemented adaptive embedded controller for the same purpose in 2016 [26]. It can be observed from the reviewed literature that the artificial intelligence based controllers have been more preferable than the classical linear and non-linear controllers due to the multivariable and high order structure of the ball and plate system. The artificial intelligence tools provide great convenience to easy design and implement the optimal and adaptive controllers for this type of high order complex systems. For this reason, evolutionary computation based gain scheduling control method is proposed.

In detail, the aim of this study is to examine the tuning performance of evolutionary computation based optimization algorithms according to classical tuning for a platform stabilization systems discussed above on the example of ball and plate system. The evolutionary computation based algorithms are heuristic optimization tools which have short, algebraic and fast convergent program code and without derivative calculations. They are basically separated into two types: First one is the evolutionary algorithms based on Darwin's theory of evolution, such as genetic and differential evolution algorithms etc. Second one is the swarm intelligence algorithms based on food searching behavior of organisms, such as particle swarm optimization and artificial bee colony algorithms etc. In this study, two types of evolutionary computation methods are applied to the gain scheduling controller to achieve adaptive control structure for ball and plate stabilization system against internal or external parameter variations.

The paper is organized as follows. The ball and plate system and its modeling are described in Section II. The proposed gain scheduling control system designed and the evolutionary computation based algorithms are explained in Section III. The simulation and the experimental results are represented in Section IV and Section V, respectively. The discussion is performed in Section VI. Finally, concluding remarks are presented in Section VII.

II. MODEL OF BALL AND PLATE SYSTEM

In this study, 2-DOF ball and plate stabilization system made by QUANSER is utilized due to its MATLAB/Simulink software support and user friendly interfaces.

Fig.2. Ball and plate system made by QUANSER [27].

This system basically consists of a plate, a ball, an overhead camera and two servo units as presented in Fig.2. While the servo units and plate allow rolling the ball about any direction, the overhead camera measures the position of the ball for feedback to the controller. There are two QUANSER SRV02 servo units under the plate, which are connected to the plate in order to provide 2-DOF gimbal actions [27].

The model of ball and plate system for only one axis is presented in Fig.3. Actually, the plate is capable of two axes movement. But, since both axes are symmetrical according to each other, their dynamics are also assumed same and the system can be modeled only in one axis. In this point of view,

x is motion of the ball, α is angle of the plate, m_b is mass of the ball, $F_{x,r}$ is force caused from the ball's inertia and $F_{x,t}$ is translational force generated by gravity. The friction and viscous damping are neglected. In order to model the one axis system, it can be assumed that x, α and θ_l are equal to zero while the ball is stationary in the center and the plate is parallel to the ground. At the same time, some forces caused from ball's momentum and gravity affects the ball for all conditions. In theory, the force from the ball's momentum must equal to the force produced by gravity along the plate surface in the x-axis as in Equation 3.
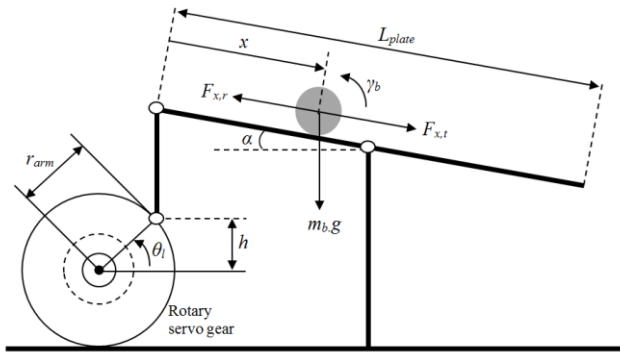

Fig.3. The one axis model of ball and plate system [27].

In addition, the mechanical parts of ball and plate system are considered into two parts: rotary servo gear mechanism and plate mechanism as depicted in Fig.4. In order to obtain the transfer function models of these parts, it can be started from Newton's first law [27];
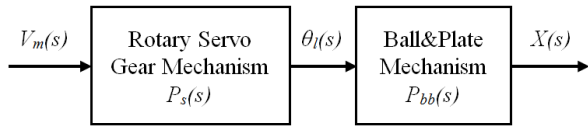

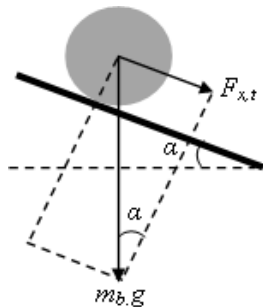Fig.4. The mechanical parts of ball and plate system [27].

Fig.5. Gravitational forces affecting the ball.

$$F = m_b.a = m_b.\frac{d^2x}{dt^2} = m_b.\ddot{x} = F_{x,t} - F_{x,r} \quad (1)$$

where $F_{x,t}$ from Fig.5, and $F_{x,r}$ from Equation 3 are computed in Equations 2 and 4,

$$F_{x,t} = m_b.g.\sin\alpha \quad (2)$$

$$T_b = F_{x,r}.r_b = J_b.a_b = J_b.\ddot{\gamma}_b \quad (3)$$

$$F_{x,r} = \frac{T_b}{r_b} = \frac{J_b.\ddot{\gamma}_b}{r_b} \quad (4)$$

In these equations, J_b is inertia of ball, T_b is torque applied to the ball, r_b is radius of ball and γ_b is rolling angle of the ball. If the angular displacement γ_b is transformed to linear displacement x by Equations 5 to 6 as depicted in Fig. 6;
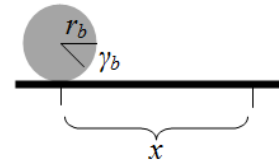
Fig.6. Transformation of angular and linear displacements.

$$2.\pi.r_b.\frac{\gamma_b}{2.\pi} = x \quad (5)$$

$$\ddot{\gamma}_b = \frac{\ddot{x}}{r_b} \quad (6)$$

$$F_{x,r} = \frac{J_b.\ddot{\gamma}_b}{r_b} = \frac{J_b.\ddot{x}}{r_b^2} \quad (7)$$

If Equation 2 and Equation 7 are substituted in Equation 1, then;

$$m_b.\ddot{x} = m_b.g.\sin\alpha - \frac{J_b.\ddot{x}}{r_b^2} \quad (8)$$

The acceleration of the ball on the plate is obtained from Equation 8;

$$a = \ddot{x} = \frac{m_b.g.\sin\alpha.r_b^2}{m_b.r_b^2 + J_b} \quad (9)$$

The relationship between the plate angle α and servo gear rolling angle θ_l can be written below, because the height h is equal to each other for both angles as represented in Fig. 7;

$$\sin\alpha = \frac{2.h}{L_{plate}} \quad (10)$$

$$\sin\theta_l = \frac{h}{r_{arm}} \quad (11)$$

From these equations,
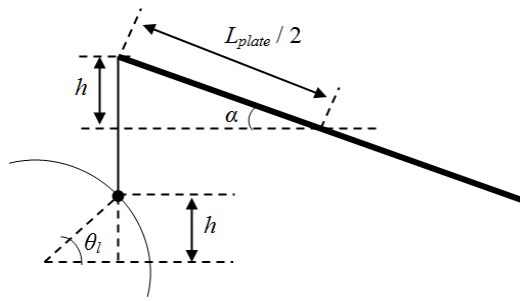
Fig.7. Relation between angle α and height h.

$$\sin \alpha = \frac{2.r_{arm}.\sin\theta_l}{L_{plate}} \qquad (12)$$

If Equation 12 is substituted in Eq. 9, then the nonlinear acceleration equation of the ball on the plate is obtained below;

$$\ddot{x} = \frac{2.m_b.g.r_{arm}.r_b^2}{L_{plate}.(m_b.r_b^2 + J_b)}.\sin\theta_l \qquad (13)$$

To linearize this equation, servo gear rolling angle θ_l can be taken near zero. In this case, the linear acceleration equation of the ball on the plate is obtained as Equation 15;

$$\theta_l \cong 0 \Rightarrow \sin\theta_l = \theta_l \qquad (14)$$

$$\ddot{x} = \frac{2.m_b.g.r_{arm}.r_b^2}{L_{plate}.(m_b.r_b^2 + J_b)}.\theta_l \qquad (15)$$

The transfer function model of the ball and plate system between servo gear rolling angle θ_l and motion of the ball x is obtained from Equation 15 using Laplace transformation. In this equation, the constant multiplied by angle θ_l is defined as K_{bb}.

$$s^2.X(s) - s.x(0) - x'(0) = K_{bb}.\theta_l(s) \qquad (16)$$

If the initial values of the motion are accepted zero, then the linear transfer function model of the ball and plate mechanism $P_{bb}(s)$ can be obtained as such [27];

$$\frac{X(s)}{\theta_l(s)} = \frac{K_{bb}}{s^2} = P_{bb}(s) \qquad (17)$$

On the other hand, the rotary servo gear mechanism can be modeled as a two-order transfer function by using classical DC motor armature circuit and gear train modeling sequence as determined in Equation 18 [28].

$$P_s(s) = \frac{\theta_l}{V_m} = \frac{K}{s(\tau.s + 1)} \qquad (18)$$

where V_m is DC servo motor input voltage, K is servo gain and τ is servo time constant. As a result, the fourth-order linear complete transfer function model of complete ball and plate system can be computed as;

$$P(s) = P_s(s).P_{bb}(s) \qquad (19)$$

$$P(s) = \frac{X(s)}{V_m(s)} = \frac{K}{s(\tau.s + 1)}.\frac{K_{bb}}{s^2} = \frac{K.K_{bb}}{s^3.(s.\tau + 1)} \qquad (20)$$

The model parameters are presented in Table 1 [27, 28].

TABLE I
PARAMETERS OF THE BALL AND PLATE SYSTEM MODEL [27]

Parameters	Parameter values
m_b	0.0252 kg
r_b	0.017 m
g	9.81 m/s^2
J_b	2.89.10^{-6} kg.m
L_{plate}	0.275 m
r_{arm}	0.0254 m
K	1.53 rad/V.s
τ	0.0248 s

III. PROPOSED CONTROL METHOD

The utilized ball and plate system is originally controlled by two sequential Proportional-Derivative (PD) and Proportional (P) control loops for ball position control and servo speed control, respectively [27]. Because each controller has constant control parameters which have previously calculated, the ball and plate system is completely sensitive to internal and external parameter variations. For this reason, the gain scheduling adaptive control method is suggested for the ball and plate stabilization system and comparatively discussed in this study. Basically, it is expected from this approach that controller parameters of the system are tuned to optimal values at normal condition and when the system parameters such as mass of the ball, and gain and/or time constant of the servo system, change in the range of ±50% for any reason at any time. Also, it is evaluated that the proposed controller will be able to be implemented as an embedded controller in the future.

3.1 Gain Scheduling Control

Gain scheduling control is an adaptive control method tuning controller parameters according to different operating points where the system works. The gain scheduling control method is more suitable for nonlinear processes and time and/or parameter varying processes. In principle, all the desired system variables are measured firstly, and then the control parameters are tuned by a scheduling mechanism. The main superiority of this method is simpler design and implementation than the other adaptive control techniques as well as relatively fast adaptation ability to provide quick response to changes in system dynamics [29, 30].

In this study, it is suggested that the scheduling process is performed with evolutionary computation based optimization algorithms in order to examine the tuning performance of these types of algorithms according to classical tuning for a platform stabilization system on the example of ball and plate system. For this purpose, swarm intelligence based PSO and evolutionary algorithm based DE algorithms are chosen due to their better performance than others. The results are compared to the original P and PD controller given on the current system. The block diagram of proposed control method is represented in Fig. 8.
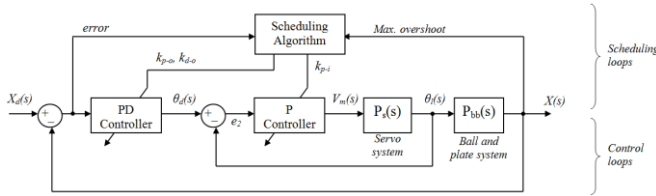

Fig.8. Proposed gain scheduling controller for 1-axis and 2-DOF ball and plate system.

3.2 Particle Swarm Optimization (PSO) Algorithm

PSO algorithm which was first introduced by Kennedy and Eberhart in 1995 is a swarm intelligence-based optimization algorithm [30]. Swarm intelligence is the study of evolutionary computation inspired by the collective food searching behavior of the bird flocks. It provides high speed convergence and high quality solutions with its short and algebraic program code without derivative calculations.

The algorithm basically models the food searching behavior of bird flocks or fish schools. Mathematically, it uses particles whose positions represent potential solutions of the problem and each particle flies in search space at a certain velocity which can be adjusted in light of preceding flight experiences. The positions of the particles are updated by the equations below, which include sufficient randomness;

$$v_i^{t+1} = w.v_i^t + c_1.r_1.(p_i^t - x_i^t) + c_2.r_2.(g_i^t - x_i^t) \qquad (21)$$

$$x_i^{t+1} = x_i^t + v_i^{t+1} \qquad (22)$$

where, $i = 1, \ldots, n$ and n defines the size of swarm, w is inertia weight decreased linearly for each iteration, c_1 and c_2 are positive constants for weighting local or global search activity, r_1 and r_2 are random numbers distributed uniformly between 0 and 1, superscript t is the iteration number, p_i represents the best previous position of the ith particle and g represents the best particle position among all the particles in the swarm. At the end of the iterations, the best position g will be optimum solution of the problem. Pseudo code of PSO algorithm is represented below;

```
Initialization
   Repeat
   Evaluate the fitness values of particles
   Compare the fitness values to determine the p and g
   Change velocity and position of the particles as to Eqs.21 and 22
Until (requirements are met)
```

3.3 Differential Evolution (DE) Algorithm

DE algorithm which was first suggested by Storrn in 1996 is the powerful stochastic optimization algorithm covered by the evolutionary algorithms. Evolutionary Algorithms is a branch of evolutionary computation concerned with computational methods inspired by the process of biological selection based on Darvin's theory of evolution [31]. In detail, DE algorithm also uses crossover, mutation and selection operators like genetic algorithms. But, the main difference of these algorithms is that while DE algorithm relies on mutation operation, the genetic algorithm is based on crossover operation. The algorithm is started with the first evaluation for the initial creation of the population. After that, recombination, evaluation, and selection processes are performed to the members of population, which are candidate solutions of the problem. The recombination is a process in which the new candidate solutions are created via selection process between two weighted random population members added to a third population member by using crossover process [32]. Pseudo code is represented below;

```
Initialization
   Evaluation
   Repeat
   Mutation
   Recombination
   Crossover
   Selection
Until (requirements are met)
```

IV. SIMULATION STUDIES AND RESULTS

The simulation studies are realized in two parts on the one-axis Simulink model of ball and plate system depicted in Fig. 9. At the first part, the original P-PD controller given with QUANSER ball and plate system is investigated. After that, the proposed evolutionary computation based controllers are applied to the system at the second part of the study. Original and obtained K_{p-o}, K_{d-o} and K_{p-i} gains of the P-PD controllers are listed in Table 2. The model of P-PD controller which is designed originally and the tracking responses obtained from this and proposed controllers are depicted in Fig. 10 and Fig. 11. In the simulations performed with the handled algorithms, the upper and the lower bounds of the K_{p-o}, K_{d-o} and K_{p-i} gains are chosen as (2, 10), (2, 10) and (10, 20) respectively. The number of iteration and the population size are determined as 10 and 20 for both algorithms by trial and error method. Also, the scaling factor is taken as 0.02 for DE algorithm.
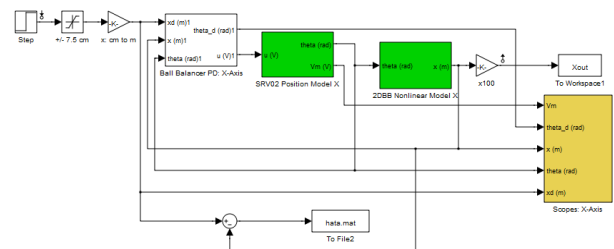

Fig.9. One-axis Simulink model of ball and plate system [27].

The integral of time weighted squared error (ITSE) function represented in Equation 23 is used as a cost function which

will be minimized for determining the optimum values of tuned parameters. The purpose of choosing this function is to help to minimize settling time due to its dependency of errors on time. Additionally, the weighted maximum overshoot value computed from the result is also added to the cost function in order to minimize the overshoot of the system.

TABLE II
ORIGINAL AND OPTIMAL PD AND P PARAMETERS

		Classic P-PD	PSO based P-PD	DE based P-PD
Outer loop	K_{p-o}	3.45	5.61	9.96
	K_{d-o}	2.11	2.69	3.42
Inner loop	K_{p-i}	14.00	14.98	16.52

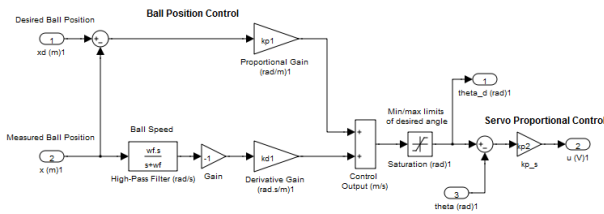$$ITSE = \int_0^t t.e^2.dt \qquad (23)$$

Fig.10. P-PD controller used in QUANSER ball and plate system [27].

The transfer functions of one-axis closed loop system according to the controller parameters obtained by the original, PSO based and DE based methods are represented in Equations 24, 25 and 26 respectively.

$$\frac{X(s)}{X_d(s)} = \frac{3237s + 50840}{5s^5 + 56.03s^4 + 1496s^3 + 13550s^2 + 34330s + 50840} \qquad (24)$$

$$\frac{X(s)}{X_d(s)} = \frac{5629s + 88420}{5s^5 + 56.03s^4 + 1557s^3 + 14500s^2 + 48060s + 88420} \qquad (25)$$

$$\frac{X(s)}{X_d(s)} = \frac{11030s + 173200}{5s^5 + 56.03s^4 + 1652s^3 + 15990s^2 + 70590s + 173200} \qquad (26)$$
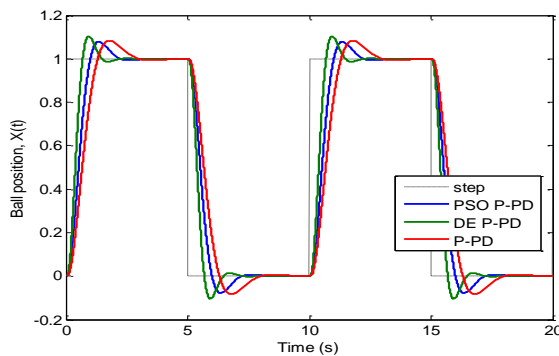

Fig.11. One-axis tracking response of the simulations.

At the end of the simulations, the tuning performance of the evolutionary computation methods according to classical method and each other is put forward by using time domain

and frequency domain analysis methods as explained below. After that, the investigation of robustness of the system tuned by chosen algorithms is also examined.

4.1 Step and Ramp Response Analysis

The step response analysis is an investigation of system behavior during the time of the beginning and the steady state. It provides the data about relative stability and response speed of the closed loop system. For example, while the amount of maximum overshoot may be related to the relative stability, the settling and rise times show the response speed of the system. On the other hand, the ramp response gives an amount of deviation from the desired output in steady-state. The results obtained at the end of the analyses are represented in Table 3 and Figs. 12 and 13.

TABLE III
STEP AND RAMP RESPONSES OF THE CLOSED LOOP SYSTEM

	Maximum Overshoot (%)	Settling Time [s] (±5% band)	Rise Time [s]	Peak Time [s]	Ramp Response [V]
Classic P-PD	8.219	2.653	0.833	1.820	0.35
PSO based P-PD	**7.830**	1.965	0.625	1.372	0.28
DE based P-PD	10.300	**1.220**	**0.422**	**0.932**	**0.21**

The unit step response analysis shows that the performances of evolutionary algorithms tuned controllers are generally better than that of original P-PD controller.
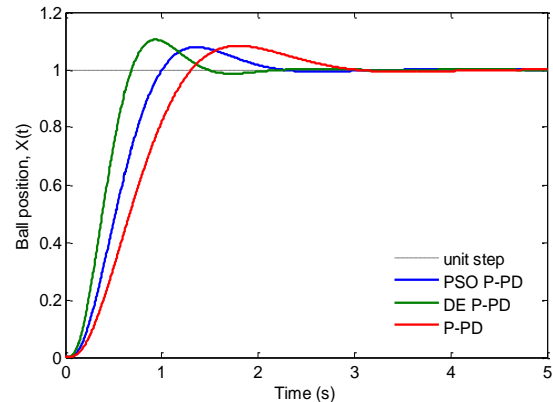
Fig.12. Unit step response of the closed loop system.

Especially, the settling time, rise time and peak time obtained with DE based controller are decreased about 50% with respect to the original P-PD controller. In this scope, it can be said that the response speed of the proposed method is better about 50% than the original one. However, it is observed that the maximum overshoot belongs to the system tuned by DE algorithm. On the other hand, the ramp responses show that the steady-state tracking error of the system is also decreased about 50% according to the original P-PD controller by using proposed P-PD controllers as represented in Table 3.

Fig.13. Ramp response of the closed loop system.

4.2 Root Locus Analysis

The root locus analysis is other time domain method which provides the data about stabilities of the closed loop system. Basically, while the placements of system poles can show whether the system is stable or not, the damping ratios of the poles emphasize information about degree of stability. The results of the analysis are presented in Table 4 and Figs. 14, 15, and 16.

TABLE IV
CLOSED LOOP POLES AND DAMPING RATIOS

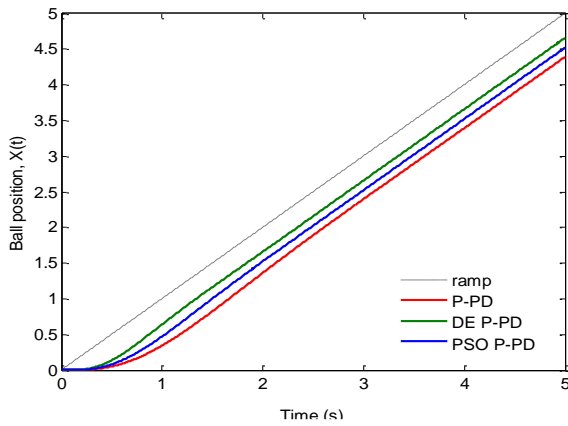| Classic P-PD		PSO based P-PD		DE based P-PD	
Closed Loop Poles	**Damping Ratio**	**Closed Loop Poles**	**Damping Ratio**	**Closed Loop Poles**	**Damping Ratio**
-21.3+j20.8	**0.714**	-21.5+j22.1	0.697	-21.7+j23.9	0.672
-21.3-j20.8	**0.714**	-21.5-j22.1	0.697	-21.7-j23.9	0.697
-10.6+j0	1	-9.12+j0	1	-7.51+j0	1
-1.43+j1.83	0.618	-1.99+j2.51	0.621	-2.58+j3.94	0.548
-1.43-j1.83	0.618	-1.99-j2.51	0.621	-2.58-j3.94	0.548

When the pole-zero maps of the closed loop system are investigated, all the system poles are at the left side of the s-plane. Hence, it can be said that all controllers provide absolute stability. In parallel, although close the each other, the better damping ratio belongs to the original P-PD controller. In contrast, the worst one belongs to the DE algorithm tuned controller in parallel to the overshoot results. These results exhibits that the original controller is more stable for given operating point.

4.3 Bode Analysis

The bode analysis which is the frequency domain analysis method gives information about the relative stability of the control system. The magnitude and phase plots are depicted in Figs. 17, 18 and 19. The peak gains and the delay, gain and phase margins are presented in Table 5.

To examine the frequency responses of the controllers, the gain and phase margins, peak gains and bandwidths are computed from the magnitude and phase curves for each controller. It is seen from these analyses that the gain and phase margins of the system based on DE algorithm have the worst values in parallel to the step response analysis. Also, the maximum bandwidth belongs to DE algorithm based system is

greater about 50% than the original P-PD based system as expected from the results of step response analysis. These results mean that the DE algorithm based controller is less stable but faster than the others.

Fig.14. Pole-zero map of the original P-PD based system.
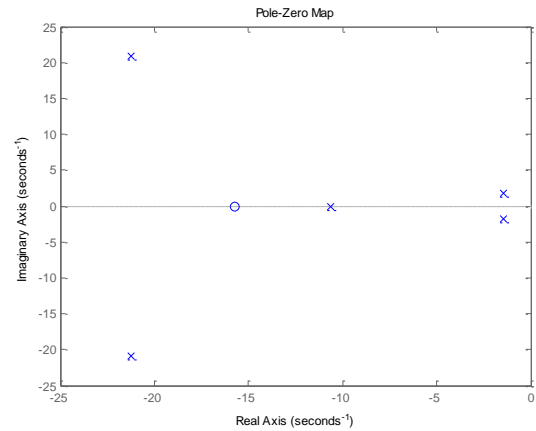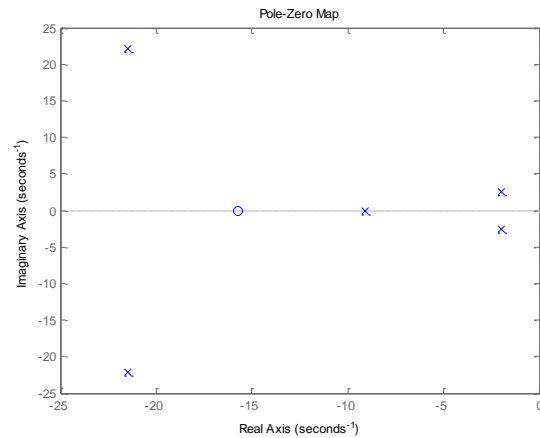

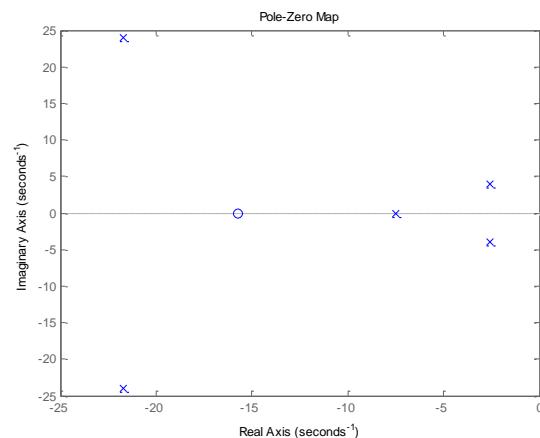Fig.15. Pole-zero map of the PSO based system.

Fig.16. Pole-zero map of the DE based system.

4.4 Robustness Analysis

To examine the tuning performances of the evolutionary computation based controllers in case of the system parameter variations, a simple robustness analysis is applied to them. For this purpose mass of the ball is externally changed, servo gain

and servo time constant are internally changed in the range of ±50% as represented in Table 6. At the end of the analysis, the controller parameters tuned by the PSO and DE algorithms are presented in Table 7. Additionally, the unit step responses obtained for these cases are also represented in Figs. 20, 21, 22, 23, 24 and 25 and in Table 8.

TABLE V
THE RESULTS OF BODE ANALYSIS

	Peak Gain (dB)	Gain Margin (dB)	Phase Margin (deg.)	Bandwidth
Classic P-PD	0.214	**18.3**	117	2.5718
PSO based P-PD	0.158	15.7	**119**	3.4552
DE based P-PD	**0.341**	12.0	97.8	**5.1931**
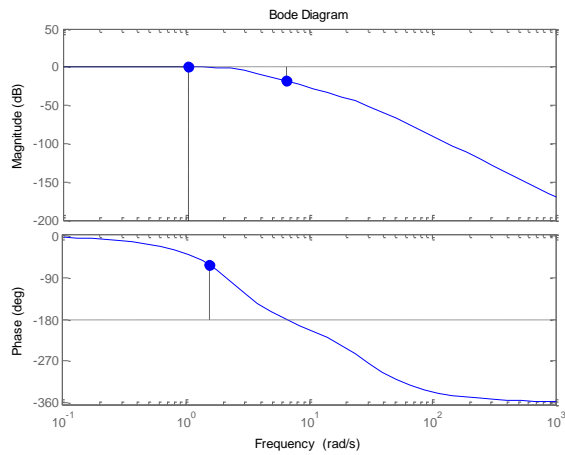
Fig.17. Bode curve of the original system.
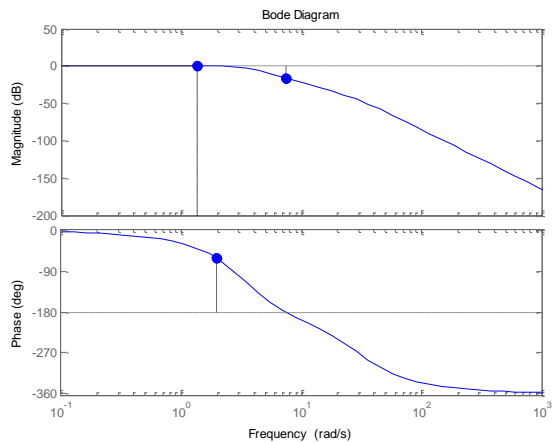
Fig.18. Bode curve of the PSO based system.

The analysis shows that although DE algorithm based controller has better tuning performance for given initial operating point, PSO algorithm exhibits better tuning capacity than DE algorithm in case of changing system parameters. In this analysis, the initial settings of the algorithms are not changed.
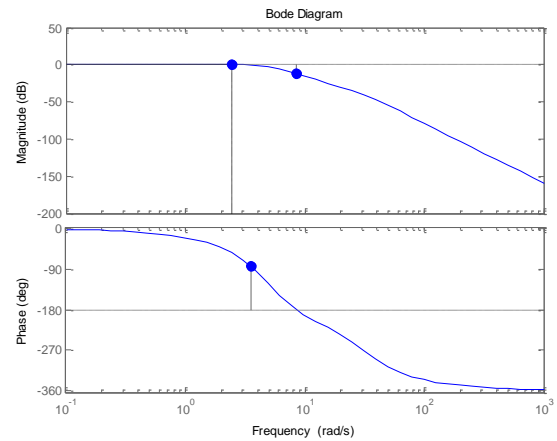
Fig.19. Bode curve of the DE based system.

TABLE VI
CASES OF SYSTEM PARAMETER CHANGING ACCORDING TO THEIR NOMINAL VALUES

Cases	Disturbances	Disturbance types
Case-1	50% decrease of Servo gain (K)	Internal
Case-2	50% increase of Servo gain (K)	
Case-3	50% decrease of Servo time constant (τ)	
Case-4	50% increase of Servo time constant (τ)	
Case-5	50% decrease of Mass of the ball (m_b)	External
Case-6	50% increase of Mass of the ball (m_b)	

TABLE VII
TUNED PARAMETERS DURING ROBUSTNESS ANALYSIS

Cases	PSO based P-PD			DE based P-PD		
	K_{p-o}	K_{d-o}	K_{p-i}	K_{p-o}	K_{d-o}	K_{p-i}
Case-1	14.66	5.96	17.22	6.78	2.67	17.96
Case-2	19.81	5.30	18.61	2.89	3.14	17.86
Case-3	14.61	5.23	18.03	7.18	4.30	19.44
Case-4	13.82	5.40	15.56	4.14	5.00	15.36
Case-5	19.99	6.63	18.85	8.53	4.03	10.28
Case-6	14.63	5.77	10.08	9.33	7.06	14.62

Fig.20. Performance comparison for 50% decrease of servo gain.

Fig.21. Performance comparison for 50% increase of servo gain.

Fig.22. Performance comparison for 50% decrease of servo time constant.

Fig.23. Performance comparison for 50% increase of servo time constant.

Fig.24. Performance comparison for 50% decrease of mass of the ball.

Fig.25. Performance comparison for 50% increase of mass of the ball.

TABLE VIII
UNIT STEP RESPONSE OF ROBUSTNESS ANALYSIS

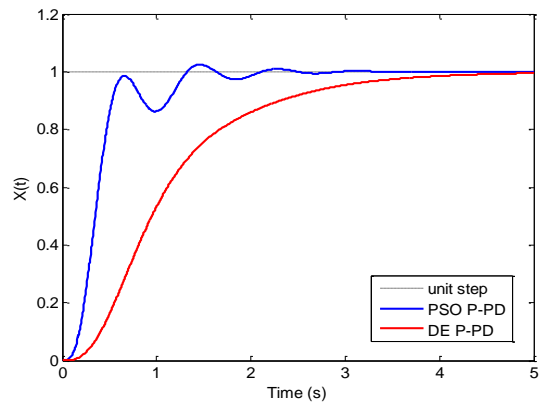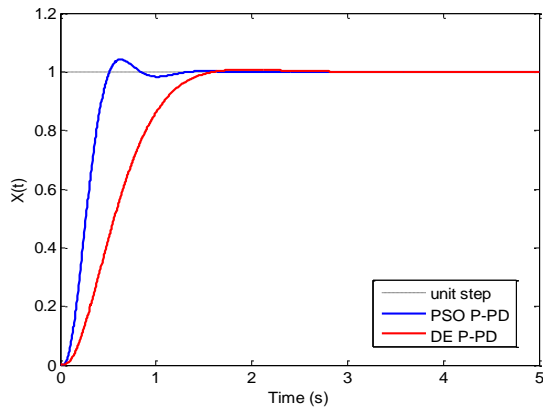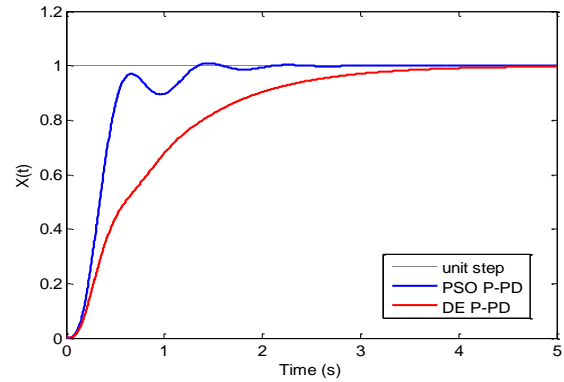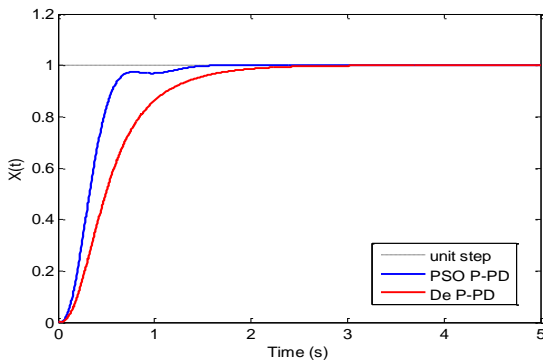| Cases	Maximum Overshoot (%)		Settling Time (s) (5% band)		Rise Time (s)	
	PSO based P-PD	DE based P-PD	PSO based P-PD	DE based P-PD	PSO based P-PD	DE based P-PD
Case-1	2.44	**0**	**1.22**	2.93	**0.34**	1.91
Case-2	4.12	**0.725**	**0.46**	1.24	**0.30**	0.86
Case-3	0	0	**0.63**	1.44	**0.41**	0.93
Case-4	0	0	**1.02**	1.38	**0.44**	0.89
Case-5	0	0	0.94	**0.82**	**0.35**	0.52
Case-6	0.91	**0**	**1.18**	2.55	**0.36**	1.77

V. EXPERIMENTAL STUDIES AND RESULTS

The controller parameters obtained by the simulation studies are applied to the real ball and plate system. The experimental hardware is represented in Fig. 26. The real one-axis tracking responses obtained by original controller and evolutionary computation based controllers are presented in Figs. 27, 28 and 29. In these figures, the black square curves are inputs and the red curves are system outputs. First of all the big magnitude oscillations are observed on all responses. Particularly, it is evaluated that they are particularly caused from the center point calibration error of the camera and inception angle errors of the plate. If the camera is not calibrated sufficiently to center point of the plate and/or if the plate is not fully parallel to horizontal plane, the controller will have to perform hysteresis behavior to keep the ball in balance, which results in various magnitude oscillations.

In this study, the tuning process is realized off-line by simulation studies. Then, the obtained controller parameters applied to the real ball and plate system. The experimental studies exhibit that the tracking responses of evolutionary computation based controllers are better than that of the original controller. Also, in fact that the response of PSO based controller has minimum oscillation means that this algorithm has better stability performance as observed from the simulation results before. On the other hand, the slopes of rising edges of these responses are investigated in order to compare the response speed of the actual results. Consequently, the slopes m_P and m_D related to PSO and DE algorithms are computed about 10.52 and 15.38 with respect

to Equation 24, respectively as represented in Fig. 30. According to these results, the response speed of DE algorithm based controller is better about 20% than that of PSO algorithm based controller as presented in simulation studies.

Fig.26. Ball and plate hardware for experimental study.

$$m = \frac{y_2 - y_1}{x_2 - x_1} \qquad (24)$$

Fig.27. One-axis tracking response for experimental study of classic P-PD controller.
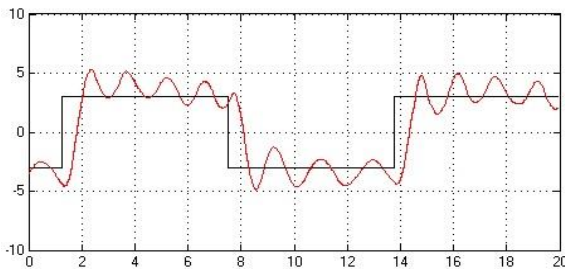
Fig.28. One-axis tracking response for experimental study of PSO based P-PD controller.
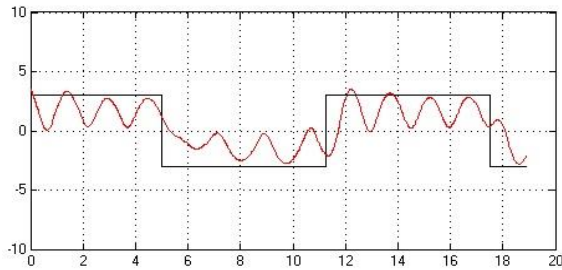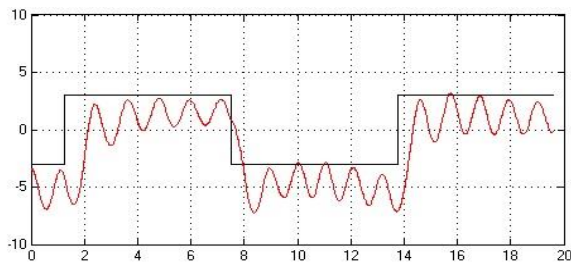

Fig.29. One-axis tracking response for experimental study of DE based P-PD controller.

| (a) | (b) |
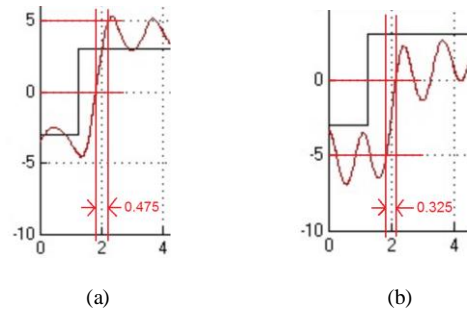
Fig.30. Slope of rising edge of tracking responses obtained from

(a) PSO and (b) DE algorithms.

VI. DISCUSSION

The tuning performance of the evolutionary computation based optimization algorithms in gain scheduling control which is designed for ball and plate stabilization system is examined using time and frequency domains and robustness analyses. After that, the simulation results are verified by experimental studies. It is clear that a controller design is required compromise between stability and response speed. Nonetheless, the control performances of original and proposed controllers are investigated for both stability and response speed. In this point of view, the results of the analyses can be separated into system stability and response speed indicators as depicted in Figs. 31 and 32. Maximum overshoots and damping ratios which can be chosen as stability indicators show that although the damping ratio of original controller is a little big, the PSO based controller can work more stable than the original one for given operating point owing to its better overshoot performance and better settling time response informing about transition time to stable condition. On the other hand, the proposed gain scheduling controllers can be still stable when the system parameters change as evidenced by robustness analysis. Also, it can be said from Fig. 31 that the stability performance of PSO algorithm is better than DE algorithm due to smaller maximum overshoot and greater damping ratio.
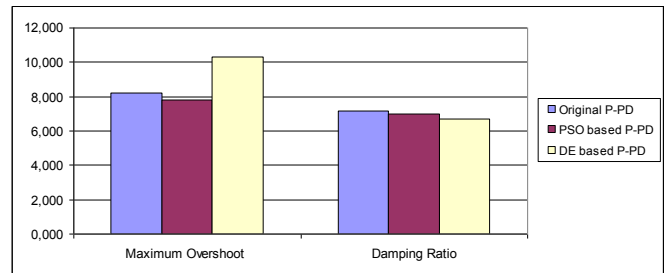
Fig.31. Results of system stability indicators.

When the response speed indictors such as settling time, rise time and bandwidth are examined, the results presented in Fig. 32 show that the proposed controllers respond faster about 50% than the original controller. Actually, this result is supported by the results of overshoot analysis. Also, the analysis shows that the response speed of DE algorithm is clearly better than that of PSO algorithm. Additionally, the DE algorithm based controller has minimum steady-state error as proved by ramp response analysis.

,
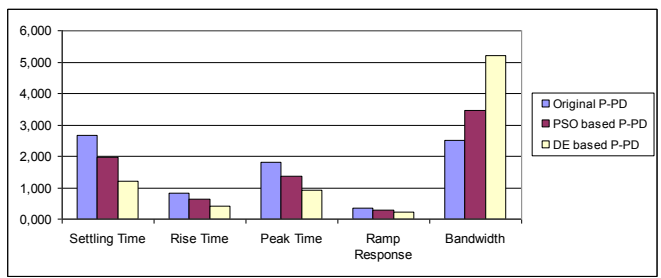
Fig.32. Results of response speed indicators.

On the other hand, the robustness analysis is performed to determine the behaviors of the proposed controllers in case of changing operating point caused by internal or external parameter variations. This analysis also exhibits interesting results about tuning performance of the chosen algorithms. According to them, the tuning performance of the swarm intelligence based PSO algorithm is more superior to that of DE algorithm based on evolution theory for different working conditions. It can be evaluated that this result is originated from better stability performance of PSO algorithm. The experimental studies largely verify these simulation results.

Finally, the evolutionary computation based optimization algorithms are successfully applied to the ball and plate stabilization system in order to tune the proposed gain scheduling P-PD controller parameters. The proposed controllers provide desired control system performances both for given operating point and for changing of system parameters. Also, it is proved by simulation and experimental studies that the results obtained by using these algorithms are better than the results belong to the original controller. In detail, while the swarm intelligence based PSO algorithm exhibits better stability performance, the evolutionary intelligence based DE algorithm indicates better response speed performance than the other.

VII. CONCLUSION

In this study, the evolutionary computation based gain scheduling controller is designed in order to comparatively examine its control performance on ball and plate stabilization system. For this purpose, the swarm intelligence based PSO algorithm and the evolution theory based DE algorithm are chosen due to their better optimization performance than the others. The results taken by time and frequency domains and robustness analyses show that the proposed gain scheduling controller provides desired control system performances both for given operating point and for changing system parameters. In detail, PSO algorithm particularly exhibits better optimization performance in case of changing system parameters. The obtained simulation results are also verified by the experimental studies. On the other hand, designed controller is an off-line gain scheduling controller. In addition, the evolutionary computation based optimization algorithms can be easy embedded in a relatively simple microcontroller system due to their algebraic and short program codes. In the future study, the proposed gain scheduling controller will be implemented in a fully adaptive structure by designing an external microcontroller circuit.

REFERENCES

[1] S. Leghmizi, S. Liu, "A Survey of Fuzzy Control For Stabilized Platforms", International Journal of Computer Science&Engineering Survey, vol.2, no.3, (2011).

[2] F.N. Barnes, "Stable Member Equations of Motion for a Three-Axis Gyro Stabilized Platform", IEEE Transaction on Aerospace and Electronic Systems, vol.7, no.5, 1971, pp. 830-842.

[3] T.H. Lee, E.K. Koh, M.K. Loh, "Stable Adaptive Control of Multivariable Servomechanisms with Application to Passive Line-of-Sight Stabilization System," IEEE Transactions on Industrial Electronics, vol. 43, no.1, 1996, pp. 98-10.

[4] J.A.R.K. Moorty, R. Marathe, "LQG/LTR Control Law for A Wideband Controller for Line of Sight Stabilization for Mobile Land Vehicles", Proceedings International Conference on Electro-Optics, 1999, pp.729–735.

[5] J.A.R.K. Moorty, R. Marathe, V.R. Sule, "H∞ Control Law for Line-of-Sight Stabilization for Mobile Land Vehicles", Society of Photo-Optical Instrumentation Engineers, Optical Engineering, vol.41, no.11, 2202, pp. 2935-2944.

[6] Y.J. Chen, S.H. Huang, W. Shanming, W. Fang, "DSP-Based Real-Time Implementation of A Neural Network Observer and Hybrid H∞ Adaptive Controller for Servo-Motor Drives", Proceedings of the 27th Chinese Control Conference, China, 2008, pp.130-134.

[7] F.R. Rubio, "Application of Position and Inertial-Rate Control to A 2-DOF Gyroscopic Platform", Robot Computer Integration Manufacturing, 2010, pp. 1-10.

[8] J.T. Spooner, K.M. Passino, "Stable Adaptive Control Using Fuzzy Systems and Neural Networks," IEEE Transactions on Fuzzy Systems, vol.4, no.3, 1996, pp. 339-359.

[9] P. Horacek, "Laboratory Experiments For Control Theory Courses: A Survey", Annual Reviews in Control, vol.24, 2000, pp. 151-162.

[10] X. Fan, N. Zhang, S. Teng, "Trajectory Planning and Tracking of Ball And Plate System Sing Hierarchical Fuzzy Control Scheme", Fuzzy Sets and Systems, vol.144, issue 2, 2004, pp. 297–312.

[11] M. Bai, H. Lu, J. Su, Y. Tian, "Motion Control of Ball and Plate System Using Supervisory Fuzzy Controller", Proceedings of the 6th World Congress on Intelligent Control and Automation, China, 2006.

[12] W. Hongrui, T. Yantao, F. Siyan, S. Zhen, "Nonlinear Control for Output Regulation of Ball and Plate System", Proceedings of the 27th Chinese Control Conference, China, 2008.

[13] M. Bai, Y. T. Tian, J. T. Su, "Position Control of Ball and Plate System Based on ANFIS", Complex Systems and Applications, vol.1, 2008, pp.165.

[14] X. Dong, Z. Zhang, J. Tao, "Design of Fuzzy Neural Network Controller Optimized by GA for Ball and Plate System", Proceedings of the Sixth International Conference on Fuzzy Systems and Knowledge Discovery,Vol.4, 2009, pp. 81-85.

[15] X. Dong, Z. Zhang, C. Chen, "Applying Genetic Algorithm to On-Line Updated PID Neural Network Controllers for Ball and Plate System", Fourth International Conference on Innovative Computing, Information and Control, 2009, pp.751-755.

[16] D. Casagrande, A. Astolfi, T. Parisini, "Switching-Driving Lyapunov Function and the Stabilization of the Ball-and-Plate System", IEEE Transactions on Automatic Control, vol.54, no.8, 2009, pp.1881-1886.

[17] M.A. Moreno-Armend´ariz, E. Rubio, C.A. P´erez-Olvera, "Design and Implementation of a Visual Fuzzy Control in FPGA for the Ball and Plate System", International Conference on Reconfigurable Computing, 2010, pp.85-90.

[18] X. Dong, Y. Zhao, Y. Xu, Z. Zhang, P. Shi, "Design of PSO Fuzzy Neural Network Control for Ball and Plate System", International Journal of Innovative Computing, Information and Control, vol.7, issue.12, 2011, pp. 7091-7103.

[19] K. Han, Y. Tian, Y. Kong, J. Li, Y. Zhang, "Tracking Control of Ball and Plate System Using An Improved PSO On-Line Training PID Neural Network", IEEE ICMA International Conference on Mechatronics and Automation, 2012, pp. 2297-2302.

[20] S. Mochizuki, H. Ichihara, "I-PD Controller Design based on Generalized KYP Lemma for Ball and Plate System", European Control Conference (ECC), Switzerland, 2013, pp.2855-2860.

[21] P. Roy, B. Kar, I. Hussain, "Trajectroy Control of a Ball In A Ball and Plate System Using Cascaded PD Controllers Tuned By PSO", Proceedings of Fourth International Conference On Soft Computing For Problem Solving, vol.2, 2014, pp.53.

[22] Y. Zhao, Y. Ge, "The Controller of Ball And Plate System Designed Based On FNN", Journal of Chemical and Pharmaceutical Research, vol.6, issue.6, 2014, pp. 1347-1352.

[23] K.W. Han, Y.T. Tian, Y.S. Kong, B.H. Zhao, C. Li, "Fuzzy Indirect Adaptive Control For Ball And Plate System", Kongzhi yu Juece/Control and Decision, vol.30, issue.2, 2015, pp. 303-310.

[24] M., Oravec, A. Jadlovska, "Model Predictive Control of a Ball and Plate laboratory Model", SAMI 2015 - IEEE 13th International Symposium on Applied Machine Intelligence and Informatics, 2015, pp. 165-170.

[25] A., Negash, N.P. Singh, "Position Control And Tracking Of Ball And Plate System Using Fuzzy Sliding Mode Controller", Advances in Intelligent Systems and Computing, vol.334, 2015, pp. 123- 132.

[26] J. Xiao, G. Buttazzo, "Adaptive Embedded Control for a Ball and Plate System", Proceedings of The Eighth International Conference on Adaptive and Self-Adaptive Systems and Applications IARIA, 2016, pp. 40-45.

[27] Quanser Inc., "2-DOF Ball Balancer Experiment for MATLAB/Simulink Users (Student Workbook)", 2013.

[28] Quanser Inc., "Rotary Servo Base Unit Workbook (Student Workbook)", 2011.

[29] D.J. Leith, W.E. Leithead, "Survey of Gain-Scheduling Analysis Design", International Journal of Control, vol.73, 1999, pp. 1001-1025.

[30] J. Kennedy, R.C. Eberhart, "Particles Swarm Optimization", IEEE International Conference on Neural Networks, 1995, pp. 1942–1948.

[31] R. Storn, "On the Usage of Differential Evolution for Function Optimization", Proceedings Fuzzy Information Processing Society, Biennial Conference of the North American, 1996.

[32] S. Das, P.N. Suganthan, "Differential Evolution: A Survey of the State-of-the-Art", IEEE Transactions on Evolutionary Computation, vol.15, issue.1, 2011, pp. 4-31.

BIOGRAPHIES

HALUK GOZDE received the B.Sc. degree in Electrical and Electronics Engineering from Karadeniz Technical University, Trabzon, Turkey, in 1997, and the M.Sc. and the Ph.D. degrees in Electrical and Electronics Engineering from Gazi University, Ankara, Turkey, in 2004 and 2010, respectively. Then, he is an Assoc.Prof. of the electrical and electronics engineering in National Defense University since 2016. His main research area consists of power system dynamics and control, artificial intelligence-based control methods, swarm intelligence-based optimization algorithms, autonomous mobile robots, swarm robotics and autonomous path planning algorithms.

Optic Disc Segmentation based on Template Matching and Active Contour Method

S. A. TUNCER

Abstract— **This paper proposes a hybrid method that is capable of automatically implementing the Optic Disc (OD) segmentation. In the hybrid method, two steps were performed. First, the location of the OD was determined by template matching. Second, the OD location coordinates obtained in the first stage were given as inputs to the Active Contour Method applied to complete the OD segmentation. Furthermore, as part of this study, Android based a program was developed to allow physicians the ability to independently access the proposed hybrid method results from anywhere and to add comments. Thus, the physician would be able to instantly track the patient. Performance evaluation of the proposed hybrid method was done separately for both localization and segmentation. The success of localization was confirmed on the basis of whether the determined coordinates corresponded to the OD. The segmentation process was assessed according to the parameters, as derived from a confusion matrix. The average Dice coefficient obtained for all images was 0.943, while the average values of accuracy, specificity and sensitivity parameters for all images were calculated as 0.90, 0.961 and 0.931, respectively. The final results obtained from the proposed hybrid method were checked by a physician, who observed that the OD was successfully segmented.**

Index Terms— **Active Contour, Optic Disc, Template Matching**

I. INTRODUCTION

THANKS to the advancements made in computerized techniques, preliminary diagnoses and regular diagnoses of diseases can be made using retinal images. Detection of impairments on structures, such as veins and Optic Disc (OD), in retinal images is crucial for disease diagnosis and follow-up. For example, diabetic retinopathy, age-related macular degeneration (ARMD), and glaucoma are included among the diseases able to be detected from degenerations on retinal images. The first step in the detection of these diseases is to examine the OD. In identifying abnormalities on the OD, false diagnoses can be made due to physical-related issues involving the physician, such as fatigue. Automatic systems are therefore needed to reduce the error rate and the workload of physicians and to speed up the identification of parameters for diagnosis of the disease. The development and use of

automated systems will serve to significantly reduce the workload of the healthcare personnel who are responsible for visually examining and analyzing very large volumes of data [1].

The OD is the part of the optic nerve that is attached to the retina. It is usually located in the middle of the eye and has a yellowish, bright and round appearance, and nerve heads. The OD is not light sensing and is positioned in an area where the blood vessels pass through. In retinal images, the average OD diameter is 1.75 mm in the vertical and 1.5 mm in the horizontal [2]. The OD structure on the retina is shown in Figure.1.
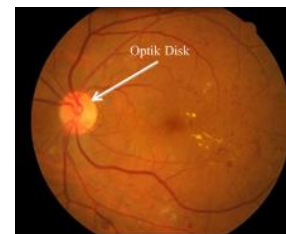
Fig.1. OD in Retinal image

OD segmentation from retinal images is the first step in diagnosing and following retinal diseases. In this paper, a hybrid method for performing OD segmentation is proposed to detect and follow retinal diseases. The proposed hybrid method involves 2 steps. In the first step, the OD location is determined using the template matching method. In the second step, OD segmentation is performed by submitting the location information of each OD as input for the Active Contour Method (ACM). In addition, a web-based system was developed to allow physicians the capability of following-up the patient in the mobile environment. An Android-based interface was created to access this developed system and obtain segmentation results.

This paper shall serve to contribute the following to the literature:

-The ACM, which is a semi-automatic method, was converted to a fully automatic method using template matching. In this way, the OD is more easily segmented.

-An android-based structure was developed to evaluate the disease. With this structure, the physician can independently access the proposed hybrid method results from anywhere and add comments.

This paper, whose focus is on optic segmentation, is organized in 6 sections, with the section above being the first.

SEDA ARSLAN TUNCER, is with Department of Software Engineering University of Firat, Elazig, Turkey, (e-mail: satuncer@firat.edu.tr).

https://orcid.org/0000-0001-6472-8306

The second section presents a literature review on OD segmentation. In the third section, the properties of the retinal image to be used in practice are given, and the process of conversion to a fully automatic method of the ACM and the proposed hybrid system for OD segmentation are presented. Section 5 provides an explanation of the proposed Android system framework. In Section 6, obtained results are discussed. And finally, the advantages of the proposed hybrid method are mentioned and talked about future work.

II. RELATED WORKS

In the literature, there are a number of pixel-based or model-based studies on the segmentation of OD on retinal images [3, 4, 5]. When examining the research conducted on determining the OD location, it was observed that many image processing techniques, such as morphological operations, edge extraction filters, segmentation, Hough transform, and thresholding, are used. Studies related to this subject have largely focused on determining the location or edge segmentation of the OD in the retinal image. In determining the location, the aim is to identify the OD center and the OD boundary with minimum error, while in the segmentation process; the challenge is distinguishing the OD from other structures in the eye.

A study by Li et al. converted retinal images to a pixel-based gray level, where regions with bright pixels were identified as candidate clusters, and these clusters were then determined using a model-based method best suited for the OD [4]. In another study using color morphology, vessels were removed from the image using the automatically activated ACM, and the image was made ready for analysis [5]. A study focusing on diagnosing glaucoma disease, detection of the OD was performed by automatic thresholding after the noise was eliminated, and the brightness was normalized for automatic segmentation [6]. In [7], the retinal image was first converted to gray scale using the Basic Component Analysis method. The Stochastic Watershed algorithm was then applied to this transformed image to perform OD localization. In 110 eye images, the OD location was determined with an accuracy of 86.89%. In [8], authors conducted a study where they used the Haar Wavelet Transformation method to determine the location of the OD over the green color channel, and the edge extraction was performed by applying the Hausdorff-based matching method. In this study, the success rate was obtained 93% over 40 images. In [9], authors obtained edges of ODs by applying the Sobel Edge Removal Filter to the retinal image. In the same study, by applying the Circular Hough Transformation on this extracted image, they were able to detect the OD location, and a 97% success rate was achieved over 40 images. The literature shows that hybrid methods have been proposed for automatic segmentation of the OD [10,11,12]. For example, In [10] was developed a fully automated method using the region growing method and the L1 minimization algorithm, which are semi-automatic methods for obtaining OD segmentation. With the proposed hybrid method in Tuncer's study, there was 92% and 87% similarity according to the similarity indices of Dice and Jaccard, respectively. In [11], authors segmented the OD using

the hybrid vessel phase portrait analysis, where the results showed that true negatives and true positives were obtained in 94.67 and 98.13% of cases, respectively. In [12], OD was segmented with 98.67% success using a hybrid approach involving the ACM and ellipse fit method. In [13], OD was determined by histogram matching technique to identify the presence of pathological regions. Success rates for used data sets were 100%, 98.9%, and 91.36% for the datasets, respectively. In [14], authors proposed an alternative technique for automatic segmentation of OD. The technique is based on a circular transformation which was implemented to detect circular boundary and colour variation. Technique was applied to the three data sets. Accuracy for data sets was 98.77%, 97.5% and 99.75%, respectively. In [15], the OD location was first determined by the brightness-based method. Then supervised descent method was used to segment the optical disc. The proposed method has compared with the circular Hough transform, the directional matched filtering and level-sets method, the principal component analysis and mathematical morphology based method, the sliding band filter method, the snake-based contour refinement method and the super pixel-based classification method. The results showed that the proposed approach outperformed the existing methods. In [16], authors have presented a novel method to automatically segment OD in fundus images based on variational model with multiple energies. Firstly, to localize the OD center has used a sparse coding based technique. Next, OD segmentation has been regarded as an energy minimization problem, and a variational model integrating three energy terms has been proposed to evolve the curve to the OD boundary. Experimental results demonstrate that the proposed method outperforms the state-of-the art techniques. In [17], a fully automatic method for the OD segmentation in retinal images has proposed. This method is a multiresolution sliding band filter (SBF). An average overlapping area of 83%, 89% and 85% has achieved for the images in three datasets, respectively. In [18] was developed and trained a convolutional neural network to automatically and simultaneously segment optic disc, fovea and blood vessels. The results shown that, OD were segmented with 92.68% accuracy. In [19], an entropy-based method was proposed to determine the OD location. Five data sets were used and the accuracy was determined between 75% and 100%.

III. MATERIAL

The retinal images used in this paper were obtained from Firat University Department of Ophthalmology retina database. A total of 40 retinal images were used for segmentation, with the images being in 45 ° FOV and jpeg format. Both healthy and diseased images were randomly selected from the data on the right and left eyes. The resolution of each image was 565 × 584 pixels.

IV. PROPOSED HYBRID METHOD

The hybrid method for fully automated OD segmentation procedure that was proposed in this paper is shown in Figure 2. To carry out the hybrid method, first, pre-processing was

done for each image, such as filtering and gamma conversion. Next, the template matching method was applied to determine OD location. The obtained location information was then used as input to the ACM for segmentation. Lastly, a performance evaluation was conducted to determine the accuracy of the OD segmentation.
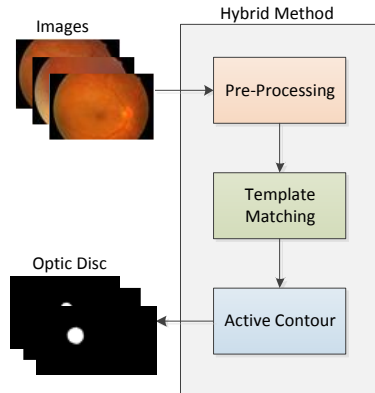

Fig.2. Proposed Hybrid Method for OD segmentation

A. Template Matching

Template Matching is a method for searching and finding the location of a template image in a larger image. The template image is routed over the large image and similarity is measured by mapping on each pixel. The first step for the detection of pathological areas in the OD is segmentation. For this, template matching algorithm is applied after preprocessing step. In the proposed hybrid system, five retinal images were used as templates to identify the OD. For the template, three histograms were created, each corresponding to a color component. A histogram is a graph that shows the number of pixels at different density values in an image. An median filter was applied to the retinal images to reduce the noisy effect in the images. Then, a window with an OD size of 80 x 80 pixels was used to remove the OD from each retinal image. In the next step, the histogram of each color component was obtained by separating each OD color component (red, blue and green). Finally, for all retinal image samples, the average histogram of each color component was used as a template and the OD location was determined. The process for determining the OD location can be explained in detail as follows.

Each moving window channel (red, blue and green) is separated and the histogram of each channel is obtained. Then, the correlation between the histogram of each channel in the moving window and the histogram of the corresponding channel in the template is calculated. The function used for the correlation between two histograms is expressed as in equation 1.

$$c = \frac{1}{(1+\sum_i (a_i-b_i)^2)} \qquad (1)$$

where a and b are the two histograms for which we want to calculate the correlation. The correlation used to determine template and OD similarity and relationship of force takes value at 0-1 interval. If two histograms (a and b) are completely similar, then c is equal to 1 otherwise 0. Figure 3 shows a histogram example of one of the data used as template.
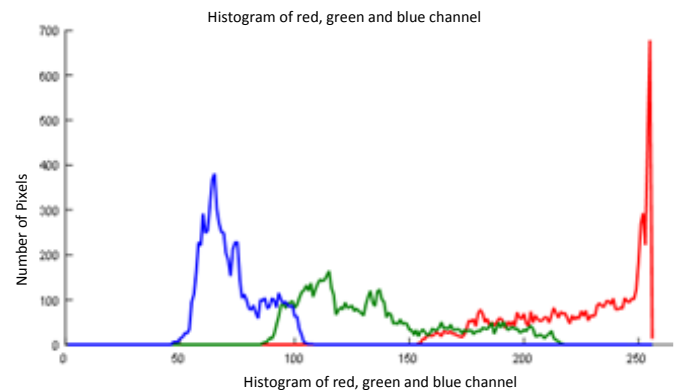

Fig.3 r, g, b histogram values for an image used as a template

For each moving window, we obtain three values as the results of correlation between the histograms. The result of histograms matching is computed as the weighted sum of the three obtained values:

$$C(i, j) = t_r x c_r + t_g x c_g + t_b x c_b \qquad (2)$$

where (i,j) is the center of moving window. c_r, c_g, and c_b are the results of correlation for three channels (red, green, and blue) and t_r, t_g, and t_b are weights used for each channel. In Equation (2), we can use different weights for c_r, c_g, and c_b. The green channel has the highest weight because the contrast of the green channel is higher than red and blue channels [27,13]. In some retinal images, blue channel is noisy; therefore, to decrease the effect of blue channel on our localizing method, we determine the lowest weight for blue channel. The best weights that result high accuracy rate for OD localizing method are t_r=0.5, t_g=2, and t_b=1. To localize the center of OD, we apply thresholding on the correlation function $C(i,j)$. For finding the best threshold, we did a global scanning of different values and the best equation to determine the threshold (T_h) was obtained as follows.

$$T_h = 0.5 * max(C) \qquad (3)$$

where $max(C)$ is the element of C with the maximum value. Therefore, the threshold value for each image is half of the maximum value of the correlation function. The center of gravity of the binary image obtained from thresholding is considered as the center of OD. Three retina images used to remove the OD histograms in the data set are shown in figure.4.

The specified OD coordinates are marked with the x symbol. Coordinate information of OD is given as an input to the Active Contour Method which is a semi-automatic method. Thus, thanks to the proposed hybrid method, region of interest, namely the OD, is obtained by a fully automatic method.
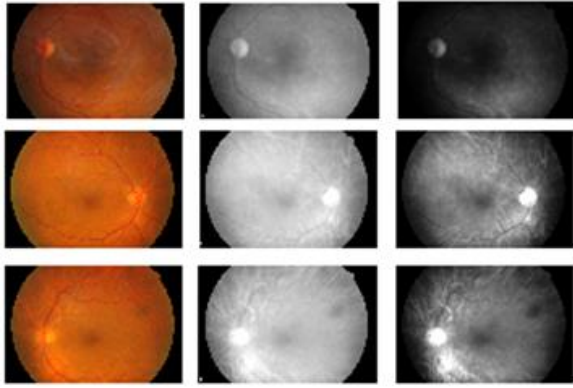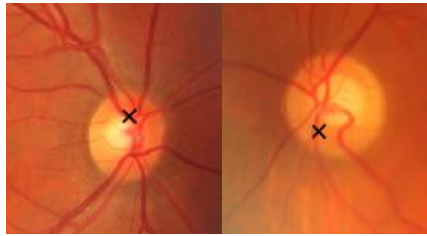
Fig.4. The three retinal images used as templates

Fig.5 OD coordinates determined by template matching

B. Active Contour Method

The Active Contour Model (ACM) is a method used to segment the boundaries of an object on an image from other areas. It is the most commonly used model-based method for deformable models. In deformable models, segmentation is done by internal, external and image forces. In order to define the boundary of an OD, the closed curves must first be positioned close to the desired boundary. Then the number of curves is formed from the number of iterations. Internal forces ensure that the curve remains smooth throughout the deformation, while external forces guarantee that the curve is kept at a local minimum. Image forces ensure the curve is oriented towards apparent points like edges in the retinal image. The ACM is a method for semi-automatic segmentation by minimizing the energy function through iteration [20]. The path to form the curve is determined by minimizing the energy of the starting point selected by the user as being close to the optic boundary [21]. In other words, a curve is drawn inside or outside the OD; iterations are performed so that the curve takes the shape of the OD and segmentation is achieved by moving the curve by considering energy minimization [21, 22].

$$E(v) = E_{img}(\vec{v}) + E_{int}(\vec{v}) + E_{ext}(\vec{v}) \tag{4}$$

where E_{int} indicates the internal force caused by snakes. It is expressed by the tension and flexibility deformation of the contour. E_{img} represents the image force, while E_{ext} is the external force [23].

At the point where all forces are in balance, the position of ACM corresponds to the overall local minimum. In other words, the equation determines four boundary regions and minimizes the energy through orientation by external and image forces. The image energy equation in the ACM algorithm is given as follows:

$$E_{img}(\vec{v}) = -\int_0^1 P(\vec{v}(s,t))\,ds \tag{5}$$

Where, $P(\vec{v}(s,t))$ shifts the ACM algorithm to the edges and is the magnitude of the image gradient [23].

$\nabla I(\vec{v}(s,t))$ prevents the algorithm moving towards lower-image energy positions by smoothing the image and removing insignificant points. Furthermore, it orients the algorithm to more apparent details [23].

$$P(\vec{v}(s,t)) = |\nabla I(\vec{v}(s,t))| \tag{6}$$

$$E_{int}(\vec{v}) = \frac{1}{2}\int_0^1 \alpha(s)\left|\frac{\partial \vec{v}(s,t)}{\partial s}\right|^2 + \beta(s)\left|\frac{\partial^2 \vec{v}(s,t)}{\partial s^2}\right|^2 ds \tag{7}$$

where $\alpha(s)$ and $\beta(s)$ are the functions adjusting the stiffness and tension of the ACM algorithm. Contour strain is controlled by $\alpha(s)$, while tension is controlled by $\beta(s)$. Tension constraints are performed by the terms in the first line and make the ACM algorithm behave like a membrane. For stiffness, second-order terms are used to constrain the ACM algorithm to move like a thin layer. Thus, the balance of energies is achieved [23].

$$E_{ext}(\vec{v}) = \int_0^1 P(\vec{v}(s))\,ds \tag{8}$$

The external force equation orients the algorithm image details for lines and edges in the retinal image [23].

$$E(\vec{v}) = -\int_0^1 P(\vec{v}(s,t))\,ds + \frac{1}{2}\int_0^1 \alpha(s)\left|\frac{\partial \vec{v}(s,t)}{\partial s}\right|^2 + \beta(s)\left|\frac{\partial^2 \vec{v}(s,t)}{\partial s^2}\right|^2 ds \tag{9}$$

This indicates the overall energy function of the ACM algorithm [23].

$$E(\vec{v}) = \int |\nabla I(v)|^2 ds + \alpha(s)\int |(v_s)|^2 ds + \beta(s)\int |(v_{ss})|^2 ds \tag{10}$$

where $\alpha(s)$ and $\beta(s)$ are weight parameters, v_s is the first derivative with respect to curve parameter s, and the v_{ss} parameter is the second derivative. In accordance with these equations, when the curve reaches the OD boundaries where high image gradients are present, the progression stops and the OD boundaries are determined [24–26].

C. Performance Evaluation

In the performance measurement of the proposed hybrid method, both OD localization and segmentation were evaluated separately. Whether localization was correct, was evaluated by template matching. Knowledge of a specialist physician was needed to evaluate the OD locations obtained by template matching. According to the specialist physician, all positions obtained by the template matching method were within the OD area, and the success rate was 100%. In other

words, the OD locations obtained from forty retinal images were correctly determined.

For segmentation of the OD, the positional information obtained by the template matching method was given as an input to the ACM. Then, the boundaries of the OD were determined by running the ACM. Expert physician skills were consulted to show that the segmented OD area was correctly determined. For each image, the OD areas were evaluated by the physician using the OD location and dimensions determined by the Active Contour. The Dice coefficient, accuracy, specificity and sensitivity were parameters used for performance evaluation. As a result of the process mentioned above, the OD obtained from a retinal image is shown in Figure 6.
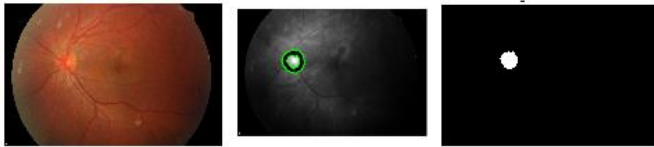

Fig.6. OD results segmented by using the ACM

The representative demonstration in Figure 7 was used to evaluate the OD area obtained manually by the physician from retinal images against the OD areas obtained by the ACM. The area A indicates the area segmented by the ACM, while the area M shows the actual OD area obtained by the physician. The intersecting area shows the OD area correctly determined by the applied method. The area of $A \cap M$ is indicated by True Positive (TP), $A-M$ False Positive and $M-A$ False Negative. The OD area obtained by the ACM was first evaluated using the Dice coefficient. Furthermore, the accuracy, specificity and sensitivity parameters defined by the confusion matrix can be evaluated whether or not the OD area was correctly determined.
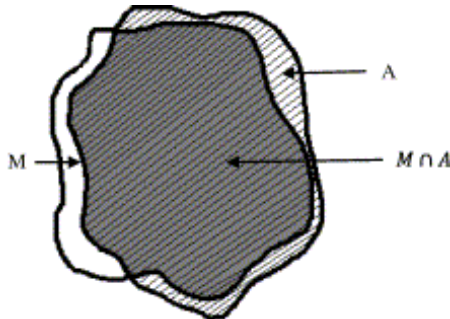
Fig.7. Representative OD area for segmentation

In addition to the Dice coefficient, the confusion matrix shown in Table 1 can be used to evaluate the performance of segmentation areas. In the confusion matrix, the rows show the OD areas determined by the physician and the columns indicate the OD areas determined by the Active Contour. The parameters *TP*, *TN*, *FP*, *FN* given in the matrix are their values in pixels.

TABLE I
CONFUSION MATRIX

		Actual Value (as confirmed by experiment)	
		Positives	Negatives
Predicted Value (predicted by the test)	Positives	TP True Positive	FP False Positive
	Negatives	FN False Negative	TN True Negative

The most popular and simple parameters used to measure the performance of models in published literature are accuracy, specificity and sensitivity. Equations 11, 12 and 13 are used for the accuracy of the correctly determined OD area in terms of pixels.

$$Accuracy = \frac{TP+TN}{TP+TN+FP+FN} \tag{11}$$

The specificity given in Equation 12 is the ratio of the correctly determined pixel number to the OD area determined by the physician.

$$Specificity = \frac{TP}{TP+TN} \tag{12}$$

It is the ratio of the number of correctly classified positive samples to the overall number of positive samples.

$$Sensitivity = \frac{TP}{TP+FN} \tag{13}$$

Figure 8 shows accuracy, sensitivity and specificity changes obtained for forty retinal images.

Fig.8. Accuracy, sensitivity and specificity values

Fig.9. Dice coefficient for each retinal image

The criteria of accuracy, specificity and sensitivity are not enough to obtain a meaningful comparison result. Therefore, it is also necessary to determine the Dice coefficient, known as the f-criterion. The Dice Similarity Coefficient takes a value between 0 and 1. A value close to 1 means that the result is closest to that of the physician. According to published literature, a Dice coefficient greater than 0.7 indicates that the segmentati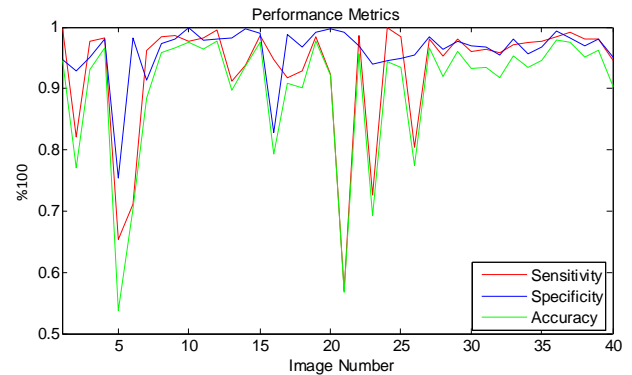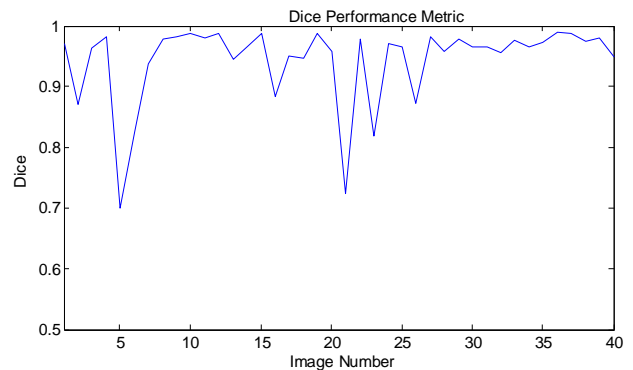on process is acceptable. Equation 14 shows the mathematical expression of the Dice coefficient, while Figure 9 shows the Dice coefficient change for fourth retinal images.

V. PROPOSED ANDROID SYSTEM FRAMEWORK

The Android-based system developed for the physician to monitor each patient using a mobile phone is shown in Figure 10. First, the OD is segmented by template matching and the Active Contour for each retinal image on the server. The OD sizes obtained manually and automatically are recorded in a database with the patient ID number. The physician can monitor the results of the OD by remotely connecting to the database with a mobile phone. The pseudo code for the application developed for this purpose is shown in Algorithm 1. The physician can link to the database on the internet (using a URL) with a username and password. If the connection is valid, the physician can access the results using the patient's ID number and add comments about the patient.

Figure 11 shows the developed Android-based interface and the results obtained from the database.

Algorithm.1 Pseudo code of Android-based developed application

```
// Connecting to the database
public class Connect {
        private String url="……..//";
        private String user;
        private String passwd;
        Connection myCon;
        PreparedStatement pstatment;
        ResultSet result;
 public Connect(String url,String port,String user,String passwd){
         this.url+=url+port;
        this.user=user;
        this.passwd=passwd;
        connection();
}
// Checking the connection to the database
private void connection() {     }
// Checking a valid ID number
public boolean isID(String fromURL,String id){
}
// Obtaining the results of the ID number from the database
public String getData(String columName,String fromURL,String id){
}
// Saving physician comments to database
public void setMessage(String columName,String fromURL,String id,String message){
}
```
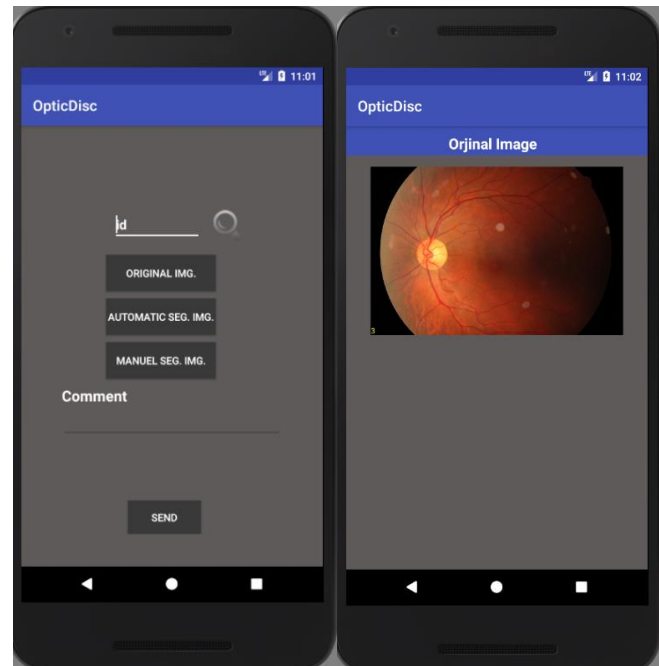
Fig.10. Android interface and a sample retinal image
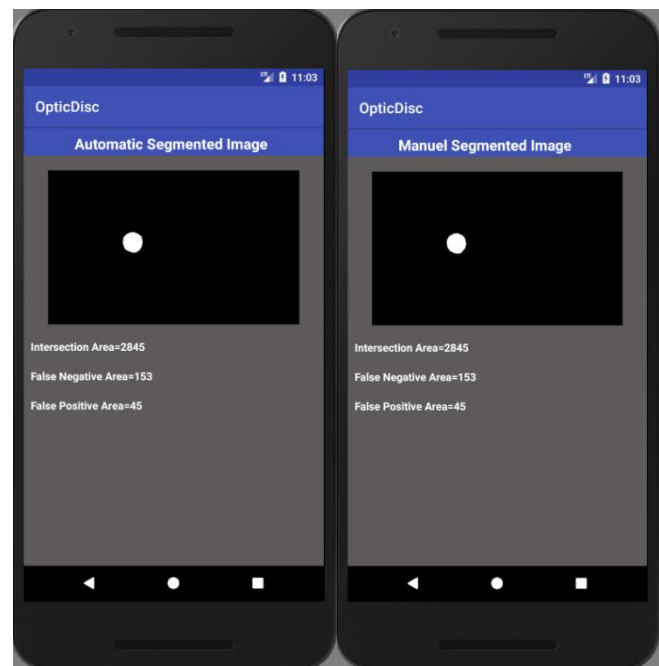
Fig.11. The results obtained from the database with the android system.

VI. DISCUSSION

OD segmentation in retinal images is the first step in the diagnosis of diseases such as diabetic retinopathy, age-related macular degeneration, and glaucoma. The correct and precise segmentation of the OD will increase the correct diagnosis. In this paper, a hybrid method based on active contour and template matching is proposed for fully automatic segmentation of OD. According to the results obtained, the Dice coefficient

was determined to be at the limit of its values in the 4th and 15th retinal images. The average Dice coefficient obtained for all images was 0.9432. Furthermore, the accuracy, specificity and sensitivity parameters were also determined to be less than 0.7 for the 4th and 15th images. The average values of these parameters for all images were calculated to be 0.90, 0.961 and 0.931, respectively. As a result, because the average values of the parameters obtained by the Active Contour were calculated to be larger than 0.7, the segmentation process was deemed to be acceptable. The OD segmentation results and literature comparisons are shown in Table 2.

TABLE.II
OD SEGMENTATION RESULTS and LITERATURE COMPARISONS

Ref.No.	Methods	Success Rates
[7]	Component Analysis Method, Stochastic Watershed Algorithm	A=86.89%
[8]	Haar Wavelet Transformation, Hausdorff Based Matching	A=93%
[9]	Sobel Edge Removal Filter, Hough Transformation	A=97%
[10]	L1 Minimization, Region Growing	D=92% J=87%
[11]	Hybrid Vessel Phase Portrait	TN=94.67% TP=98.13%
[12]	Active Contour, Ellipse Fit Method	A=98.67%
[13]	Histogram Matching	A=100% A=98.9% A=91.36%
[14]	Circular Transformation	A=98.77% A=97.5% A= 99.75%
[15]	Brighness Based Method, Supervised Descent Method	O=89.44%
[16]	Sparse Coding Technique, Variotional model with multiple Energies	O=91% O=90% O=92%
[17]	Multiresolution Sliding Band Filter	O=89% A=99.5%
[18]	Convolutional Neural Network	A=92.68%
[19]	Sliding Window Technique	A_{min}=75% A_{max}=100%
The Proposed Method	**Template Matching, Active Contour**	**A=90% S=96.1% Se=93.1% D=94.32%**

O:Overlapping, A: Accuracy, S:Specificity, Se:Sensitivity, D:Dice, J:Jaccard

Different applied methods to OD segmentation were presented in Table.2. Some methods used a small dataset, while some used different datasets to train and test the algorithm. Methods were tested on both normal retinal images and on pathological images. The images in the data sets have different properties, so it may not be right to compare these methods with each other. Roughly, if we compare the proposed method to the other methods, the performance metrics are acceptable average level.

VII. CONCLUSION

In preliminary steps for the detection of many diseases, such as glaucoma and diabetic retinopathy, locating the OD is important in diagnosing the disease. In this paper, OD segmentation was performed from the retinal images obtained from Firat University Ophthalmology Department. For this, a hybrid method was used to separate the OD from other areas of the eye. In this method, the OD location was determined by using the template matching algorithm. The obtained location information was used as input to the ACM, which is a semi-automated method. Thus, the ACM was converted to a fully automated method and the OD was segmented. Furthermore, An Android-based interface was prepared so that the physician could independently access the proposed hybrid method results from anywhere and add some comments. In the future, we intend to include the disease detection module to the android software interface. As a result, we think that the proposed software system can be used as a building block in developing an automated system for early detection of diseases.

ACKNOWLEDGMENT

REFERENCES

[1] Z. Yavuz, C. Ikibas, U. Şevik, C. Köse, "Retinal Görüntülerde Optik Diskin Otomatik Olarak Çıkartılması İçin Bir Yöntem", 5th International Advanced Technologies Symposium, Karabük, Türkiye, 13-15 Mayıs 2009, pp.8.
[2] J. Kaur, H.P. Sinha, "Automated localisation of optic disc and macula from fundus images", International Journal of Advanced Research in Computer Science and Software Engineering, 2(4), 2012, pp.242-249.
[3] C. İkibaş, 1Retinal İmgelerde Optik Disk ve Makulanın Tespiti ve Değerlendirilmesi", PhD thesis, Karadeniz Teknik Üniversitesi, 2012.
[4] H. Li, O. Chutatape, "Automatic location of optic disc in retinal images", International Conference on Image Processing, Thessaloniki, Greece, 2001, pp. 837– 840.
[5] A. Osareh, M. Mirmehdi, B. Thomas, R. Markham, "Colour Morphology and Snakes for Optic Disc Localisation", 16th IEEE Int. Conf. Pattern Recognition, vol.1, 2002, pp. 743–746.
[6] A. Ahmed, B. Ritambhar, R. Kaamran, L. Vasudevan, ''Optic Disc and Optic Cup Segmentation Methodologies for Glaucoma Image Detection: A Survey", Journal of Ophthalmology, Article ID 180972, 2015, pp.28.
[7] S. Morales, V. Naranjo J. Angulo M. Alcañiz, "Automatic Detection of Optic Disc Based on PCA and Mathematical Morphology", IEEE Transactions on Medical Imaging, 32(4), 2013, pp. 786-796.
[8] M. Lalonde, M. Beaulieu, L. Gagnon, "Fast and robust optic disc detection using pyramidal decomposition and hausdorff-based template matching", Medical Imaging, IEEE Transactions, 20(11), 2001, pp. 1193 – 1200.

[9]   T. Chaichana, S. Yoowattana, et al, '"Edge detection of the optic disc in retinal images based on identification of a round shape", International Symposium Communications and Information Technologies, 2008, pp. 670 –674.

[10] S.A. Tuncer, T. Selçuk M. Parlak, A. Alkan, '"Hybrid approach optic disc segmentation for retinal images", International Artificial Intelligence and Data Processing Symposium (IDAP), 2017, pp.1-6.

[11] N. Muangnak, P. Aimmanee, S. Makhanov, "Automatic optic disc detection in retinal images using hybrid vessel phase portrait analysis",Med Biol Eng Comput., 56(4), 2018, pp.583-598.

[12] R. Fulonga L. Wei, Y. Jinzhua et.al, "Automatic optic disc localization and segmentation in retinal images by a line operator and level sets", Technology and Health Care, 24(2), 2016, pp. S767-S776.

[13] A. Dehghani, H. A. Moghaddam, M. S. Moin, "Optic disc localization in retinal images using histogram matching", EURASIP Journal on Image and Video Processing, 2012, 2012(19).

[14] S. Lu, "Accurate and efficient optic disc detection and segmentation by a circular transformation", IEEE Transactions on Medical Imaging, 30(12), 2011, pp. 2126–2133.

[15] A. Li, Z. Niu, J. Cheng, et.al., "Learning supervised descent directions for optic disc segmentation", Neurocomputing, 275, 2018, pp.350-357.

[16] B. Dai, X. Wu, W. Bu, "Optic disc segmentation based on variational model with multiple energies", Pattern Recognition, 64, 2017, pp. 226-235.

[17] B. Dashtbozorg, A. Mendonça, M.A. Campilho, "Optic disc segmentation using the sliding band filter", Computers in Biology and Medicine, 56, 2015,pp. 1-12.

[18] J. H. Tan, U.R. Acharya, S.V. Bhandary et. al. "Segmentation of optic disc, fovea and retinal vasculature using a single convolutional neural network", Journal of Computational Science, 20, 2017, pp.70-79.

[19] L.A. Muhammed, "Localizing Optic Disc in Retinal Image Automatically with Entropy Based Algorithm", International Journal of Biomedical Imaging, Article ID 2815163, 2018, pp.7.

[20] T.F. Chan, L.A. Vese, "Active contours without edges", IEEE Transactions on Image Processing, 10(2), 2001.

[21] M. Kass, A.Witkin, D. Terzopoulos, "Snakes: active contour models", International Journal of Computer Vision, 1, 1988, pp.321-331.

[22] P.P.R. Filho, P.C. Cortez, A.C. da S. Barros, et.al., "Novel Adaptive Balloon Active Contour Method based on internal force for image segmentation A systematic evaluation on synthetic and real images", Expert Systems with Applications, 41, 2014, pp.7707–7721.

[23] T.F. Chan, L.A. Vese, "Active contours without edges", IEEE Transactions on Image Processing, 10(2), 2001.

[24] E. Isıkcı, D.G. Duru, "Multiple Skleroz Manyetik Rezonans Görüntülerinde Aktif Kontur Modeli ile Lezyon Tespiti", Tıp Teknolojileri Ulusal Kongresi, Muğla,Türkiye, 2015.

[25] S.A. Tuncer, A. Alkan, "Segmentation of thyroid nodules with K-means algorithm on mobile devices", 16th IEEE International Symposium on Computational Intelligence and Informatics, Budapest, Hungary, 2015, pp. 345-348.

[26] A. Alkan, S.A. Tuncer, M. Gunay, "Comparative MR image analysis for thyroid nodule detection and quantification", Measurement, 47, 2014, pp. 861-868.

[27] M. Niemeijer, B. van Ginneken, F. Ter Haar et.al., "Automatic detection of the optic disc, fovea and vascular arch in digital color photographs of the retina", Proceedings of the British Machine Vision Conference 2005, 109-118.

BIOGRAPHIES

Seda ARSLAN TUNCER was born in Kahramanmaraş, Turkey 1983. She received the B.S. and M.S. degree in computer engineering from the Firat University in Elazig 2005 and 2008 respectively. She received the Ph.D. degrees in electrical-electronics engineering from Kahramanmaras Sutcu Imam University in 2014.   From 2010 to 2014, she was a lecturer at department of informatics, Firat University, Elazig, Turkey. Since 2014, she has been an Assistant Professor at software engineering. Her research interest include biomedical, image and signal processing, embedded systems, random numbers generators.

Real-time Implementation of Image Based PLC Control for a Robotic Platform

K. K. AYTEN and O. KURNAZ

Abstract—**In this study, image based real-time control of a linear robotic platform was performed. This robotic platform is used to determine the location of the mushroom and to direct the linear platform to the detected position in real time with PLC control. Haar-Cascade classifier was used to detect mushroom position and Visual Studio C # .NET platform was used to test the Cascade classifier and write other evaluation codes. One of the most important outputs of this work is to determine the actual position in the global coordinate from the pixel-based location of the object in the image using an ordinary USB camera or built-in camera. Calibration technique was used for this determination.**

Index Terms—**Image processing, Object tracking, Trajectory control, Automation, Haar-Cascade Classifier, Camera calibration, PLC control.**

I. INTRODUCTION

AUTONOMOUS SYSTEMS, which have emerged as a result of the developments in technology, have become applications that are used in many areas like production, agriculture, construction and health. The concept of Industry 1.0 has taken its place in the literature with the invention of steam machines and then the concept of Industry 2.0 has emerged with the use of electricity in production. With the combination of electronic devices and software technologies, production systems have become autonomous day by day and at the end of this period, Industry 3.0 has begun. After the concept of Industry 3.0, the technology has progressed very rapidly and concepts such as cloud technologies, internet of objects, cyber physical systems have started to be discussed more. As a result of this, Industry 4.0 concept which has started to enter into every area of our life in a fast way has emerged. Hence, the production quality is steadily increasing,

and many faulty production details that people cannot realize in production stages are easily defined by autonomous systems. The agricultural sector is one of the areas where the autonomous production concept is widely used. In this sector, the production quality varies depending on the differences in the growing conditions of the products during the production stages. Considering the growing conditions, one of the products that require a difficult process of production is the mushroom [1].

In the literature, there are many technology-related studies on the aforementioned agricultural products. For example, in [2], described a new method in order to separate tomato pictures from each other by classifying them according to their maturity. In another study [3], necessary image processing techniques were applied after the images of hazelnut fruit were obtained from the camera. Then, the size and area data of the hazelnuts were calculated with the help of these techniques and these data were evaluated and divided into 3 classes: small, medium and large. In [4], introduced a mobile robot developed in order to ensure the quality control of agricultural products. In this project, Aforge.Net library is used with C # interface and the robot has 2 cameras. The first of these helps to display the path followed by the robot during the movement towards the location of the product. The other camera provides a better viewing and crop quality control by applying the necessary filtering processes for the detected product. In [5], described the application of the visual feedback control system in the robots used for harvesting. The movements of the fruits were analyzed in the image plane and along the optical axis of the camera. In [6], described a harvest robot with an image-based architecture designed for product detection and collection. In [7], discussed the design and simultaneous simulation problems for tomato harvest robots. In [8], have implemented a real-time product matching application with high accuracy. In [9], described fresh tomato harvesting robot design and testing works. In their study, tomatoes, which are determined grown up were collected by a mobile moving platform and a robot manipulator on it. In [10], mentioned the image processing methods to perform autonomous harvesting of the products. The mushroom was used as a sample product. The identification of the mushroom images taken from the image systems is done with the Support Vector Machine (SVM). After taking the necessary morphological processes on the mushroom picture, the feature extraction and evaluation problem of the mushroom growing is performed with SIFT. In the final stage, the mushroom evaluated is classified by the

KAĞAN KORAY AYTEN, is with Department of Electrical Engineering University of Erzurum Technical University, Erzurum, Turkey, (e-mail: kagan.koray@erzurum.edu.tr).

https://orcid.org/0000-0002-8933-612X

OĞUZHAN KURNAZ, is with Department of Mechatronics Engineering University of Bursa Technical University, (e-mail: oguzhan.kurnaz@btu.edu.tr).

https://orcid.org/0000-0002-4595-8031

SVM method. Apart from agricultural applications, there are other areas where image processing techniques are applied. In [11], described the simulation of the movement of robotic arms to movement of human arm by real-time image processing. In another study [12], suggestions for the solution of the problem of human detection, which may be needed in studies using intelligent systems, surveillance applications and advanced robots are presented and the results are evaluated with numerical data. In [13], Pfinder system (person finder) is a real-time system that enables people to detect and monitor their behaviour.

The motivations we get from the studies and the results, in this study, the design and implementation of an image based linear robotics platform was made. In this study, the robotic mushroom picking system was used to determine the location of the product in the case and to direct the linear actuator to the position where the product was determined. Image processing methods will be used to detect mushroom. The determination of the product as the mushroom is carried out by Haar-Cascade classifier which is one of the image processing object detection methods. Visual Studio C # .NET platform was used to test the Cascade classifier and write other evaluation codes. With the classifier used, the product will be detected and the mushroom will be monitored from the camera. While tracking the mushroom, the position information of the mushroom followed up at the same time will be sent to the PLC simultaneously with the help of camera calibration method. These position information sent to the PLC will be evaluated and the coordinates obtained as a result of this evaluation will be sent to the stepper motor drivers by PLC. At the last part of this, with the help of motors, drivers and encoders ensured that the linear actuator is transferred to the position in this coordinate.

II. MATERIALS AND METHODS

Robotic platform is an autonomous system that enables the detection of mushroom and location information. In this system, the identification of the mushroom and the location of it is realized by means of image processing techniques. Haar-Cascade classifier was used to determine the location of the mushroom. The XML file will then be created for use in the classifier training and software codes. Then the camera will be calibrated and the position information of the mushroom will be identified. The information received will then be sent to the PLC device as position information and the PLC will provide to drive the motors to the position where the mushroom is located.

A. Haar-Cascade Classifier

The Haar-Cascade Classifier is a classifier for object detection. This algorithm; The Haar features are composed of sections such as Integral Image, AdaBoost learning algorithm and Cascade classifier [14]. In this study, all steps of the classifier will be applied to determine the mushroom object. For object detection, the algorithm must be trained first. For this training, there is a need for a set of positive images that contain the object to be detected and a set of negative images without an object. First, the pictures of the mushroom object

are recorded as positive pictures. Afterwards, in these positive pictures, the areas where the mushroom object is located are introduced into the quadrature region and introduced to the classifier. The target object boundaries must be chosen in a proper way to ensure that the accuracy of object detection is high. After the target object selection is made, the classifier then initiates scanning operations by placing Haar-like features shown in Figure 1 into this quadrilateral field [14].
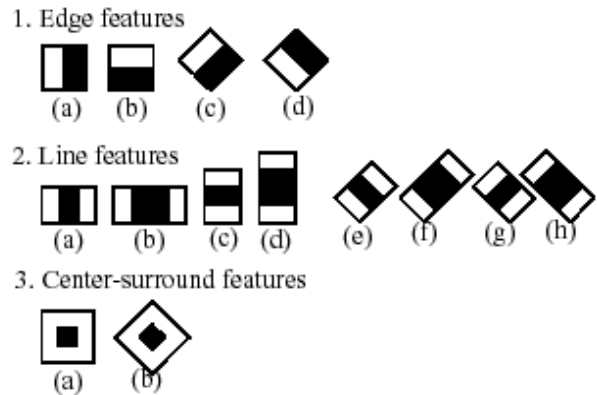

Fig.1. Haar-like features

After each feature is inserted, the sum of the values of the remaining pixels in the black and white areas is found. Then, as a result of the difference between the values obtained from this black region and the white region, the density of the feature is calculated in Equation 1.

$$f(x) = \sum_{BlackArea}(Density) - \sum_{WhiteArea}(Density) \qquad (1)$$

The density of the feature in the equation indicated above is also considered to be a weak classifier. In the next step, these weak classifiers are collected according to a particular formulation, such as in Equation 2, and strong classifiers are obtained. In the Equation 2, the use of features of weak classifiers will form a strong classifier.

$$F(x) = a_1 f_1(x) + a_2 f_2(x) + a_3 f_3(x) + \ldots .. \qquad (2)$$

In this equation $f_n(x)$ is considered as weak classifier, and F(x) as strong classifier. In the last step of the algorithm, the cascade classifier shown in Figure 2 is obtained with the successive application of these strong classifiers. Each $C_1, C_2 \ldots C_N$ element is a strong classifier. In the rectangular area where the object is located, using each of the weak classifiers and applying the required formulations as in Equation 2, strong classifiers ($F(x)$ or C_N) will be obtained These strong classifiers obtained in the final stage of all these processes are applied to the image taken into the system and the detection process is performed to determine whether the object is present in the image.
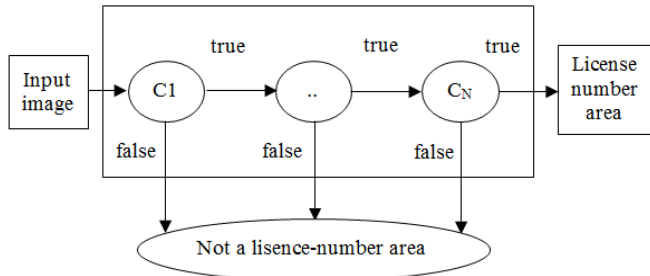
Fig. 2. Cascade Classifier

B. Camera Calibration

In this study, the camera calibration process is performed by transforming the coordinate systems shown in Figure 3 in order for the system to work properly.
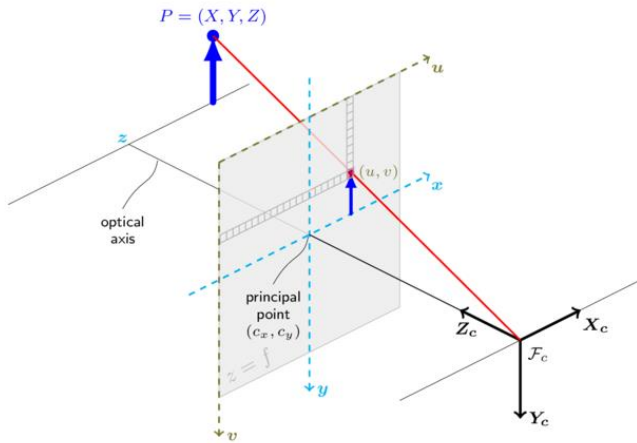

Fig. 3. Camera Calibration Coordinate System

For calibration, the transformation of the actual coordinate system to the camera coordinate system is provided by Equation 3 below.

$$\begin{pmatrix} X_C \\ Y_C \\ Z_C \end{pmatrix} = R \begin{pmatrix} X_P \\ Y_P \\ Z_P \end{pmatrix} + t \tag{3}$$

Here, R is a 3x3 dimensional rotational matrix and t is a 3x1 dimensional transformation matrix. Then the camera coordinate system is then obtained by the Equation 4 which is given below the physical coordinates in the image plane coordinate system using the pinhole camera model method [15].

$$\begin{pmatrix} x \\ y \end{pmatrix} = \begin{pmatrix} X_C/Z_C \\ Y_C/Z_C \end{pmatrix} \tag{4}$$

Including radial and tangential lens distortions, the extended physical coordinates in the picture plane coordinate system are obtained from Equation 5 below.

$$\begin{pmatrix} x_q \\ y_q \end{pmatrix} = (1 + k_1 r^2 + k_2 r^4) x \begin{pmatrix} X_C/Z_C \\ Y_C/Z_C \end{pmatrix} + \begin{pmatrix} 2p_1 xy + p_2(r^2 + 2x^2) \\ p_1(r^2 + 2y^2) + 2p_2 xy \end{pmatrix} \tag{5}$$

Here, the radial distortion coefficients k_1 and k_2, p_1 and p_2 are the tangential distortion coefficients and also $r_2 = x_2 + y_2$. Finally, the resulting extended physical coordinates are converted to pixel coordinates as follows.

$$\begin{pmatrix} u \\ v \end{pmatrix} = \begin{pmatrix} f_x x_q + u_0 \\ f_y y_q + v_0 \end{pmatrix}, \ \ f_x = f.\frac{s}{\Delta x} \ \ ve \ \ f_y = f/\Delta y \tag{6}$$

In the equation (u_0, v_0) is the basic point and is usually selected as the center of the picture. f is the focal length of the camera. s is the scale factor. Δx is the value in mm of the distance between two adjacent pixels in the horizontal axis. Δy is the value in mm of the distance between two adjacent pixels in the vertical axis. Using these equations the following equation is obtained:

$$s.p = A(R|t).P \tag{7}$$

In this equation, $p = (u, v, 1)^T$ is the homogeneous coordinate of the pixel point of the picture. $P = (X, Y, Z, 1)^T$ is the homogeneous coordinate of the point in the spatial plane. A is the matrix in which the camera's intrinsic parameters are located. $(R|t)$ is the matrix with extrinsic parameters. This equation expresses the relationship between a point in the image and a point in the space plane [16].

In accordance with the above, in the stage of performing camera calibration in the system we propose, calibration will be performed visually using the chessboard pictures with the Emgu.CV library. Then the parameters to be obtained by calibration, and using the location of the object detected in the image of the center pixel, the actual location of the object will be determined. For calibration, as shown in Figure 4, the picture of the chessboard will be displayed from different angles to the camera and the pictures will be saved. After that, the corner points of these images will be provided. After the corner points are found, intrinsic and extrinsic parameters will be found and error analysis will be performed. The position of the mushroom in the space plane will be determined by using the location information of the pixel in the centre of the image of the mushroom detected with these intrinsic and extrinsic parameters. By means of the determined position, the robot will be directed to this position.
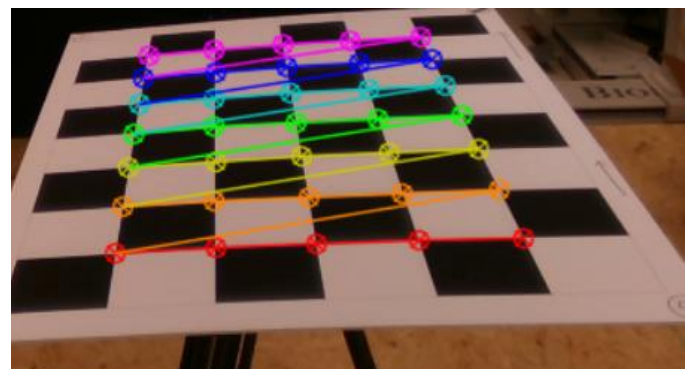

Fig. 4. Detecting the corners of the chessboard for Camera Calibration

Normally, the 3-dimensional axis is used to obtain the projection feature. To use the projection feature, the stereo camera system must be used. However, in this study, since a single camera is used for product identification and location information in the system, location calculation operations will be performed in a different way.

With this calibration process carried out in the system we recommend, focal lengths in the X and Y axis of the camera used are taken as a priority. These focal lengths are then used in the calculation of the position and the positions in the X, Y, and Z axis are obtained by adapting the formulations (Equations 8-10) used in the study for the determination of the mushroom position to our system [17].

$$d_z = (((f_x + f_y)/2) * ((dg_x + dg_y)/2))/ \\ ((mrm_x + mrm_y)/2) \qquad (8)$$

$$d_x = ((-d_z) * ((mrb_x + \left(\frac{mrm_x}{2}\right)) - (kg_x)))/(f_x) \qquad (9)$$

$$d_y = -((d_z) * ((mrb_y + \left(\frac{mrm_y}{2}\right)) - (kg_y)))/(f_y) \qquad (10)$$

where dz is the position on the Z axis, dy is the position on the Y axis, dx is the position on the X axis, also f_x, f_y are the focal lengths of camera on the X and Y axis, respectively. mgb_x, mgb_y are actual horizontal and vertical length of mushroom, respectively. mrb_x, mrb_y are horizontal and vertical length of the image plane of mushroom, respectively. $mrbn_x, mrbn_y$ are the value of the starting point in the image plane of the mushroom on the X and Y axis, respectively. kg_x, kg_y are the length of the image which is taken from the camera on the X and the Y axis, respectively.

III.   HARDWARE AND SOFTWARE OF THE PROPOSED SYSTEM

A. PLC and TIA PORTAL Software

In the control system with the PLC device which is the second stage of the robotic mushroom collection system, coordinate data of mushroom which is determined by image processing techniques is transferred to the PLC device. Then, this coordinate data coming to the PLC device pass through the necessary evaluation stages and the robot is sent to these coordinates. These coordinates are the coordinate data in the actual coordinate system of the central pixel of the detected object. This data is sent to the stepper motor drives after passing the necessary evaluation stages in the PLC device and the motors are sent to these coordinates with the help of the drivers. The PLC type to be used in this study is S7-1200 type. The picture of the model is presented in Figure 5.

Technical details about S7-1200 type PLC can be found [18].

In order to program the PLC, the TIA PORTAL interface has been developed. The TIA (Totally Integrated Automation) PORTAL software is a very useful interface which is developed by SIEMENS and providing solutions to problems such as communication with PLC, HMI, Scada systems and similar problems.
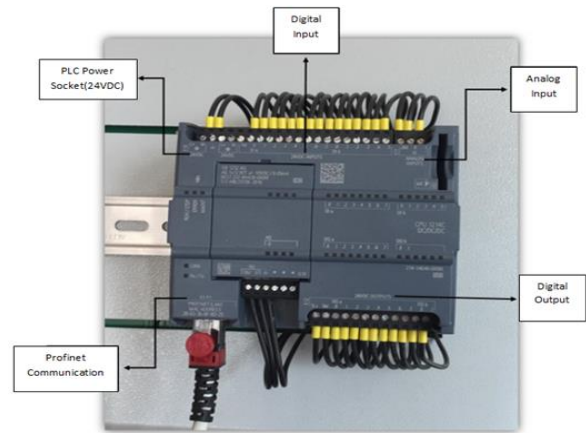
Fig. 5. S7-1200 PLC Device

B. Stepper Motor and Driver

In the robotic platform, stepper motor EMMS-ST-57-S-SE-G2 which is a product of FESTO company will be used. The image of the motor is shown in Figure 6 and the technical information is shown in Table-1.
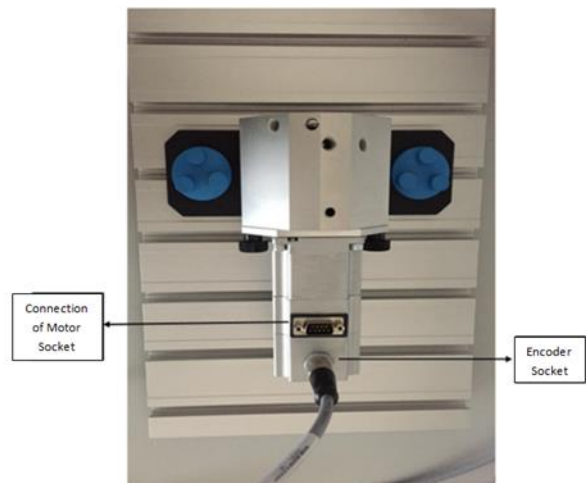
Fig. 6. Stepper Motor and Connection Parts

TABLE-1
TECHNICAL DETAILS OF STEPPER MOTOR

Size of Motor		57-S
Nominal Voltage	[V DC]	48
Nominal Current	[A]	5
Max. rotational speed	[rpm]	2720
Holding torque	[Nm]	0.8
Stepper angle	[°]	1.8±5%
Winding resistance	[Ω]	0.15±10%
Winding inductance	[mH]	0.5
Output mass moment of inertia	[$kgcm^2$]	0.29/0.30
Radial load on shaft	[N]	52
Axis load on shaft	[N]	10
Mass moment of inertia of rotor	[$kgcm^2$]	0.29

The motor drives are used for two stepper motors in robotic platform. These drives are also CMMS-ST-C8-7-G2 stepper motor drivers manufactured by FESTO, which is the stepper motor manufacturer. Figure 8 shows the image of the motor driver used in the system.

Fig. 8. Stepper Motor Driver used in the system

The motor drive and motor connection in the system are shown in Figure 9.

Fig. 9. Connection between Stepper Motor and Stepper Motor Driver

Fig. 10. Connection between PLC and Stepper Motor Driver

The connections between the PLC device and the motor drive are shown in Figure 10. Here is shown the sockets which are used for the output signals from the PLC to the drive and

input signal pins from the drive to the PLC device. In the driver part, the speed and position information from the encoder is provided by the connection from the encoder socket to the dr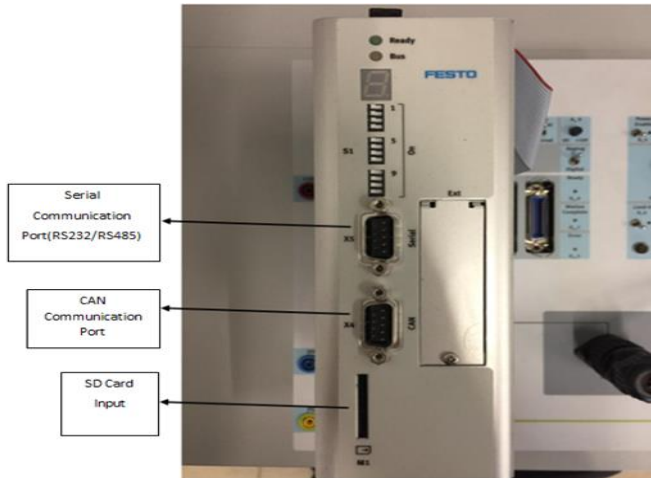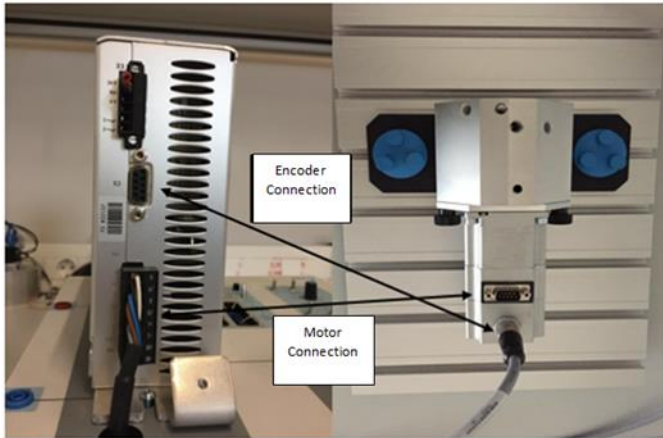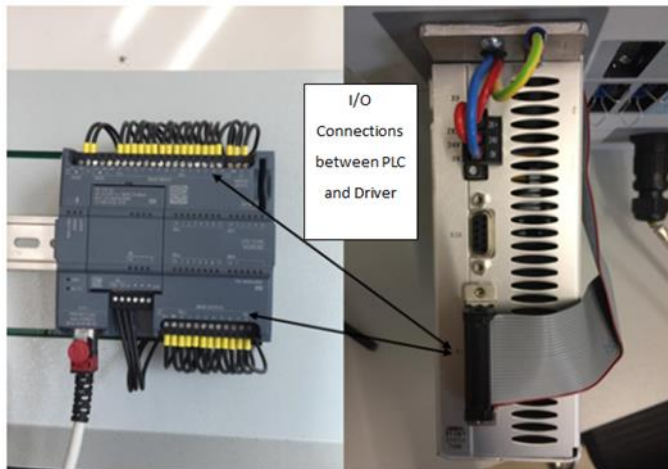ive. This speed and position information from the encoder are sent as an output signal from the driver to the PLC device. The driver information to be supplied to the motor after this information is evaluated in the PLC is sent as input to the driver from the output terminals and is output to the motor connected to the motor socket after evaluating on the drive.

C. Communication of Visual Studio C# and TIA PORTAL

Visual Studio C# is the software in which image processing steps are performed. The PLC device is the hardware part where the control part takes place. Communication with the PLC device is carried out with TIA PORTAL. It is impossible for C# to communicate directly with TIA software. To eliminate this problem, there are several libraries of C# language. In this study, S7.Net library is used and this section will compile the code and communicate with TIA PORTAL [19].

S7.Net is a library that works only with the SIEMENS PLC and communicates only using Ethernet protocol. This library is written for C #. Therefore, without the need for any extra files, only the library can be compiled by adding the library. The following codes are written in the C# program language;

Plc Plc = new Plc(CpuType.S71200, "192.168.0.1", 1, 0); (11)

In this command, the PLC definition is performed. In this way, PLC is defined by entering the PLC type, communication IP address, Rack and Slot parameters.

Plc.Open ();   (12)

In this command (12), at the start of the process, the PLC is ready for communication.

Plc.Write ("DB9.DBW0.0", axis_x);   (13)
Plc.Write ("DB9.DBW4.0", axis_y)   (14)

In DataBlock-9, an integer is assigned to the address 0.0 of the PLC to the mushroom position of the x axis and other integer is also assigned to the address 4.0 of the PLC to the mushroom position of y axis. In this system, there are only two motors that provide movement in the x and y axis, so only the position information of these axis is sent. In case of need, third axis or other information can be sent to TIA interface.

IV.   EXPERIMENTAL RESULTS

In the mushroom picture used as sample data in the real-time testing phase of the system, the mushroom was first detected. Then, the location of the mushroom was determined and these position information obtained from the TIA Portal software communicating in real time with the Visual Studio C#.NET software were sent to the PLC instantly. The product detection and location information carried out in the testing phase with the PLC is shown as in Figure 11.
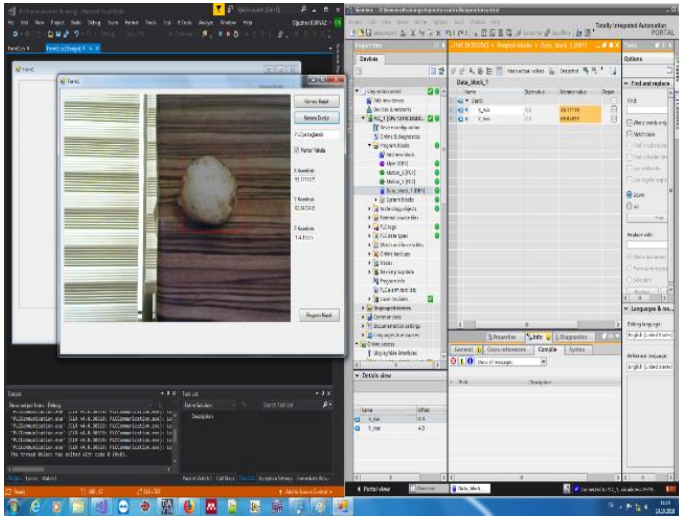
Fig. 11. Mushroom Detection and Sending Position Data to PLC

In Figure 11, the state of the system is shown. Firstly, the compilation process of the form interface developed by C# software language was performed on the Visual Studio platform. In the event that no error related to the code part is encountered after the compilation process, the form application has been executed and the image acquisition of the object from the camera has been provided by pressing the form 'Start Camera' button on the form interface. In the case of communication with the PLC connected to the system, the text box shows 'Connected to PLC System'. After this text appears, PLC communication with Visual Studio has been realized and the system has been made available for data exchange. The next step is the detection of the mushroom and if the 'Catch Mushroom' option is selected under the text box, the system is ready for the detection of the mushroom object. In the upper picture, the option is active and the detected mushroom object is enclosed in a red rectangle. The position of the center point of the quadrilateral area in the XYZ plane is shown in the 'X Coordinate', 'Y Coordinate' and 'Z Coordinate' in boxes. Because of the task performed in the system sends position information to the motors moving in X and Y plane, X and Y coordinate information is sent to the PLC. The right side of the picture shows the connected PLC device. The variables defined in the 'Data Block' section appear on the left side. These defined variables are used in the 'Motion_X 'and 'Motion_Y' function blocks on the left side and the stepper motors are controlled. 'X Coordinate' value obtained in the Visual Studio form interface is sent to the PLC device and assigned to the 'X_Axis' variable. Similarly, 'Y Coordinate' value obtained in the Visual Studio form interface is sent to the PLC device and assigned to the 'Y_Axis' variable. These values can be seen simultaneously on both the form interface and the PLC device. The orange-coloured parts on the right show that the PLC device is connected and the incoming data is displayed instantly. The graph with position and speed information is shown in Figure 12 during the desired motion.

The graph shown in Figure 12 shows the change of the position data of the X axis depending on time from the form

interface. Location data are given in cm. In the blue part, the parts belonging to the Y axis are shown. Local changes in a period of approximately 70 seconds are shown graphically. In the pink section, the speed data of the X axis are shown. The motor which moves in X axis is moving at constant speed and 100 mm/Sec. This motor has a constant speed and its representation is linear. Similarly, in the turquoise colour, the speed data of the motor which provides the movement of the Y axis is shown. Again in this axis, the motor moves at 100 mm / sec and the speed of the motor is constant and the its representation is linear.
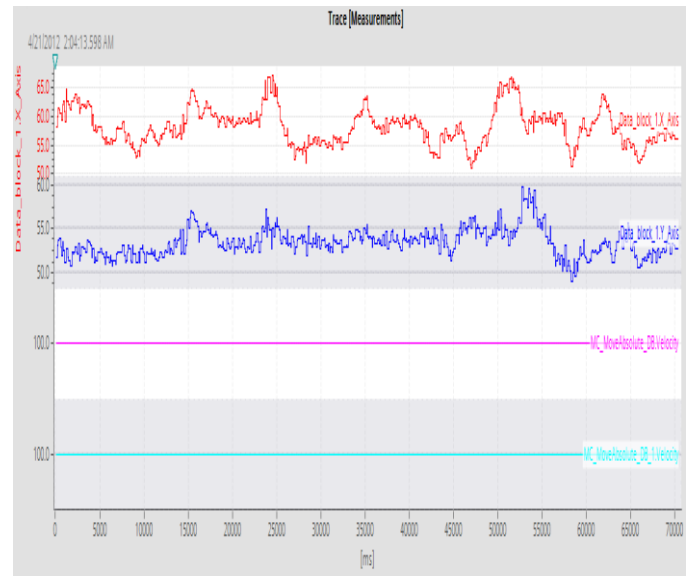
Fig. 12. Graphics of position and velocity data on X and Y axis

The following table shows the location information in which the mushroom detected in 10 different positions is detected and the details of the points in the global coordinate system are given in Table 2. The given position information is calculated in mm. Changes in X axis and Y axis are shown in Figure 13 and Figure 14.

TABLE-2
ACTUAL AND CALCULATED POSITION INFORMATION AND ERROR RATES IN X AND Y AXES

Data	Real location		Calculated Location		Error Rate in X Axis	Error Rate in Y Axis
	X	Y	X	Y		
1	146	44	135	38	7,53%	13,64%
2	140	132	144	132	2,86%	0,00%
3	96	78	92	76	4,17%	2,56%
4	148	132	144	107	2,70%	18,94%
5	140	126	143	106	2,14%	15,87%
6	122	106	123	85	0,82%	19,81%
7	110	104	108	81	1,82%	22,12%
8	102	110	102	109	0,00%	0,91%
9	120	104	119	103	0,83%	0,96%
10	118	104	134	95	13,56%	8,65%

Fig. 13. Graphical representation of the actual position and calculated positions in the X axis

Fig. 14. Graphical representation of the actual position and calculated positions in the Y axis

Fig. 15. Graphical representation of the test platform

In the test platform shown in Figure 15, the desired orbital movements were also applied.

V. CONCLUSION

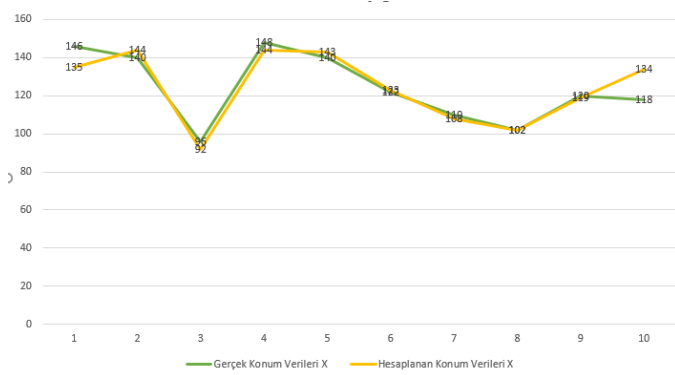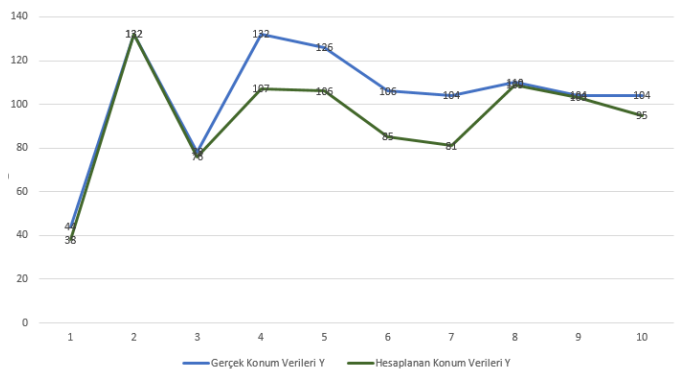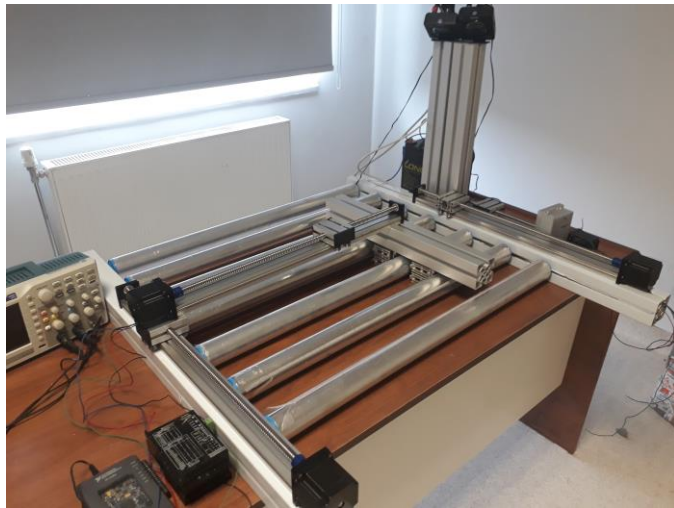In this study, the position of a mushroom in three-dimensional space was determined by means of an image-based controlled robotic platform. One of the biggest achievement of this work is to determine the actual position in the global coordinate

from the pixel-based location of the object in the image using an ordinary USB camera or built-in camera by means of calibration technique.

In the robotic platform, the first step was to determine the product by using image processing techniques. Firstly Haar-Cascade classifier was used for mushroom detection. For the use of this classifier, firstly, the stage of classifier training was carried out. Classifier training was carried out by introducing positive and negative images to software. The places where the mushrooms are located are called positive pictures. The places where the mushrooms are not located are called negative pictures. In the positive pictures, the parts of the mushroom are introduced to the system and the training is carried out. At the end of this process, .xml file is obtained. Thanks for this file introduced in the software, it is ensured that the mushroom object is detected when the system is running. After the solution of the problem of mushroom detection by using image processing techniques and camera, In the PLC, the position information evaluation steps are started. After making the necessary optimizations, these locations are sent to the stepper motor drivers and the motors were sent to these points. Using these position information, the motors are sent to this position. In the studies we are planning to perform in the future, the evaluation of the growth status of the detected mushroom and the studies of the harvesting of the product according to the result of this evaluation will be performed.

REFERENCES

[1] Anonymous, "Mantar yetiştiriciliği", ss. 2–5, 2017. [Online]. Available at: https://istanbul.tarim.gov.tr/Belgeler/KutuMenu/Brosurler/Sebzecilik/mantar.pdf. [Access: 27-Oct-2018].

[2] Y. A. Sari ve S. Adinugroho, "Tomato ripeness clustering using 6-means algorithm based on v-channel otsu segmentation", *5th International Symposium on Computational and Business Intelligence, ISCBI 2017*, ss. 32–36, 2017.

[3] S. SOLAK ve U. ALTINIŞIK, "Görüntü İşleme Teknikleri ve Kümeleme Yöntemleri Kullanılarak Fındık Meyvesinin Tespit ve Sınıflandırılması", *SAÜ Fen Bilimleri Enstitüsü Dergisi*, c. 22, num. 1, ss. 1–1, 2018.

[4] M. S. A. Mahmud, M. S. Z. Abidin, ve Z. Mohamed, "Development of an autonomous crop inspection mobile robot system", *2015 IEEE Student Conference on Research and Development, SCOReD 2015*, ss. 105–110, 2015.

[5] S. S. Mehta ve T. F. Burks, "Adaptive Visual Servo Control of Robotic Harvesting Systems", *IFAC-PapersOnLine*, c. 49, num. 16, ss. 287–292, 2016.

[6] Y. Zhao, L. Gong, Y. Huang, ve C. Liu, "A review of key techniques of vision-based control for harvesting robot", *Computers and Electronics in Agriculture*, c. 127, ss. 311–323, 2016.

[7] W. Jun, Z. Zhou, ve D. U. Xiaodong, "Design and Co-simulation for Tomato Harvesting Robots", *Proceedings of the 31st Chinese Control Conference*, ss. 5105–5108, 2012.

[8] B. Li, M. Wang, ve L. Li, "A real-time pineapple matching system based on speeded-up robust features", *Proceedings - 2010 International Conference on Computational Intelligence and Security, CIS 2010*, ss. 243–247, 2010.

[9] Q. Feng, X. Wang, G. Wang, ve Z. Li, "Design and test of tomatoes harvesting robot", *2015 IEEE International Conference on Information and Automation, ICIA 2015 - In conjunction with 2015

IEEE International Conference on Automation and Logistics, num. August, ss. 949–952, 2015.

[10] A. Masoudian, "COMPUTER VISION ALGORITHMS FOR AN AUTOMATED HARVESTER (Thesis format: Monograph)", num. December, 2013.

[11] A. Shaikh, G. Khaladkar, R. Jage, ve T. P. J. Taili, "Robotic Arm Movements Wirelessly Synchronized with Human Arm Movements Using Real Time Image Processing", *2013 Texas Instruments India Educators' Conference*, ss. 277–284, 2013.

[12] M. Enzweiler ve D. M. Gavrila, "Monocular pedestrian detection: Survey and experiments", *IEEE Transactions on Pattern Analysis and Machine Intelligence*, c. 31, num. 12, ss. 2179–2195, 2009.

[13] C. R. Wren, A. Azarbayejani, T. Darrell, ve A. P. Pentland, "Pfinder: real-time tracking of the human body", *IEEE Transactions on Pattern Analysis and Machine Intelligence*, c. 19, num. 7, ss. 780–785, 1997.

[14] P. Viola ve M. Jones, "Rapid object detection using a boosted cascade of simple features", *Proceedings of the 2001 IEEE Computer Society Conference on Computer Vision and Pattern Recognition. CVPR 2001*, c. 1, s. I-511-I-518, 2001.

[15] C. Olsson, "Lecture 1 : The Pinhole Camera Model", c. 3, num. 2, ss. 2–5, 2013.

[16] Y. M. Wang, Y. Li, ve J. B. Zheng, "A camera calibration technique based on OpenCV", *3rd International Conference on Information Sciences and Interaction Sciences (ICIS 2010), Chengdu, China*, ss. 403–406, 2010.

[17] E. Wood ve A. Bulling, "Eyetab: Model-based gaze estimation on unmodified tablet computers", *Proceedings of the Symposium on Eye Tracking …*, ss. 3–6, 2014.

[18] Anonymous, "S7-1200 DataSheet", 2012. [Online]. Available at: https://cache.industry.siemens.com/dl/files/465/36932465/att_106119/v1/s71200_system_manual_en-US_en-US.pdf. [Access: 20-Nov-2018].

[19] Anonymous, "S7.Net documentation Create a PLC instance , connect and disconnect", 2016. [Online]. Available at: https://github.com/S7NetPlus/s7netplus/blob/master/Documentation/Documentation.pdf. [Access: 23-Sep-2018].

BIOGRAPHIES

KAĞAN KORAY AYTEN was born in Ankara, Turkey, in 1981. He received the B.S. degree in electronic engineering from Pamukkale University, Denizli, Turkey, in 2004, the M.S. degree in electrical & electronic engineering from Cardiff University, UK, in 2007, and the Ph.D. degree in electrical engineering from Bath University, England, UK, in 2013. He is currently an Associate Professor with the Department of Electrical and Electronics Engineering, College of Engineering, Erzurum Technical University, Erzurum. His work has focused on the development and application of control theory to a variety of mechatronic systems, with a focus on observation and estimation-based control. Much of his recent work has focused on the analysis and control of dynamical systems that arise in engineering applications.

OĞUZHAN KURNAZ was born in Erzurum, Turkey, in 1993. He received the B.S. degree in Mechatronic Engineering from Erciyes University, Kayseri, Turkey, in 2016. He continues his M.S. degree from 2016 in Erzurum Technical University, Erzurum, Turkey. He is currently a Research Assistant with the Department of Mechatronic Engineering, College of Engineering and Nature Sciences, Bursa Technical University, Bursa, Turkey from June 2018. His works have focused on the developments and applications of object detection, feature extraction, object tracking, object recognition, and image processing. His areas of interest also include Machine Learning Methods, Artificial Intelligence Algorithms, Deep Learning Methods, Neural Networks and their applications to mechatronic systems.

Design, Construction and Implementation of Low Cost Photovoltaic Water Pumping System for Agricultural Irrigation

A. GUNDOGDU and B. GURE

Abstract— **In this study, design, manufacturing and installation of a new agricultural irrigation system with a 2.2 kW photovoltaic (PV) panel, which has a lower volume and lower cost in terms of size and cost, was carried out within the boundaries of Batman province that has a long sunshine duration. Through making winding and connection changes on a 380v-star connected asynchronous submersible motor with 2.2 kW power, which operates compatibly with HSPL/H2200H model inverter, the HSPL/H2200L model inverter was brought in compliance with the delta having 220v between its phases and having output voltage. Dimension analysis of a photovoltaic system that was independent of the grid and where this new voltage level would be obtained was performed and the operation of rewinding the motor and changing the connection shape was explained. The real-time current, voltage and power data obtained after the installation are presented in tables and graphs. The advantages of this low-cost new irrigation system over the existing irrigation systems with similar power are explained in detail through the size and cost analyses.**

Index Terms—**Photovoltaic Energy, PV System, Agricultural Irrigation.**

I. INTRODUCTION

BOTH THE INEFFICIENT use of conventional energy sources and the rapid depletion of them have led mankind to use clean and non-depleted renewable energy sources. Considering the high cost of the energy generated from conventional energy sources and their harmful effects on the environment, solar energy, which is used widely in heating and electricity generation, has an important place among renewable energy sources.

The use of renewable energy sources has increased seriously due to their environmental and economic benefits, being abundant and widespread, rapid improvements provided for them to compete with other manufacturing technologies, developing technologies and thereby decreasing costs, concerns about the environmental impact of fossil fuels, major and significant incentives given in many countries of the world ($120 billion in 2015) [1].

According to the IEA [1] and EIA [2], by 2040, worldwide hydropower and other renewable energy sources consumption is expected to increase by 3.2% and 2.9%, respectively. It is forecasted that the largest installed power contribution to the increase in renewable resources will come from wind energy with 863 GW and solar energy (PV) with 815 GW. The share of renewable energy sources in the electricity generation is estimated to reach from 22.6% in 2014 to 26.0% in 2020 and to 29.0% in 2040 [1].

It is seen that there have been significant increases in the applications of generating electric energy from solar energy with the help of photovoltaic panels in recent years. It has reached important levels in the European Union (87 GW), especially in Germany and Italy [4]. China (28 GW), Japan (23 GW) and the United States (19 GW) are among the countries that are making progress in this area [3].

Looking at the global greenhouse gas emissions, it is seen that the largest share belongs to the Energy Sector with 34.6% and 25% of this is due to the oil, natural gas, and coal used in electricity and heat production [5, 6]. Most CO_2-emitting countries are listed as China, the United States, the EU, India, Russia, and Japan. Turkey ranks 17th in this list [7].

According to the previous research, it is stated that 26% of the energy needs on a global scale can be met from solar energy by 2040 and serious employment areas will be provided in this sector. It is known that in our country, which is largely based on agriculture, electrical energy is consumed seriously in agricultural irrigation applications.

Our country has 78 million hectares of land and about 28 million hectares of this is used as agricultural land. Irrigable agricultural land is about 8.5 million hectares [8]. In this regard, solar energy should be used for agricultural irrigation purposes. In our country, which has high sunshine duration, photovoltaic systems that produce electricity primarily for agricultural purposes should be installed in rural areas where there is no electrical energy or where the energy transmission lines do not reach. With the establishment of these systems, high energy and production costs in grid-connected irrigation systems can be reduced. Although the first installation cost of these systems is high and its efficiency depends on instant

AHMET GÜNDOĞDU, is with Department of Electrical Engineering University of Batman University, Batman, Turkey, (e-mail: ahmet.gundogdu@batman.edu.tr).
https://orcid.org/0000-0001-7240-204X

BAYRAM GÜRE, is with Gure Engineering, Batman, Turkey, (e-mail: editor@bajece.com).
https://orcid.org/0000-0003-1653-6451

weather conditions [9], it is seen as an economic solution in the long term.

Some recent studies on agricultural irrigation with photovoltaic solar energy and the results of these studies are summarized below.

Yeşilata and Aktacir focused on the design of the solar-powered water pump systems and they created graphs to facilitate the selection of the elements forming the system [10].

By taking advantage of variable-speed centrifugal pumps, opportunities to increase the efficiency of deep well pumps operating with photovoltaic effect were investigated by Fiaschi et al., and comparisons were made taking into consideration the photovoltaic system which produces 30 m^2 and about 3 kW power that can draw water from 100 m deep wells [11].

Kavlak and Güngör stated that it would be more convenient to use solar-powered water pumps instead of diesel engine pumping system operating with diesel fuel [12].

Purohit and Kandpal investigated the renewable energies that could be used in water pumping systems in India and examined the systems comprised of pumps operating with photovoltaic system, biogas and wind propellers [13].

A converter for a three phase 12/8 pole reluctance motor with 300 W power was designed by Dursun and Saygın. This driver was used to operate the pump in the irrigation system [14].

A mathematical model for the solar powered agricultural irrigation system was created by Glasnovic and Margeta (2007). In Croatia, analyses were carried out taking into account radiation, climate, irrigation methods and planted plants for 30 regions. As a result of these analyses, it was concluded that solar energy could be used in irrigation, but it was also concluded that because the sunshine duration was varied, it had a negative effect on agricultural irrigation [15].

Ramos and Ramos examined the usability of the solar energy systems in the methods of water drawing from wells, especially in developing countries such as Africa, North Asia and Latin America. They indicated that it had many areas of usage. And, they calculated an initial investment cost and the water cost associated with this cost [16].

In another research, a study was carried out on both lighting and irrigation with a 610 W photovoltaic system, which was independent from the grid, by Kaldellis et al. [17].

In Guatemala, a Central American country, Granich and Elmore investigated whether the water transported from the deep water well to a high tank with a pump system and accumulated in this tank can meet the water requirement at home. It was concluded that the generated electrical energy was not sufficient for the pumping system. It was also concluded that this system was not economical, but it could be economical when compared with the installation of the grid line in the areas where there was no electrical grid system [18].

By Dursun and his colleagues, the performance analyses of the photovoltaic, wind turbine and fuel cell power generation systems were made for the Aegean region [19].

Chen et al. explained wind and solar energy generation systems, which are among the renewable energy sources, and made cost, benefit, and risk analyses for the generation of solar wind hybrid energy [20].

Mokeddem et al. designed a photovoltaic system for use in different climate conditions and radiation values and they conducted an efficiency analysis of the DC pump used in that system [21].

It was emphasized by Belgacem that it would be economical to make irrigation in rural areas in less developed countries with the help of photovoltaic energy. It was proved that solar energy can be used for pumping water, especially in Tunisian conditions having 3000 hour yearly sunshine duration and 6 kWh/m2 daily values [22].

In order to evaluate solar energy potential in the South East Anatolia region, Yusufoğlu made agricultural irrigation with a photovoltaic system using a DC pump [23].

Gençoğlu carried out the design of a solar powered photovoltaic water pumping system controlled by PLC, which was independent of the grid [24].

Gündoğdu analyzed the effects of shading affecting the system performance adversely in terms of current, voltage, and power in a photovoltaic system having 5x5 matrix array. The effects of shading, which emerges based on atmospheric and environmental conditions, on both panel efficiency and overall system efficiency were studied. The simulation model of this system consisting of 25 panels and having a maximum power point of 2.1 kW was created in the MATLAB/Simulink environment [25].

Especially in mountainous and remote agricultural lands where there is no grid electricity, diesel generators are generally used for irrigation. With the electrical energy obtained from these generators, submersible water motor are operated and irrigation is performed. Because of the high fuel costs, this system is not seen as very useful. Given this situation, the use of photovoltaic panels in agricultural irrigation in the short and long term is inevitable. In accordance with this aim, design, manufacturing and field application of a low-cost photovoltaic water pumping system for agricultural irrigation was carried out in this study.

II. DESIGN OF PHOTOVOLTAIC WATER IRRIGATION SYSTEM

PV systems are a good solution for irrigation in remote agricultural areas where electrical energy is not available. For this purpose, either fixed or portable systems have been designed. Although fixed systems are relatively cheaper than portable systems, they are also at risk of theft due to the fact that they are far away from the residential areas. In this respect, portable PV systems are more suitable for use.

Up to a certain power, photovoltaic systems can be designed as having storage. However, this type of design is not preferred because of the high cost of storage elements. When the sun is insufficient or especially during the night, systems without storage do not work. However, in systems without storage that we want it to operate during the night, the pool or water tanks that provide the storage of water is used. The system designed in this study is a grid independent system that is carried out without the use of energy storage elements. The general principal scheme of this irrigation system is given in Figure 1.
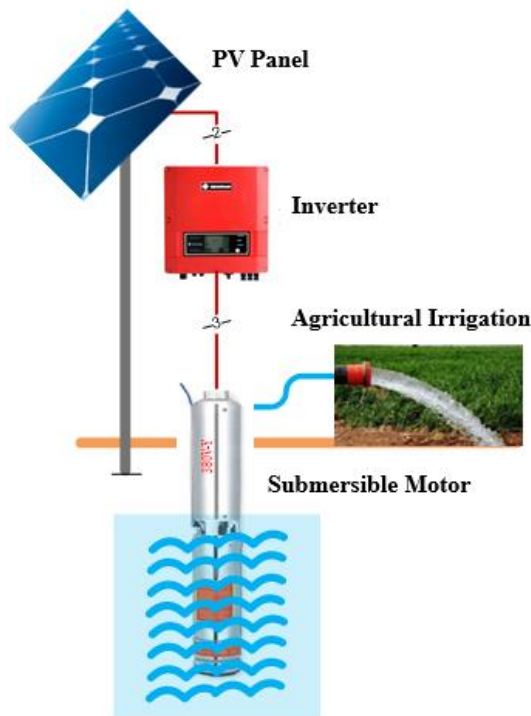
Figure 1. The principal scheme of the photovoltaic agricultural irrigation system

A. Selection of Submersible Pump

In the designed system, there is a 50-ton water tank where the water drawn from the ground will be stored, and this tank is intended to be filled in approximately 6 hours. The well is 65 m deep and there are 200 m distance between the well and the water tank. The submersible motor will be taken down to 50 m below the ground. In addition, the height difference between the exit point of the well and the tank (elevation difference) is 0 m. In order to fill the tank within 6 hours, 50/6=8.3 m^3/h water must be supplied from the well. The closest value to the water amount of 8.3 m^3/h that should be supplied per hour is 9 m^3/h. Taking into account this data, the outer diameter of the polyethylene hose to be laid on the soil ground along a distance of 200 m was found to be 63 mm with the help of Table I.

TABLE I
PLASTIC PIPE SELECTION TABLE

Outer Diam. of Plastic Pipe		25	40	50	63
Nom. Diam. of Plastic Pipe		20	32	40	50
Metal Water Pipes		3/4"	1"1/4	1"1/2	2"
m^3/h	l/min	l/s	Friction loss per 100 m		
2.1	35	0.6	29.8	2.8	0.9	0.3
↓	↓	↓	↓	↓	↓	↓
9	150	2.5		63	24.5	4.7

If the friction loss in the polyethylene hose, which will be used in 200 meter horizontal distance, is 4.7 m for every 100 m distance, it is calculated as 2 x 4.7=9.4 m for 200 m. In this case, the depth to which the submersible motor needs to be taken down is calculated as 50 + 9.4 = 59.4 m. Depending on the water amount of 8.3 m^3/h per hour and the depth of 59.4 m, to which the submersible motor needs to be taken down, and with the help of Table II, the power of the submersible motor was determined as 3 Hp and pump type was determined as S4 8/13.

TABLE II
PUMP SELECTION TABLE

Pump Type	Hp	Flow Rate									Outlet	Height	Weight
		m^3/h	0	4.8	5.4	6	7.2	8.4	9.6	10.8	12	inch	mm	Kg
		l/s	0	1.33	1.5	1.67	2	2.33	2.67	3	3.33			
S4 8/ 06	1.5	MSS	38	35	34	33	31	28	24	19	14	2"	356	3.4
S4 8/ 08	2		52	47	45	44	41	37	31	25	18		418	4
S4 8/ 13	3		82	75	73	71	66	59	50	40	30		573	5.5
S4 8/ 17	4		108	98	96	94	87	79	70	58	46		697	6.6
S4 8/ 23	5.5		148	134	131	127	118	108	95	79	60		959	9.4
S4 8/ 32	7.5		202	182	178	172	160	143	125	105	80		1276	12

B. Motor and Inverter Selection

Whether they are fixed or portable, photovoltaic systems have high installation costs in today's conditions. In order to reduce this cost, a different approach was proposed in this study and the validity of this proposal was verified by the conducted studies. With this new approach, a low cost 380V star-connected asynchronous submersible motor with 3 Hp (2.2 kW) power, which was commonly found in the market, was used as a submersible pump motor.

There is no motor operating with phase to phase voltage 220v in Turkey standards because the voltage between phases is 380v and 380v star-connected motor types are widely used. The connection of this 380v star-connected motor was transformed into a 220v delta-connection, thus a decrease in the number of photovoltaic panels that would supply this motor was ensured. The decrease in the number of panels also provided an opportunity to realize the whole system at less cost and smaller sizes.

In the selection of inverter, values related to two different inverter models that have two different maximum power point (MPP) values and that are widely used in the market were taken into consideration. The power, voltage and model information for both inverter models are given in Table III.

TABLE III
INVERTER SELECTION TABLE

Inverter Model	Inverter Power	Inverter Input Volt.	Inverter Output Volt.	Motor
HSPL/ H2200H	3 Hp	400-780 V	380/400/440 V	Star
HSPL/ H2200L	3 Hp	200-450 V	220/240 V	Delta

According to Table 3, the suitable inverter model for the asynchronous submersible motor which is converted into a 220v delta-connection is HSPL/H2200L. The input voltage values of both inverters show variance according to both connection shapes of the selected motor. While this value is in the range of 200v-450v in the HSPL/H2200L inverter model, it is in the range of 400v-780v in the HSPL/H2200H model.

When determining the number of panels to be used, motor connection shape, operating voltage and inverter input and output voltages given in the table were taken into account. The number of panels that will be used to capture inverter input voltage in HSPL/H2200H is greater than the number of panels that will be used in HSPL/H2200L.

With the HSPL/H2200H model inverter, the 380v star-connected motor can be easily operated and also the 220v delta motor can be easily operated with the HSPL/H2200L model inverter. HSPL/H2200L model inverter with input voltage 200v-450v DC and output voltage 220/240v AC was preferred in this designed new photovoltaic system.

C. Calculation of the Photovoltaic Panel Power

The selection and sizing of photovoltaic solar panels was determined according to the selection of asynchronous submersible motor and inverter to be used in the pump system.

The number of panels and the dimension analysis to be used in the photovoltaic system where we will obtain the voltages required for the star and delta connected states of 3 Hp asynchronous submersible motor are given below separately. For use in the system, catalog values of some of the OSP coded polycrystalline panels are given in Table IV. Among these, the OSP250 model panel with the value of 250 Wp was preferred.

TABLE IV
PHOTOVOLTAIC PANEL SELECTION TABLE

	OSP150	OSP250	OSP260
P_{max}(W)	150	250	260
V_{oc}(V)	22,3	37,8	38
V_{mpp}(V)	18,6	30,5	30,8
I_{sc}(A)	8,5	8,7	8,96
I_{mpp}(A)	8,1	8,2	8,45
n (%)	15,4	15,7	16
(Kg)	10	18	18
piece	36	60	60
E/B/K	994*1014*40	1640*992*40	1640*992*40
(STC)	E=1000w/m², AM=1,5,T)=25 °C		

In case of using the 380v star-connected submersible motor, determination of the number of panels required and calculation of the total voltage were made as follows. The voltage between phases that the motor needs according to the connection shape is 380v. The output voltage of HSPL/H2200H inverter model given in Table III is 380v and it is suitable for the motor. However, the DC bus input voltage range of this inverter is 400v-780v and its MPP voltage is greater than 500V. Minimum number of panels that will provide this input voltage to the inverter is;

$$\text{Min. Panel Number (Star)} = \frac{500}{30.5} \cong 16 \qquad (1)$$

Depending on the width and height catalog values of 1640x992 mm, the area of a panel is calculated as follows:

$$\text{Area of a Panel} = 1.64 \times 0.992 = 1.626 \text{ m}^2 \qquad (2)$$

The total area of 16 panels is found as 1.626 x 16 = 26 m². The arrangement of these 16 pieces OSP250 model panels connected in series is given in Figure 2. Taking into account the unit price of the used photovoltaic panel as 155 $ including VAT as of November 2018, the total panel cost is calculated as 16x155 $=2480 $.
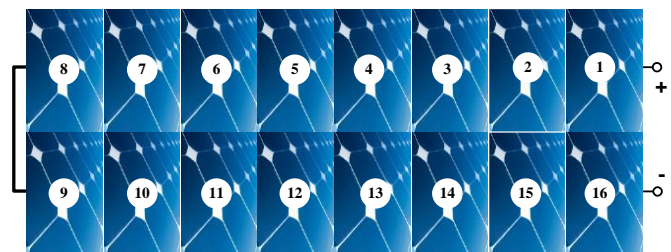

Figure 2. Arrangement of 16 photovoltaic panels

In case of use of 220v star-connected submersible motor, determination of the needed number of panels and calculation of the total voltage was done as follows. The voltage between phases that the motor needs according to the connection shape is 220v. The output voltage of HSPL/H2200H inverter model given in Table III is 220V and this is suitable for the motor. However, the DC bus input voltage range of this inverter is 200v-450v and its MPP voltage is greater than 300V. Minimum number of panels that will provide this input voltage to the inverter is;

$$Min.\ Panel\ Number\ (Delta) = \frac{300}{30.5} \cong 10 \qquad (3)$$

It should be needed that the total open circuit voltage obtained by serial connection of the panels i) do not exceed the inverter open circuit voltage and ii) it is within the range of 200v-450v which is the inverter input voltage of MPP voltage. For the photovoltaic system to operate more efficiently, the system installation can be realized up to 1.4 times of the installed power needed in practice. In this case, the total panel power is the following.

$$Total\ Panel\ Power\ (Delta) = 2200\ Wx\ 1.4 = 3080\ W \qquad (4)$$

The number of panels that is needed to be used depending on this new modified power value is:

$$Total\ Panel\ number\ (Delta) = \frac{3080}{250} \cong 12\ adet \qquad (5)$$

In the condition in which 12 panels with 250 Wp value are connected in serial,

$$Open\ Circuit\ Voltage = 12 \times 37.8\ V = 453.6\ V \qquad (6)$$

$$MPP\ Voltage = 12 \times 30.5\ V = 366\ V \qquad (7)$$

Although the total open circuit voltage is above the 453.6v ≥ 450v limit, this 0.8% voltage excess does not constitute a problem in terms of the inverter. In the condition in which the motor is delta-connected, the number of panels to provide the required operating voltage was found as 12. Since the same panels will be used, the total area to be occupied by 12 panels is calculated as 1.626x12=20 m². The arrangement of these 12 piece OSP250 model panels connected in series is given in Figure 3. Taking into account the unit price of the used photovoltaic panel as 155 $ including VAT as of November 2018, the total panel cost is calculated as 12x155 $=1860$.
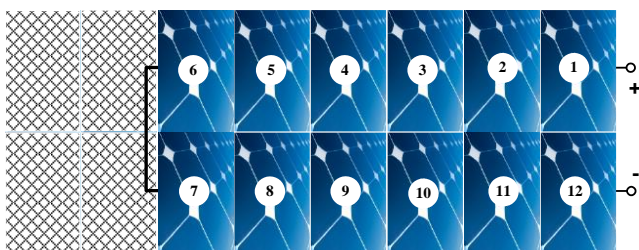

Figure 3. Arrangement of 12 photovoltaic panels

In summary, the results obtained from the above calculations for the star and delta connected states of the asynchronous submersible motor to be used are given below comparatively.

$$Panel\ Num.\ (Star) = 16\ >\ Panel\ Num.\ (Delta) = 12$$
$$PanelArea\ (Star) = 26m^2\ >\ PanelArea\ (Delta) = 20m^2 \qquad (8)$$
$$Cost\ (Star) = 13120\ TL\ >\ Cost\ (Delta) = 9840\ TL$$

As a result of the conversion of the connection shape of the asynchronous submersible motor having 380v star voltage to 220v delta, a 25% decrease in total panel number, a 25% decrease in the physical area where photovoltaic panels would be installed, and a 25% decrease in total panel cost occurred.

D. Winding and Connection Change Performed on the Motor

For steady state and in the conditions in which 380v star or 220v delta is connected, the power that the 3Hp asynchronous submersible motor used in photovoltaic irrigation system will draw from the grid is not change. Although 380v is applied between the phases of the 380v star-connected motor, 380/√3 =220 volt voltage falls to each phase winding.
If the connection of the same motor is converted to 220v delta, then 220v must be applied as phase to phase voltage. In the delta connection, the phase to phase voltage is equal to the winding voltage of each phase of the motor at the same time.

The asynchronous submersible motor whose general view, winding end diagram and terminal connection are given in Figure 4 has an operating voltage of 380v star connected as the fabrication. It has been winded as 24 slot and 2p=2 pole.
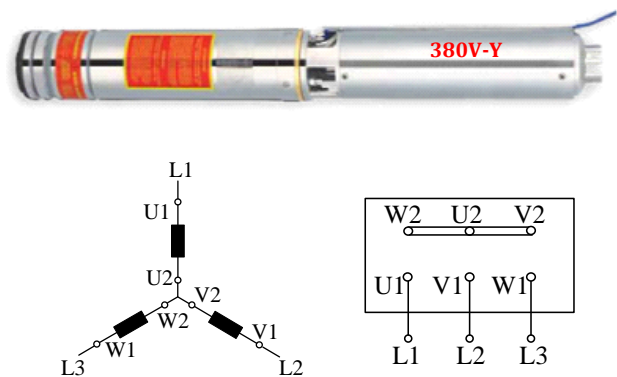

Figure 4. Winding diagram and terminal connection of the 380v star-connected asynchronous submersible motor.

In order to make, it suitable for 220v delta connection, the current motor windings of this motor, which has 24-slot stator, were removed and re-winded with the 2-pole hand-style winding scheme given in Figure 5.
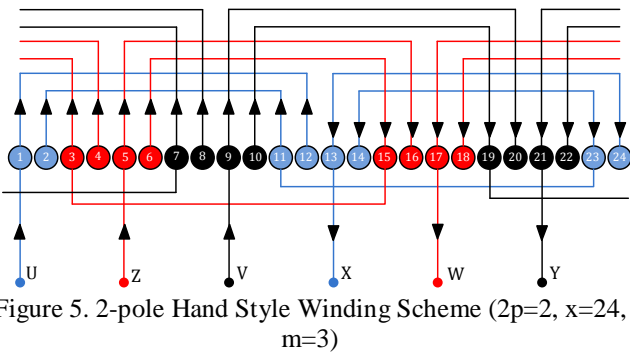
Figure 5. 2-pole Hand Style Winding Scheme (2p=2, x=24, m=3)

The photos related to the conducted winding is given in Figure 6. The coils were set in the slots by using 0, $2\pi/3$ and $4\pi/3$ mechanical settlement angles, respectively. After a total of six coils (two coils for each phase) were placed in the slots, a total of six ends were taken out. Three of these ends were phase winding input ends and the other three were phase winding output ends.

Figure 6. The photos related to motor winding process

After completion of the winding process of the stator, the required varnish, insulation and soldering were made; then, delta was connected to it and it was packaged. Figure 7 shows the winding end diagram belonging to the delta connection of the motor and also shows the terminal connections of it.

Before the packaging, by connecting firstly star and then delta to the motor whose winding process had been completed, the number of current, voltage and cycles were measured in the laboratory environment. The obtained numbers of current, voltage and speed are given in Table V below.
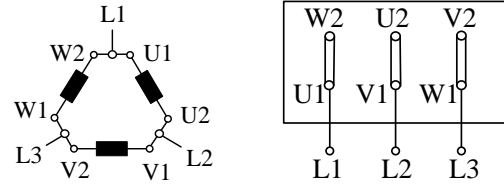

Figure 7. Winding end diagram and terminal connection of the 380v delta-connected asynchronous submersible motor.

TABLE V
CURRENT, VOLTAGE AND SPEED VALUES OF THE MOTOR WHOSE WINDING PROCESS WAS COMPLETED

	380v-star	220v-delta
Line Current (I_L)	3.18 A	5.51 A
Phase Current (Ip)	3.18 A	$5.51/\sqrt{3}$=3.18 A
Line Voltage (V_L)	380 V	220 V
Phase Voltage(Vp)	$380/\sqrt{3}$=220 V	220 V
Ref. Freq.	50 Hz	50 Hz
Speed	2985 rad/m	2991 rad/m

The catalog values of the 3-Hp asynchronous submersible motor used in the designed photovoltaic irrigation system are 3 phases, 50 Hz, 2.2 kW, 380v, 5.6A, 2800 rad/m and Cosφ=0.82.

- In the condition in which 380v-star is connected to motor, the power that the motor will pull from the grid per phase;

$$P_{phase} = U_p \times I_p \times Cos_\varphi \qquad (9)$$

The total power that the motor will draw from the grid;

$$P_T = P_R + P_S + P_T = 3 \times U_p \times I_p \times Cos_\varphi \qquad (10)$$

$$I_{line} = I_{phase} \qquad (11)$$

$$U_{line} = \sqrt{3} \times U_{phase} \qquad (12)$$

$$U_{phase} = \frac{U_{line}}{\sqrt{3}} = \frac{380}{\sqrt{3}} = 220 \text{ V} \qquad (13)$$

- In the condition in which 220v-delta is connected to the motor, the power that the motor will draw from the grid per phase;

$$P_{phase} = U_p \times I_p \times Cos_\varphi \qquad (14)$$

The total power that the motor will draw from the grid;

$$P_T = P_R + P_S + P_T = 3 \times U_p \times I_p \times Cos_\varphi \qquad (15)$$

$$U_{line} = U_{phase} = 220 \text{ V} \qquad (16)$$

$$I_{line} = \sqrt{3} \times I_{phase} \qquad (17)$$

$$I_{phase} = \frac{I_{line}}{\sqrt{3}} \qquad (18)$$

In the case of both connections, the ratio of the powers drawn by the motor from the grid to each other are shown equation (19), (20).

This result indicates that the power that the motor will draw from the grid is equal in both the star and the delta connection. That is, no change in the motor's power and performance occur when the connection shape of the motor is converted from star to the delta. Related to these both conditions (star and delta connections) in MATLAB/Simulink environment, various simulation studies were carried out on a 3-phase simple R load with a power of 2.2 kW. The current, voltage and power graphs obtained as a result of these studies are given below.

$$\frac{P_{star}}{P_{delta}} = \frac{3 \times U_p \times I_p \times Cos_\varphi}{3 \times U_p \times I_p \times Cos_\varphi} = \frac{3 \times \left(\frac{380}{\sqrt{3}}\right) \times I_p \times Cos_\varphi}{3 \times (220) \times I_p \times Cos_\varphi} = \frac{3 \times \left(\frac{380}{\sqrt{3}}\right) \times \left(\frac{U_p}{Z}\right) \times Cos_\varphi}{3 \times (220) \times \left(\frac{U_p}{Z}\right) \times Cos_\varphi} \qquad (19)$$

$$\frac{P_{star}}{P_{delta}} = \frac{3 \times (220) \times \left(\frac{220}{Z}\right) \times Cos_\varphi}{3 \times (220) \times \left(\frac{220}{Z}\right) \times Cos_\varphi} = 1 \qquad (20)$$

III. SIMULATIONS RESULTS

The MATLAB/Simulink block diagram related to the conducted simulation studies is given in Figure 8. While Figure 8a shows the simulation related to the star-connected state of the load, Figure 8b shows the delta-connected state of the load; also, the current, voltage, and power graphs obtained are given below.
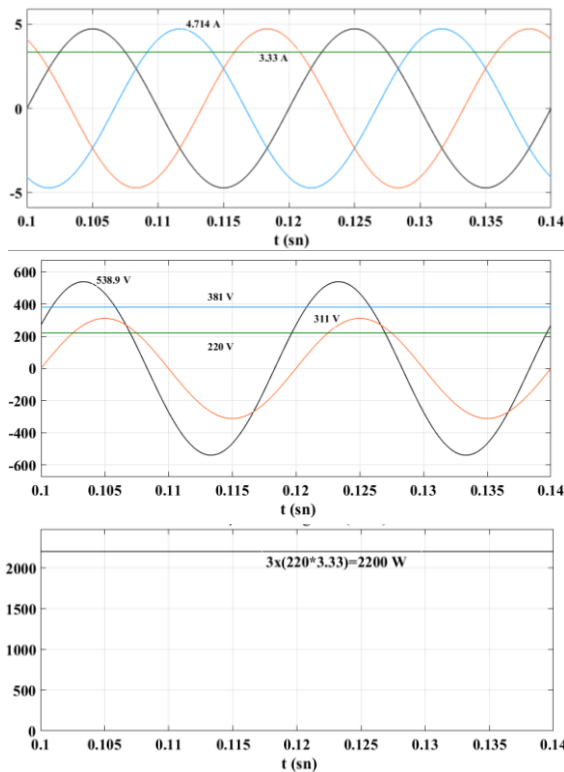

Figure 8a. Current, voltage and power graphs for star connections
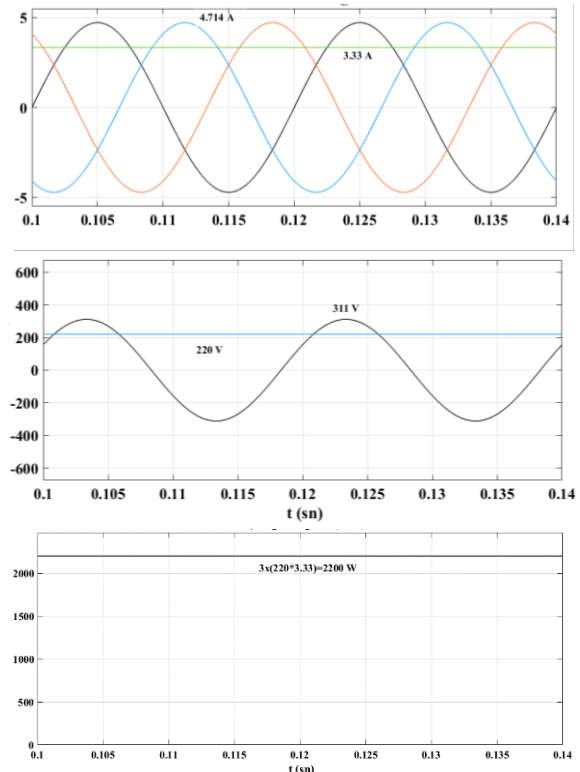

Figure 8b. Current, voltage and power graphs for delta connections

In Figure 8a, the three phase source supplying the load was modeled as an AC source in which the effective value between the phases is 381v rms.

On the other side, in Figure 8b, the three phase source supplying the load was modeled as an AC source in which the effective value between the phases is 220v rms. The effective value of each phase current obtained as a result of the measurements from the three phase star-connected R load is 3.33 A, the effective value of the voltage between phases is 381v and the effective value of the voltage of each phase winding is 220v. On the other side, the power drawn from the source according to this phase current and voltages is obtained as 3x(220x3.33)=2.2 kW.

The effective value of each phase current obtained as a result of the measurements from the three phase delta-connected R load is 3.33 A, the current between the phases and the current of phase are equal and its effective value is 220v. Similarly, the power drawn from the source according to this phase current and voltages is found as 3x(220x3.33)=2.2 kW.

Given the results obtained from simulations of the conditions for both the star and the delta connection, it is seen that in both cases, the power drawn by the load from the grid does not change. As a result, the asynchronous submersible motor, whose connection shape was transformed from 381v star to 220v delta, will continue to operate without any power change, power loss or performance degradation with the designed new photovoltaic irrigation system.

For the designed photovoltaic system, constructions to which 12 panels would be mounted were prepared and 6 panels mounted on a single leg by screwing to the stainless steel bases. The photos about the conducted mounting and field works are given in Figure 9.

Figure 9. Installation of photovoltaic system in the field

Both the size and cost analyses of the designed system were performed and the obtained data are presented in Table VI below.

TABLE VI
SIZE AND COST ANALYSIS OF PHOTOVOLTAIC SYSTEM

	Motor star connected	Motor delta connected
Total Panel Number	16	12
Total Panel Area	26 m^2	≈19.512 m^2
Total Panel Cost	2480 $	1860 $
Inverter Model	HSPL/H2200H	HSPL/H2200L
Inverter Cost	606 $	530 $
Construction Cost	473 $	378 $
AC Cable Cost	56 $	56 $
DC Cable Cost	22 $	22 $
Connector	75 $	75 $
380v Motor+Pump	284 $	284 $
Wind. and Coil Cost	-	13 $
Submer. Pump Hose	56 $	56 $
Rope	34 $	34 $
Cable Joint	6 $	6 $

IV. CONCLUSIONS AND RECOMMENDATIONS

The design of the system is based on changing the winding of a 380v star-connected asynchronous submersible motor and converting its connection shape to 220v delta-connected as the fabrication. Through changing the winding of the 380v star-connected submersible motor and converting the connection shape of it to 220v delta, a decrease in the number of photovoltaic panels required for installed power was ensured. Due to the decrease in the number of panels, the physical area that the photovoltaic panels to be installed would cover was reduced, and a significant decrease in the total panel cost, inverter, construction, wiring, connector, labor and shipping costs was ensured. Such a system, which can be installed with smaller sizes and lower costs, is expected to be preferred by investors both in agricultural irrigation and in other areas.

REFERENCES

[1] Uluslararası Enerji Ajansı (IEA), "World Energy Outlook 2016", 2016.
[2] ABD Enerji Bilgi İdaresi (EIA), "International Energy Outlook 2016", Mayıs 2016.
[3] EÜAŞ, "2016 Elektrik Üretim Sektör Raporu", Mayıs 2017.
[4] Avrupa Komisyonu,"EU Energy in Fig., Statistical Pocket Book 2016", Belçika, 2016.
[5] Intergovernmental Panel on Climate Change, "Climate Change 2014, Mitigation of Climate Change", 2014
[6] US Environmental Protection Agency, "Global Greenhouse Gas Emissions Data", https://www.epa.gov/ghgemissions/global-greenhouse-gas-emiss.-data,29 Mayıs 2017.
[7] Boden T., Andres B., Marland G., "Fossil-Fuel CO2 Emissions by Nation", http://cdiac.ornl.gov/trends/emis/tre_coun.html# , 29 Mayıs 2017.
[8] Aksoy, M.H., "Güneş ve Rüzgar Enerjisi ile Çalışan Su Pompalama Sisteminin Deneysel İncelenmesi", Selçuk Üniversitesi Fen Bilimleri Enstitüsü, Yüksek Lisans Tezi, 2011.
[9] Köksal, M.A.,"Güneş Enerjisiyle su pompalama üzerine bir araştırma", Çukurova Üniversitesi Fen Bilimleri Enstitüsü, Yüksek Lisans Tezi, 2012.
[10] Yeşilata, B. ve Aktacir, A., "Fotovoltaik Güç Sistemli Su Pompalarının Dizayn Esaslarının Araştırılması", Mühendis ve Makina Dergisi, 42 (493), 29-34, 2001.

[11] Fiaschi, D.,et al,"Improving the effectiveness of solar pumping systems by using modular centrifugal pumps with variable rotational speed", Solar Energy, 234-244, 2005.

[12] Kavlak, İ. ve Güngör, H., "Fotovoltaik Piller ve Fotovoltaik Pillerin Tarımsal Sulamada Kullanılması", I. Ulusal Güneş ve Hidrojen Enerjisi Kongresi, Eskişehir, 22-29, 2006.

[13] Purohit, B., and Kandpal, T., C., "Renewable energy technologies for irrigation water pumping in India: projected levels of dissemination, energy delivery and investment requirements using available diffusion models", Renewable & Sustainable Energy Reviews, 592-607, 2005.

[14] Dursun, M. ve Saygın, A., "Güneş Enerjisi İle Çalışan Bir Sulama Sistemi İçin Boost Konvertörlü Anahtarlamalı Relüktans Motor Sürücüsü", Erciyes Üniversitesi Fen Bilimleri Enstitüsü Dergisi, 22 (1-2), 57-65, 2006.

[15] Glasnovic, Z. and Margeta, J, "A model for optimal sizing of photovoltaic irrigation water pumping systems", Solar Energy, 81, 904–916, 2007.

[16] Ramos, J.S. and Ramos, H.M., "Solar powered pumps to supply water for rural or isolated zones: A case study. Energy Conversion and Manag.", 49, 2711–2719, 2008.

[17] Kaldellis J.K., et al., "Experimental validation of autonomous PV-based water pumping system optimum sizing", Renewable Energy, 34, 1106-1113, 2009.

[18] Granich, W. and Elmore, A.C., "An evaluation of the use of renewable energy to pump water in Sacala las Lomas, Guatemala", Environmental Earth Science, 61,4, 837-846, 2010.

[19] Dursun, E., vd., "Performance evaluation of a stand-alone photovoltaic/wind turbine/fuel cell power system for each province in the Aegean Region of Turkey", 5th International Ege Energy Symposium and Exhibition (IEESE-5), 298, 2010.

[20] Chen, H. H., et al., "Strategic selection of suitable projects for hybrid solar-wind power generation systems", Renewable and Sustainable Energy Reviews, 14, 413-421, 2010.

[21] Mokeddem, A., "Performance of a directly-coupled PV water pumping system", Energy Conversion and Management, 52, 3089-3095, 2011.

[22] Belgacem, B.G., "Performance of submersible PV water pumping systems in Tunisia", Energy for Sustainable Development, 16, 415-420, 2012.

[23] Yusufoğlu, G., "Şebeke elektriğinin bulunmadığı tarımsal alanlarda güneş enerjisiyle sulamanın yapılması", Marmara Üniversitesi, Fen Bilimleri Enstitüsü, Yüksek Lisans Tezi, 2013.

[24] Gençoğlu, E., "Güneş pili ile çalışan bir su pompalama sisteminin tasarımı ve gerçekleştirilmesi" Fırat Üniversitesi Fen Bilimleri Enstitüsü Yüksek Lisans Tezi, Elazığ, 2015.

[25] Gündoğdu, A., "Fotovoltaik Sistemlerde Kısmi Gölgelenmenin Sistem Performansı Üzerindeki Etkileri", International Engineering, Science and Education Conference, 54-64, 2016.

BIOGRAPHIES

AHMET GÜNDOĞDU, Elazığ in 1974. He received the B.S. and M.S. degrees in electrical teaching from the University of Firat, Elazığ, in 2004 and the Ph.D. degree in electrical engineering from Firat University, Elazığ, in 2012.

From 2000 to 2012, he was a Research Assistant with the electrical teaching department. Since 2013, he has been an Assistant Professor with the Electrical Engineering Department, Batman University. His research interests include magnetic levitation, electrical machines, motor control.

BAYRAM GÜRE Batman in 1974. He received the B.S. degrees in electrical teaching from the University of Dicle and M.S. degrees in renewable energy systems from the University of Batman, Batman, in 2018.

Fuzzy Variable Order Extremum-Seeking Controller Design for Mobile Robots

O. ATAN

Abstract— In this paper, a fuzzy variable order extremum-seeking control (FVO-ESC) system for a mobile robot are designed. Fractional order controllers have advantages in the control of nonlinear systems such as a wider area of stability and performance enhancement in the presence of noise. The main proposal of the paper is to increase the performance of the fractional order controller. So, a variable order controller was designed for a mobile robot, and a fuzzy logic controller was designed according to user experiences to tune the controller order. The proposed FVO-ESC approach has been validated the effects on nonlinear systems such as the mobile robot system. It has been put forward in the preliminary investigation that the order of the fractional order ESC controller affects the overshoot and time to reach the target. The results suggested that a variable-level controller would have better performance. The results show that the proposed FVO-ESC control approach provides optimum performance for mobile robot systems.

Index Terms— Mobile robots, Variable Order Systems, Extremum-Seeking Control.

I. INTRODUCTION

THE EXTREMUM SEEKING control (ESC) method aims to meet nonlinear performance criteria of a system using the adaptive control method. The ESC method has been used in a lot of engineering systems such as nuclear reactors [1, 2], tracking the maximum power point of renewable energy systems [3–5], control of chemical systems [6–8], control of bioreactors [9–13], and mobile robots [14–18]. Because the ESC method has a lot of applications in the control of physical systems, researchers are interested in this control method. Especially due to increasing interest in autonomous vehicles and renewable energy systems, researchers have focused on the ESC control method. The following studies were focused recently: Atta realized a semi-global practical asymptotic stability analysis for phasor ESC with a nonlinear dynamic system [19]. The global extremum seeking point was designed and modelled using an asymptotic perturbed ESC and was applied to a photovoltaic system and fuel cell by Thounthong [20]. Wang improved an ESC algorithm without oscillation in

steady state for an antilock braking system, and the algorithm was compared with a sliding-mode-based ESC scheme for an antilock braking system [21]. Guay and Dochain considered real-time optimization of the ESC method and applied several example systems to show the effectiveness of their proposed system [22]. Nešić worked on dynamic feature and convergence analysis of ESC [23]. Hong and Li optimized ESC parameters using the particle swarm optimization (PSO) method, which guaranteed convergence [24]. These optimization methods and others aimed to decrease the convergence error and increase the speed of ESC for engineering applications [7, 12, 14, 15, 25–30].

Malek and Chen, who introduced a different approach to the ESC method, used a fractional order integrator instead of the classical integrator in the ESC, and their work was found to outperform the classical ESC in simulation and application results [31, 32]. Because the fractional order control systems, which have non-integer order, have a wider region of stability than integer order control, fractional order control systems are shown to have better performance than classical integer control systems in the literature [33–36]. However, a significant problem in the fractional order control method is the determination of the parameters of the controller, and there are papers on determining the parameters based on intelligent systems in the literature [37–41]. The following intelligent methods for optimization of the fractional order control systems have been reported: Biswas et al. designed a fractional-order $PI^\lambda D^\mu$ controller using an improved differential evolution [37], Atan et al. used a fuzzy adaptive PSO algorithm for a fractional order PID controller and applied it to chaotic synchronization control [38]. Fractional order control parameters were optimized using PSO with improved dynamic parameter selection for a combined cycle power plant by Haji and Monje [39], and other researchers have used chaotic PSO for the optimization of the fuzzy fractional order control of a hybrid power system with renewable generation [40]. Another optimization method is based on the ABC algorithm for a fractional order controller [41]. These papers are focused on optimization of fractional order parameters, and constant values of the parameters are selected for each system. But when the parameters can be changed according to the system error, performance of the controller can be increased. It is known that the use of variable-order control systems improves the performance of the controller [42] as well as leading to successful results in variable order modelling of the systems [43].

In this paper, a variable order and fuzzy logic-based ESC method for a mobile robot model is proposed. Firstly, the

ÖZKAN ATAN, is with Department of Electrical-Electronic Engineering, Van Yüzüncü Yıl University, Van, Turkey, (e-mail: oatan@yyu.edu.tr).

https://orcid.org/0000-0001-6443-9600

analysis and numeric solution method for the modeling and simulation of variable order systems are presented, because variable order systems have different solution methods from fractional order systems. Because numerical solution techniques of variable order systems differ from the analysis of classic fractional order systems, Adams-Bashforth-Moulton analysis method, which is based on the Volterra integration method, have been used. With the stability analysis method, the order range of the system is defined in the stability area in this paper, and the other parameters are defined by the PSO method. In addition, the fractional controller parameters used for comparison are also optimized by the PSO method. To make a comparison with the proposed control system, the mobile robot system model is used as a test bench. The mobile robot can move on two axes to reach the target when controlled by the variable order ESC method and fractional order control. When the order of the ESC system is changed according to the error between the target and robot position, it is expected that the controller performance will increase.

This paper is organized as follows. The variable order system is formulated in Section II. The novel variable order extremum-seeking controller is presented in Section III. The stability of the mobile robot plant and variable order ESC are introduced in Section IV. The results are demonstrated in Section V, and finally, our conclusion is presented in Section VI.

II. VARIABLE ORDER SYSTEMS

A. Fractional Order Calculus

Despite the fact that fractional order systems have been introduced in the 17th century, which will lead to a useful paradox, the engineering applications on this topic are based on the 20th century [44]. These techniques are the Grunwald–Letnikov (GL) method (Eq. 1) and the Riemann–Liouville (RL) method (Eq. 2) [44, 45]. The GL equation is defined as the limit approximation as follows:

$$_aD_t^\alpha f(t) = \lim_{h \to \infty} \frac{1}{\Gamma(\alpha)h^\alpha} \sum_{k=0}^{[(t-a)/h]} \frac{\Gamma(\alpha+k)}{\Gamma(k+1)} f(x-kh) \quad (1)$$

where Γ is the gamma function. Another popular method is the RL method based on the continuous time function. The method is defined as:

$$_aD_t^\alpha f(t) = \frac{1}{\Gamma(m-\alpha)} \left(\frac{d}{dt}\right)^m \int_a^t \frac{f(\tau)}{(t-\tau)^{1-(m-\alpha)}} d\tau \quad (2)$$

where m is defined as $m-1 < \alpha < m$. In recent years, many papers on fractional order systems analysis, which uses the Laplace transform method, have also appeared. GL approximation has been used for all the analysis in this paper.

B. Analysis of Variable Order System.

Several analysis methods have been proposed for variable order differential equations. Because the variable order differential equation is much more complex than the fractional order differential equations, a comprehensive study must be realized [46]. Although they have some negative features, researchers have focused on variable order systems because

their success has been shown in several papers in the literature [47–50], and the researchers used generally Volterra integration model in the works. For variable order system analysis, Volterra integration can be used as follows:

$$x(t) = \sum_{l=0}^{[\alpha]} x_0^{(l)} \frac{t^l}{l!} + \int_0^t \frac{(t-\tau)^{\alpha(\tau)-1}}{\Gamma(\alpha(\tau))} f(\tau, x(\tau)) d\tau \quad (3)$$

Voltera integration model is used continuous time model. For numerical solution methods, Adams-Bashforth-Moulton method is used. In this section, the Adams-Bashforth-Moulton predictor-corrector method is applied to implement the numerical solution of a function as:

$$x_{k+1} = x_0 + \frac{h^{q_1(t_{k+1})}}{\Gamma(q_1(t_{k+1})+2)} f_1(x_{k+1}^p)...$$
$$...+ \sum_{i=0}^{n} \frac{h^{q_1(t_{k+1})} \gamma_{1,k+1}}{\Gamma(q_1(t_{k+1})+2)} f_1(x_i) \quad (4)$$

where x_{k+1}^p, t_{k+1}, $\gamma_{i,k+1}$, and $\beta_{1,k+1}$ are given as follows:

$$x_{k+1}^p = x_0 + \sum_{i=0}^{n} \frac{\beta_{1,k+1}}{\Gamma(q_1(t_{k+1})+2)} f_1(x_i) \quad (5)$$

$$t_{k+1} = (n+1)h$$

$$\gamma_{i,k+1} = \begin{cases} k^{q_i(t_{k+1})+1} - (k-q_i(t_{k+1}))(k+1)^{q_i(t)} & i=0 \\ (k-i-2)^{q_i(t_{k+1})+1} + (k-i)^{q_i(t_{k+1})+1}... \\ ...-2(k-i+1)^{q_i(t_{k+1})+1} & 1 \le i \le k \\ 1 & i=k+1 \end{cases} \quad (6)$$

$$\beta_{i,k+1} = \frac{h^{q_i(t_{k+1})}}{q_i(t_{k+1})} \left((k-i+1)^{q_i(t_{k+1})+1} - (k-i)^{q_i(t_{k+1})+1}\right)$$

where Γ, h, and k parameters are given respectively gamma function, step range, and step. The numerical analysis method, which is used in this paper, is the most widely used in variable order calculus.

III. VARIABLE ORDER EXTREMUM-SEEKING CONTROLLER

A. Classical Extremum-Seeking control

Definition: ESC was firstly defined by Draper and Li in 1951. Although different algorithms for classical ESC have been presented, the sinusoidal perturbed ESC structure has drawn the most interest in the literature [31, 51]. There are high- and low-pass filters in classical ESC, but the low-pass filter is eliminated to simplify the ESC. The form of a simplified ESC for a MIMO system is shown in Figure 1. As shown in Figure 1, periodic perturbation ($sin(\omega t)$ and $cos(\omega t)$) is used to estimate $\hat{x}$ and $\hat{y}$ There are high-pass filters in the scheme, and it is used to eliminate the DC signal in x and y. In here, even if the filters do not directly affect the time taken to reach the target, they reduce the oscillation amplitude [31, 51]. The difference between the system points and extremum points in the classical ESC algorithm generates the amplitude of the sinus signal. In the system, in order to $\hat{x}$ and $\hat{y}$ estimate approximately estimate the extremum x^* and y^*, J is defined as:

$$J = k_a - k_x(\hat{x}-x^*)^2 - k_y(\hat{y}-y^*)^2 \qquad (7)$$

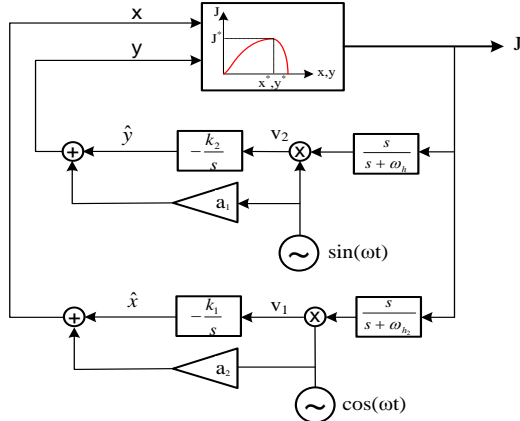where k_a, k_x, and k_y, which are adjusted approximation speed, and they are constant parameters.

Fig. 1. Classical simplified extremum-seeking control (ESC)

$$v = \begin{bmatrix} v_1 \\ v_2 \end{bmatrix} \begin{bmatrix} sin(\omega t).\left[J(x,y)*L^{-1}\left(\dfrac{s}{s+\omega_h} \right) \right] \\ cos(\omega t).\left[J(x,y)*L^{-1}\left(\dfrac{s}{s+\omega_h} \right) \right] \end{bmatrix} \qquad (8)$$

$$\begin{bmatrix} x \\ y \end{bmatrix} = \int \begin{bmatrix} -k_1 & 0 \\ 0 & -k_2 \end{bmatrix} \begin{bmatrix} v_1 \\ v_2 \end{bmatrix} dt + \begin{bmatrix} a_1 & 0 \\ 0 & a_2 \end{bmatrix} \begin{bmatrix} sin(\omega t) \\ cos(\omega t) \end{bmatrix} \qquad (9)$$

The parameters (k_a, k_x, k_y, a_1, a_2, ω_h) in the control system are important for the performance of the system. So, for determination of the parameters, which must be tuned and calibrated adequately, ESC design rules are given in the literature [31, 52].

B. Stability of Simplified ESC:

For the stability of the ESC, the method given by Krstic in [53] is used in this paper. The model in Figure 1 is described by the equations:

$$J = j^* + k_x(x-x^*)^2 + k_y(x-x^*)^2 \qquad (10)$$

$$x = a.cos(\omega t) - \frac{k}{s}(v_1)$$
$$y = a.sin(\omega t) - \frac{k}{s}(v_2) \qquad (11)$$

$$v_1 = a.cos(wt).\left[\frac{s}{s+\omega_h} * j(x,y) \right]$$
$$v_2 = a.sin(wt).\left[\frac{s}{s+\omega_h} * j(x,y) \right] \qquad (12)$$

When Lemmas 3.1–3.3 in [53] are applied to the system, it can be seen that the system has achieved stability conditions.

$$v_1 = a.\frac{1}{2}.\left(e^{i\omega t}+e^{-i\omega t}\right)\left[\frac{s}{s+\omega_h} \right] j(x,y)$$

$$= a.\frac{1}{2}.L^{-1}\left[\frac{\frac{s}{(s-i\omega)(s+\omega_h)}+...}{...\frac{s}{(s+i\omega)(s+\omega_h)}} \right] j(x,y) \qquad (13)$$

$$= \frac{1}{2}a\left[\frac{1}{2}e^{-itw}(1-i)+\frac{1}{4}e^{-tw}(a+2-i(2-a))... \\ ...+\frac{1}{4}ae^{itw}(1+i) \right] j(x,y)$$

$$v_2 = a.\frac{1}{i2}.\left(e^{i\omega t}-e^{-i\omega t}\right)\left[\frac{s}{s+\omega_h} \right] j(x,y)$$

$$= a.\frac{1}{i2}.L^{-1}\left[\frac{\frac{s}{(s+i\omega)(s+\omega_h)}...}{...-\frac{s}{(s-i\omega)(s+\omega_h)}} \right] j(x,y) \qquad (14)$$

$$= \frac{1}{2}a\left[-\frac{1}{2}e^{-itw}(1-i)-\frac{1}{4}e^{-tw}(a+2+i(a+2))... \\ ...+\frac{1}{4}ae^{itw}(1-i) \right] j(x,y)$$

where the stability conditions of the system are:
$$0 < \omega$$

$$a < \infty$$

C. Design of Variable Order Extremum-Seeking Controller

Fractional order ESC: A fractional order ESC, which is a combination of the ESC and fractional order systems, has been put forward by Malek and Chen [31]. The novelty in [31] is that the fractional order of the control system is defined with a fractional model, and the method has been used to increase the performance of the system. The block diagram of the fractional order ESC system is shown in Figure 2, and the effect of the fractional order on the control system is seen in Figure 3.

In Figure 3, it can be seen that the order of the fractional ESC affects the control performance. It is observed that the overshoot is increased but the setting time is decreased when the order (φ) of the fractional ESC is decreased. Similarly, it is seen in Figure 3 that the optimum result is in the range of;
$$0.9 < \varphi < 1.2$$

If the order can change according to the error of the mobile robot position, the increase of the system performance can be observed. Therefore, in order to improve the performance of the mobile robot, the variable order ESC method is used in this paper.

D. Control Order Changed by Fuzzy Logic

Classical ESC, which is given in Figure 1, uses two low-pass filters and two integrators. In [31, 32], a fractional order integrator is used instead of a conventional integrator to increase the performance of the controller. The novelty in our work is that variable integrators are used instead of the classical integrators and fractional integrators, and the orders of the integrators are adjusted by fuzzy logic.

A fuzzy variable order controller has been put forward by Pan and Xue [17], which changes the order of a variable order PI by the fuzzy logic method. The advantages of fuzzy adaptive control have been given in some papers [54, 55].
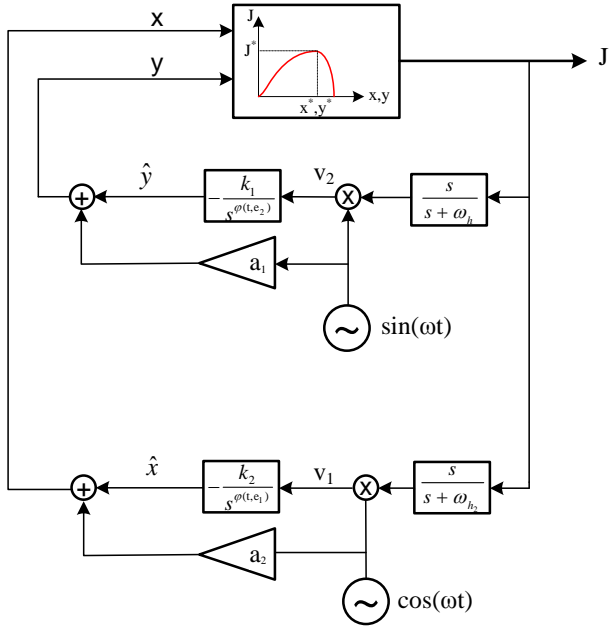

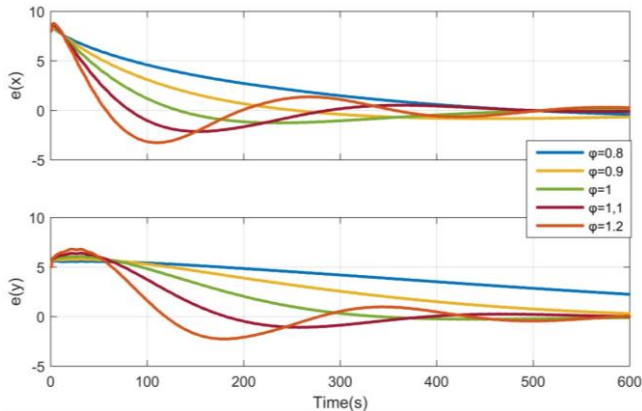Fig. 2. Block diagram of the variable order ESC system

Fig. 3. Effect of the different order on performance of the system

These papers show effects of the adaptive control system such as overshoot, setting time, and the chattering phenomenon. In this paper, the orders of the variable-order ESC according to the rule bases in the fuzzy logic are changed in order to decrease the setting time. The fuzzy rules have two inputs and two outputs involved in the ESC. The system inputs are the x position error, the y position error, and their derivatives:

$$e_1 = x - x^*$$
$$e_2 = y - y^* \tag{15}$$

where $e_{1,2}$ and $e_{1,2}$ are errors and the other system input is the derivative of the error. The variable order ESC φ_1 and φ_2 are the outputs of the fuzzy system.

$$\varphi_{1,2} = 0.9 + \varphi_{fuzzy_{1,2}} \tag{16}$$

where $\varphi_{fuzzy_{1,2}}$ is calculated by fuzzy rules. The fuzzy system is designed using fuzzification, rule bases, and defuzzification.

The rules and membership functions are created according to the results from Figure 3. Rule bases are given in Table 1, and membership functions, which have mainly triangular shapes and five linguistic variables, are given in Figure 4. The linguistic variables are negative big (NB), negative (N), zero (Z), positive (P), and positive big (PB).

TABLE 1
FUZZY RULE BASE FOR $\varphi_{fuzzy_{1,2}}$

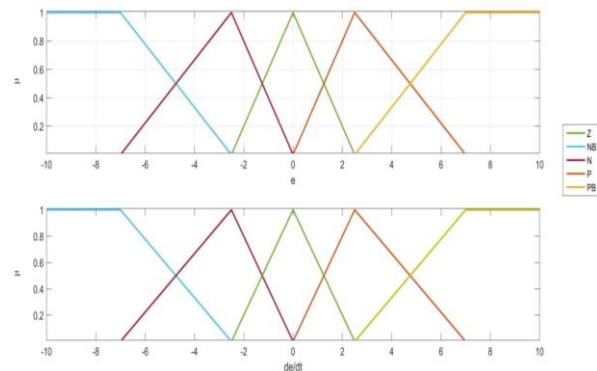| e \ $\dot{e}$	NB	N	Z	P	PB
NB	NB	NB	NB	N	N
N	N	N	NB	N	N
Z	PB	P	Z	N	NB
P	PB	PB	PB	P	P
PB	PB	PB	PB	PB	PB

Fig. 4. Membership functions of $e_{1,2}$ and $\dot{e}_{1,2}$

IV. FUZZY VARIABLE ORDER EXTREMUM-SEEKING CONTROLLER FOR MOBILE ROBOT

In this paper, in order to see the performance of the fuzzy variable order ESC and compare it with the other ESC methods, a mobile robot which is a 2D point mass vehicle, is employed (Figure 5). The system has two axes (x, y) and velocities (v_x and v_y) on the axes. The system dynamics are:

$$\dot{x} = v e^{j\theta} = v_x + j v_y$$
$$\dot{\theta} = \omega \tag{17}$$

where v_x and v_y are the velocity on the x and y axes, and ω is the angular velocity.

In order to compare the performance of the fuzzy variable order ESC and classical ESC, both control methods use the same parameters in the control system.

A. Fractional order ESC

In this section, the performances of the mobile robot have been compared with the fractional order ESC. It is worth mentioning that the orders of the fractional order ESC were also defined by the performance index and the performance index has been chosen as x and y position errors.
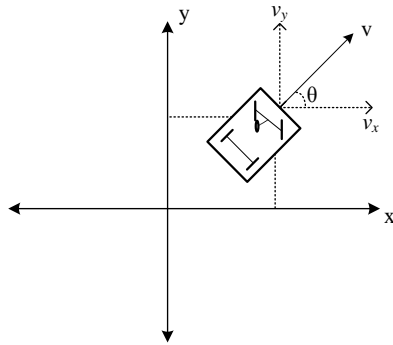
Fig. 5. A mobile robot on 2D points

The fractional order ESC and mobile robot parameters are given in Table 2, and to compare the performances of the mobile robot, the results of classical ESC and fractional order ESC for the same parameters are presented in Fig. 6.

TABLE 2
PARAMETERS OF THE CONTROLLER

Control Parameters						
k_1	k_2	a_1	a_2	ω_1	ω_2	Ω
1	1	0.5	0.5	1	1	20
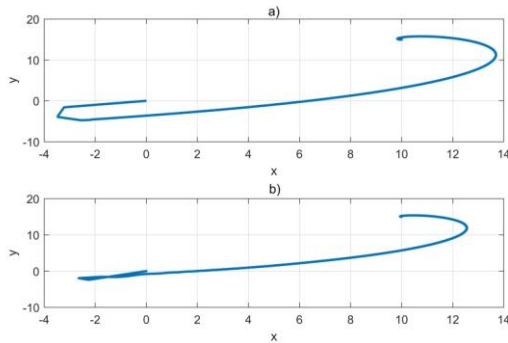
Fig. 6. Performance comparisons of mobile robot a) classical ESC b) fractional order ESC

It can be seen in Fig. 6 that the mobile robot employed to test the fractional-order ESC reached the destination by a shorter path and in a shorter time and clearly showed better performance than the classical ESC. From Figure 7, it can be clearly seen that the controller order affects the values of the overshoot and setting time. As the controller order increases, the overshoot increases, but this reduces the time it takes to reach a steady state. Based on this result, if the error has a small value, a small order is selected, and the order of the proposed controller increases in proportion with depending on the increase of the error. So, the performance indexes (setting time and overshoot) may have better values.
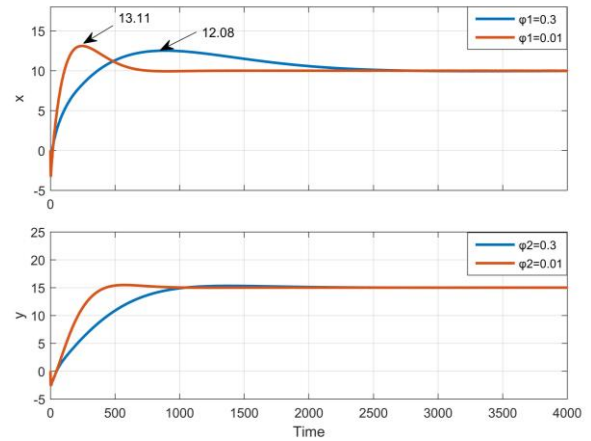

Fig. 7. Position errors of mobile robot for different fractional orders

B. Fuzzy Variable ESC

During the simulation, the mobile robot target vehicle follows the trajectory for x = 15 and y = 10 with the parameters set to the values given in Table 2. The value of J is initially high and then decreases during the simulation when using the proposed control method. Fractional order ESC has a more impressive result (overshoot and setting time) compared with classical ESC. The performance of the proposed control method shown in Figure 8, and the results have been compared with the results shown in Figure 6.

From Figure 8, it can be seen that fuzzy variable order ESC maintains satisfactory performance, namely a short rise time and less overshoot, when compared with classical ESC and fractional order ESC. For very complex systems such as mobile robot, the robot has better performance than classical ESC and fractional order ESC, as shown in Figure 9.

Changing of the fuzzy fractional order ESC, as shown in Figure 10, the system order is changed by the error. To compare with fractional order ESC and proposed controller, performance criteria such as overshoot and setting time are given in Table 3. It can be seen that the proposed controller has better performance than fractional order ESC. The overshoot decreased significantly (5.8%) in the x-axis, and relatively less in the y-axis. It is seen in Table 3 that there is a sitting time close to the average of both values in the fractional order controller.
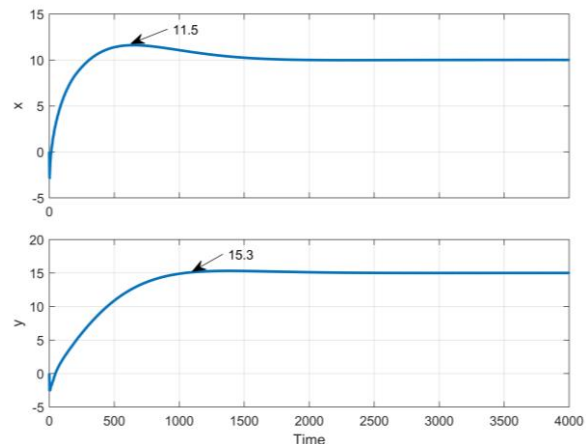

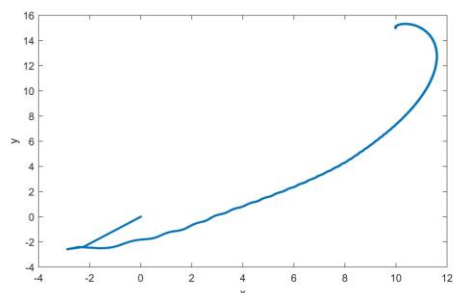Fig. 8. Performance results of the proposed control method

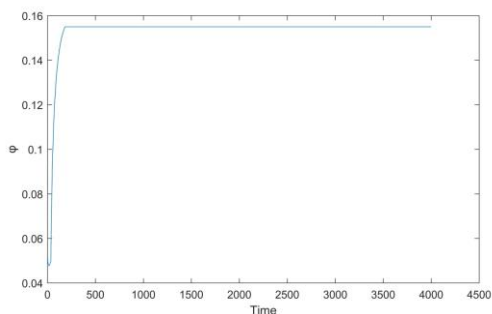Fig. 9. Motion of the mobile robot on 2D points

Fig. 10. The change of the system order

TABLE 3
OBTAINED RESULTS FROM PROPOSED CONTROLLER METHOD
AND FRACTIONAL ORDER ESC

		Control Method		
		Fractional Order ESC		Proposed Control
Parameters		$\varphi=0.01$	$\varphi=0.3$	
x	Overshoot	3.11	2.08	1.5
	Setting time	720s	2400s	1540s
y	Overshoot	0.45	0.5	0.3
	Setting time	934s	2110s	1452s

V. CONCLUSION

This paper proposes variable order ESC using fuzzy logic for a mobile robot. The order of the ESC controller is based on fractional calculus, adaptively adjusted with fuzzy logic. The performance analyses based on the overshoot and rise time show that the proposed variable order of the controller can provide improvements in performance improvement compared to the fractional order ESC algorithm. The fractional order ESC model was first designed by Malek and Chen [31], [32], who proved that ESC provides good performance against noise and uncertainties. The controller order affects the overshoot and the setting time for the mobile robot have shown, and the approach provides a remarkable performance enhancement, because a decrease in the value of the order causes an increase in the amount of overtaking but gives a better result in terms of setting time. So, if the controller order according to the tracking error can be changed, it will show better performance than classical fractional order control. The simulation results for a mobile robot in this paper justify the performance enhancement.

REFERENCES

[1] D. Carnevale, A. Astolfi, C. Centioli, S. Podda, V. Vitale, and L. Zaccarian, "A new extremum seeking technique and its application to maximize RF heating on FTU," Fusion Eng. Des., vol. 84, no. 2–6, pp. 554–558, Jun. 2009.
[2] Y. Ou et al., "Design and simulation of extremum-seeking open-loop optimal control of current profile in the DIII-D tokamak," Plasma Phys. Control. Fusion, vol. 50, no. 11, p. 115001, Nov. 2008.
[3] U. Ciri, M. A. Rotea, and S. Leonardi, "Model-free control of wind farms: A comparative study between individual and coordinated extremum seeking," Renew. Energy, vol. 113, pp. 1033–1045, 2017.
[4] B. Hu, Y. Li, B. Mu, S. Wang, J. E. Seem, and F. Cao, "Extremum seeking control for efficient operation of hybrid ground source heat pump system," Renew. Energy, vol. 86, pp. 332–346, 2016.
[5] N. Bizon, "Global Maximum Power Point Tracking (GMPPT) of Photovoltaic array using the Extremum Seeking Control (ESC): A review and a new GMPPT ESC scheme," Renew. Sustain. Energy Rev., vol. 57, pp. 524–539, 2016.
[6] H. C. Lee, S. Kim, J. P. Heo, D. H. Kim, and J. Lee, "Wiener Model and Extremum Seeking Control for a CO Preferential Oxidation Reactor with the CuO-CeO2 catalyst," IFAC-PapersOnLine, vol. 48, no. 8, pp. 574–579, 2015.
[7] G. Lara-Cisneros, R. Aguilar-López, and R. Femat, "On the dynamic optimization of methane production in anaerobic digestion via extremum-seeking control approach," Comput. Chem. Eng., vol. 75, pp. 49–59, 2015.
[8] D. Krishnamoorthy, A. Pavlov, and Q. Li, "Robust Extremum Seeking Control with application to Gas Lifted Oil Wells," IFAC-PapersOnLine, vol. 49, no. 13, pp. 205–210, 2016.
[9] P. Cougnon, D. Dochain, M. Guay, and M. Perrier, "On-line optimization of fed-batch bioreactors by adaptive extremum seeking control," IFAC Proc. Vol., vol. 43, no. 6, pp. 108–113, 2010.
[10] M. Titica, D. Dochain, and M. Guay, "Real-Time Optimization of Fed-Batch Bioreactors via Adaptive Extremum-Seeking Control," Chem. Eng. Res. Des., vol. 81, no. 9, pp. 1289–1295, 2003.
[11] P. Cougnon, D. Dochain, M. Guay, and M. Perrier, "On-line optimization of fedbatch bioreactors by adaptive extremum seeking control," J. Process Control, vol. 21, no. 10, pp. 1526–1532, 2011.
[12] A. Vargas, J. A. Moreno, and A. Vande Wouwer, "Super-twisting estimation of a virtual output for extremum-seeking output feedback control of bioreactors," J. Process Control, vol. 35, pp. 41–49, 2015.
[13] O. Trollberg and E. W. Jacobsen, "Greedy Extremum Seeking Control with Applications to Biochemical Processes," IFAC-PapersOnLine, vol. 49, no. 7, pp. 109–114, 2016.
[14] Y. Zhang, O. Makarenkov, and N. Gans, "Extremum seeking control of a nonholonomic system with sensor constraints," 2016.
[15] V. Koropouli, A. Gusrialdi, S. Hirche, and D. Lee, "An extremum-seeking control approach for constrained robotic motion tasks," Control Eng. Pract., vol. 52, pp. 1–14, 2016.
[16] A. S. Matveev, M. C. Hoy, and A. V. Savkin, "3D environmental extremum seeking navigation of a nonholonomic mobile robot," Automatica, vol. 50, no. 7, pp. 1802–1815, 2014.
[17] Y. Tian, N. Sarkar, Y. Tian, and N. Sarkar, "Control of a Mobile Robot Subject to Wheel Slip," J Intell Robot Syst, vol. 74, pp. 915–929, 2014.
[18] C. Li, Z. Qu, and M. A. Weitnauer, "Distributed extremum seeking and formation control for nonholonomic mobile network," Syst. Control Lett., vol. 75, pp. 27–34, 2015.
[19] K. T. Atta, A. Johansson, and T. Gustafsson, "On the stability analysis of phasor and classic extremum seeking control," Syst. Control Lett., vol. 91, pp. 55–62, 2016.
[20] P. Thounthong, M. Raducu, and L. M. Constantinescu, "Designing and modelling of the asymptotic perturbed extremum seeking control scheme for tracking the global extreme," Int. J. Hydrogen Energy, vol. 42, no. 28, pp. 17632–17644, 2017.
[21] L. Wang, S. Chen, and K. Ma, "On stability and application of extremum seeking control without steady-state oscillation," Automatica, vol. 68, pp. 18–26, 2016.
[22] M. Guay and D. Dochain, "A time-varying extremum-seeking control approach," Automatica, vol. 51, pp. 356–363, Jan. 2015.
[23] D. Nešić, "Extremum Seeking Control: Convergence Analysis," Eur. J. Control, vol. 15, no. 3–4, pp. 331–347, Jan. 2009.

[24] C. Hong and K. Li, "Swarm intelligence-based extremum seeking control," Expert Syst. Appl., vol. 38, no. 12, pp. 14852–14860, Nov. 2011.

[25] M. Haring, N. van de Wouw, and D. Nešić, "Extremum-seeking control for nonlinear systems with periodic steady-state outputs," 2013.

[26] C. Yin, B. Stark, and S. Zhong, "Adaptive minimum energy cognitive lighting control: Integer order vs fractional order strategies in sliding model-based extremum seeking," Mechatronics, vol. 23, no. 7, pp. 863–872, 2013.

[27] K. T. Atta, A. Johansson, and T. Gustafsson, "Extremum seeking control based on phasor estimation," Syst. Control Lett., vol. 85, pp. 37–45, 2015.

[28] S. Z. Khong, D. Nešić, and M. Krstić, "Iterative learning control based on extremum seeking," 2016.

[29] B. Mu, Y. Li, J. M. House, and T. I. Salsbury, "Experimental evaluation of anti-windup extremum seeking control for airside economizers," Control Eng. Pract., vol. 50, pp. 37–47, 2016.

[30] C. Yin, S. Dadras, X. Huang, J. Mei, H. Malek, and Y. Cheng, "Energy-saving control strategy for lighting system based on multivariate extremum seeking with Newton algorithm," Energy Convers. Manag., vol. 142, pp. 504–522, 2017.

[31] H. Malek and Y. Chen, "Fractional Order Extremum Seeking Control: Performance and Stability Analysis," IEEE/ASME Trans. Mechatronics, vol. 21, no. 3, pp. 1620–1628, Jun. 2016.

[32] H. Malek, S. Dadras, and Y. Chen, "Performance analysis of fractional order extremum seeking control," ISA Trans., vol. 63, pp. 281–287, 2016.

[33] C. A. Monje, Y. Chen, B. M. Vinagre, D. Xue, and V. Feliu, Fractional-order Systems and Controls. London: Springer London, 2010.

[34] S. E. Hamamci, "An Algorithm for Stabilization of Fractional-Order Time Delay Systems Using Fractional-Order PID Controllers," IEEE Trans. Automat. Contr., vol. 52, no. 10, pp. 1964–1969, Oct. 2007.

[35] Y. Chen, I. Petras, and D. Xue, "Fractional order control - A tutorial," in 2009 American Control Conference, 2009, pp. 1397–1411.

[36] M. Beschi, F. Padula, and A. Visioli, "The generalised isodamping approach for robust fractional PID controllers design," Int. J. Control, vol. 90, no. 6, pp. 1157–1164, Jun. 2017.

[37] A. Biswas, S. Das, A. Abraham, and S. Dasgupta, "Design of fractional-order PIλDμ controllers with an improved differential evolution," Eng. Appl. Artif. Intell., vol. 22, no. 2, pp. 343–350, Mar. 2009.

[38] O. Atan, M. Turk, and R. Tuntas, "Fractional Order Controller Design for Fractional Order Chaotic Synchronization," Int. J. Nat. Eng. Sci., vol. 7, no. 1, pp. 71–77, 2013.

[39] V. Haji Haji and C. A. Monje, "Fractional order fuzzy-PID control of a combined cycle power plant using Particle Swarm Optimization algorithm with an improved dynamic parameters selection," Appl. Soft Comput., vol. 58, pp. 256–264, Sep. 2017.

[40] I. Pan and S. Das, "Fractional order fuzzy control of hybrid power system with renewable generation using chaotic PSO," ISA Trans., vol. 62, pp. 19–29, May 2016.

[41] H. Senberber and A. Bagis, "Fractional PID controller design for fractional order systems using ABC algorithm," in 2017 Electronics, 2017, pp. 1–7.

[42] L. Liu, F. Pan, and D. Xue, "Variable-order fuzzy fractional PID controller," ISA Trans., vol. 55, pp. 227–233, Mar. 2015.

[43] S. Ma, Y. Xu, and W. Yue, "Numerical Solutions of a Variable-Order Fractional Financial System," J. Appl. Math., vol. 2012, pp. 1–14, Sep. 2012.

[44] I. Podlubny, Fractional differential equations : an introduction to fractional derivatives, fractional differential equations, to methods of their solution and some of their applications. Academic Press, 1999.

[45] S. M. Miller and R. Bertram, An Introduction to the Fractional Calculus and Fractional Differential EquationsNo Title. USA: Wiley, 1993.

[46] S. Ma, Y. Xu, and W. Yue, "Numerical Solutions of a Variable-Order Fractional Financial System," J. Appl. Math., vol. 2012, pp. 1–14, 2012.

[47] D. Sierociuk and M. Macias, "Comparison of variable fractional order PID controller for different types of variable order derivatives," in Proceedings of the 14th International Carpathian Control Conference (ICCC), 2013, pp. 334–339.

[48] P. Ostalczyk, D. Brzezinski, P. Duch, M. Łaski, and D. Sankowski, "The variable, fractional-order discrete-time PD controller in the IISv1.3 robot arm control," Open Phys., vol. 11, no. 6, pp. 750–759, Jan. 2013.

[49] P. Ostalczyk, "Variable-, fractional-order discrete PID controllers," in 2012 17th International Conference on Methods & Models in Automation & Robotics (MMAR), 2012, pp. 534–539.

[50] A. Razminia, A. F. Dizaji, and V. J. Majd, "Solution existence for non-autonomous variable-order fractional differential equations," Math. Comput. Model., vol. 55, no. 3–4, pp. 1106–1117, Feb. 2012.

[51] Q. Zheng and Z. Gao, 2010 29th Chinese Control Conference. I E E E, 2010.

[52] K. B. Ariyur and M. Krstić, Real-Time Optimization by Extremum-Seeking Control, vol. 0, no. 0. 2003.

[53] M. Krstiã, "Performance improvement and limitations in extremum seeking control," Syst. Control Lett., vol. 39, pp. 313–326, 2000.

[54] Y. Li, S. Sui, and S. Tong, "Adaptive Fuzzy Control Design for Stochastic Nonlinear Switched Systems with Arbitrary Switchings and Unmodeled Dynamics," IEEE Trans. Cybern., pp. 1–12, 2016.

[55] A. Boulkroune, "A fuzzy adaptive control approach for nonlinear systems with unknown control gain sign," Neurocomputing, vol. 179, pp. 318–325, Feb. 2016.

Özkan ATAN He received the M.Sc. and Ph.D. degrees in Electrical and Electronics Engineering from Yüzüncü Yıl University (Van, Turkey) and Fırat University (Elazığ, Turkey) in 2007 and 2014, respectively. He is an Assistant Professor in the Electrical and Electronics Engineering Department of Yüzüncü Yıl University. He works on control systems, chaotic & nonlinear systems, fractional order systems.

An Approximate Short Circuit Strategy for Transient MPPT Performance of Uniformly Irradiated Photovoltaic Modules

M.E. BAŞOĞLU

Abstract—**This paper presents an improved strategy to provide better maximum power point tracking (MPPT) performance and increase energy yield during transient state of MPPT process. This strategy is based on the estimation of short circuit current (SCC) of the photovoltaic (PV) system without short circuit. Besides that, this strategy aims to decrease convergence time to maximum power point (MPP) by preventing real short circuit of PV source and eliminating the additional switch requirement. To determine performance of the proposed strategy, simulation studies have been performed in MATLAB/Simulink and this strategy has been compared with fractional SCC (FSCC) technique and perturb and observe (P&O) algorithm. In addition, to make validation experimentally, a low powered single ended primary inductance converter (SEPIC) is realized. Both simulation and experimental results show that proposed strategy performs better transient MPPT performance than FSCC technique and P&O algorithm.**

Index Terms— **Fractional short circuit current, Maximum power point tracking, photovoltaic module, perturb and observe.**

I. INTRODUCTION

MAXIMUM power extraction of a PV system is an essential operation since PV systems have small power conversion efficiency. To obtain maximum efficiency, a power processing unit (PPU) is inserted between PV modules/array and load, battery and/or electrical grid. A PPU in a PV system should provide energy conversion with maximum efficiency. Lots of MPPT techniques have been presented to get the biggest efficiency and maximize energy from PV modules/arrays [1].

Among MPPT algorithms, P&O algorithm is widely used in industrial applications due to ease of implementation. However, its performance is poor in dynamic environmental conditions. Therefore, some parameters of P&O should be

MUSTAFA ENGİN BAŞOĞLU, is with Department of Electrical and Electronics Engineering University of Gümüşhane, Gümüşhane, Turkey,(e-mail: menginbasoglu@gumushane.edu.tr).

https://orcid.org/ 0000-0002-6228-4112

optimized [2]. For example, this algorithm has a paradigm about response time and fluctuation at steady state. Therefore, adaptive and variable duty step size approaches contribute performance of P&O [3]. In [4], in order to achieve fast MPPT operation, two step size incremental conductance (IC) is applied to boost converter. On the other hand, dynamic step size approach can be more useful compared with the fixed and/or two step sized technique. In [5], step size optimization on MPPT algorithm is studied deeply. Since P&O is easy to implement practically, its modification is very popular. In [6], changes in current, voltage and power are monitored and checked to make correct decision in rapid insolation variations. By additional checking of ΔI, failure operation in rapid insolation change is eliminated. IC is another popular algorithm. It also checks ΔI/ΔV to track MPP. One advantage of this algorithm is the high correctness in MPPT under rapidly changing weather conditions [7]. A fixed step sized model predictive control (MPC) based MPPT algorithm including IC is proposed in [8]. Results show that it performs better than conventional IC under dynamic weather condition. A modified version of IC is proposed for partially shaded PV systems to track global MPP [9]. In order to increase the performance of the hill climbing type MPPT techniques, a design guide is proposed to determine perturbation time and perturbation frequency correctly in MPPT systems [10]. A two stage global MPPT algorithm, including variable step size P&O and segmentation rule search approach, is proposed. This algorithm is developed after extensive simulations of many PV module manufacturer datasheets [11]. The first $0.8V_{OC}$ based algorithm is proposed by [12]. It samples the power in every consecutive peaks and compares values of power at these peaks to determine the global MPP. Recently, a hybrid algorithm containing $0.8V_{OC}$ model and P&O has been proposed for distributed MPPT applications in which each module realizes its own MPPT operation [13]. In this algorithm, global MPP is tracked effectively in a short duration which improves the dynamic MPPT performance. In another study, typical voltage-current (V-I) characteristic feature is used to perform MPPT in a single ended primary inductance converter (SEPIC) to realize tracking in a partially shaded and uniform irradiation conditions [14]. With the help of a look-up table and converter based formulation, PV module is roughly operated at the vicinity of MPP. A modified IC algorithm is presented in [15] to increase tracking speed in

uniform irradiance conditions. Even if this approach has a fast tracking capability, performance of this algorithm mainly depends on the PV parameters and loading conditions. A polynomial model of PV array is developed from a single diode circuit to determine MPP. Optimal selection of parameters is the main issue to be addressed in this study [16]. According to the results, this model is useful compared with the classical P&O. Because it has zero oscillation and no failure performance in rapidly changing weather conditions.

TABLE I
LIST OF ABBREVIATIONS AND NOMENCLATURE

Abbreviations		Definitions
MPPT	:	Maximum power point tracking
SCC	:	Short circuit current
PV	:	Photovoltaic
MPP	:	Maximum power point
FSCC	:	Fractional short circuit current
PPU	:	Power processing unit
SEPIC	:	Single ended primary inductance converter
DC	:	Direct current
P&O	:	Perturb and observe
IC	:	Incremental conductance
STC	:	Standard test condition
PWM	:	Pulse width modulation
RMS	:	Root mean square
I_{PH} / I_{SC}	:	Photo current / Short circuit current
Q_A / Q_R	:	Ambient irradiance / Reference irradiance
T_J / T_R	:	Junction / Reference temperature
V_{PV} / I_{PV}	:	Voltage and current of PV module
V_O / V_{IN}	:	Output and input of SEPIC voltage
K_I	:	Temperature coefficient
q / k	:	Electron charge / Boltzmann constant
A	:	Diode ideality factor
R_S / R_P	:	Series and parallel resistor
R_L / R_{PV}	:	Load resistor / Equivalent resistance of PV
I_O	:	Output current of SEPIC
L_P / L_S	:	Primary and secondary inductance
C_O / C_S	:	Output capacitor / AC capacitor
ΔV_{IN} / ΔV_O	:	Ripple on input voltage / output voltage
f_P	:	Switching frequency
ΔI_{Lp} / ΔI_{Ls}	:	Current ripples of inductors

FSCC is one of the conventional MPPT techniques using linear relationship between SCC and maximum power current [17]. It is generally accepted that ratio of SCC and maximum power current is a constant since variations in solar irradiance and temperature does not affect this ratio significantly. On the other hand, FSCC requires additional semiconducting switch and integrated circuit for gate driving, resulting low tracking speed and small tracking efficiency because of the periodical disconnection between PV module/array and load, battery and/or electrical grid. The main idea behind this research is to improve transient MPPT performance of PV systems in uniform irradiance condition. A strategy is proposed for the purpose of estimation the value of SCC without additional switch. Thanks to this estimation, PV system is not short circuited and more energy can be transferred from PV sources

to the output of the PPU. To determine performance of this strategy, one of the advanced buck-boost converter topology, low power SEPIC has been designed and realized. Remains of the paper continue as follows. Theory of the proposed strategy is presented in the next section. In Section III, design steps of the SEPIC and simulation results are given. Experimental results are presented in the Section IV. Finally, main outcomes of the proposed strategy is summarized in Section V.

II. THEORY OF THE PROPOSED STRATEGY

PV modules are nonlinear power sources having exponential I-V characteristic. They are combined with many PV cells connected in series and/or parallel. Nonlinearity of the PV cell is come from its p-n structure which is similar to basic diode. A typical PV cell can be modelled by a controlled current source, a diode, and two resistors. [18]. A common type of equivalent circuit of a PV cell is presented in Fig. 1.
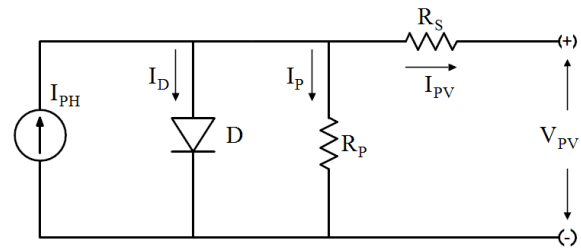

Fig.1. One diode electrical model of a typical PV cell

PV cells can be considered as controlled direct current (DC) source. The electrical current generated from the PV cell mainly depends on the irradiance received by the PV cell. In addition, temperature and coefficients have minor effect on the changes in PV power/current. Photo/light current of a PV cell can be calculated as in (1) [18].

$$I_{PH} = I_{SC}\frac{Q_A}{Q_R} - K_I(T_J - T_R) \tag{1}$$

In (1), I_{PH} is the photo current of the cell, Q_A is the ambient irradiance, Q_R is the reference irradiance, K_I is the temperature coefficient of the current, T_J and T_R are the junction temperature and reference temperature, respectively.

Photo current of a PV cell is the maximum available current generally defined as short circuit current. By extracting the diode current from the photo current, PV current feeding to the load can be found as in (2) [19].

$$I_{PV} = I_{PH} - I_S\left(e^{\left[\frac{q(V_{PV} - I_{PV}R_S)}{kT_JA}\right]} - 1\right) - \frac{V_{PV} - I_{PV}R_S}{R_P} \tag{2}$$

In (2), I_{PV} and V_{PV} are the current and voltage of PV module, I_S is the diode saturation current, q is the electron charge, k is the Boltzmann constant, R_S is the series resistor, R_P is the parallel resistor and A is the ideality factor of diode.

Conventional MPPT algorithms have some disabilities such as low response time causing small tracking efficiency and big power fluctuation at steady state condition. Therefore, modern MPPT techniques have two stages at least. In the first stage, operation in vicinity of MPP is aimed. Then, a typical MPPT technique such as P&O, IC and constant voltage algorithm are used. In this study, performance improvement in the first stage is focused.

In order to estimate SCC of the PV module/array, first, power-voltage (P-V) characteristic curves of the PV system are analyzed. Number of P-V curves is determined by the value of solar irradiance step which is 100W/m^2 [12]. Minimum and maximum values of irradiance are 100W/m^2 and 1000W/m^2 [12]. Number of these curves is calculated by the combination of C(10,1)=10. According to these P-V curves, equivalent resistances seen by the PV module for all irradiances are determined by (3) [14]. P-V and I-V curves of the PV module used in this study are presented in Fig. 2.

$$R_{PV(n)} = \frac{V_{MPP(n)}}{I_{MPP(n)}} = \frac{V_{MPP(n)}^2}{P_{MPP(n)}} \tag{3}$$

In (3), $V_{MPP(n)}$ and $I_{MPP(n)}$ are the nth voltage and current of the PV module, respectively. $R_{PV(n)}$ is the nth average value of resistance seen from output of the PV module.
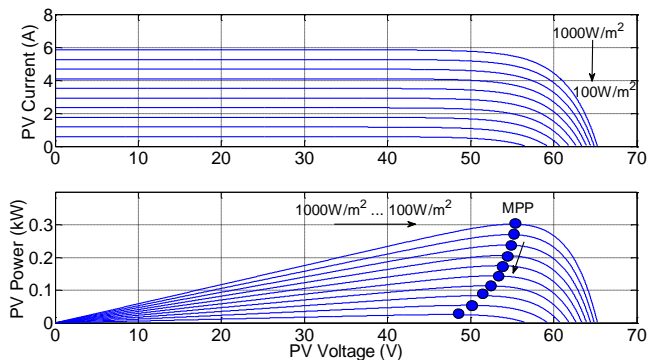
Fig.2. I-V and P-V characteristic curves of selected PV module

Specifications of the PV module at standard test conditions (STC) used in this study are listed in Table II. Type of PV cell used in this module is monocrystal. Characteristic curves given in Fig. 2 corresponds to the PV system in which three PV modules are connected in series to form a small PV array. To simplify the validation of the proposed strategy, resistive load is selected which is connected to the output of the SEPIC. As known, SEPIC is a kind of buck-boost converter. Its voltage gain can be formulated as in (4) [20].

$$V_O = V_{IN} \frac{D}{1-D} \tag{4}$$

In (4), V_O and V_{IN} are the output and input voltage of converter, respectively. D is the duty ratio of the pulse width modulation (PWM). Since input port of the converter is

connected to the PV module, $V_{IN}=V_{PV}$. V_O and V_{PV} can be formulated as in (5) and (6), respectively.

$$V_O = I_O R_L \tag{5}$$

$$V_{PV} = I_{PV} R_{PV} \tag{6}$$

TABLE II
SPECIFICATION OF THE PV MODULE at STC

Specification	Value
Maximum power	101W
Maximum power voltage	18.4V
Maximum power current	5.51A
Open circuit voltage	21.7
Short circuit current	5.85
Type of cell used in the module	Monocrystal

In (5), I_O is the output current of the converter, R_L is the load resistance. By combining (4), (5) and (6), duty ratio of PWM for irradiance conditions providing MPPT operation is specified as in (7) [14]. Number of duty ratio is n.

$$D(n) = \frac{1}{1 + \sqrt{\dfrac{R_{PV(n)}}{R_L}}} \tag{7}$$

It is easily said that value of D(n) is the biggest for highest irradiance condition since $R_{PV(n)}$ is smaller in 1000W/m^2 than that of the other irradiance conditions. So, to guarantee the operation in the constant current region which represents the left region of the MPP, the biggest value of duty ratio for a specified load is applied to the converter. In this way, vicinity of short circuit operation is provided without the need of real short circuit. Illustration of this operation is presented for ten different irradiance conditions in Fig. 3. For example, first, PV module is operated at the vicinity of MPP where red circles are located. Then P&O is activated to finely tune the operation point at MPP.
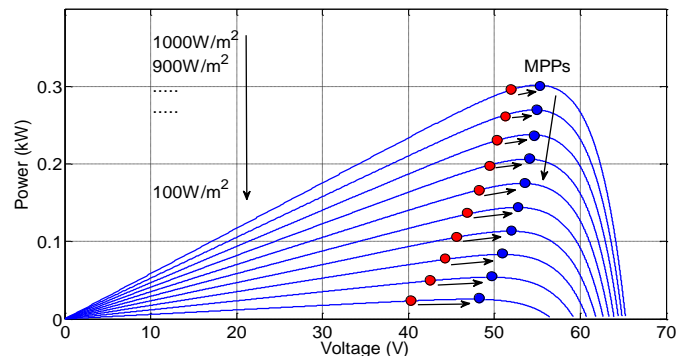

Fig.3. Illustration of the proposed strategy

III. DESIGN OF THE POWER STAGE OF THE SEPIC

In order to validate the proposed strategy, SEPIC is selected as a PPU since it is one of the buck-boost converters. It can increase or decrease the voltage which is a typical requirement

in a MPPT application. Typical SEPIC converter consists of two inductors, three capacitors, a power switch and a power diode as shown in Fig. 4. For a typical MPPT application, a current transducer and voltage dividing resistors are also used to sense current and voltage of PV module for MPPT operation. When power switch is turned on primary inductance is energized by the PV source and current of primary inductance increases linearly and saves energy. Voltage of primary inductance, V_{Lp} is equal to input voltage and voltage of PV module ($V_{Lp}=V_{IN}=V_{PV}$). Besides, secondary inductance has same voltage while the power switch is conducting. Current change in these inductances are formulated as in (8). Since voltages of these inductances are same, they can be wound on the same core and values of inductances are halved [21].

$$\Delta I_{Lp} = \Delta I_{Ls} = \frac{1}{2}\frac{V_{IN}t_{ON}}{L_P} \qquad (8)$$

In (8), ΔI_{Lp} and ΔI_{Ls} are the current ripples of coupled inductor, t_{on} is the conducting time of switch and L_p is the primary inductance value.
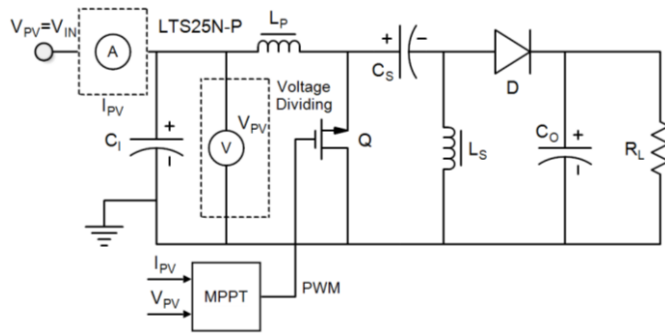
Fig.4. Electrical scheme of the MPPT system

Peak to peak voltage ripple and root mean square (RMS) current rating are the main parameters for capacitor selection [21]. Output voltage of the SEPIC is calculated as in (9). D_{crt} is critical duty ratio corresponding to maximum value of D_{crt} and output current multiplication. In (9), f_P is the switching frequency. Voltage value across the output capacitor and its equivalent series resistance are the significant parameters [20].

$$C_O = \frac{D_{crt}I_O}{\Delta V_O f_P} \qquad (9)$$

Calculation of coupled capacitor is made similarly. Voltage of C_S is equal to input voltage in steady state condition. This capacitor is calculated as following equation [20].

$$C_S = \frac{D_{crt}I_O}{\Delta V_{IN} f_P} \qquad (10)$$

A. Simulation Results

In order to observe the performance of the proposed MPPT strategy, some simulation studies have been performed in MATLAB/Simulink. Furthermore, proposed strategy has been compared with FSCC approach and P&O algorithm. Fig. 5 presents the simulation results the case of irradiance change. In this simulation case, irradiance is changed from 1000W/m^2 to 500W/m^2 at t=2s. Duty ratio is updated in proposed strategy and new MPP is tracked a few milliseconds. Although FSCC performs better than P&O, it has performed worse than proposed SCC strategy. According to the result of FSCC seen in Fig. 5, voltage and power of PV module decreases to zero since PV module is short circuited. In this results, energy discontinuity and additional switch are the prominent drawbacks.

IV. PROTOTYPE CIRCUIT AND EXPERIMENTAL RESULTS

In this section, prototype of SEPIC converter, sensing and measurement circuits for MPPT operation, the other hardware requirements and results of experimental studies are presented. A low power SEPIC which consists of a coupled inductor, input, output and coupled capacitor, a semiconducting switch (MOSFET) from International Rectifier, IRFP450 and a fast diode named as MUR860. Primary and secondary inductance values are 569uH. To stabilize the voltage of PV module two parallel capacitors are used. Their values are 470uF. In the output of the SEPIC, a 150 electrolytic capacitor is used. In order to realize MPPT operation, voltage and current of PV module are sensed by a voltage dividing circuit and LTS25NP current transducer. Voltage dividing circuits contain two resistor and a capacitor. Their values are 33k, 2,7k and 10nF, respectively. So as to generate PWM for MOSFET switching, a microprocessor from Microchip, PIC18F452, has been used. However, PWM signal obtained from this component does not provide enough current to drive MOSFET's gate. Therefore, a gate driver integrated circuit from International Rectifier, IR2118 is used. All components used in this prototype circuit, measurement devices and model of PV emulator are listed in Table III.
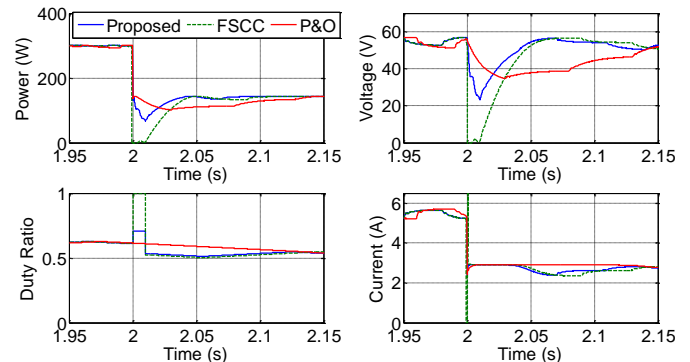

Fig.5. Simulation results of proposed strategy, FSCC and P&O algorithm

In experimental validation, specifications of the PV module given in Table I are used. As a PV source, three PV modules are connected in series to form a PV array. This array is irradiated by 700W/m^2 which is set through interface program

of the PV emulator. Experimental test platform is shown in Fig. 6. As listed in Table I, parameters of monocrystalline type PV module is used in the PV emulator. If another type of cell is used, performance of the proposed strategy is not affected since approximate short circuit and its duration time is related to the power stage of the system.

TABLE III
SPECIFICATIONS OF THE SEPIC AND MEASUREMENT DEVICES

Components / Measurement	Value / Brand / Model
Input capacitor	2//470μF, 100V
Output capacitor	150μF, 200V
Coupled inductance (L_P / L_S)	569μH / 569μH
Coupled capacitor	220μF, 100V
MOSFET	IRFP450
Diode	MUR860
Current transducer	LTS25NP
Voltage dividing resistors / capacitor	33k/2,7k – 10nF
Microprocessor	PIC18F452
Switching frequency	20kHz
Current probe	Fluke 80i-110s
Oscilloscope	GW Instek -GDS3254
PV emulator	CHROMA 62050-600S
Resistive Load	24Ω – 200W
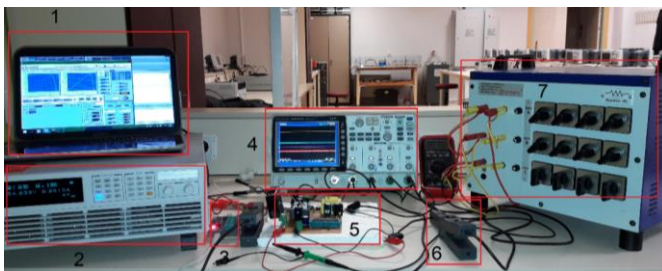
Fig.6. Test platform 1: Computer for PV emulator programming and PIC18F452 programming, 2: PV emulator, 3: PICKIT2, 4: Oscilloscope, 5: Prototype SEPIC, 6: Current Probe, 7: Resistive loading bank)

A. Experimental Results

As explained in the Section II, proposed strategy provides proper initialization without short circuit and an operation point near exact MPP is tracked. Then, P&O algorithm completes the tracking. Fig. 7 presents the result of the proposed strategy. When zooming the region presented in rectangle, proposed strategy tracks the MPP in a few hundred milliseconds. In this figure, voltage, current and power of the PV module and duty ratio are presented.
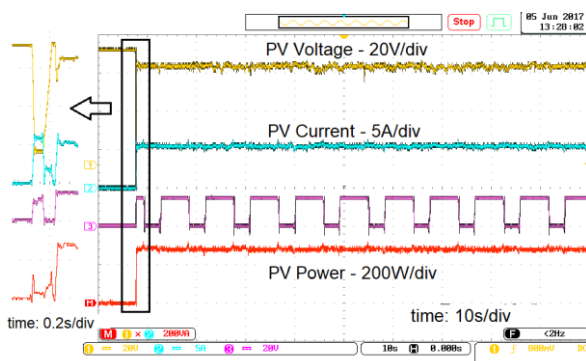

Fig.7. Experimental results of the proposed strategy

Experimental results of the proposed strategy and FSCC are presented in Fig. 8. In this case, first, solar irradiance is set to 1000W/m^2 and MPP is tracked. After thirty seconds, solar irradiance decreases to 500W/m^2 by emulator. In this condition, approximate short circuit is realized. The result of the proposed strategy can be seen in the first circle in Fig. 8. In the proposed strategy, PV array is not short circuited completely. It can be easily understood by the variations of PV module voltage. Normally, if PV array is completely short circuited, voltage sharply decreases to zero immediately. However, voltage of PV array decreases to half of the first value. To observe the difference between the proposed strategy and FSCC, twenty seconds later, PV array is short circuited. With full short circuit condition, shown in the second circle in Fig. 8, voltage of PV module converges to zero. Therefore, proposed strategy collects more energy during initialization interval compared with the FSCC approach.

As is verified in the last two results presented in Fig. 7 and Fig. 8, proposed strategy initiates the operation point near the MPP, providing fast tracking. For comparison the other approach, P&O algorithm is used in same power level. As it is clear in Fig. 9 that tracking of MPP is very slow compared with the proposed strategy and FSCC algorithm. Tracking is completed in 1 second in Fig. 9. On the other hand, proposed strategy tracks the MPP in about 100 milliseconds. Normally, transient process of the MPPT is very small compared with the steady state condition. However, in a cloudy day, MPP changes frequently and number of transient processes increases. Prominence of the proposed strategy in such cases can be better understood.
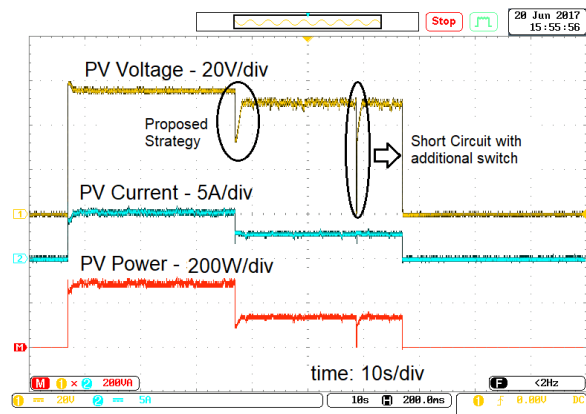

Fig.8. Comparison of the proposed strategy and FSCC

V. CONCLUSIONS AND FUTURE WORK

In this study, an approximate short circuit strategy improving the transient process of MPPT is introduced. Proposed strategy uses ratio of maximum power current and short circuit current and initiates the operation point near the MPP. One advantage of this strategy compared with classical FSCC, additional switch is not required and PV module is not short circuited. So, more energy can be collected in the proposed strategy. Simulation and experimental results show that proposed strategy outperforms than FSCC and P&O

algorithm. In the future study, this strategy will be used in a commercially available power optimizer and/or micro inverter circuits with different power ratings.
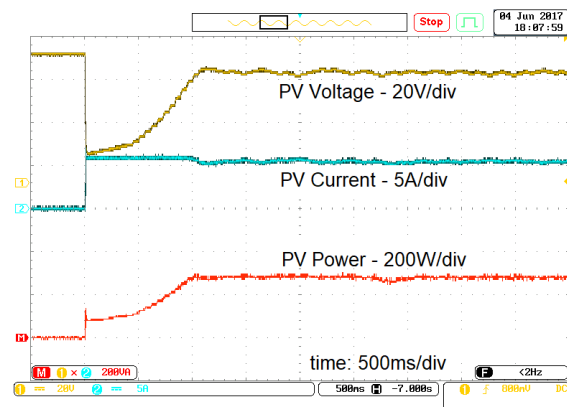

Fig.9. Experimental result of P&O algorithm

REFERENCES

[1] Esram T., Chapman P.L., Comparison of photovoltaic array maximum power point tracking techniques, IEEE Transactions on Energy Conversion, vol. 22, no. 2, pp. 439-449, 2007.
[2] Fernia N., Petrone G., Spagnuolo G., Vitelli M., Optimization of perturb and observe maximum power point tracking method, IEEE Transactions on Power Electronics, vol. 20, no.4, pp. 963-973, 2005.
[3] Liu F., Duan S., Liu F., Liu B. Kang Y., A variable step size INC MPPT method for PV systems, IEEE Transactions on Industrial Electronics, vol. 55, no. 7, pp. 2622-2628, 2008.
[4] Belkaid A. Gaubert J. Gherbi A., Design and implementation of a high-performance technique for tracking PV peak power, IET Renewable Power Generation, vol. 11, no. 1, pp. 92-99, 2017.
[5] Tang L., Xu W. Mu C., Analysis for step-size optimization on MPPT algorithm for photovoltaic systems, IET Power Electronics, vol. 10, no. 13, pp. 1647-1654, 2017.
[6] Killi M., Samanta S., Modified perturb and observe MPPT algorithm for drift avoidance in photovoltaic systems, IEEE Transactions on Industrial Electronics, vol. 62, no. 9, pp. 5549-5559, 2015.
[7] Safari A., Mekhilef S., Simulation and hardware implementation of incremental conductance MPPT with direct control method using cúk converter, IEEE Transactions on Industrial Electronics, vol. 58, no. 4, pp. 1154-1161, 2011.
[8] Mosa M. Shadmand M.B., Balog R.S., Rub H.A., Efficient maximum power point tracking using model predictive control for photovoltaic systems under dynamic weather conditions, IET Renewable Power Generation, vol. 11, no. 1, pp. 1401-1409, 2017.
[9] Tey K.S., Mekhilef S., Modified incremental conductance algorithm for photovoltaic system under partial shading conditions and load variation, IEEE Transactions on Industrial Electronics, vol. 61, no. 10, pp. 5384-5392, 2014.
[10] Kivimäki J., Kolesnik S., Sitbon M., Suntio T. Kuperman A., Design guidelines for multiloop perturbative maximum power point tracking algorithms, IEEE Transactions on Power Electronics, vol. 33, no.2, pp. 1284-1293, 2018.
[11] Liu Y., Chen J., Huang J., Global maximum power point tracking algorithm for PV systems operating under partial shading conditions using segmentation search method, Solar Energy, vol. 103, pp. 350-363, 2014.
[12] Patel H. Agarwal V., Maximum power point tracking scheme for PV systems operating under partially shaded conditions, IEEE Transactions on Industrial Electronics, vol. 55, no. 4 pp. 1689-1698, 2008.
[13] Başoğlu M.E., Çakır B., Hybrid global maximum power point tracking approach for photovoltaic power optimisers, IET Renewable Power Generation, vol. 12, no. 8, pp. 875-882, 2018.
[14] Başoğlu M.E., Çakır B., A novel voltage-current characteristic based global maximum power point tracking algorithm in photovoltaic systems, Energy, vol. 112, pp. 153-163, 2016.
[15] Başoğlu M.E., Çakır B., An improved incremental conductance based MPPT approach for PV modules, Turkish Journal of Electrical Engineering & Computer Sciences, vol. 23, pp. 1687-1697-2015.
[16] Zadeh M.J.Z., Fathi S. H., A new approach for photovoltaic arrays modeling and maximum power point estimation in real operating conditions, IEEE Transactions on Industrial Electronics, vol. 64, no. 12, pp. 9334-9343, 2017.
[17] Noguchi T. Togashi S., Nakamoto R., Short current pulse based maximum power point tracking method for multiple photovoltaic and converter module system, IEEE Transactions on Industrial Electronics, vol. 49, no.1, pp. 217-223, 2002.
[18] Jiang L.L., Nayanasiri D.R., Maskell D.L., Vilathgamuwa D.M., A hybrid maximum power point tracking for partially shaded photovoltaic systems in the tropics, Renewable Energy, vol. 76, pp. 53-65, 2015.
[19] Nguyen T.L., Low K., A global maximum power point tracking scheme employing direct search algorithm for photovoltaic systems, IEEE Transactions on Industrial Electronics, vol. 57, no. 10, pp. 3456-3467, 2010.
[20] Mohan N., Undeland T.M., and Robbins W.P., Power Electronics: Converter, Applications, and Design, Wiley, 1995, p. 315.
[21] Falin J., Designing DC/DC converters based on SEPIC topology, Texas Instruments, 2008.

BIOGRAPHY

MUSTAFA ENGİN BAŞOĞLU was born in 1988. He received the M.Sc. degree of Electrical Engineering at Kocaeli University, Turkey in 2013. He receives Ph.D. in 2017 with thesis "Development and implementation of a new maximum power point tracking method for photovoltaic systems". From 2012, he is research assistant in the department of Electrical Engineering in University Kocaeli. From 2018, he is assistant professor in Electrical and Electronics Department of Gümüşhane University. His research interests include: photovoltaic systems, maximum power point tracking algorithms, power electronics, switch mode power supplies and control of electrical machines.

Design of Hybrid Refractive/Diffractive Lenses for Wearable Reality Displays

F. E. SAHIN

Abstract— **Wearable reality displays promise revolutionary developments for a wide range of applications. The key to achieving a high-quality wearable reality display system is to design a comfortable-to-wear, compact, lightweight system that can provide high resolution and high contrast. One potential method for achieving a compact and high-resolution display system is through designing a hybrid refractive/diffractive lens. With this approach, a chromatically-corrected optical system can be implemented with a single-element lens.**

Index Terms—**Diffractive optics, Displays, Lens design, Optical system design, Virtual Reality.**

I. INTRODUCTION

WEARABLE REALITY systems are generally considered as the next frontier in human computer interaction. These systems include virtual, augmented and mixed reality systems. Wide range of applications of these devices include medical, defense, consumer, entertainment, industrial and educational applications [1-4]. Significant research and development efforts, together with recent developments in optical design, materials, and manufacturing technologies [5-7] and computational imaging and displays [8-10] enable rapid progress for introduction of mainstream virtual reality technologies. With the inclusion of cameras to view the environment and eye-tracking cameras in virtual reality (VR) display systems, video see-through augmented and mixed reality systems can also be implemented [11-13].

A virtual reality display system can be constructed by viewing a display through a positive lens. This configuration is similar to viewing an object through a magnifying glass. In this case, the display image appears magnified and at a large distance from the eye. This allows for a comfortable viewing experience without user eye strain. A very simple VR solution was introduced by Google with the Cardboard device. This device uses two plastics lenses (one for each eye) and a smartphone as the display, all enclosed in a cardboard enclosure

Furkan E. SAHIN, is with Advanced Research and Development division of Maxim Integrated Inc., San Jose, CA. (e-mail: furkansahin@gmail.com).

https://orcid.org/0000-0003-4332-5158

[14]. More complex devices, such as VR systems from Oculus or HTC [15,16], have more complex lens designs. Even though these devices still have a single-element plastic lens, the lens surface shapes and profiles are optimized for high resolution displays.

Virtual reality systems should at the same time be compact and lightweight and provide an engaging experience for users. The user's eyes should be relaxed and there should be ample clearance between the eyes and the system's lenses. Realizing a compact system is possible with large field of view lenses. Wide-angle and fisheye lenses are common for a variety of imaging applications [17-19], typically with multi-element, aberration-corrected lenses. However, achieving wide field of view with single element lenses in VR systems is a challenging task.

In this paper, lens design of a chromatically corrected virtual reality display system is presented. As background information, a brief review of hybrid diffractive/refractive optical systems is introduced. The reference display for the device is a standard smartphone and the system achieves high resolution as evidenced by the high MTF curves. The system consists of a single lens, which is a hybrid refractive/diffractive element. The lens has two aspherical refractive surfaces and in addition, one of the surfaces has a diffractive phase profile. Two different designs, in which the diffractive surface is placed either on the first or the second surface of the lens are presented and evaluated.

II. HYBRID REFRACTIVE/DIFFRACTIVE LENSES

Typical imaging systems such as cameras and microscopes usually have refractive optical elements, i.e. lenses with spherical or aspherical surfaces. Optical materials are inherently dispersive, that is different wavelengths of light are refracted differently (Fig. 1, a). In order to achieve a broadband system for operation over a wide range of wavelengths, multi-element lenses with positive and negative lens elements can be designed to correct chromatic aberration. In a simple sense, positive elements are made of optical materials with low dispersion, whereas negative elements are made of optical materials with high dispersion, to correct chromatic aberrations at the image plane. Refractive lenses typically focus short wavelengths more than long wavelengths. If the visible spectrum is considered, blue light is focused closer to the lens than red light.

The Abbe number (V) of an optical material shows how dispersive the material is and is defined as:

$$Abbe\ number\ (V) = \frac{n_{center} - 1}{n_{short} - n_{long}} \qquad (1)$$

in which n_{center}, n_{short} and n_{long} are the refractive indices of the center, short and long wavelengths, respectively. Typically for the visible spectrum, Fraunhofer d-, F- and C- lines define these wavelengths. The center wavelength is 588 nm (d-line), the short wavelength is 486 nm (F-line) and the long wavelength is 656 nm (C-line). Abbe numbers for optical materials typically range from 20 to 85, lower Abbe numbers mean the material is more dispersive. The Abbe number of PMMA material used in the design of the lenses in this paper is 59.2 [20].
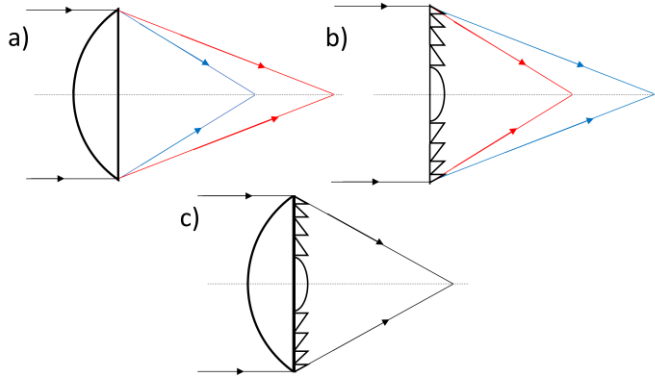
Fig. 1. a) Dispersion characteristics for a refractive lens, blue wavelength has a shorter focal length compared to red wavelength. b) Dispersion characteristics for a diffractive lens, red wavelength has a shorter focal length compared to blue wavelength. c) With a hybrid refractive/diffractive lens, chromatic aberration correction can be achieved, such that both red and blue wavelengths are focused to the same point.

A different class of lenses is known as diffractive lenses. Instead of relying on refraction at interfaces, these lenses have structures on the order of light's wavelength and rely on diffraction of light to achieve ray bending. Diffractive lenses typically focus long wavelengths of light more than short wavelengths (Fig. 1, b).

Analysis of the dispersion characteristics of a diffractive lens shows that dispersion does not depend on material refractive index but is related to the wavelength [21]. An effective Abbe number (V_{diff}) for a diffractive surface can be defined as:

$$Diffractive\ Abbe\ number\ (V_{diff}) = \frac{\lambda_{center}}{\lambda_{short} - \lambda_{long}} \qquad (2)$$

in which λ_{center}, λ_{short} and λ_{long} are the center, short and long wavelengths, respectively. For the above stated d, F, C-lines, the diffractive Abbe number is −3.45.

A hybrid refractive/diffractive system can be designed to achieve a chromatically corrected optical system. With this approach, the positive Abbe number of the refractive lens is compensated for by the negative Abbe number of the diffractive lens for chromatic correction.

III. USING A SMARTPHONE AS VIRTUAL REALITY DISPLAY

Apple iPhone X smartphone was introduced in 2017. This was the company's first smartphone with an organic light emitting diode (OLED) display. OLED displays provide high contrast due to their ability to turn pixels off completely for

displaying black colors. iPhone X's screen size is 5.8", with a 19.5:9 aspect ratio. The full specifications of the iPhone X display are listed in Table 1.

As iPhone is a widely used smartphone, and the display size is similar to many other smartphones in the market, the design of the virtual reality lens was based around this phone. Another smartphone with a similar display size and resolution can also be used with the designed optical system.

TABLE I
SPECIFICATIONS OF APPLE IPHONE X DISPLAY [22]

Screen size	5.8"
Resolution	2436 × 1125 pixels
Pixel size	55 μm × 55 μm
Spatial Frequency	9 cycles/mm

IV. OPTICAL DESIGN OF VIRTUAL REALITY LENSES

The virtual reality optical system is a projection system, that is the image on the display is projected to the pupil of the eye. The optical system can also be modeled as an imaging system which focuses light onto the display plane, due to the optical principle of reversibility [23]. With this approach, optical analysis techniques such as spot size and modulation transfer function (MTF) can be utilized to evaluate the performance of the system.

There are several important requirements and related parameters for virtual reality displays to establish a pleasant experience for users. The lenses in the VR system should have sufficient clearance from the wearer's eyes, this is known as eye relief. In addition, the VR system should be lightweight and compact in size. This sets an upper limit on the distance between the eye and the display. Based on these requirements, the system level parameters for the designed VR optical system are listed in Table 2.

TABLE II
SYSTEM PARAMETERS FOR THE DESIGNED VIRTUAL REALITY
OPTICAL SYSTEM (PER EYE)

Pupil diameter	4 mm
Eye relief	15 mm
Distance between pupil and display	< 80 mm
Screen size	62 mm × 62 mm
Lens diameter	20 mm

The entrance pupil of the optical system is assumed to be 4 mm in diameter for the lens designs. This corresponds to the pupil diameter of a typical, undilated human eye. The two lens systems were modeled, optimized and analyzed in Zemax OpticStudio software [24]. In optical analyses, F-d-C wavelengths are specified to cover the full visible spectrum. The lens diameters are set to be 20 mm.

PMMA plastic was selected as the optical material for the lenses. PMMA is a thermoplastic material commonly used in optics and is especially suited for injection molding for high-volume manufacturing. Its refractive index is 1.49 (at 588 nm) and Abbe number is 59.2 [20].

A. Lens Design Procedure

Lens design process started by designing and optimizing a monochromatic lens with only refractive surfaces, operating at 588 nm wavelength. In this case, the distance from the pupil to the lens vertex was fixed to be 15 mm, to enforce the eye-relief requirement. Optimization constraints were also included to ensure the perpendicular distance between the pupil and the lens to be greater than 15 mm for the full lens diameter. In order to have an easy to manufacture lens, the center-edge and edge-center thickness ratios were limited to be less than 3 during lens optimization [25]. The total track length (TTL: distance from the pupil to the image plane) was also constrained to be less than 80 mm. Once the monochromatic lens was optimized, the design was made broadband and achromatized with the introduction of a diffractive surface profile and re-optimization of the full system.

Two different hybrid refractive/diffractive lenses were designed, with the main difference being the position of diffractive surface. In the first lens design the diffractive surface is placed on the front side of the lens (facing the user), whereas in the second lens design the diffractive surface is placed on the rear side of the lens (facing the display).

B. Lens Design with Front Side Diffractive Surface

Schematic drawing of the lens design with front side diffractive surface is shown in Fig. 2. In this figure, the field angles go up to 40°, which corresponds to a paraxial image height of 44.9 mm. The first surface has a gullwing shape and the second surface is convex. The effective focal length of the lens is 53.5 mm and the TTL for the lens is 75.6 mm. The center and edge thicknesses of the lens are 12 mm and 5.88 mm, respectively.
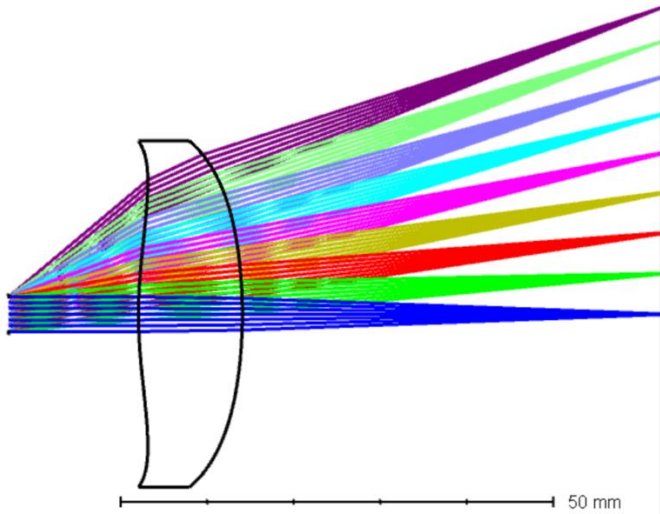
Fig. 2. Schematic drawing for the lens design with front side diffractive surface.

The modulation transfer function (MTF) analysis of the lens is shown in Fig. 3. This plot shows that on-axis and in the central field of view, the lens provides high contrast. With larger field angles, contrast is reduced.
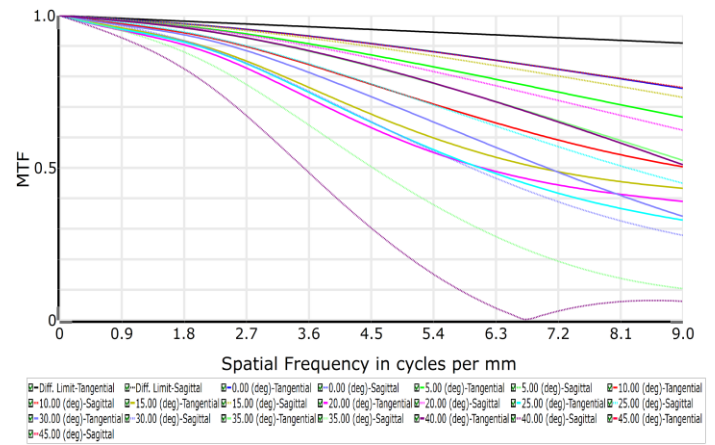

Fig. 3. MTF plot for the lens design with front side diffractive surface.

C. Lens Design with Rear Side Diffractive Surface

Schematic drawing of the lens design with rear side diffractive surface is shown in Fig. 4. In this figure, the field angles go up to 40°, which corresponds to a paraxial image height of 45.2 mm. Both lens surfaces have a convex shape. The effective focal length for the lens is 53.8 mm and the TTL for the lens is 75.7 mm, both values are very similar to the previous design. The center and edge thicknesses of the lens are 12 mm and 5.35 mm, respectively.
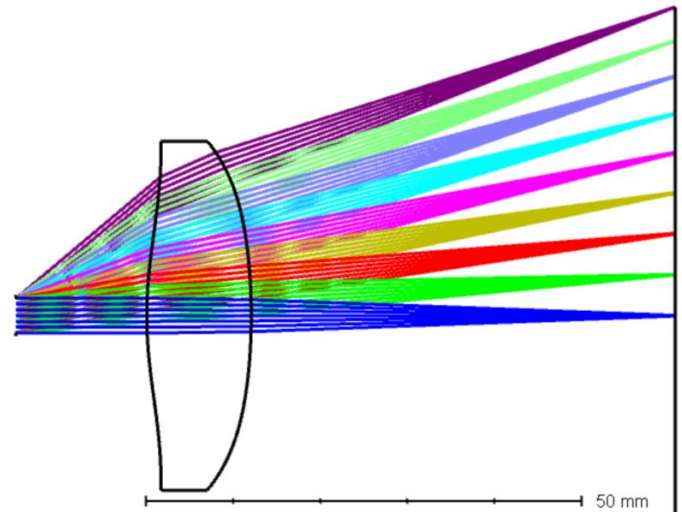

Fig. 4. Schematic drawing for the lens design with rear side diffractive surface.

The modulation transfer function (MTF) analysis of the lens is shown in Fig. 5. This plot shows that modulation at the display spatial frequency of 9 cycles/mm, is greater than 0.5 in the central ±10° field of view and greater than 0.28 up to ±30° field of view.
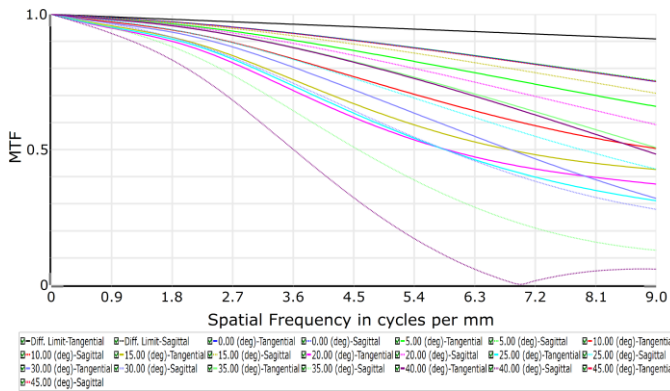
Fig. 4. MTF plot for the lens design with rear side diffractive surface.

When analyzed in imaging configuration, both lenses have negative (barrel) distortion. This means that in the projection configuration, they have the opposite, positive (pincushion) distortion. Due to this pincushion distortion effect of VR lenses, it is common practice to pre-distort display video feed of virtual reality systems through digital image processing [26]. If an image that is pre-distorted with the unique distortion profile of the lens is displayed on the screen, and a VR system with the corresponding lens is used to view this image, the viewer would see a distortion-free (i.e. rectilinear) image. Designing an optical system to have some optimal degree of distortion can also allow for correcting other optical aberrations more effectively [27-29].

V. DISCUSSIONS

The two hybrid refractive/diffractive lenses presented above have similar optical performance, as can be seen by comparing the MTF plots shown in Fig. 3 and Fig. 5. Both designs provide high contrast in the central field of view, and performance degradation is apparent at large field angles. Either lens design can be manufactured to implement high-resolution VR displays systems.

As shown in Fig. 2, the lens design with front side diffractive surface has a "gull-wing" profile for the front surface. This gullwing type of surface profile is difficult to manufacture and test [30]. Therefore, from a robust, high-volume manufacturing perspective, the lens design with rear side diffractive surface (as shown in Fig. 4) would be preferred over the other lens design.

VI. CONCLUSION

Optical design and performance analysis of a high-contrast wearable display system is presented. A compact and simple design with a single plastic lens element is achieved through a hybrid refractive/diffractive lens design approach.

REFERENCES

[1] L. P. Berg and J. M. Vance, "Industry use of virtual reality in product design and manufacturing: a survey," *Virtual Reality,* vol. 21, pp. 1-17, 2017.
[2] Seth, J. M. Vance and J. H. Oliver, "Virtual reality for assembly methods prototyping: a review," *Virtual reality,* vol. 15, pp. 5-20, 2011.
[3] L. Freina and M. Ott, "A Literature Review on Immersive Virtual Reality in Education: State Of The Art and Perspectives.," *eLearning & Software for Education,* 2015.

[4] N. E. Seymour, A. G. Gallagher, S. A. Roman, M. K. O'brien, V. K. Bansal, D. K. Andersen and R. M. Satava, "Virtual reality training improves operating room performance: results of a randomized, double-blinded study," *Annals of surgery,* vol. 236, p. 458, 2002.
[5] F. E. Sahin, "Open-source optimization algorithms for optical design," *Optik,* vol. 178, pp. 1016-1022, 2019.
[6] L. Livshits and D. C. Dilworth, "Trends in optical design from 1988 to 2018… where to from here?," *Advanced Optical Technologies,* vol. 7, pp. 335-341, 2018.
[7] F. E. Sahin, "Lens design for active alignment of mobile phone cameras," *Optical Engineering,* vol. 56, p. 065102, 2017.
[8] R. Konrad, N. Padmanaban, K. Molner, E. A. Cooper and G. Wetzstein, "Accommodation-invariant Computational Near-eye Displays," *ACM Trans. Graph. (SIGGRAPH),* no. 36, 2017.
[9] F. E. Sahin and R. Laroia, "Light L16 Computational Camera," in *Applied Industrial Optics: Spectroscopy, Imaging and Metrology*, 2017.
[10] Lanman and D. Luebke, "Near-eye light field displays," *ACM Transactions on Graphics (TOG),* vol. 32, p. 220, 2013.
[11] J. P. Rolland, R. L. Holloway and H. Fuchs, "Comparison of optical and video see-through, head-mounted displays," in *Telemanipulator and Telepresence Technologies*, 1995.
[12] F. E. Sahin, B. P. McIntosh, P. J. Nasiatka, J. D. Weiland, M. S. Humayun and A. R. Tanguay, "Eye-tracked extraocular camera for retinal prostheses," in *Frontiers in Optics*, 2015.
[13] Cutolo, P. D. Parchi and V. Ferrari, "Video see through AR head-mounted display for medical procedures," in *Mixed and Augmented Reality (ISMAR), 2014 IEEE International Symposium on*, 2014.
[14] Google Cardboard, https://vr.google.com/cardboard/ (Last accessed: Dec 6, 2018).
[15] Oculus VR, https://www.oculus.com/ (Last accessed: Dec 6, 2018).
[16] HTC Vive, https://www.vive.com/ (Last accessed: Dec 6, 2018).
[17] S.-W. Yang, K.-L. Huang, C.-Y. Chen and R.-S. Chang, "Wide-angle lens design," in *Computational Optical Sensing and Imaging*, 2014.
[18] F. E. Sahin, "Fisheye lens design for sun tracking cameras and photovoltaic energy systems," *Journal of Photonics for Energy,* vol. 8, p. 035501, 2018.
[19] J. Kumler and M. L. Bauer, "Fish-eye lens designs and their relative performance," in *Current Developments in Lens Design and Optical Systems Engineering*, 2000.
[20] N. Sultanova, S. Kasarova and I. Nikolov, "Dispersion properties of optical polymers," *Acta Physica Polonica-Series A General Physics,* vol. 116, p. 585, 2009.
[21] M. Schaub, J. Schwiegerling, E. Fest, R. H. Shepard and A. Symmons, "Molded Optics: Design and Manufacture," CRC Press, 2016, pp. 28-32.
[22] Apple iPhone X, https://www.apple.com/iphone-x/ (Last accessed: Sep. 12, 2018)
[23] Hecht, "Optics," Pearson Education, 2001, p. 107.
[24] Zemax OpticStudio, Zemax LLC, Washington, USA. https://www.zemax.com/
[25] S. Thibault, J. Parent, H. Zhang, X. Du and P. Roulet, "Consumer electronic optics: how small can a lens be: the case of panomorph lenses," in *Current Developments in Lens Design and Optical Engineering XV*, 2014.
[26] S. Lee and H. Hua, "A robust camera-based method for optical distortion calibration of head-mounted displays," *Journal of Display Technology,* vol. 11, pp. 845-853, 2015.
[27] F. E. Sahin, P. J. Nasiatka, J. D. Weiland, M. S. Humayun and A. R. Tanguay, "Optimal Design of Miniature Wide-Angle Computational Cameras for Retinal Prostheses and Wearable Visual Aids," in *Frontiers in Optics*, 2014.
[28] F. E. Sahin, P. J. Nasiatka and A. R. Tanguay, "Lateral Chromatic Aberration Optimization in Wide-Field-of-View Computational Cameras," in *Frontiers in Optics*, 2015.
[29] F. E. Sahin and A. R. Tanguay, "Distortion optimization for wide-angle computational cameras," *Optics Express,* vol. 26, pp. 5478-5487, 2018.
[30] Symmons, J. Huddleston and D. Knowles, "Design for manufacturability and optical performance trade-offs using precision glass molded aspheric lenses," in *Polymer Optics and Molded Glass Optics: Design, Fabrication, and Materials 2016*, 2016.

BIOGRAPHIES

FURKAN EMRE SAHIN received his B.S. degree from Bogazici University, Istanbul, Turkey, and his Ph.D. from the University of Southern California, Los Angeles, USA, in Electrical Engineering. His work in the industry includes optical system design of miniature cameras and optical sensors. His research interests include development of innovative imaging and sensing systems for consumer, industrial and biomedical applications, optical system design, and computational photography.

Active Only Realization of Image Reject Complex Filter

H. A. YILDIZ

Abstract— **A new complex-filter which offers substantial area reduction is presented. According to this topology, the real-active only integrator is used for implementing the first order image reject filter. We have also discussed the design of a new area effective second order complex filter using lossy integrator building blocks. Using SPECTRE simulation tool, we have also justified the feasibility of the proposed circuit.**

Index Terms— **Real active-only integrator, Complex filters, Low-IF Receivers, Integrated Circuits.**

I. INTRODUCTION

IN ORDER to remedy the limitation of the zero IF and conventional IF receivers, low-IF architectures are proposed and effectively used in state-of the art RF transceivers [1]. This architecture provides a good trade-off in terms of power dissipation, integration capability and complexity.

However, the image problem is one major problem of such architectures and reduces overall system performance. The common approach to overcome this problem is to use complex filters which is usually used in the low-IF wireless receiver to filter out the image signal, for its easy integration on chip [2-6]. This kind of filters are formed from two paths in which a pair of signals (I and Q channels) with equal amplitude and quadratic phases are applied at their inputs.

In IC realization, these filters are intended to reject low image frequencies, therefore they require with capacitors with large values; hence occupy very large chip area due to the value of IF frequency [7-10].

On the other hand, circuits called as real active only filters, which use the intrinsic capacitors of the active devices at the various nodes of circuit, may be employed to implement IF filters with small chip area [11].

Herein, in order to achieve the issues encountered in realizing image-reject complex filters, it is proposed a design of a new area-effective first order complex-filter topology capable of providing electronically adjustable time constant.

To further justify the usefulness of the proposed approach, a second order complex filter using lossy integrator building blocks is proposed.

HACER ATAR YILDIZ, is with Department of Electronics and Communication Engineering University of Istanbul Technical University, Istanbul, Turkey,(e-mail: haceryildiz@itu.edu.tr).

https://orcid.org/0000-0002-2306-6008

In order to illustrate the feasibility of the filter, simulation results using SPECTRE in the CADENCE design tool are provided. The obtained results verify that the circuit is indeed feasible and can be used to implement area-effective complex filter circuit.

II. LOW IF RECEIVER ARCHITECTURE

A typical low-IF receiver architecture is given in Fig.1. The image reject complex filter entails very large time constants due to the low frequency operation in low IF circuits. Therefore, this kind of filters are required large value capacitors which occupy large chip area.

In order to achieve this issues, a new design of area effective complex filter topology is proposed in this paper. This filter employs real active-only integrator which operates at high-frequencies and provides electronically adjustable time constant with wide tuning area.
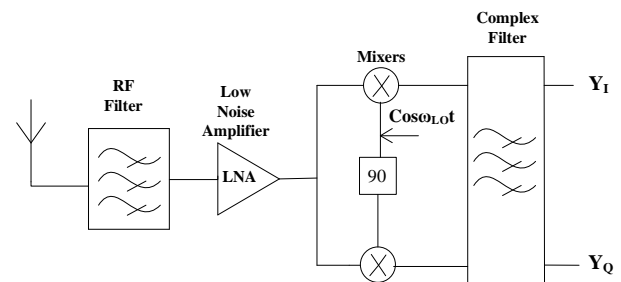

Fig.1. Block diagram of a typical low-IF Receiver [12]

III. CIRCUIT IMPLEMENTATIONS

A. Basics of Complex Filter

For realization of first order complex filter, the basic topology is given in Fig.2. After routine analysis, the equivalent transfer function is obtained as follows:

$$H(s) = \frac{V_0^I + jV_0^Q}{V_i^I + jV_i^Q} = \frac{g_m}{sC_p + g_0 - jg_{m,cpl}} \quad (1)$$

where g_0 is the nonzero output conductance of the CCCII. The complex first-order filter consists of a pair of real lossy integrators which are cross-coupled by the transconductors $g_{m,cpl}$. The transfer function of a complex first-order filter could be easily derived by performing a frequency shifting of the transfer function of the corresponding real first-order filter according to the transformation $s \rightarrow s - j\omega_0$
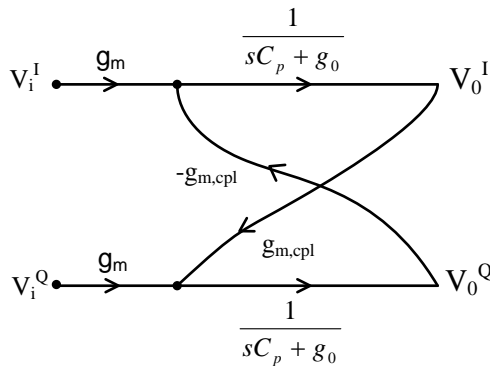
Fig.2. Basic topology for active-only first-order filter implementation

where ω_0 is the frequency shift given by:

$$\omega_0 \approx g_{m,cpl}/C_p \ , \quad \frac{g_{m,cpl}}{C_p} \rangle\rangle \frac{g_0}{C_p} \qquad (2)$$

As it can be seen from the equation above, it is derived an asymmetrical band-pass filter function from a first order filter function by providing frequency transformation.

The possible procedure is given in Fig.3 in accordance with the topology of Fig.2. This procedure describes how to turn a given active-only first-order filter into a complex filter.
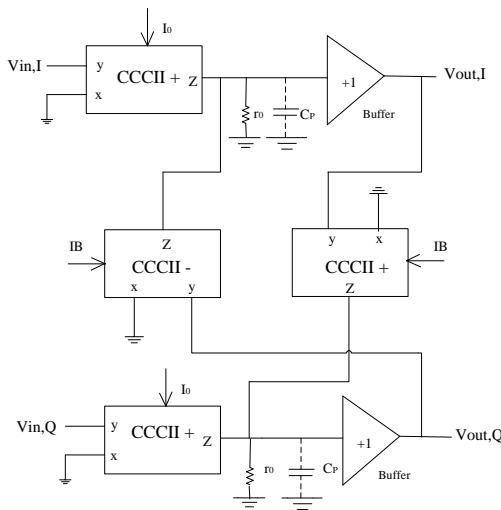
Fig.3. The functional block diagram of proposed first order complex filter

The cross-coupled branch's admittance $g_{m,cpl}$ can be realized by using intrinsic resistance of CCCII element, as shown in Fig.3. By coupling of these elements, first-order filter is converted into active-only complex filter. Taking into account all these modifications, we can obtain the following node equation:

$$V_0^Q = \frac{1}{sC_p + g_0}(g_m V_i^Q + g_{m,cpl} V_0^I) \qquad (3)$$

It should be also noted that in Fig.3, the transconductances of the CCCII elements are given by $g_{m,cpl} \approx \omega_0 C_P$, where ω_0 is the center frequency of the complex bandpass filter. Since the

basic first-order filter frequency is obtained as $\omega_p \approx g_m/C_P$ from (3), the transconductance ratio $g_{m,cpl}/g_m$ should be ω_0/ω_p.

B. Active only Integrator

As it can be seen from Fig.4a, it is showed a typical integrator which is commonly used in many filter circuits as the main building block. The transconductance element is used to perform the basic voltage to current converter in this circuit. The integrator's time constant of this circuit is described by the ratio of the equivalent capacitor seen at the output of the transconductance element (C_p) and the transconductance gain (g_m), which is the inverse of the CCCII's x-terminal parasitic resistance, r_x. x-terminal parasitic resistance is an electronically controllable parameter through a biasing current I_0. For the CMOS CCCII realization in [14], the expression that relates r_x to I_0 is given by:

$$r_x = \left(K\mu_n C_{ox} \frac{W}{L} I_0 \right)^{-1/2} \qquad (4)$$

where μ_n, C_{ox}, W/L and I_0 are respectively the electron mobility of NMOS, gate oxide capacitance per unit area, transistor aspect ratio and bias current of CCCII, while K is a constant dependent on the circuit topology.

In addition, the equivalent capacitor C_p consists of the parallel combination of the z-terminal intrinsic capacitors of the CCCIIs and the input capacitance of the voltage buffers at the circuit outputs.

The input capacitance of the voltage buffer is substantially dominated by the gate-source capacitance of the MOSFET transistors and accepted highly linear as long as the transistors remain in saturation [13]. Therefore, the size of the MOS transistors at the buffer input are chosen as large as possible. In this manner, the capacitance C_p becomes much more dominant than the z-terminal parasitic capacitances of the CCCIIs, so the proper integrator design is provided. Considering the design criteria described above, the obtained integrator transfer function is characterized by the following transfer function:
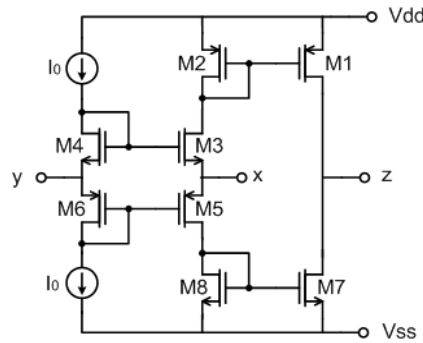
$$V_0(s)/V_i(s) = 1/(sc_p + g_0)r_x \qquad (5)$$

The aspect ratio of the MOSFETs in Fig 4.b are chosen as given in Table 1.

Table.1 Transistor dimensions of CCCII

M_1	42μm/0.4μm
M_2	42μm/0.4μm
M_3- M_4	15μm/0.4μm
M_5- M_6	35μm/0.4μm
M_7	15μm/0.4μm
M_8	15μm/0.4μm
NMOS current mirrors	12 μm /1 μm
PMOS current mirrors	30 μm /1 μm
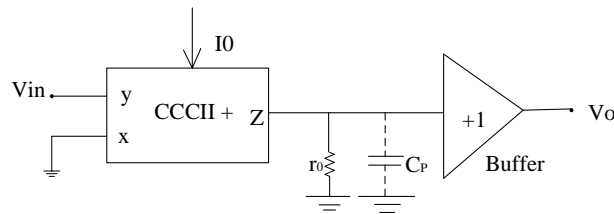
(a)

(b)

Fig.4 a) Active-only integrator block. b) Transistor level realization of the CCCII

IV.   REALIZATION OF SECOND ORDER IMAGE-REJECT COMPLEX FILTER

In this section, it is considered the design issues of a second order complex filter based on real active-only filter with two integrator loop configurations in Fig.5. As it can be seen from this figure, two of CCCIIs are used to realize voltage–to-current conversion in the filter feedback loops [11].

It is possible to find the filter transfer functions with routine analysis as follow:

$$\frac{V_{LP}}{V_{in}} = -\frac{H_1\omega_0^2}{s^2 + s\dfrac{\omega_0}{Q} + \omega_0^2}, \qquad \frac{V_{LP}}{V_{in}} = -\frac{H_2 s\dfrac{\omega_0}{Q}}{s^2 + s\dfrac{\omega_0}{Q} + \omega_0^2} \qquad (6)$$

$$\omega_0 = \sqrt{\frac{1}{r_{x2}r_{x3}C_{p1}C_{p2}}} \qquad Q = \sqrt{\frac{C_{p1}}{C_{p2}}}\frac{r_{x4}}{\sqrt{r_{x2}r_{x3}}} \qquad (7)$$

where $\qquad H_1 = \dfrac{r_{x3}}{r_{x5}}$, $\qquad H_2 = \dfrac{r_{x4}}{r_{x5}}$

As it can be seen from the transfer function given above, it is possible to set the center frequency of the filter electronically to the desired value by intrinsic resistances r_{x2}, r_{x3}. It can be also adjusted the filter's quality factor by the intrinsic resistance, r_{x4}, after adjusting center frequency to the desired value.
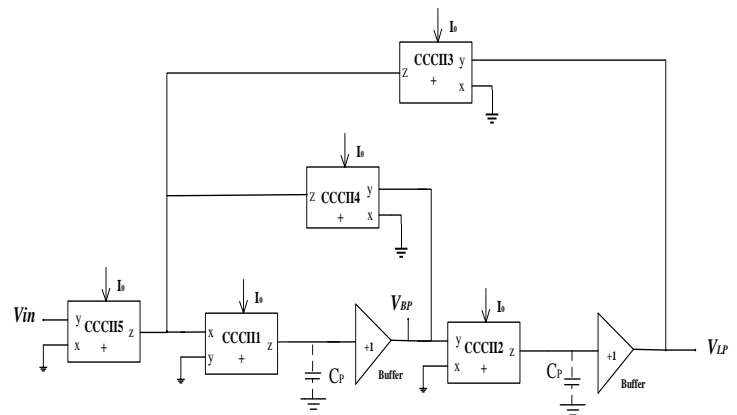
Fig. 5 Real active-only two integrator loop filter

By applying the procedure described in Section III to the circuit in Fig.5, we can obtain the second order complex filter shown in Fig.6. For this circuit implementation, two of the real active only loop filters are interconnected according to the procedure defined in Section III by appropriate using the intercoupling branches.

From the other side, as it can be known, in-phase (I) and quadrature (Q) components have equal amplitude and 90-degree phase difference in an ideal low IF mixer. In case of the gain and phase mismatch between in-phase and quadrature signals, IQ imbalance calibration circuit should be used. Therefore, it should be also noted that, the proposed second order complex filter implementation is realized without using any cascade configuration. Hence, it is expected that the IQ imbalance calibration circuit would be simple, in case of any gain and phase mismatches between in-phase and quadrature signals.

It can be seen that from the Fig.6, the proposed filter with all key parameters are electronically adjustable. It should be noted that, the lack of passive capacitors and resistors in the circuit design has significantly reduced the area covered by the filter.

Note that, the current conveyors which are used for cross-coupled branches are connected to the quadrature part of the filter as the same way and only one half of the circuit is shown for the sake of simplicity.
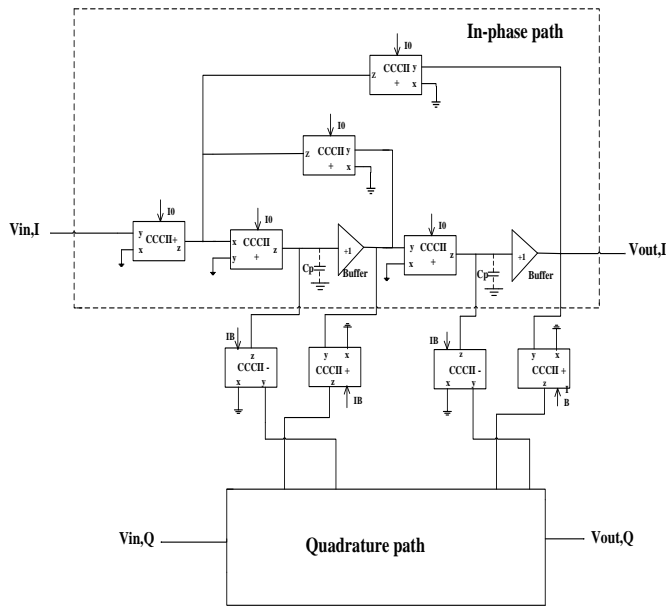
Fig.6 Implementation of the second-order complex filter (for the sake of simplicity, the quadrature part of the complex filter is not shown).

V. SIMULATION RESULTS

In order to justify the usefulness of the proposed approach, we have simulated first-order complex filter using design tool in CADENCE environment. All the current mirrors are designed by using simple current mirrors and the ±1.65V power supply is used for circuit biasing. The complex band-pass filter with a central frequency of 2MHz and a bandwidth of 1MHz is realized. For this design, integrator's cut-off frequency and frequency shift value are required to be 500kHz and 2MHz respectively. According to this implementation, the image-reject ratio is obtained to be as approximately 18dB, as shown in Fig.7.

As explained above, the complex band pass filter's center frequency and first order filter frequency are obtained respectively, such as: $\omega_0 = g_{m,cpl}/C_p$ and $\omega_p = g_m/C_p$. According to these equations, for a 2MHz bandpass filter characteristic with a bandwidth of 1MHz, the transconductance ratio should be 4 ($g_{m,cpl}/g_m = \omega_0/\omega_p$). Considering square-law characteristic of CMOS, it can easily be said that the current ratio is obtained also 16.
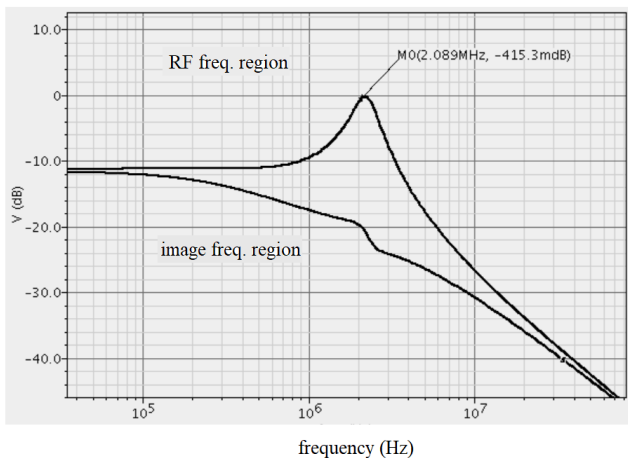
Fig.7 Normalized simulation result of first order complex filter

In addition, the proposed second order complex filter is realized with a center frequency of 8.5MHz and bandwidth of 2MHz by using 0.35um AMS CMOS process.
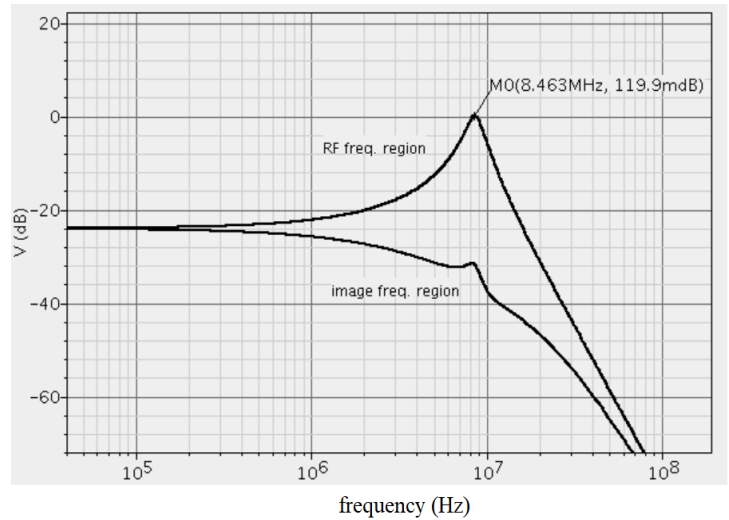
Fig.8 Normalized simulation result of second order complex filter

For the second order complex filter characteristic, the image rejecttion ratio is obtained approximately 30dB. The simulation results verfy that the proposed filters operate properly.

In addition to these simulations, it is obtained the simulation results of the second order complex filter for different biasing currents of CCCIIs. As shown in Fig.9, the bandpass filter can be adjusted electronically from 4.3 MHz to 9.3 MHz by controlling the biasing currents. As it can be seen clearly from these results, the bandpass filter has an electronic tuning range of about half a decade.
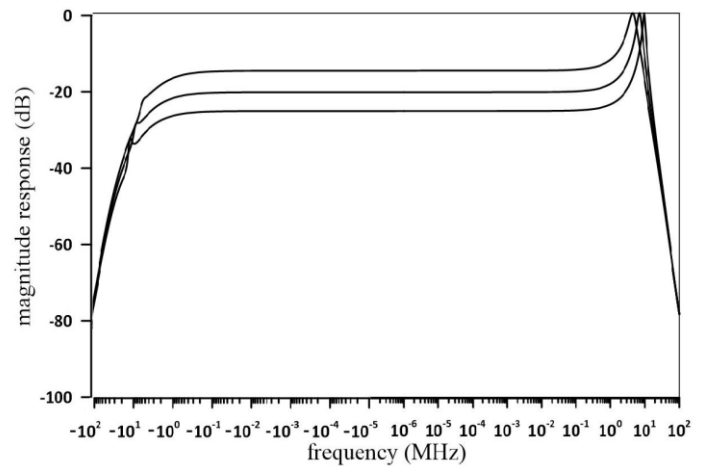

Fig.9 Normalized bandpass filter response of the second order complex filter for different values of the biasing currents

It should be said that, one of the important point to be considered in filter design is the sensitivity of the filter's quality factor (Q) and center frequency (ω_0). As a result, the sensitivity of the basic parameters of the filter circuit is shown below:

$$-S_{rx2}^{\omega 0} = -S_{rx3}^{\omega 0} = -S_{Cgs1}^{\omega 0} = -S_{Cgs2}^{\omega 0} = 0.5 \text{ and}$$

$$S_{Cp1}^{Q} = -S_{Cp2}^{Q} = -S_{rx2}^{Q} = -S_{rx3}^{Q} = 0.5$$

As it can be seen here, the sensitivities of the filter are smaller than one.

VI. CONCLUSION

In this paper, a first order and second order complex filters having a simple topology with electronically adjustable filter parameters are presented. The proposed filters are simulated using SPECTRE in the CADENCE without using any on chip bulky capacitors.

In order to illustrate the feasibility of the circuits, simulation results are obtained by using design tool in CADENCE environment. Note that in this implementation, it is achieved not only substantial reduction in the chip area but also complex filters capable of providing electronically controllable parameters. The another advantage of the filters is that it is possible to cascade the circuits. Therefore, it should be noted that, in application where high-order filters are required, the proposed complex filters can be used in cascade configuration to provide necessary image rejection.

REFERENCES

[1] B.Razavi, "RF Microelectronics". Englewood Cliffd, NJ: Prentice-Hall, 1998.
[2] F. Behbahani, Y. Kishigami, J. Leete, and A. A. Abidi, "CMOS mixers and polyphase filters for large image rejection," IEEE J. Solid-State Circuits, vol. 36, 2001, pp. 873–887.
[3] P. Andreani and S. Mattison, "A CMOS gm-C IF Filter for Bluetooth", IEEE 2000 Custom integrated circuits conference, pp 391-394.
[4] P. Khumsat and A. Worapishet, "Design of 1.8-V CMOS Polyphase Filter for Dual-Mode Bluetooth/ZigBee Transceiver", ECTI transactions on electrical Eng. Electronics and communications vol.4 no. 1, 2006, pp. 29-34.
[5] A. A. Emira and E. Sánchez-Sinencio, "A Pseudo Differential Complex Filter for Bluetooth With Frequency Tuning", IEEE transactions on circuits and systems II: Analog and Digital Signal Processing, vol. 50, no. 10, 2003, pp. 742-754.
[6] Martin K. Complex Signal Processing is not complex. IEEE Transactions on Circuits and Systems I: Regular Papers, vol. 51; 2004. pp. 1823–1836.
[7] Behbahani F., Leete J., Kishigami Y., Roithmeier A., Hoshino K., Abidi A.A. (2000). A 2.4 GHz low-IF receiver for wideband WLAN in 0.6μm CMOS architecture and front-end, IEEE Journal of Solid –State Circuits, Vol. 35, 1908-1916.
[8] Galal S.H., Ragaie H.F., Tawfik M.S.(2000). RC sequence asymmetric polyphase networks for RF integrated transceivers, IEEE Transactions on Circuits and Systems-II: Analog and Digital Signal Processing, Vol.47, 18-27.
[9] Haddad F., Zaid L., Frioui O. (2000). Polyphase filter design methodology for wireless communication applications, INTECH Open Access Publisher.
[10] Laoudias C., Psychalinos. C. (May 2010). Low-voltage bluetooth/ZigBee Complex filter using current mirrors, Proc. ISCAS, 1268-1271.
[11] H. Atar Yıldız, A. Toker and S. Özoğuz, 'On the design and implementation of real active-only filters', Proc. 35th International Conference on Telecommunications and Signal Processing (TSP'2012), pp. 369-373, Prague, Czech Republic, 2012, July 3-4.
[12] D. Rabaey and J. Sevenhans, "The challenges for analog circuit design in mobile radio VLSI chips," in Proc. AACD Workshop, Leuven, Mar. 1993, vol. 2, pp. 225-236.
[13] H. Atar Yıldız, S. Özoğuz, A. Toker and O. Çiçekoğlu, 'On the realization of MOS-only allpass filters' Circuits, Systems & Signal Processing (CSSP), Vol. 32, No.3, 2013, pp. 1455-1465.
[14] A. Fabre, O.Saaid, H.Barthelemy, "On the frequency limitation of the circuits based on second generation current conveyors,"Analog Int. Circ. Sign.Process., vol.7, 1995, pp. 113- 129.

BIOGRAPHY

HACER ATAR YILDIZ was born in Trabzon, Turkey. She received the B.Sc. and M.Sc. degrees in Electronics Engineering from the Faculty of Electrical and Electronics Eng., Karadeniz Technical University, Turkey in 1997 and 2000, respectively. She received her Ph.D. degree in 2015 in Electronics Engineering from Istanbul Technical University. Her research interests include analog circuit design, active-only filters and analog neural networks.

Publication Ethics

The journal publishes original papers in the extensive field of Electrical-electronics and Computer engineering. To that end, it is essential that all who participate in producing the journal conduct themselves as authors, reviewers, editors, and publishers in accord with the highest level of professional ethics and standards. Plagiarism or self-plagiarism constitutes unethical scientific behavior and is never acceptable.

By submitting a manuscript to this journal, each author explicitly confirms that the manuscript meets the highest ethical standards for authors and coauthors

The undersigned hereby assign(s) to *Balkan Journal of Electrical & Computer Engineering* (BAJECE) copyright ownership in the above Paper, effective if and when the Paper is accepted for publication by BAJECE and to the extent transferable under applicable national law. This assignment gives BAJECE the right to register copyright to the Paper in its name as claimant and to publish the Paper in any print or electronic medium.

Authors, or their employers in the case of works made for hire, retain the following rights:

1. All proprietary rights other than copyright, including patent rights.
2. The right to make and distribute copies of the Paper for internal purposes.
3. The right to use the material for lecture or classroom purposes.
4. The right to prepare derivative publications based on the Paper, including books or book chapters, journal papers, and magazine articles, provided that publication of a derivative work occurs subsequent to the official date of publication by BAJECE.
5. The right to post an author-prepared version or an of ficial version (preferred version) of the published paper on an i nternal or external server controlled exclusively by t he author/employer, pr ovided that (a) such posting is noncommercial in nature and the paper is made available to users without charge; (b) a copyright notice and full citation appear with the paper, and (c) a link to BAJECE's official online version of the abstract is provided using the DOI (Document Object Identifier) link.

CONTENTS